


Summer 8-15-2018

Building on Nature: Spectroscopic Studies of Photosynthesis-Inspired Pigments, Fused Light Harvesting Proteins, and Bacterial Reaction Center Mutants

Kaitlyn Faries

Washington University in St. Louis

Follow this and additional works at: https://openscholarship.wustl.edu/art_sci_etds

 Part of the [Biochemistry Commons](#), and the [Physical Chemistry Commons](#)

Recommended Citation

Faries, Kaitlyn, "Building on Nature: Spectroscopic Studies of Photosynthesis-Inspired Pigments, Fused Light Harvesting Proteins, and Bacterial Reaction Center Mutants" (2018). *Arts & Sciences Electronic Theses and Dissertations*. 1620.
https://openscholarship.wustl.edu/art_sci_etds/1620

This Dissertation is brought to you for free and open access by the Arts & Sciences at Washington University Open Scholarship. It has been accepted for inclusion in Arts & Sciences Electronic Theses and Dissertations by an authorized administrator of Washington University Open Scholarship. For more information, please contact digital@wumail.wustl.edu.

WASHINGTON UNIVERSITY IN ST. LOUIS

Department of Chemistry

Dissertation Examination Committee:

Dewey Holten, Chair

Christine Kirmaier, Co-Chair

Robert Kranz

Liviu Mirica

Jacob Schaefer

Building on Nature: Spectroscopic Studies of Photosynthesis-Inspired Pigments, Fused Light Harvesting Proteins, and Bacterial Reaction Center Mutants

by

Kaitlyn Faries

A dissertation presented to
The Graduate School
of Washington University in
partial fulfillment of the
requirements for the degree
of Doctor of Philosophy

August 2018
St. Louis, Missouri

© 2018, Kaitlyn Faries

Table of Contents

Acknowledgments.....	v
Abstract of the Dissertation	vii
Chapter 1: Backgrounds and Methods.....	1
Background.....	1
Experimental Methods	15
Collaborations and Contributions	17
References.....	18
Chapter 2: Photophysical Properties and Electronic Structure of Chlorin-Imides: Bridging the Gap between Chlorins and Bacteriochlorins.....	23
Abstract.....	24
1. Introduction.....	25
2. Experimental Section	31
3. Results.....	32
4. Discussion.....	48
5. Outlook	53
References.....	55
Chapter 3: Augmenting light coverage for photosynthesis through YFP-enhanced charge separation at the <i>Rhodobacter sphaeroides</i> reaction centre.....	62
Abstract.....	63
1. Introduction.....	64
2. Methods.....	66
3. Results.....	77
4. Discussion.....	94
References.....	99
Chapter 4: High Yield of Secondary B-side Electron Transfer in Mutant <i>Rhodobacter capsulatus</i> Reaction Centers	103
Abstract.....	104
1. Introduction.....	105
2. Materials and Methods.....	107
3. Results and Discussion.....	109
References.....	138

Chapter 5: Optimizing Multi-Step B-side Charge Separation in Photosynthetic Reaction Centers from <i>Rhodobacter capsulatus</i>	143
Abstract	144
1. Introduction	145
2. Material and Methods	149
3. Results	151
4. Discussion	166
References	173
Chapter 6: Species Differences in Unlocking B-side Electron Transfer in Bacterial Reaction Centers	178
Abstract	179
1. Introduction	180
2. Materials and Methods	184
3. Results	186
4. Discussion	193
References	200
Chapter 7: Manipulating the energetics and rates of electron transfer in <i>Rhodobacter capsulatus</i> reaction centers with asymmetric pigment content	205
Abstract	206
1. Introduction	207
2. Materials and Methods	211
3. Results and Discussion	215
References	244
Conclusions/Outlook	249
Appendices	250
Appendix 1. Supporting Information for Chapter 2	250
Appendix 2. Supporting Information for Chapter 3	256
Appendix 3. Supporting Information for Chapter 5	265
Appendix 4. Supporting Information for Chapter 6	277
Appendix 5. Supporting Information for Chapter 7	296

Acknowledgments

A dissertation such as the one presented below does not come to fruition without the constant and steadfast support of mentors, colleagues, friends and family. I'd first like to thank the two best mentors a graduate student could ever hope to have – Dr. Christine Kirmaier and Dr. Dewey Holten. These two people care for their students like family, and without them I could never have come this far. And like a family, I would also like to thank the former and current members of the Holten Research Group who taught me techniques, ideas, and were always there to lend a helping hand. Additionally, I'd like to thank numerous collaborators because without their samples, complementary research, and fruitful discussions, the following dissertation would never have been possible: Dr. Philip Laible and Dr. Deborah Hanson, Dr. Jonathan, Dr. David Bocian, and Dr. Neil Hunter, Dr. Katie Grayson, Dr. David Swainsbury, and Elizabeth Martin. Furthermore, I am forever grateful to the NSF GRFP, the Monticello Foundation's Mr. and Mrs. Spencer T. Olin Fellowship, and the Virginia J. Stooker Endowed P.E.O. Scholarship for financially supporting me throughout my graduate school journey. Finally, a most special thanks to my incredible and loving family. To Sean, who has always treated me as his 'favorite' and his only want for me is to achieve my dreams. To my loving parents, who still treat me like the most important thing in their life and have been with me through every step of this sometimes-rocky road. To my sisters, who, although very different people, continue to inspire me in their own ways every day. And last (but not least) I want to thank to my daughter Akasha, my greatest achievement, for teaching me what is truly important in life.

Kaitlyn Faries

Washington University in St. Louis

August 2018

Abstract of the Dissertation

Building on Nature: Spectroscopic Studies of Photosynthesis-Inspired Pigments, Fused Light
Harvesting Proteins, and Bacterial Reaction Center Mutants

by

Kaitlyn Faries

Doctor of Philosophy in Chemistry

Washington University in St. Louis, 2018

Professor Dewey Holten, Chair

Professor Christine Kirmaier, Co-Chair

Photosynthesis is the dominant form of solar energy conversion on the planet, making it critical to understand the fundamentals of the process in order to effectively mimic and improve upon it for human energy needs. The initial stages of photosynthesis include light harvesting and chemical conversion of that harvested energy via electron transport, with both of these stages relying on pigments (or chromophores) such as chlorophyll and specific protein architectures for the processes. In this work, the fundamental underpinnings of photosynthetic light harvesting and electron transport are explored via spectroscopy of various photosynthetic systems with altered natural pigments and proteins. Specifically, these include: 1) chlorophyll-like chromophores containing unnatural functional groups and their altered photophysical properties (such as red-shifted absorption), 2) purple bacterial reaction centers with modified native protein architecture and pigment content with increased 'wrong-way' electron transfer, and 3) purple bacteria wherein the non-photosynthetic pigment-protein complex yellow fluorescent protein (YFP) was added to the bacteria's natural reaction center, resulting in enhanced light-harvesting capacity.

Chapter 1: Backgrounds and Methods

Background

The sun is an incredible source of energy for our planet, and is responsible for sustaining the majority of life and energy needs of the planet.¹ Thus, it is of great interest to humans to exploit solar energy to meet growing global needs. Photosynthesis is the prevailing natural process (found in plants, algae, and some types of bacteria) that converts solar energy into chemical energy and can serve as a model for our own solar harvesting systems. However, photosynthesis is a complex process with several key elements, including light harvesting and energy conversion. The processes considerably rely on protein-pigment complexes, known as antennas (light-harvesting)² and reaction centers (electron transfer)³ respectively. While the structure of the complexes can vary significantly depending on the organism¹, in common to all light harvesting and reaction center complexes are pigments/chromophores known as tetrapyrroles.

Tetrapyrroles, Gouterman's Four-Orbital Model, and the Importance of Structure

The light harvesting and energy conversion stages of photosynthesis are fundamentally driven by pigments and their intrinsic properties. Specifically, photosynthesis primarily utilizes tetrapyrroles, a class of chromophores that includes porphyrins like hemes found in cytochromes (and blood)⁴⁻⁶, chlorins like chlorophyll *a* (Chl *a*) in plants and cyanobacteria⁷⁻⁹, and bacteriochlorins such as bacteriochlorophyll *a* (BChl *a*) found in purple bacteria (Fig. 1)^{8,10}. The absorption of ultraviolet (UV)/visible (VIS)/near-infrared (NIR) light by tetrapyrroles, which is exploited by photosynthesis, is strongly influenced by their aromatic, 18 π electron macrocyclic structures (Fig. 1). Additionally, the subsequent reduction of double bonds (positions 17-18 in

chlorins; positions 7-8 and 17-18 in bacteriochlorins) that are conjugated to the primary macrocycle leads to a dramatic change in intensity and wavelength of absorption in the UV/Vis/NIR (Fig. 2).¹¹ Moreover, addition/changes to substituents on the macrocycle can further influence absorption (to be discussed in detail below).

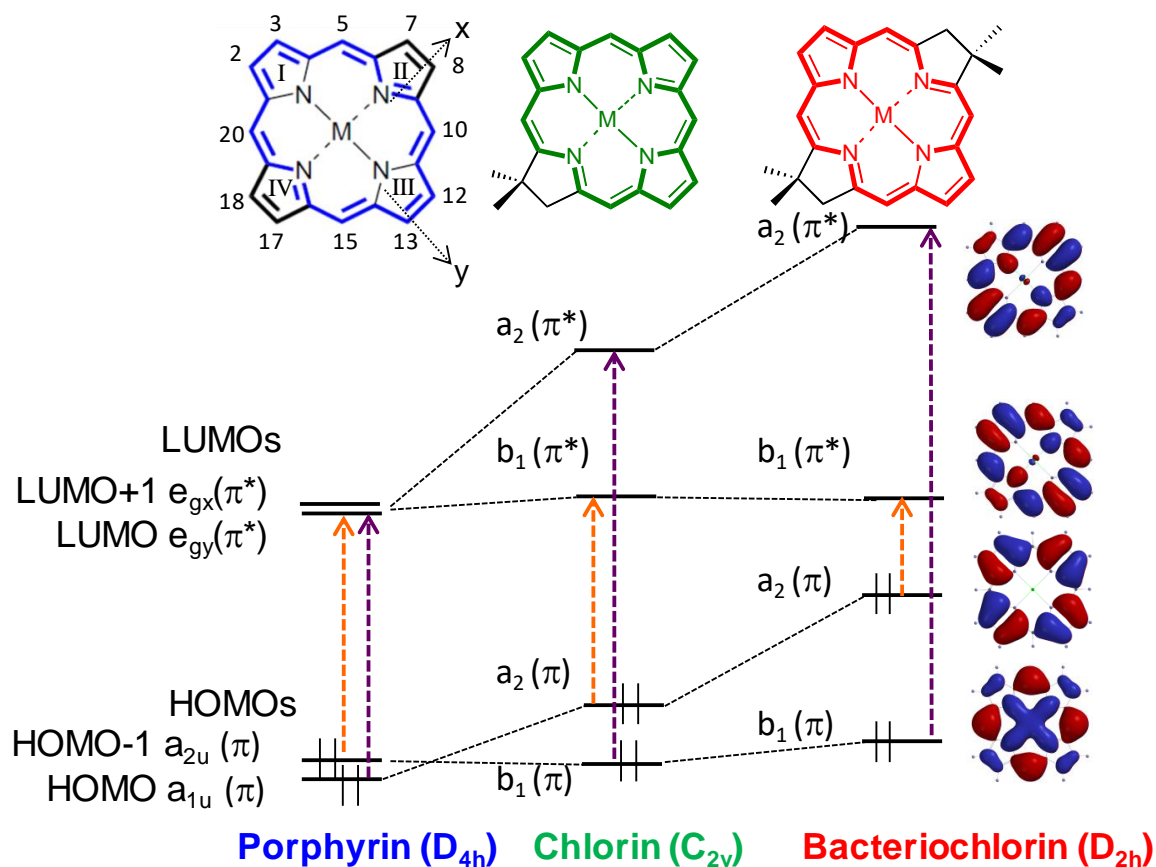


Figure 1. Basic macrocycles of the three classes of tetrapyrroles: porphyrins (blue), chlorins (green), and bacteriochlorins (red), the associated energy levels of their four frontier molecular orbitals, and the electron density maps of the four orbitals. The arrows through the porphyrin macrocycle indicate the axes of symmetry for tetrapyrroles, the numbers the positions for substituents on the macrocycle, and roman numerals label the rings.

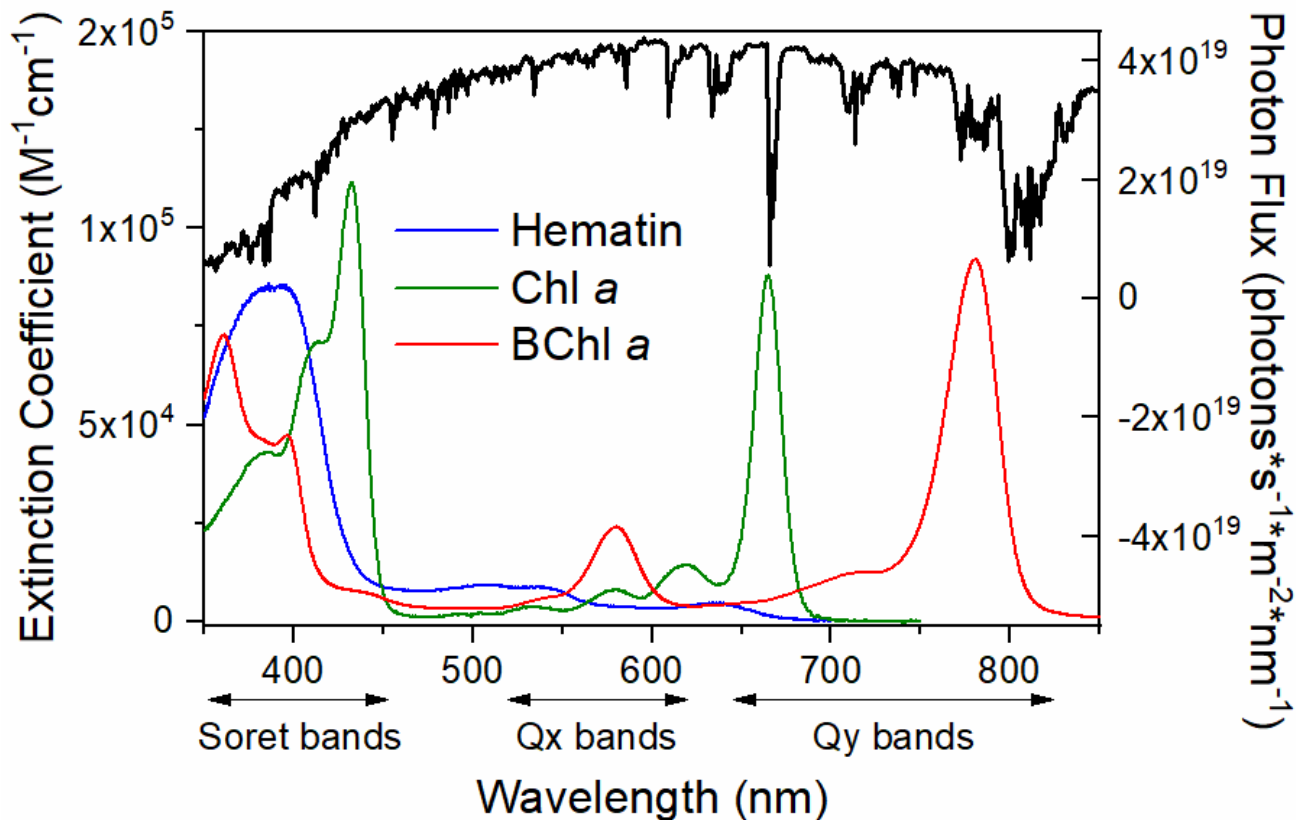


Figure 2. Molar absorptivity spectra of the porphyrin hematin (blue), chlorin Chl *a* (green), and bacteriochlorin BChl *a* (blue). The sun's output (e.g. the solar spectrum) is also shown (black).

Gouterman's Four Orbital Model¹²⁻¹⁴ can be used to describe and predict absorption changes due to macrocycle and substituent alterations. Typically, as π -conjugation is increased in a system, the lower the energy absorbed by that system for electronic transitions – a phenomenon consistent with the particle in a box model of quantum theory.^{15,16} However, tetrapyrroles exhibit the opposite trend (Fig. 2) – as the degree of π -conjugation is increased from bacteriochlorin \rightarrow chlorin \rightarrow to porphyrin, so too does the energy required for electronic transitions. In order to explain this reversal, Gouterman proposed the Four Orbital Model – a theory that states that the electronic transitions of tetrapyrroles involves not the simple promotion of an electron from the highest occupied molecular orbital (HOMO) to the lowest unoccupied molecular orbital (LUMO). Rather, more complex linear combinations of frontier molecular orbitals (HOMO-1,

HOMO, LUMO, LUMO-1) are invoked. Shown below are the equations (Eq. 1-2) for the biologically relevant y-polarized Soret (B_y) and Q (Q_y) region transitions:

$$B_y = B_y^0 \cos \eta_y + Q_y^0 \sin \eta_y \quad (1a)$$

$$Q_y = Q_y^0 \cos \eta_y - B_y^0 \sin \eta_y \quad (1b)$$

$$\left. \begin{matrix} B_y^0 \\ Q_y^0 \end{matrix} \right\} = \frac{1}{\sqrt{2}} [(\text{HOMO-1} \rightarrow \text{LUMO+1}) \pm (\text{HOMO} \rightarrow \text{LUMO})] \quad (2)$$

$$\eta_y = [\tan^{-1}(\Delta E_{\text{dif}}/2\delta)]/2 \quad (3)$$

$$\delta = \int (\text{HOMO-1} \rightarrow \text{LUMO}) \mathbf{H} (\text{HOMO} \rightarrow \text{LUMO+1}) d\nu \quad (4)$$

$$\Delta E_{\text{dif}} = [E(\text{LUMO+1} - \text{HOMO-1}) - E(\text{LUMO} - \text{HOMO})] \quad (5a)$$

The η_y term (Eq. 3), also known as the ‘unmixing’ coefficient, is a key parameter in determining where the absorption bands will be and their relative intensities. η_y is in turn influenced by:

1) the configuration interaction energy (δ , Eq. 4), which is related to orbital overlap, electron repulsion, and electron density. η_y decreases from porphyrin \rightarrow chlorin \rightarrow bacteriochlorin because the orbitals move further apart in energy (Fig. 1), but it is largely unaffected by small substituent changes.

2) the orbitals’ energy difference (ΔE_{dif} , Eq. 5a), which is significantly altered as the macrocycle changes from porphyrin \rightarrow chlorin \rightarrow bacteriochlorin (Fig. 1) as the HOMO and LUMO+1 orbitals are destabilized, and also by substituent changes (depending on the position of the change, discussed in greater detail below).

It is clear from Eq. 5a (and Fig. 1) that as orbital energies change from porphyrin \rightarrow chlorin \rightarrow bacteriochlorin, ΔE_{dif} will become larger and cause η_y (Eq. 3) to increase (this can also occur if substituents are added/changed and affect the electron density of the orbitals). And as η_y (and ΔE_{dif}) increases, the splitting (σ_y) of the B_y and Q_y peaks increases (Eq. 6&8), the energy of the Q_y transition decreases (Eq. 7b), and intensity of absorption is shifted to the Q_y peak (Eq. 9).

$$\Delta E_{\text{avg}} = [E(\text{LUMO}+1 - \text{LUMO}-1) + E(\text{LUMO} - \text{HOMO})]/2 \quad (5b)$$

$$\sigma_y = 2\delta/\cos(2\eta_y) \quad (6)$$

$$E_{B_y} = \Delta E_{\text{avg}} + \sigma_y/2 \quad (7a)$$

$$E_{Q_y} = \Delta E_{\text{avg}} - \sigma_y/2 \quad (7b)$$

$$\sigma_y = \Delta E_{\text{dif}} / \sin(2\eta_y) \quad (8)$$

$$\Sigma_{Q_y}/\Sigma_{B_y} = [1-\cos(2\eta_y)]/[1+\cos(2\eta_y)] \quad (9)$$

In other words, the Q_y band becomes more intense and bathochromically shifted as the orbital energies become increasingly further apart and mix less in porphyrins \rightarrow chlorins \rightarrow bacteriochlorins.

Increasing the Q_y absorption and red-shifting it is of great interest in synthetic chemistry due to the large proportion of solar photons that are emitted in the red and near-infrared (NIR) regions of the solar spectrum (Fig. 1, black line). These changes in the Q_y band can be accomplished not only by shifting the tetrapyrrole macrocycle from porphyrin \rightarrow chlorin \rightarrow bacteriochlorin, but as previously indicated, by altering substituents on the macrocycle. Extensive characterization of the effect of substituent changes on the electronic properties of numerous types of porphyrins^{17,18,19}, chlorins^{7,20, 21,22,23,24,25} and bacteriochlorins^{10,26,27,28} has been

detailed in the literature. Generally, the key positions/substituents (Figure 1) on the macrocycle that lead to red-shifted and increased Q_y absorption are those that stabilize the LUMO orbital by expanding the conjugated system, such as electron-withdrawing groups (formyl, acetyl) at the 3- and 13-positions.²³ Furthermore, the addition of ring structures to the macrocycle at certain positions can also lead to enhanced and bathochromically shifted Q_y bands, and this effect in chlorins is explored in detail in Chapter 2 (for bacteriochlorins, see Ref. 28).

The Role of Tetrapyrroles and Proteins in Photosynthetic Light-Harvesting

As detailed in the previous section, tetrapyrroles are very versatile and can be engineered to absorb a variety of wavelengths. Nature has capitalized on the unique absorption properties of tetrapyrroles and they are used almost exclusively to harvest light from the sun in the early stages of photosynthesis. In nature however, there are only a limited number of tetrapyrroles utilized in light harvesting (Table 1, Fig. 3).

Table 1. Natural photosynthetic tetrapyrroles, macrocycle type (e.g. porphyrin, chlorin, or bacteriochlorin), and the position of the Q_y peak in solvent.

Tetrapyrrole	Macrocycle-type	Q_y Peak (nm)
Chl <i>a</i> [†]	Chlorin	665
Chl <i>b</i> [†]	Chlorin	646
Chl <i>c</i> ²⁹	Porphyrin	629
Chl <i>d</i> [†]	Chlorin	691
Chl <i>f</i> ³⁰	Chlorin	705
BChl <i>a</i> [†]	Bacteriochlorin	780
BChl <i>b</i> ³¹	Bacteriochlorin	798
BChl <i>c</i> ³²	Chlorin	671
BChl <i>d</i> ^{33,34}	Chlorin	658
BChl <i>e</i> ^{33,34}	Chlorin	660
BChl <i>g</i> ³²	Bacteriochlorin	773

[†]From this author in toluene. ²⁹From Ref. 29 in acetone. ³⁰From Ref. 30 in acetone-methanol. ³¹From Ref. 31 in methanol/acetonitrile/ethyl acetate. ³²From Ref. 32. in pyridine. ^{33,34}From Ref. 33&34 in pyridine.

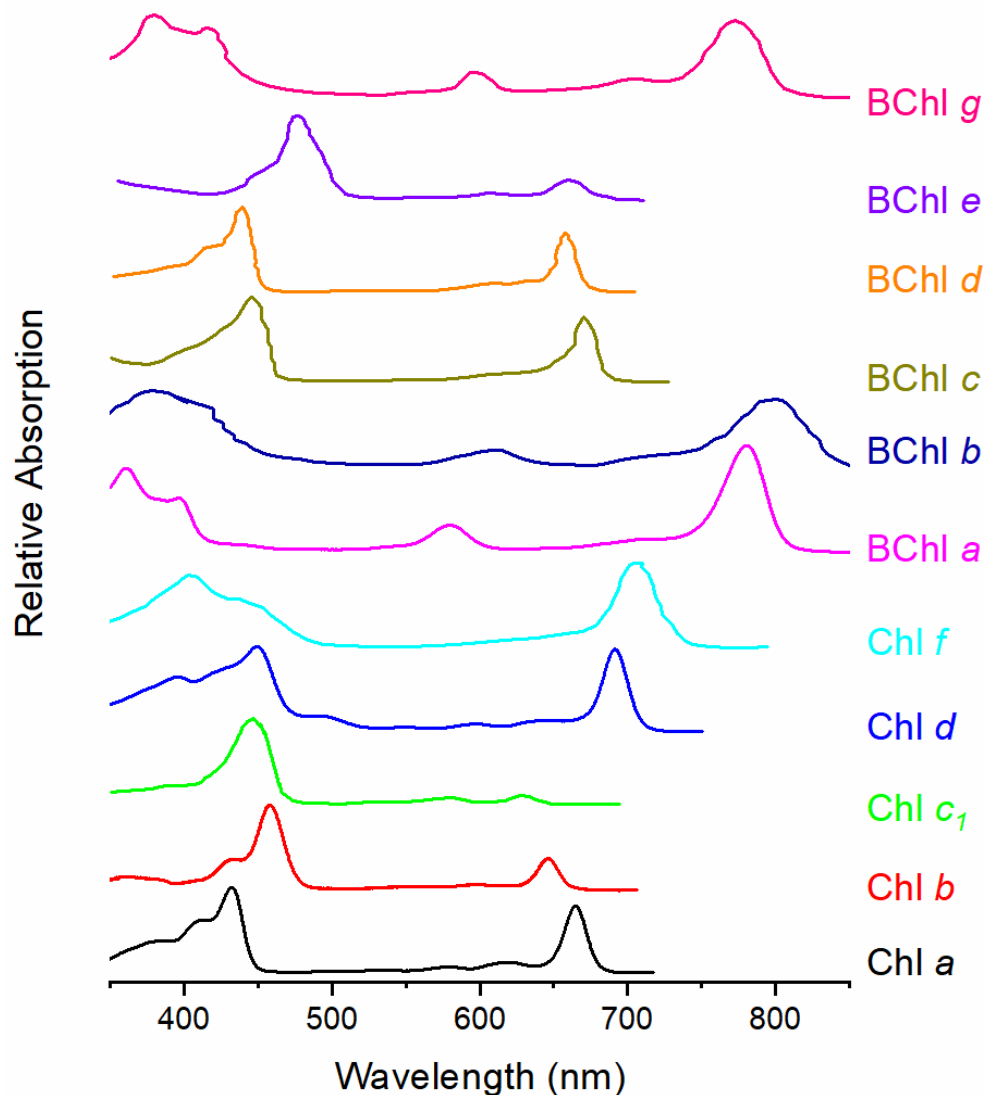


Figure 3. Absorption spectra of natural photosynthetic tetrapyrroles.

Table 1 and Figure 3 illustrate the limited absorption ranges of individual tetrapyrroles. To compensate, organisms often include accessory pigments, such as carotenoids, to absorb additional wavelengths of light, typically in the yellow-green region (~500-550 nm).^{35,36} Another (arguably more important) tactic adopted by photosynthetic organisms to alter/increase light harvesting capability is to modify the protein environment surrounding the pigments. An excellent example of this concept is the light-harvesting (LH) 1 and 2 proteins of purple bacteria

– the slight differences in these protein architectures (Fig. 4) lead to considerable variation in the spectra of BChl *a* (Fig. 5) despite the pigments themselves being unchanged. More specifically, both LH1 and LH2 use similar helical peptides (referred to as α and β subunits) that form ring-like structures and also house the BChl *a* pigments (via coordination to histidine residues for the dimeric BChls; carbonyls for the monomeric BChls³⁷). The positioning of the dimeric BChls (Fig. 4, red tetrapyrroles) in such close proximity to one another results in strongly coupled pigments that lead to a significant red-shift in the Q_y absorption of the BChls – 875 nm in the larger LH1 ring vs. 850 nm for the smaller LH2 ring vs. 780 nm for monomeric BChl *a* in solution. This excitonic coupling also occurs in the monomeric BChls (Fig. 4, blue tetrapyrroles) but to a lesser extent because they are spaced further apart than their dimeric counterparts – 800 nm vs. 780 nm for monomeric BChl *a* in solution.

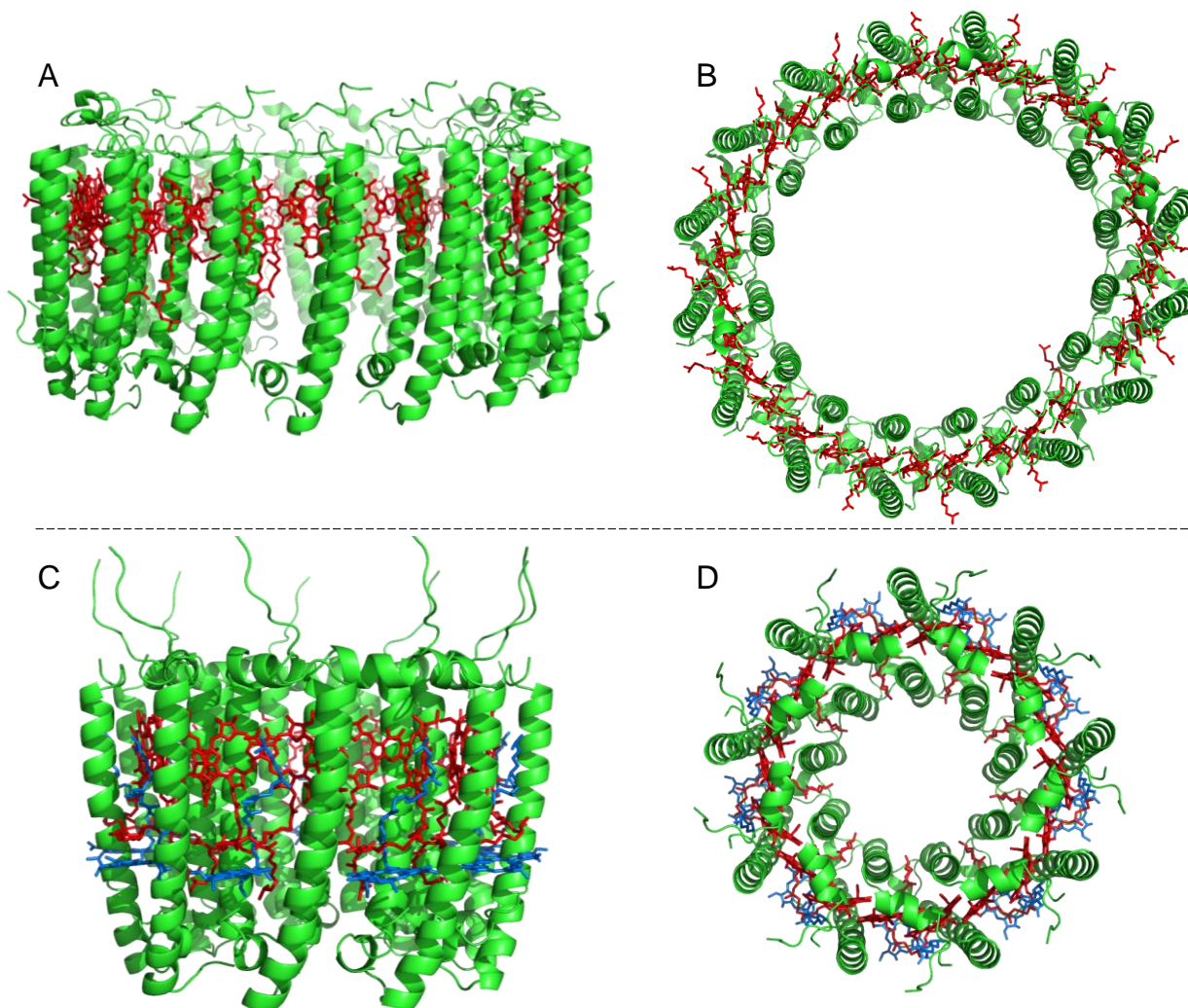


Figure 5. Crystal structures of light-harvesting complex LH1 from *T. tepidum* (PDB 5Y5S³⁸; A – side view; B – top view) and LH2 and *Rps. acidophila* (PDB 1NKZ³⁹; C – side view; D – top view). Dimeric and monomeric BChl *a* pigments are shown in red and blue respectively, with the protein α/β peptides shown in green.

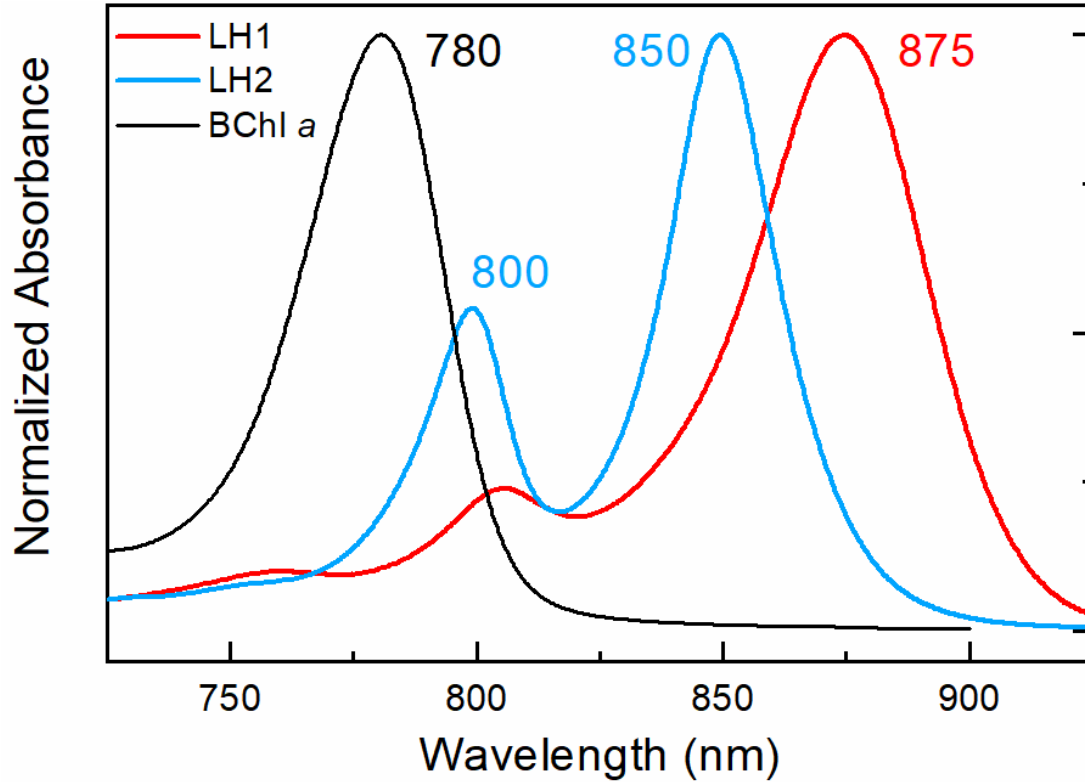


Figure 6. Absorption spectra of bacteriochlorophylls in LH1 and LH2 from *Rb. sphaeroides*.

The role of the protein goes beyond just altering the wavelengths of light utilized by the organism – it is also critical for the execution of energy transfer between pigments doing the light-harvesting and those involved in the chemical conversion of light (detailed more in the next section) by the very specific positioning of the pigments. The process by which tetrapyrroles (and other pigments) perform energy transfer can be described by Förster Theory^{40,41,42}, detailed in Eq. 10:

$$k_{EET} = \frac{1}{\tau_s} (R_0/R)^6 \quad (10)$$

where k_{EET} is the rate of energy transfer between donor and acceptor pigments, τ_s is the singlet excited state lifetime of the donor pigment, R is the distance between the pigments, R_0 is the Förster radius (in Angstroms (Å)) defined by Eq. 11:

$$R_0^6 = 8.79 \times 10^{-5} J \kappa^2 n^{-4} \quad (11)$$

where n is the refractive index, κ is the orientation factor of the transition dipoles (Eq. 12, Fig. 6), and J is the energy overlap factor (Eq. 13, Fig. 7),

$$\kappa = (\cos\alpha - 3\cos\beta_1\cos\beta_2)^2 \quad (12)$$

$$J = \int \varepsilon(\lambda)F_D(\lambda)\lambda^4 d\lambda \quad (13)$$

where ε is the extinction coefficient of the acceptor and F_D the emission spectrum of the donor.

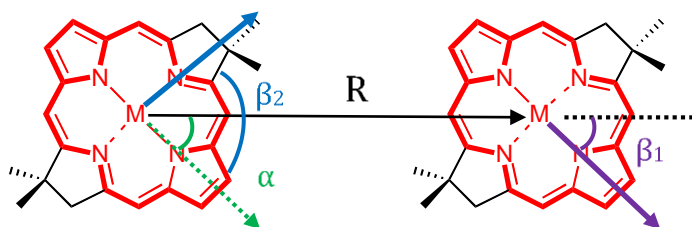


Figure 6. Transition dipole angles used to obtain the orientation factor (κ) in Förster energy transfer theory. Typically, the average value for random transition dipole orientation (0.667) is used.

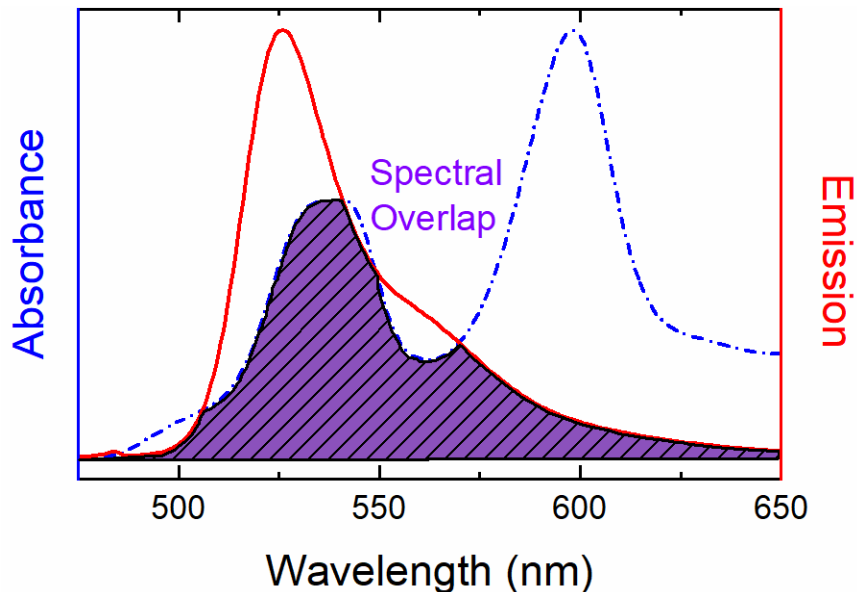


Figure 7. Example of the spectral overlap (purple region) of a donor (yellow fluorescent protein, red solid line) and acceptor (reaction center of *Rb. sphaeroides*, blue dotted line).

It is clear from Eqs. 10-13 and Figs. 6-7 that proteins in photosynthesis strongly influence energy transfer yields between pigments because of the effect the protein scaffold has on both

the photophysical properties and the orientations of the pigments. Recognizing this, researchers are increasingly utilizing protein scaffolds in pigment-protein complexes assembled *in vitro*, such as ‘biohybrid’ systems of synthetic tetrapyrroles and native α/β peptides from purple bacteria⁴³, artificial dyes attached to reaction centers⁴⁴, and wholly synthetic maquettes⁴⁵, to name a few. Additionally, many of these systems are designed to expand the light-harvesting capability of the natural system *in vitro* (recall the gaps in harvested wavelengths shown in Figure 3). However, little work has been done to increase light-harvesting capabilities of an organism *in vivo*. Chapter 3 details this very premise via the incorporation of a non-native, non-photosynthetic fluorescent protein (FP) from a jellyfish into the genome of purple bacteria to generate a fused FP-reaction center complex with increased light-harvesting capability.

Reaction Centers: Pigment-Protein Complexes Involved in the Chemical Conversion of Light

The previous section clearly shows how light-harvesting tetrapyrrole-protein complexes are critically important in the beginning stages of photosynthesis because they are exceptionally well-adapted for capturing (certain) solar wavelengths of light and performing energy transfer. But another type of tetrapyrrole-protein complex, called a reaction center (RC), plays an equally important role in the early stages of photosynthesis because it converts solar energy (obtained either directly or via light funneled to it by the light-harvesting complexes) into chemical energy via doing electron transfer across membrane. The following section details how RC complexes are perfectly suited for electron transfer reactions, in part due to the unique redox characteristics of tetrapyrroles, and the use of proteins for ideally poisoning the energetics of the forward electron transfer reaction between chromophores.

Electron transfer rates (and thus efficiency) in biological systems can be described by Marcus theory^{46,47} as follows:

$$k_{ET} = h(V_R^2)(FC) \quad (14)$$

Note that Eq. 14 includes an electronic component (V), which is driven largely by distance between the donor and acceptor chromophores (in a similar vein to light-harvesting complexes, where the protein also plays a crucial role in the positioning of the tetrapyrroles at particular distances favorable for energy transfer). Specifically,

$$V_R^2 = V_0^2 e^{(-\beta R)} \quad (15)$$

where V_0^2 is the maximum electronic coupling, β is the coefficient of decay with R , and R is the distance between the donor and acceptor. Interestingly, the electronic coupling plays a lesser role in determining the ultimate rate of electron transfer.⁴⁸ Rather, the free and reorganization energies of the chromophore states (described in the Franck-Codon (FC) term, Eq. 16) play a more substantial role:

$$FC = (4\pi kT)^{-1/2} e^{-[(-\Delta G^\circ - \lambda)^2 / 4\lambda kT]} \quad (16)$$

where k is the Boltzman constant, T is the temperature, λ is the reorganization energy (which internally is small for electron transfer between like molecules such as tetrapyrroles), and ΔG° is the difference in free energy between the donor and acceptor states. It is notable that the greatest rate of electron transfer occurs when the free energy change equals that of the reorganization energy, and that the protein environment can substantially influence both terms.

RCs are well designed to do efficient electron transfer reactions (they do so at near unity yields) because 1) the tetrapyrroles used in the RC, despite tetrapyrroles being difficult to oxidize in the ground state (porphyrin > chlorin > bacteriochlorin⁴⁹), in the excited state, are very strong reductants¹ and 2) the protein structure tightly controls the pigment distances (important for electronic coupling and reducing charge recombination) and the side chain residues fine-tune the free and external reorganization energies of the pigments. Figure 8A shows the typical structure

of a Type II RC (in this case that of a purple bacterium), which is an integral membrane protein of pseudo- C_2 symmetry with a dimer of tetrapyrroles (denoted P) used to initiate *unidirectional* electron transfer, monomeric tetrapyrroles as secondary electron acceptors, and quinones used as acceptors and/or electron shuttles (Note: Type I RCs are iron-based and electron transfer is bi-directional, but this work focuses on Type II RCs)⁵⁰. Ultimately, the final quinone acceptor is doubly reduced, binds two hydrogens, diffuses into the cytoplasm, and creates a gradient across the membrane used in synthesizing ATP.

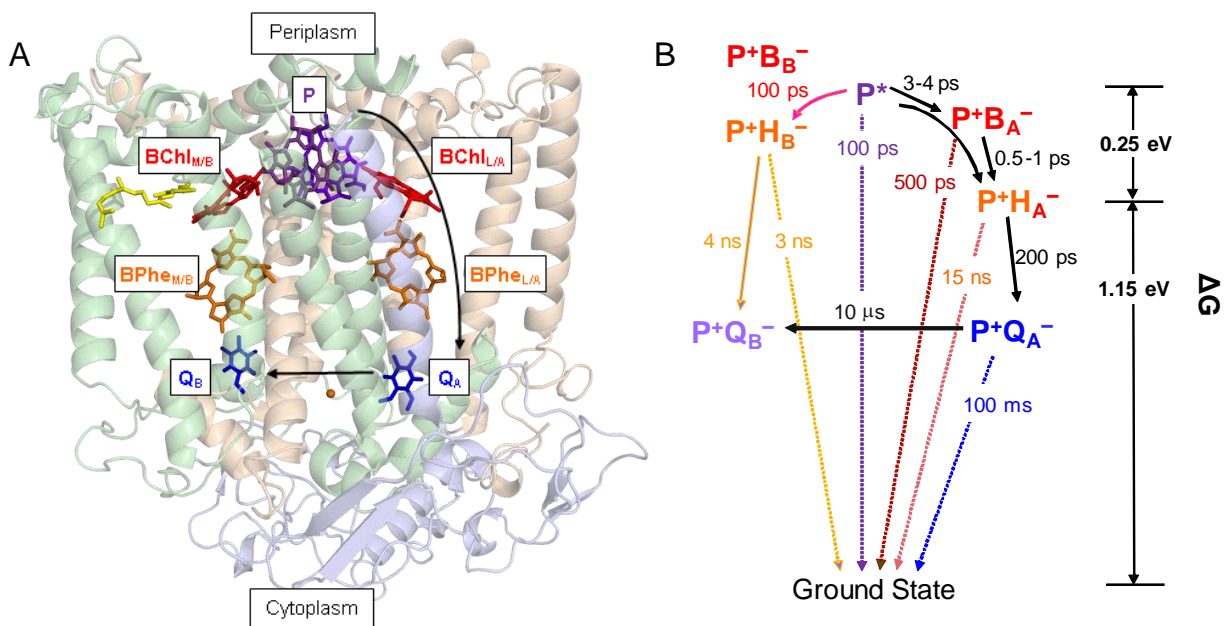


Figure 8. (A) Crystal structure of the *Rb. sphaeroides* reaction center (PDB 1PCR⁵¹) with the M-, L-, and H-subunits (green, tan, and lavender respectively) and the embedded pigments: BChl *a* dimer (P; purple), monomeric BChls (red), bacteriopheophytins (orange), quinones (blue), and carotenoid (spheroidene, yellow). Arrows indicate the direction of electron transfer. (B) Rates of forward electron transfer (black arrows) and charge recombination (color arrows).

Because of the prominent role they play in photosynthesis and their high efficiency at doing electron transfer, RCs are some of the most well-studied proteins in biology. However, to this day it is still not well-understood how the protein modulates the redox properties of the pigments such that in Type II RCs the A-side is 100% efficient at electron transfer and the B-side

is completely detuned – as such, this phenomenon of unidirectional electron transfer (despite the apparent symmetry of the A and B sides) has been extensively studied for decades, often by generating mutant RCs in purple bacteria (which is a focus in this work) and investigating the effects of the protein alterations on subsequent electron transfer using ultrafast transient absorption (TA) spectroscopy. Specifically, much work has focused on mutations that aim to detune the rates of A-side electron transfer (Fig. 8B) and/or enable electron transfer via the B-side cofactors^{52,53,54,55}. This rich history of using mutagenesis and TA spectroscopy to study the unidirectionality of electron transfer in the field of RCs is expanded further in Chapters 4-7 of this work, specifically by studying the effects of changing B-side residues to mimic the A-side (Chapter 4) or combining multiple mutations (Chapter 5), comparing residue changes in different purple bacterial species (Chapter 6), and altering tetrapyrrole composition (Chapter 7).

Experimental Methods

Static Spectroscopy

Ground state absorption (all chapters)

Measurements from 300-1100 nm were taken at room temperature on either a Cary-100 or Shimadzu UV-1800 using a 0.2 nm step size and 0.1 s integration time. Samples were contained in 1 cm or 2 mm pathlength glass or quartz cuvettes. Blank solvent or buffer solution spectra were obtained separately and manually subtracted (to ensure no offset). Sample concentration varied depending on complementary experiments: ~1 μM for samples used in fluorescent quantum yield measurements (Ch. 2-3) or pigment analysis (Ch. 7) or ~20 μM for TA experiments (Ch. 3-7).

Fluorescence (to obtain fluorescence spectra and quantum yields, Ch. 2-3)

Fluorescence data was obtained at room temperature using either a Spex Fluorolog Tau 2 or Horiba Nanolog using 2 nm steps, 0.1 s integration times, and 4 nm excitation/emission bandwidths. Spectra were corrected for the non-uniformity of the lamp, gratings, detector, and

solvent/buffer blank. Samples were prepared such that the absorbance at the excitation wavelength was ≤ 0.1 ($\sim 1 \mu\text{M}$) in 1 cm pathlength glass cuvettes and were degassed with Argon prior to measurements. Fluorescent yields were obtained either using an absolute method (Horiba Quanti-Phi integrating sphere) or versus a standard (such as Chl *a* or fluorescein; Eq. 17):

$$\Phi_{f, \text{sample}} = \Phi_{f, \text{std}} \times \frac{Em_{\text{sample}}}{Em_{\text{std}}} \times \frac{Abs_{\text{std}}}{Abs_{\text{sample}}} \times \frac{n_{\text{sample}}^2}{n_{\text{std}}^2} \quad (17)$$

where Φ_f is the quantum yield of fluorescence, Em is the integrated emission spectrum, Abs is the absorbance at the excitation wavelength, and n is the refractive index of the solvent/buffer.

Time-resolved fluorescence (to obtain singlet lifetimes, Ch. 2-3)

A nitrogen-dye laser (PTI Laserstrobe TM-3) was used to obtain fluorescence decay curves from samples with an absorbance of ≤ 0.1 ($\sim 1 \mu\text{M}$) at the excitation wavelength. Data was fit to a single exponential with an IRF of ~ 1 ns.

Redox Measurements (Ch. 4)

The midpoint oxidation potentials of P/P⁺ in RC samples (2 μM) were obtained with a SEC-C thin layer (1 mm pathlength) quartz cell (BASi EF-1358) with a platinum counter electrode (BASi EF-1356) and Ag/AgCl double junction reference electrode (BASi MF-2079, MF-2030) with 100 mM potassium chloride as the filling solution. The reference electrode was calibrated⁵⁶ prior to use. Ferrocyanide (0.25 M) was used to ensure P was fully reduced prior to titration with ferricyanide (1 M) in small (μL) increments. The absorption spectrum of the RCs was recorded after each addition. Subsequent reduction of the P band at ~ 865 nm was fit to the Nernst equation in Origin.

Pigment Analysis (Ch. 7)

The BChl to BPhe ratio in RCs was determined using the methods detailed in Ref. 57 scaled down to utilize small (μL) volumes.

TA spectroscopy

These methods generally apply to Chapters 3-7. The assay for $P^+Q_B^-$ formation utilized a home-built millisecond screening apparatus described previously⁵⁵ and $\sim 2 \mu\text{M}$ RCs at room temperature in a clear-bottomed, 96-well plate (black-walled) and a path of ~ 2 mm. All ultrafast TA measurements utilized $\sim 20 \mu\text{M}$ samples at room temperature containing 100X ascorbate to prevent P oxidation, 25X terbutryn (40 mM stock in ethanol, less than 1% ethanol in final solution) to displace Q_B for 1 kHz experiments (to eliminate the $P^+Q_B^-$ state that lives for seconds), and 10% glycerol (to allow freezing and reuse of RCs containing terbutryn). TA measurements were performed using an amplified Ti:Sapphire laser system (Spectra Physics) and Helios and Eos spectrometers for the 0.5 ps – 7 ns and 500 ps – 40 μs time ranges respectively (Ultrafast Systems). RCs were held in a 2-mm pathlength cell with stirring and excited at either 860 nm (for visible region spectra) or 600 nm (for NIR region spectra) using 100-fs excitation flashes at 1 kHz focused to a diameter of 1 mm.

Data Analysis (all chapters)

Generally, spectra were processed and Origin, which was used to generate graphs, perform curve fitting, integrate spectra, and combine data matrices. Surface Explorer (Ultrafast Systems) was used to correct TA spectra (subtract background and de-chirp the data). Global analysis (Ch. 7) was performed using Carpetview (Light Conversion). PhotochemCAD⁵⁸ was used for calculating energy transfer yields (Ch. 3).

Collaborations and Contributions

Chapter 2

All chlorins used in this chapter were synthesized at the Lindsey lab at North Carolina State University. The Bocian lab at University of California-Riverside performed DFT calculations for estimating the energies of the four frontier molecular orbitals. I provided all the

photophysical data obtained via static spectroscopy and participated in the analysis and authoring of the work.

Chapter 3

All the biological YFP, RC, and YFP-RC samples were made in the Hunter lab at the University of Sheffield in the UK. Additionally, growth curves and electron and fluorescence microscopy were performed there. I did the spectroscopy experiments – specifically, static absorption and fluorescence, time-resolved fluorescence, and TA (note that and time correlated single photon counting and TA spectroscopy were performed in the PARC Laser Facility run by D. Niedzwiedski) – energy transfer calculations, subsequent data analysis, and contributed to writing the publication.

Chapters 4-7

All RCs were provided by the Laible lab at Argonne National Lab. I performed the spectroscopy experiments (static absorbance and TA), redox measurements, and pigment analysis. Additionally, I was intimately involved in the data analysis and the writing of the publications.

References

- (1) Blankenship, R.E. (2014) *Molecular mechanisms in photosynthesis*, 2nd edition. John Wiley Blackwell, Oxford.
- (2) Green, B.R. and Parson, W.W., eds. (2003) *Light-harvesting antennas in photosynthesis*. Dordrecht: Kluwer Academic Press.
- (3) Allen, J.P. and Williams, J.C. (1998) Photosynthetic reaction centers. *FEBS Lett* 438, 5-9.
- (4) Widger, W.R., Cramer, W.A., Herrmann, R.G., Trebst, A. (1984) Sequence homology and structural similarity between cytochrome *b* of mitochondrial complex III and chloroplast *b_{6-f}* complex: Position of the cytochrome *b* hemes in membrane. *Proc. Natl. Acad. Sci. USA* 81, 674-678.
- (5) Trumpower, B.L. (1990) Cytochrome *bc₁* complexes in microorganisms. *Microbiol. Rev.* 54, 101-129.
- (6) Fermi, G., Perutz, M.F., Shaanan, B., Fourme, R. The crystal structure of human deoxyhaemoglobin at 1.74 Å resolution. *J. Mol. Biol.* 175, 159-174.

- (7) Mass, O., Taniguchi, M., Ptaszek, M., Springer, J.W., Faries, K.M., Diers, J.R., Bocian, D.F., Holten, D., Lindsey, J.S. (2011) Structural characteristics that make chlorophylls green: interplay of hydrocarbon skeleton and substituents. *New J. Chem* 35, 76-88.
- (8) Scheer, H. (2006) An overview of chlorophylls and bacteriochlorophylls: biochemistry, biophysics, functions and applications. In: *Chlorophylls and bacteriochlorophylls. Biochemistry, biophysics, functions and applications. Advances in Photosynthesis and Respiration*, vol. 25, 1-26. Grimm, B., Porra, R.J., Rudiger, W., Scheer, H., eds. Dordrecht: Springer.
- (9) Bjorn, L.O., Papegeorgiou, G.C., Blankenship, R.E., Govindjee. (2009) Why chlorophyll *a*? *Photosyn. Res.* 99, 85-98.
- (10) Taniguchi, M., Cramer, D.L., Bhise, A.D., Kee, H.L., Bocian, D.F., Holten, D., Lindsey, J.S. (2008) Accessing the near-infrared spectral region with stable, synthetic, wavelength-tunable bacteriochlorins. *New J. Chem* 32, 947-958.
- (11) Muthiah, C., Taniguchi, M., Kim, H., Schimdt, I., Kee, H.L., Holten, D., Bocian, D.F., Lindsey, J.S. (2007) *Photochem Photobiol* 83, 1513-1528.
- (12) Gouterman, M. (1959) Study of the effects of substitution on the absorption spectra of porphin. *J. Chem. Phys.* 30, 1139-1161.
- (13) Gouterman, M. (1961) Spectra of porphyrins. *J. Mol. Spectrosc.* 6, 138-163.
- (14) Gouterman, M. (1978) Optical spectra and electronic structure of porphyrins and related rings. In *The Porphyrins* Vol. III, Dolphin: Academic Press, 1-165.
- (15) Pedersen, T.G. (2000) Particle-in-a-box model of one-dimensional excitons in conjugated polymers. *Phys. Rev. B.* 61, 10504-10510.
- (16) Pedersen, T.G. (2000) Particle-in-a-box model of exciton absorption and electroabsorption in conjugated polymers. *Phys. Rev. B* 62, 15424-15426.
- (17) Yang, S.I., Seth, J., Strachan, J.P., Gentemann, S., Kim, D., Holten, D., Lindsey, J.S., Bocian, D.F. (1999) Ground and excited state electronic properties of halogenated tetraarylporphyrins. Tuning the building blocks for porphyrin-based photonic devices. *J. Porph. Phthal.* 3, 117-147.
- (18) Retsek, J.L., Medforth, C.J., Nurco, D.J., Gentemann, S., Chirvony, V.S., Smith, K.M., Holten, D. (2001) Conformational and electronic effects of phenyl-ring fluorination on the photophysical properties of non-planar dodecaarylporphyrins. *J. Phys. Chem. B* 105, 6396-6411.
- (19) Mandal, A.K., Taniguchi, M., Diers, J.R., Niedzwiedzki, D.M., Kirmaier, C., Lindsey, J.S., Bocian, D.F., Holten, D. (2016) Photophysical properties and electronic structure of porphyrins bearing zero to four *meso*-phenyl substituents: New insights into seemingly well understood tetrapyrroles. *J. Phys. Chem A* 120, 9719-9731.
- (20) Kee, H. L., Kirmaier, C., Tang, Q., Diers, J. R., Muthiah, C., Taniguchi, M., Laha, J. K., Ptaszek, M., Lindsey, J. L., Bocian, D. F., Holten, D. (2007) Effects of Substituents on Synthetic Analogues of Chlorophylls. Part 1: Synthesis, Vibrational Properties and Excited-State Decay Characteristics. *Photochem. Photobiol.* 83, 1110-1124.
- (21) Kee, H. L., Kirmaier, C., Tang, Q., Diers, J. R., Muthiah, C., Taniguchi, M., Laha, J. K., Ptaszek, M., Lindsey, J. L., Bocian, D. F., Holten, D. (2007) Effects of Substituents on Synthetic Analogues of Chlorophylls. Part 2: Redox Properties, Optical Spectra and Electronic Structure *Photochem. Photobiol.* 83, 1125-1143.

- (22) Mass, O., Ptaszek, M., Taniguchi, M., Diers, J. R., Kee, H. L., Bocian, D. F., Holten, D., Lindsey, J. S. (2009) Synthesis and Photochemical Properties of 12-Substituted versus 13-Substituted Chlorins. *J. Org. Chem* 74, 5276-5289.
- (23) Springer, J.W., Faries, K.M., Diers, J.R., Muthiah, C., Mass, O., Kee, H.L., Kirmaier, C., Lindsey, J.S., Bocian, D.F., Holten, D. (2012) Effects of substituents on synthetic analogs of chlorophylls. Part 3: The distinctive impact of auxochromes at the 7- versus 3-positions. *Photochem Photobiol* 88, 651-674.
- (24) Aravindu, K., Kim, H.J., Taniguchi, M., Dilbeck, P.L., Diers, J.R., Bocian, D.F., Holten, D., Lindsey, J.S. (2013) Synthesis and photophysical properties of chlorins bearing 0-4 distinct *meso*-substituents.
- (25) Yuen, J.M., Harris, M.A., Liu, M., Diers, J.R., Kirmaier, C., Bocian, D.F., Lindsey, J.S., Holten, D. (2015) *Photochem Photobiol* 91, 331-342.
- (26) Krayner, M., Yang, E., Diers, J.R., Bocian, D.F., Holten, D., Lindsey, J.S. (2011) *De novo* synthesis and photophysical characterization of annulated bacteriochlorins. Mimicking and extending the properties of bacteriochlorophylls. *New J. Chem.* 35, 587-601.
- (27) Yang, E., Kirmaier, C., Krayner, M., Taniguchi, M., Kim, H.J., Diers, J.R., Bocian, D.F., Lindsey, J.S., Holten, D. (2011) *J. Phys. Chem. B* 115, 10801-10816.
- (28) Vairaprakash, P., Yang, E., Sahin, T., Taniguchi, M., Krayner, M., Diers, J.R., Wang, A., Niedzwiedzki, D.M., Kirmaier, C., Lindsey, J.S., Bocian, D.F., Holten, D. (2015) Extending the short and long wavelength limits of bacteriochlorin near-infrared absorption via dioxo- and bisimide-functionalization. *J. Phys. Chem. B* 119, 4382-4395.
- (29) Zapata, M., Garrido, J.L., Jeffrey, S.W. (2006) Chlorophyll c pigments: current status. In: *Chlorophylls and bacteriochlorophylls. Biochemistry, biophysics, functions and applications. Advances in Photosynthesis and Respiration*, vol. 25, 39-53. Grimm, B., Porra, R.J., Rudiger, W., Scheer, H., eds. Dordrecht: Springer.
- (30) Behrendt, L., Brejnrod, A., Schliep, M., Sorensen, S.J., Larkum, A.W.D., Kuhl, M. (2015) Chlorophyll *f*-driven photosynthesis in a cavernous cyanobacterium. *ISME Journal* 9, 2108-2111.
- (31) Canniffe, D.P., Hunter, C.N. (2014) Engineered biosynthesis of bacteriochlorophyll *b* in *Rhodobacter sphaeroides*. *Biochem Biophys Acta* 1837, 1611-1616.
- (32) Niedzwiedzki, D.M., Blankenship, R.E. (2010) Singlet and triplet excited state properties of natural chlorophylls and bacteriochlorophylls. *Photosynth Res* 106, 227-238.
- (33) Orf, G.S., Blankenship, R.E. (2013) Chlorosome antenna complexes from green photosynthetic bacteria. *Photosynth Res* 116, 315-331.
- (34) Orf, G.S., Collins, A.M., Niedzwiedzki, D.M., Tank, M., Thiel, V., Kell, A. Bryant, D.A., Montano, G.A., Blankenship, R.E. (2017) Polymer-chlorosome nanocomposites consisting of non-native combinations of self-assembling bacteriochlorophylls. *Langmuir* 33, 6427-6438.
- (35) Siefermann-Harms, D. (1985) Carotenoids in photosynthesis. I. Location in photosynthetic membranes and light-harvesting function.
- (36) Dilbeck, P.L., Tang, Q., Mothersole, D.J., Martin, E.C., Hunter, C.N., Bocian, D.F., Holten, D., Niedzwiedzki, D.M. (2016) Quenching capabilities of long-chain carotenoids in light-harvesting-2 complexes from *Rhodobacter sphaeroides* with an engineered carotenoid synthesis pathway. *J. Phys. Chem. B* 120, 5249-5443.

- (37) Oba, T., Tamiaki, H. (2014) Asymmetry of chlorophylls in photosynthetic proteins: from the viewpoint of coordination chemistry. *J. Porph. Phthal.* 18, 919-932.
- (38) Yu., L., Suga, M., Wang-Otomo, Z.Y., Shen, J.R. (2018) *To be published.*
- (39) Papiz, M.Z., Prince, S.M., Howard, T., Cogdell, R.J., Isaacs, N.W. (2003) The structure and thermal motion of the B800-850 LH2 complex from *Rps. acidophila* at 2.0 Å resolution and 100K: new structural features and functionality relevant motions. *J. Mol. Biol.* 326, 1523-1538.
- (40) Förster, T. (1965) Delocalized excitation and excitation transfer.
- (41) Sener, M., Strümpfer, J., Hsin, J., Chandler, D., Scheuring, S., Hunter, C.N., Schulten, K. (2011) Förster energy transfer theory as reflected in the structures of photosynthetic light-harvesting systems. *ChemPhysChem* 12, 518-531.
- (42) Krishnan, R.V., Varma, R., Mayor, S. (2001) Fluorescence methods to probe nanometer-scale organization of molecules in living cell membranes. *J. Fluor.* 11, 211-226.
- (43) Springer, J.W., Parkes-Loach, P.S., Reddy, K.R., Krayner, M., Jiao, J., Lee, G.M., Niedzwiedzki, D.M., Harris, M.A., Kirmaier, C., Bocian, D.F., Lindsey, J.S., Holten, D., Loach, P.A. (2012) Biohybrid photosynthetic antenna complexes for enhanced light-harvesting. *J. Am. Chem. Soc.* 134, 4589-4599.
- (44) Dutta, P.K., Lin, S., Loskutov, A., Levenberg, S., Jun, D., Saer, R., Beatty, J.T., Liu, Y., Yan, H., Woodbury, N.W. (2014) Reengineering the optical absorption cross-section of photosynthetic reaction center. *J. Am. Chem. Soc.* 136, 4599-4604.
- (45) Kodali, G., Mancini, J.A., Solomon, L.A., Episova, T.V., Roach, N., Hobbs, C.J., Wagner, P., Mass, O.A., Aravindu, K., Barnsley, J.E., Gordon, K.C., Officer, D.L., Dutton, P.L., Moser, C.C. (2017) Design and engineering of water-soluble light-harvesting protein maquettes. *Chem. Sci.* 8, 316-324.
- (46) Marcus, R.A., Sutin, N. (1985) Electron transfers in chemistry and biology. *Biochem Biophys Acta* 811, 265-322.
- (47) Moser, C.C., Keske, J.M., Warncke, K., Farid, R.S., Dutton, P.L. (1992) Nature of biological electron transfer. *Nature* 355, 796-802.
- (48) Harris, M.A., Luehr, C.A., Faries, K.M., Wander, M., Kressel, L., Holten, D., Hanson, D.K., Laible, P., Kirmaier, C. (2013) Protein influence on charge-asymmetry of the primary donor in photosynthetic bacterial reaction centers containing a heterodimer: effects on photophysical properties in electron transfer. *J. Phys. Chem. B* 117, 4028-4041.
- (49) Wang, J., Yang, E., Diers, J.R., Niedzwiedzki, D.M., Kirmaier, C., Bocian, D.F., Lindsey, J.S., Holten, D. (2014) Distinct photophysical and electronic characteristics of strongly coupled dyads containing a perylene accessory pigment and a porphyrin, chlorin, or bacteriochlorin. *J. Phys. Chem. B* 117, 9288-9304.
- (50) Zeng, Y., Feng, F., Medova, H., Dean, J., Koblizek, M. (2014) Functional type 2 photosynthetic reaction centers found in the rare bacterial phylum Gemmatimonadetes. *Proc. Nat. Acad. Sci. USA* 111, 7795-7800.
- (51) Ermler, U., Fritzsch, G., Buchanan, S.K., Michel, H. (1994) Structure of the photosynthetic reaction centre from *Rhodobacter sphaeroides* at 2.65 Å resolution: cofactors and protein-cofactor interactions. *Structure* 2, 925-936.
- (52) Wakeham, M.C., Jones, M.R. (2005) Rewiring photosynthesis: engineering wrong-way electron transfer in the purple bacterial reaction center. *Biochem. Soc. Trans.* 33, 851-857.

- (53) Chuang, J.I., Boxer, S.G., Holten, D., Kirmaier, C. (2006) High yield of M-side electron transfer in mutants of *Rhodobacter capsulatus* reaction centers lacking the L-side bacteriopheophytin. *Biochem.* 45, 3845-3851.
- (54) Carter, B., Boxer, S.G., Holten, D., Kirmaier, C. (2009) Trapping the PB initial intermediate state of charge separation in photosynthetic reaction centers from *Rhodobacter capsulatus*. *Biochem.* 48, 2571-2573.
- (55) Faries, K.M., Kressel, L.L., Wander, M.J., Holten, D., Laible, P.D., Kirmaier, C., Hanson, D.K. (2012) High throughput engineering to revitalize a vestigial electron transfer pathway in bacterial photosynthetic reaction centers. *J. Biol. Chem.* 287, 8507-8514.
- (56) O'Reilly, J.E. (1973) Oxidation-reduction potential of the ferro-ferricyanide system in buffer solutions. *Biochim. Biophys. Acta* 292, 509-515.
- (57) van der Rest, M., Gingras, G. (1974) Pigment complement of photosynthetic reaction center isolated from *Rhodospirillum rubrum*. *J. Biol. Chem.* 249, 6446-6453.
- (58) Dixon, J.M., Taniguchi, M., Lindsey, J.S. (2005) PhotochemCAD 2. A redefined program with accompanying spectral databases for photochemical calculations. *Photochem. Photobiol.* 81, 212-213.

Chapter 2: Photophysical Properties and Electronic Structure of Chlorin-Imides: Bridging the Gap between Chlorins and Bacteriochlorins

Reprinted with permission from Faries, K.M.; Diers, J.R.; Springer, J.W.; Yang, E.; Ptaszek, M.; Lahaye, D.; Krayner, M.; Taniguchi, M.; Kirmaier, C.; Lindsey, J.S.; Bocian, D.F.; Holten, D. (2015) Photophysical properties and electronic structure of chlorin-imides: bridging the gap between chlorins and bacteriochlorins. *Journal of Physical Chemistry B*, *119*, 7503-7515.

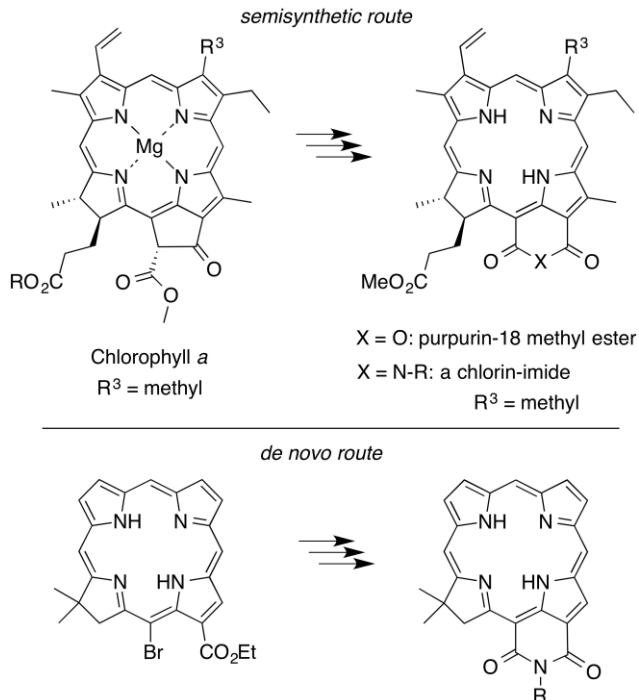
Abstract

Efficient light harvesting for molecular-based solar-conversion systems requires absorbers that span the photon-rich red and near-infrared (NIR) regions of the solar spectrum. Reported herein are the photophysical properties of a set of six chlorin-imides and nine synthetic chlorin analogues that extend the absorption deeper (624–714 nm) into these key spectral regions. These absorbers help bridge the gap between typical chlorins and bacteriochlorins. The new compounds have high fluorescence quantum yields (0.15–0.34) and long singlet excited-state lifetimes (4.2–10.9 ns). The bathochromic shift in Q_y absorption is driven by substituent-based stabilization of the lowest unoccupied molecular orbital, with the largest shifts for chlorins that bear an electron-withdrawing, conjugative group at the 3-position in combination with a 13,15-imide ring.

1. Introduction

An essential goal for the construction of light-harvesting architectures for solar energy conversion systems is to elucidate the molecular design principles that allow tailoring of the absorption wavelengths (and intensities) across the photon rich red and near-infrared (NIR) regions of the spectrum. Natural photosynthetic pigments such as chlorophyll *a* (**Chl *a***; Chart 1, top left) exhibit a red-region absorption band that is enhanced by the keto-bearing five-membered ring spanning the 13,15 positions that is fused to the chlorin macrocycle. The ring structure locks the 13-keto group into coplanarity with the macrocycle and thereby engenders substantial π -electron conjugation involving the keto and macrocycle components. Bathochromic shifts of synthetic chlorins also can be attained by the introduction of auxochromes such as acetyl or formyl groups at various positions, particularly the 3-position, which like the 13-keto group, lies coincident with the long-wavelength (Q_y) transition-dipole moment.^{1,2}

Chart 1. Semisynthetic and *de novo* Routes to Chlorin-imides



Although such synthetic chlorins have reached the red-region (Q_y) absorption wavelength of **Chl *a*** (665 nm), few have approached that of **Chl *d*** (697 nm), in which a 3-formyl group replaces the 3-vinyl group of **Chl *a***.³ Such chlorins (native or synthetic) also have rarely reached the short-wavelength end of the Q_y range for native (or synthetic) bacteriochlorins. A traditional approach to prepare long-wavelength-absorbing chlorins to span this gap has been to carry out synthetic transformations of **Chl *a***.^{4,5} One prevalent method for such semisynthesis, dating to the work of Conant⁶ and of Fischer^{7,8} in the 1930s, entails expansion of the five-membered exocyclic ring to give a six-membered imide (Chart 1, top right). The resulting chlorophyll derivatives (previously termed purpurinimides) are chlorin-imides. The imide unit spans positions 13 and 15 on the chlorin macrocycle. Such chlorin-imides typically exhibit the following features: (i) bathochromic shift of the long-wavelength absorption band, (ii) versatile

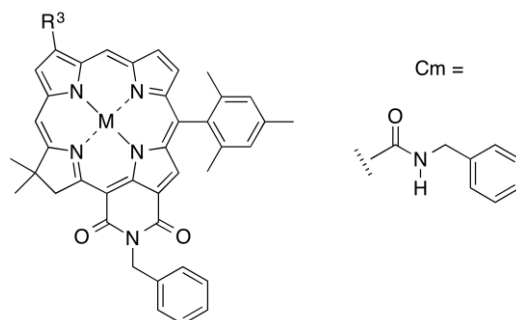
synthetic handle at the nitrogen of the imide, and (iii) stability toward adventitious dehydrogenation.

While chlorin-imides remain of active interest,⁹⁻³³ one drawback of naturally derived chlorin-imides is the limited control over the nature of substituents at other sites about the perimeter of the macrocycle. We recently developed a *de novo* synthesis of chlorin-imides beginning with simple, readily available starting materials (Chart 1; bottom).³⁴ The *de novo* synthesis requires considerable investment in synthesis yet affords commensurate control over substituents. The key synthetic transformation is the conversion of a chlorin bearing 13-ester and 15-bromo groups to the corresponding chlorin-imide. The Q_y absorption band of members of this family of synthetic zinc and free base chlorins (including 13¹-oxophorbines) resides in the range of 598–687 nm,^{34,35} whereas the chlorin-imides absorb in a longer wavelength region, from 660–714 nm. A number of chlorins have been prepared that also have long-wavelength absorption (*vide infra*).^{23,36-72} The chlorin-imides are distinctive as synthetically accessible and tailorable chromophores that fill the gap in the spectral progression of synthetic free base or zinc chlorins lacking imides (598–687 nm) to chlorin-imides (660–714 nm) and on to synthetic bacteriochlorins and bacteriochlorin-imides^{73,74} (from 709 to >800 nm).

The present study concerns the photophysical investigation of a set of 15 chlorins, including six chlorin-imides and nine synthetic chlorin analogues obtained along the route to the chlorin-imides. The chlorin-imides include three free bases (Fb) and three zinc chelates (Chart 2). The free base chlorin-anhydride contains the 13,15-keto groups of the imide but has an oxygen atom in place of the imide nitrogen atom (Chart 3). The synthesis of the chlorin-imides afforded chlorins with ester or benzylcarbamoyl groups at the 3-, 13-, and/or 15-positions (Chart 4). This set comprises an additional four free base and four zinc chlorins. All of the chlorins and

chlorin-imides contain a mesityl (i.e., 2,4,6-trimethylphenyl) group at the 10-position, which enhances solubility in organic solvents yet has little effect on spectral properties. Certain combinations of the imide or anhydride ring and the 3-substituents results in a Q_y band bathochromically shifted to up to 714 nm. Spectral comparisons of the new chlorins and chlorin-imides are made to other chlorins that contain 13-substituents (Chart 5), the exocyclic 5-membered ring (i.e., the oxophorbine, Chart 6), and bacteriochlorins and bacteriochlorin-imides (Chart 7). The molecular orbital (MO) characteristics obtained from density functional theory (DFT) calculations indicate that the Q_y shift primarily derives from the stabilization of the lowest unoccupied frontier MO (LUMO). In addition to the spectral properties, the singlet excited-state lifetime, fluorescence yield, and radiative and nonradiative rate constants have been determined. The results reported herein concerning synthetic chlorin-imides complement the very limited prior photophysical studies of naturally derived chlorin-imides, including chlorin-imide monomers^{15,23} and as one constituent in a dyad.^{13,14,30} Collectively, the results bridge a key spectral and photophysical gap spanning four classes of tetrapyrroles: chlorins, chlorin-imides, bacteriochlorins, and bacteriochlorin-imides.

Chart 2. Synthetic Chlorin-imides



Cmpd	M	R ³
ZnClm	Zn	H
ZnClm-Es ³	Zn	-CO ₂ CH ₃
ZnClm-Cm ³	Zn	-Cm
FbClm	H, H	H
FbClm-Es ³	H, H	-CO ₂ CH ₃
FbClm-Cm ³	H, H	-Cm

Chart 3. Chlorin-anhydride

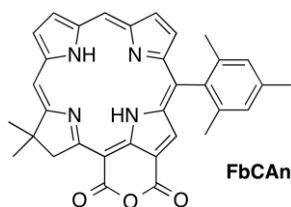
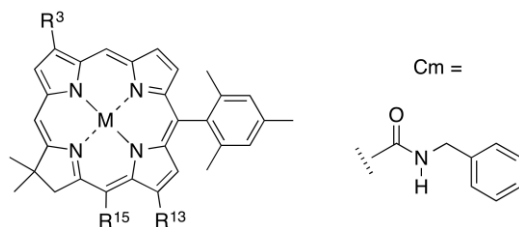
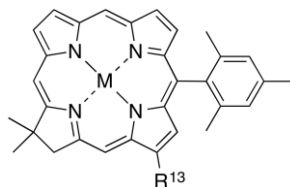


Chart 4. Substituted Chlorin Analogues of Chlorin-imides



Cmpd	M	R ³	R ¹³	R ¹⁵
ZnC-Es ^{3,13}	Zn	-CO ₂ CH ₃	-CO ₂ CH ₃	H
ZnC-Es ^{13,15}	Zn	H	-CO ₂ CH ₃	-CO ₂ CH ₃
ZnC-Cm ¹³	Zn	H	-Cm	H
ZnC-Cm ^{3,13}	Zn	-Cm	-Cm	H
FbC-Es ^{3,13}	H, H	-CO ₂ CH ₃	-CO ₂ CH ₃	H
FbC-Es ^{13,15}	H, H	H	-CO ₂ CH ₃	-CO ₂ CH ₃
FbC-Cm ¹³	H, H	H	-Cm	H
FbC-Cm ^{3,13}	H, H	-Cm	-Cm	H

Chart 5. Previously Characterized Chlorins



Cmpd	M	R ¹³
ZnC	Zn	H
ZnC-Es ¹³	Zn	-CO ₂ CH ₃
FbC	H, H	H
FbC-Es ¹³	H, H	-CO ₂ CH ₃

Chart 6. Oxophorbines

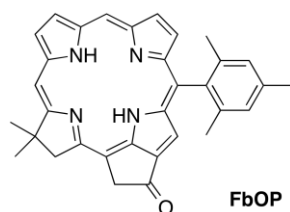
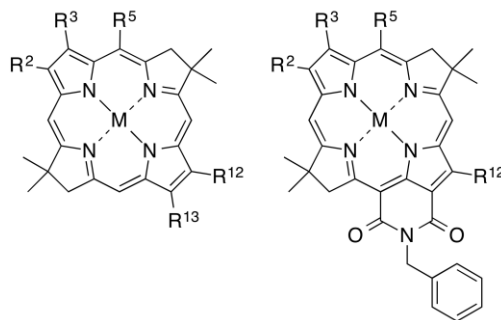


Chart 7. Bacteriochlorins and Bacteriochlorin-imides



2. Experimental Section

Synthesis. The preparation of the chlorins (for which the full photophysical and MO characterization are presented here for the first time) have been reported previously.³⁴

Photophysical Measurements. All measurements were taken at room temperature and in toluene (unless otherwise noted). Dilute samples (μM ; absorbance ≤ 0.1 at excitation wavelength) were argon-purged prior to taking measurements. Static absorption spectra were acquired on a Cary 100 Bio or Shimadzu UV-1800 UV-Vis spectrometer. Static fluorescence spectra were acquired using a Spex Fluorolog Tau 2 utilizing 2 mm excitation and 4 mm emission bandwidths, 0.2 nm data intervals, and the appropriate emission colored glass filter. The emission spectra were corrected for detection-system spectral response. Fluorescent yields were obtained relative to one of the following standards in toluene: (1) argon-purged **Chl a**, for which $\Phi_f = 0.325$,⁷⁵ the same value found in benzene,⁷⁶ or (2) non-degassed free base *meso*-tetraphenylporphyrin (**FbTPP**), for which $\Phi_f = 0.07$, and which was obtained relative to the nondegassed zinc chelate (**ZnTPP**) in nondegassed toluene ($\Phi_f = 0.03$ ⁷⁷), consistent with prior measurements on **FbTPP**.⁷⁸ Singlet lifetimes (τ_s) were obtained by two methods: (1) a phase-modulation technique (Spex Fluorolog Tau 2) using 10 to 200 MHz frequencies to analyze the fluorescence phase shift and modulation amplitude and/or (2) fitting to single-exponential

fluorescence decay curves obtained using a stroboscopic detection method with an overall instrument response function of ~1 ns (PTI Laserstrobe TM-3). In both cases, the fluorescence was normally obtained using excitation in the Soret region.

Molecular Orbital Calculations. DFT calculations were performed with Spartan '10 for Windows version 1.2.0⁷⁹ in parallel mode on a PC equipped with an Intel i7-975 cpu, 24 GB ram, and three 300 GB, 10k rpm hard drives. The calculations employed the hybrid B3LYP functional and basis set 6-31G*. The equilibrium geometries were fully optimized using the default parameters of the Spartan program. MO images were plotted from Spartan using an isovalue of 0.016.

3. Results

Absorption and Fluorescence Spectra. Figure 1A shows absorption spectra for the four new zinc chlorins: **ZnC-Cm¹³**, **ZnC-Cm^{3,13}**, **ZnC-Es^{3,13}** and **ZnC-Es^{13,15}**. Figure 1B shows spectra for the three new zinc chlorin-imides: **ZnClm**, **ZnClm-Es³** and **ZnClm-Cm³**. Figures 1C and 1D show spectra for the analogous free base chlorins and chlorin-imides, respectively. The spectrum for the free base chlorin-anhydride (**FbCAn**) is also shown in Figure 1D.

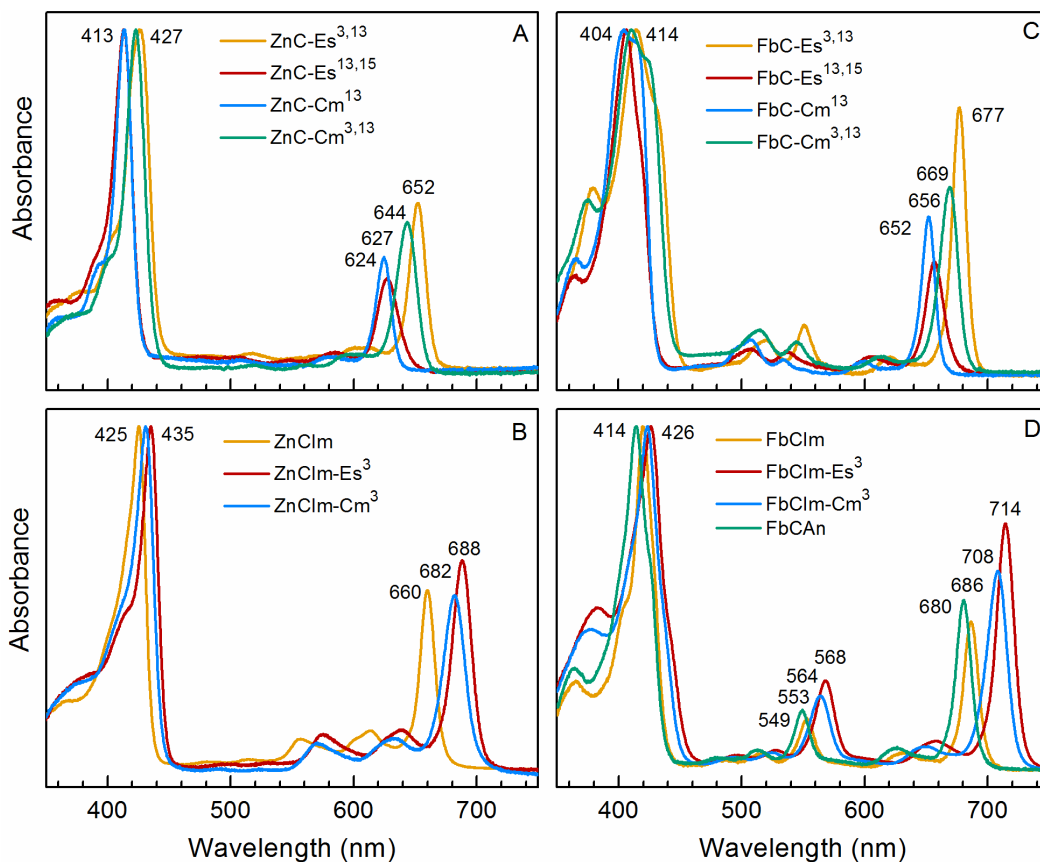


Figure 1. Absorbance spectra for new zinc (A and B) and free-base (C and D) chlorins ($\sim 2 \mu\text{M}$) in toluene at room temperature. Panels A and C are for substituted chlorin benchmarks while panels B and D are for chlorins with imide or anhydride rings.

The absorption spectra exhibit the characteristic features expected for synthetic chlorins. These characteristics are (1) strong near-UV (NUV) Soret (B_y and B_x) features that overlap almost completely for the zinc chelates but are split to varying degrees for the free base analogues, (2) much weaker Q_x absorption between ~ 480 and ~ 600 nm that is even weaker for the zinc chelates than free base compounds, and (3) a strong Q_y band in the red or NIR region. Each of these origin bands is flanked by at least one vibronic satellite to shorter wavelength with spacing on the order of 1000 cm^{-1} . For the Q_x absorption, the (1,0) satellite band is often stronger than the (0,0) band because of vibronic intensity borrowing from B_x .¹ The $Q_y(2,0)$

satellite band can extend into the nominal Q_x region. The spectra in Figure 1 are all normalized to the Soret (B_y , B_x) maximum, which is a common manner of presentation for chlorophylls and synthetic analogues to give a first-order indication of how the relative intensity of the Q_y band varies with macrocycle substituents.

The fluorescence spectra for the new chlorins and chlorin-imides are shown in Figure 2, panel A for the zinc chelates and panel B for the free base analogues. Each spectrum is dominated by the Q_y origin band, with a weaker (0,1) band to longer wavelength. The fluorescence maximum is generally within ~ 5 nm of the corresponding Q_y absorption maximum, reflecting a relatively small absorption-fluorescence ‘Stokes’ shift.

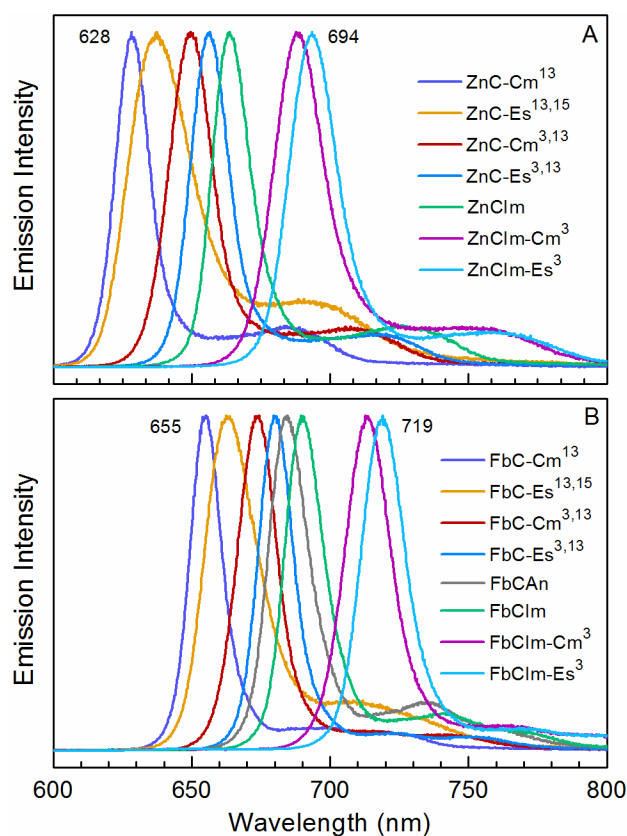


Figure 2. Fluorescence spectra for new zinc (A) and free-base (B) chlorins and chlorin-imides in toluene at room temperature. The spectra are normalized to the same peak intensity for easier depiction of the differences in peak wavelength. The fluorescence yields are given in Table 1.

Figure 3 focuses on the Q_y position and relative intensity for select compounds, again normalized to the Soret maximum (as in Figure 2). Figure 3A shows spectra for **ZnC-Es^{13,15}** and **ZnClmEs³** studied here along with those for other chlorins **ZnC**, **ZnC-Es¹³** and **ZnC-A^{3,13}** studied previously (Tables 1 and S1) where A is an acetyl group.⁸⁰⁻⁸² Figure 3B shows spectra for the corresponding free base compounds. The spectra in Figure 3 reveal that the addition of a 15-ester group to a chlorin that already bears a 13-ester (and 10-mesityl) gives a minimal shift in the Q_y position, along with a small diminution in peak (and integrated) intensity. However, closure to give the 13,15-imide ring gives rise to a substantial bathochromic shift and intensification of the Q_y band to a position ~25 nm to longer wavelengths than the 3,13-diacetyl analogue, which is near the red-limit achieved previously by synthetic chlorins of the type described herein.

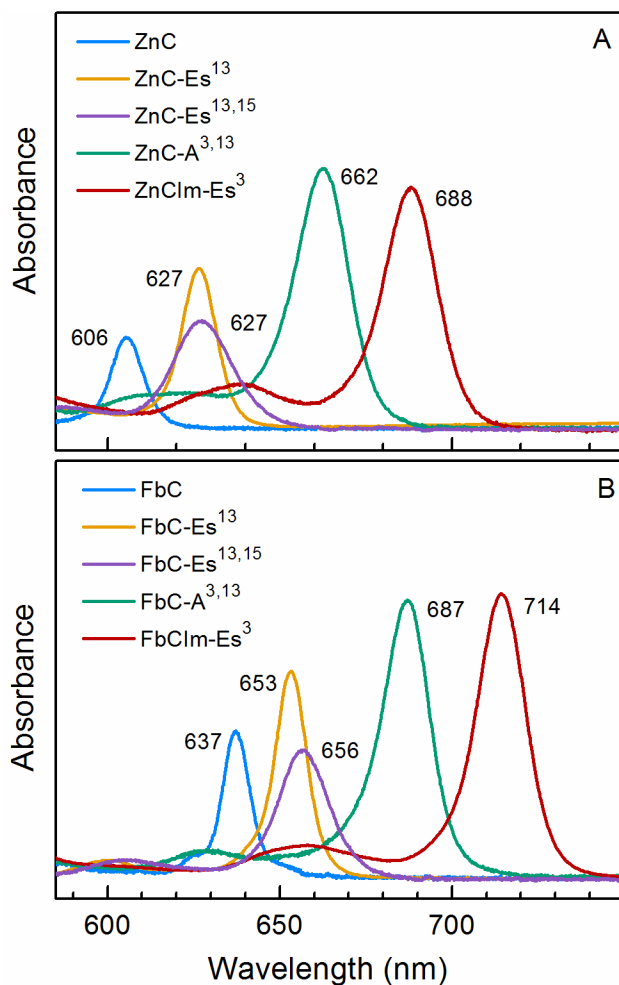


Figure 3. Comparison of Q_y -region absorption spectra for zinc (A) and free base (B) chlorins bearing a 10-mesityl group and various substituents at the 3-, 13-, and/or 15-positions, including a 13,15-imide ring. All spectra are for the compounds in toluene at room temperature and have been normalized to the peak of the NUV Soret (B-region) absorption band (as in Figure 1). The spectral intensity ratios are given in Table 1.

The absorption and fluorescence spectral data for the new chlorins and chlorin-imides are given in Table 1 along with data for representative chlorins studied previously (see also Table S1). Figure 4 focuses on the position of the Q_y band (normalized to the same peak amplitude) for a selection of these molecules along with representative bacteriochlorins and bacteriochlorin-imides (Chart 7, Table S3) studied previously; Figure 4A shows data for free base compounds whereas Figure 4B concerns the zinc chelates. These spectra show the bridge that the chlorin-imides provide in the overall chlorin-bacteriochlorin spectral landscape. One key point

illustrated in Figure 4 is that the Q_y absorption of zinc chelates of chlorins is hypsochromically shifted versus the free base, whereas that of the zinc chelates of bacteriochlorins is bathochromically shifted versus the free base. The chlorin-imides and bacteriochlorin-imides behave like the parent macrocycles with regard to spectral effects upon zincation. Hence, the longest wavelength absorbing chlorin-imide is a free base whereas the longest wavelength bacteriochlorin-imide is a zinc chelate.

Table 1. Photophysical Properties of Synthetic Chlorins^a

Code ^b	Compound	B _{max} abs (nm)	Q _y (0,0)) abs (nm)	Q _y (0,0)) emis (nm)	I _{Q_y} / I _B	Σ _{Q_y} / Σ _B	Φ _f	τ _s (ns)	k _f ⁻¹ (ns)	k _{nr} ⁻¹ (ns)
<i>New</i>	<i>zinc chlorins</i>									
A	ZnC-Cm¹³	414	624	628	0.34	0.31	0.21	4.2	20	5.3
B	ZnC-Es^{13,15}	413	627	637	0.29	0.36	0.20	4.3	22	5.4
C	ZnC-Cm^{3,13}	423	644	650	0.45	0.42	0.32	6.2	19	9.1
D	ZnC-Es^{3,13}	427	652	656	0.50	0.38	0.34	7.1	21	11
E	ZnClm	425	660	664	0.53	0.40	0.15	4.4	29	5.2
F	ZnClm-Cm³	431	682	688	0.53	0.43	0.19	4.4	23	5.4
G	ZnClm-Es³	435	688	694	0.59	0.43	0.18	4.4	24	5.4
<i>New</i>	<i>free base chlorins</i>									
H	FbC-Cm¹³	404	652	655	0.45	0.20	0.29	10.9	38	15
I	FbC-Es^{13,15}	406	656	663	0.33	0.24	0.18	6.2	34	7.6
J	FbC-Cm^{3,13}	411	669	674	0.56	0.25	0.33	10.1	31	15
K	FbC-Es^{3,13}	414	677	680	0.77	0.27	0.32	10.2	32	15
L	FbCAn	414	680	684	0.48	0.26	0.20	5.7	29	7.1
M	FbClm	420	686	690	0.43	0.25	0.17	5.6	33	6.7
N	FbClm-Cm³	423	708	713	0.56	0.30	0.17	5.7	34	6.9
O	FbClm-Es³	426	714	719	0.71	0.31	0.16	6.3	39	7.5
<i>Prior</i>	<i>zinc chlorins</i>									
P	ZnC	405	606	608	0.23	0.23	0.060	1.5	25	1.6
Q	ZnC-Es¹³	415	627	630	0.42	0.29	0.24	4.8	20	6.3
<i>Prior</i>	<i>free base chlorins</i>									
R	FbC	396	637	639	0.37	0.14	0.22	9.1	41	12
S	FbC-Es¹³	405	653	656	0.53	0.19	0.29	9.8	34	14
T	FbOP	413	656	659	0.59	0.23	0.35	14.2	41	22

^aAll compounds contain a 10-mesityl group. All data were collected at room temperature in toluene. Columns 6 and 7 give the peak (I_B/I_{Q_y}) and integrated (Σ_B/Σ_{Q_y}) intensity ratios of the Q_y and Soret (B) absorption manifolds. The singlet excited-state decay rate constants given in the last two columns were obtained from the two observables using the expressions k_f = Φ_f/τ_s and k_{nr} = (1 - Φ_f)/τ_s. The typical errors (percent of value) are as follows: τ_s (±7%), Φ_f (±5%), Φ_{nr} (±5%), k_f (±12%), k_{nr} (±12%). ^bIdentifier of data shown in Figures 4, 5 and 7.

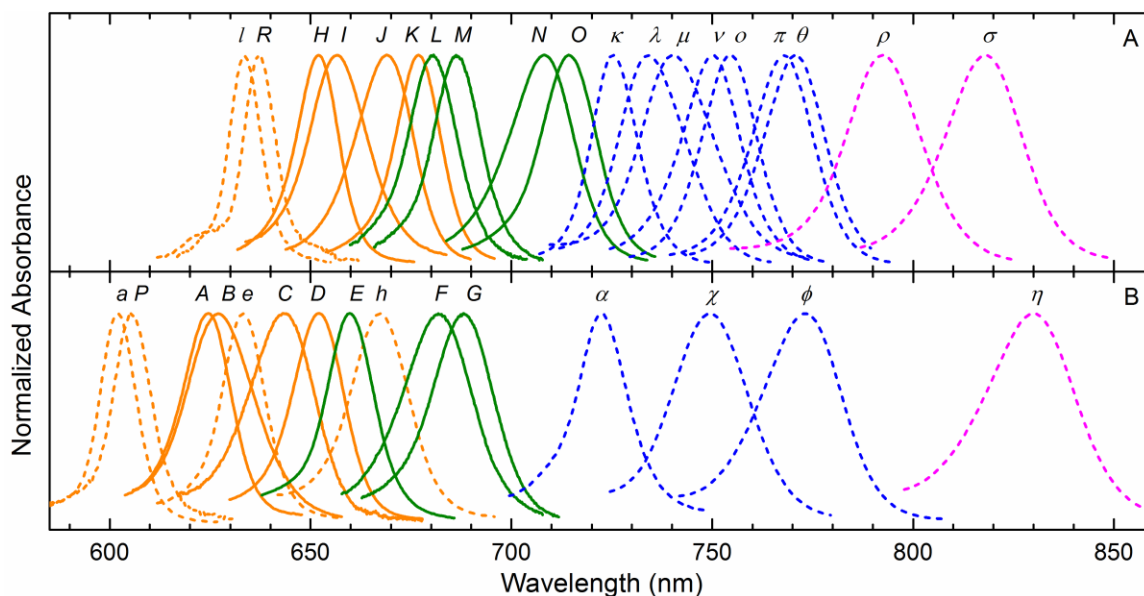


Figure 4. Absorption spectra of representative free base (A) and zinc (B) chlorins (orange), chlorin-imides (green), bacteriochlorins (blue) and bacteriochlorin-imides (magenta) studied here (solid) and previously (dashed). A capital letter above a spectrum identifies the molecule according to the code in Table 1. A lower case letter identifies a chlorin in Tables S1 and S2, and a Greek letter a bacteriochlorin in Tables S3 and S4, where data for the prior characterized tetrapyrroles are given. The spectra are normalized to the same peak Q_y intensity to emphasize the trend in peak wavelength. The spectral intensity ratios are given in Tables 1 and S1.

Excited-State Properties. Table 1 gives the fluorescence yields (Φ_f) and singlet excited-state lifetimes (τ_s) for the new chlorins and chlorin-imides and chlorins studied previously (see also Table S1). The Φ_f values range from 0.15 to 0.34 and the τ_s values from 4.2 to 7.1 ns for the zinc chelates. For the free base analogues, the span of Φ_f values (0.16 to 0.33) is similar to the zinc chelates but the τ_s values (5.6 to 10.9 ns) are about 30% greater. For both observables, the chlorin-imides are at the lower end of the ranges and the chlorins bearing benzylcarbamoyl (Cm) and ester (Es) groups at the 3,13-positions are near or at the upper end of the ranges.

The measured τ_s and Φ_f are both related to the fluorescence (k_f), internal conversion (k_{ic}) and intersystem crossing (k_{isc}) decay rate constants of the lowest (Q_y) singlet excited state via the expressions $\tau_s = (k_f + k_{ic} + k_{isc})^{-1}$ and $\Phi_f = k_f \cdot \tau_s$. The internal conversion and intersystem crossing pathways can be combined into a single nonradiative rate constant $k_{nr} = k_{ic} + k_{isc}$. In

this way, the radiative (fluorescence) and net nonradiative decay rate constants can be obtained from the two observables using the expressions $k_f = \Phi_f/\tau_S$ and $k_{nr} = (1 - \Phi_f)/\tau_S$. These last two quantities are cast as the associated time constants (in nanoseconds) in the last two columns of Table 1. Figure 5 shows the trends in the measured photophysical properties τ_S and Φ_f and the derived excited-state time constants k_f^{-1} and k_{nr}^{-1} for spanning the new chlorins and chlorin-imides studied here and select chlorins,⁸⁰⁻⁸² bacteriochlorins and bacteriochlorin-imides^{73,74} from prior studies. A specific comparison that can be made at this point concerns the photophysical properties of the chlorin-imide motif studied here versus the oxophorbine ring (also spanning positions 13,15) explored previously.^{75,82} For a chlorin of a given metalation state and set of substituents, compared to the oxophorbine ring, the imide (or anhydride) ring gives rise to a bathochromically shifted Q_y band by ~25 nm and roughly half the fluorescence yield and singlet excited-state lifetime (Tables 1 and S1). Collectively, these findings are consistent with the extension by the chlorin-imides of the spectral/photophysical range past the oxophorbines to near that of the free base bacteriochlorins.

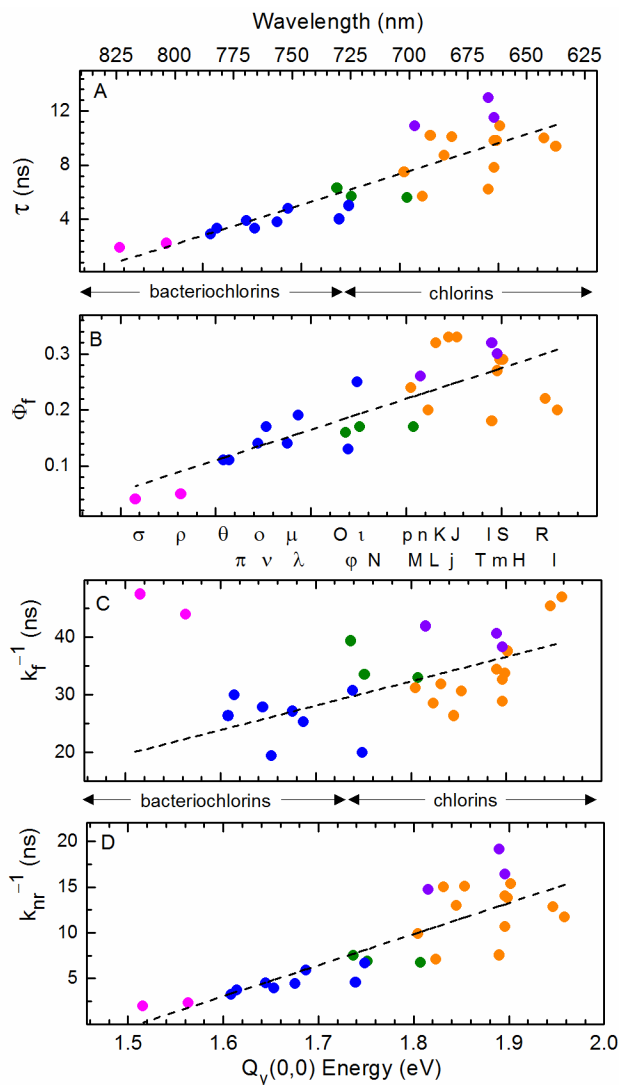


Figure 5. Summary of photophysical properties versus Q_y energy (wavelength) for free base chlorins (orange), chlorin-imides (green), oxophorbins (violet), bacteriochlorins (blue), and bacteriochlorin-imides (magenta). The letters above panel C identify the molecules as indicated in the legend to Figure 4. The dashed lines are provided as a guide to the eye.

Molecular Orbital Characteristics. The MO characteristics of the compounds were obtained via DFT calculations. The structures obtained by DFT methods are in close agreement with those obtained by X-ray crystallography where data are available for chlorin-imides.⁸³ Table 2 lists the energies of the highest occupied MO (HOMO) and the lowest unoccupied MO (LUMO) along with the HOMO-1 and LUMO+1; Table S2 gives values for additional chlorins and Table S4 for bacteriochlorins and bacteriochlorin-imides studied previously. Figure 6 shows

the electron densities for these four frontier MOs for selected zinc chlorins and zinc chlorin-imides. The illustration shows the effects of progressive addition of substituents to the parent zinc chlorin macrocycle, the latter bearing only 18,18-dimethyl (to stabilize the macrocycle) and 10-mesityl (to enhance solubility) groups. The additions (left to right) are (1) 13-ester, (2) 13,15-diester, (3) 3,13-diester, (4) closure of the 13,15-diester to give the 13,15-imide ring, and (5) 3-ester along with the 13,15-imide ring.

Table 2. MO Energies of Synthetic Chlorins^a

Code ^b	Compound	H-1	H	L	L+1	L - H	L+1 - H-1	ΔE_{avg}	ΔE_{di}
<i>New</i>	<i>zinc chlorins</i>								
<i>A</i>	ZnC-Cm¹³	-5.17	-4.88	-2.32	-1.64	2.56	3.53	3.05	0.97
<i>B</i>	ZnC-Es^{13,15}	-5.32	-5.00	-2.44	-1.74	2.56	3.58	3.07	1.02
<i>C</i>	ZnC-Cm^{3,13}	-5.21	-4.95	-2.46	-1.72	2.49	3.49	2.99	1.00
<i>D</i>	ZnC-Es^{3,13}	-5.28	-5.03	-2.58	-1.80	2.45	3.48	2.97	1.03
<i>E</i>	ZnClm	-5.62	-5.25	-2.79	-1.99	2.46	3.63	3.05	1.17
<i>F</i>	ZnClm-Cm³	-5.65	-5.30	-2.92	-2.03	2.38	3.62	3.00	1.24
<i>G</i>	ZnClm-Es³	-5.69	-5.34	-2.99	-2.10	2.35	3.59	2.97	1.24
<i>New</i>	<i>free base chlorins</i>								
<i>H</i>	FbC-Cm¹³	-5.08	-4.96	-2.36	-1.75	2.60	3.33	2.97	0.73
<i>I</i>	FbC-Es^{13,15}	-5.22	-5.09	-2.51	-1.86	2.58	3.36	2.97	0.78
<i>J</i>	FbC-Cm^{3,13}	-5.11	-5.04	-2.51	-1.83	2.53	3.28	2.91	0.75
<i>K</i>	FbC-Es^{3,13}	-5.18	-5.12	-2.64	-1.91	2.48	3.27	2.88	0.79
<i>L</i>	FbCAn	-5.72	-5.5	-3.04	-2.25	2.46	3.47	2.97	1.01
<i>M</i>	FbClm	-5.54	-5.33	-2.88	-2.09	2.45	3.45	2.95	1.00
<i>N</i>	FbClm-Cm³	-5.57	-5.38	-3.00	-2.13	2.38	3.44	2.91	1.06
<i>O</i>	FbClm-Es³	-5.61	-5.41	-3.08	-2.2	2.33	3.41	2.87	1.08
<i>Prior</i>	<i>zinc chlorins</i>								
<i>P</i>	ZnC	-5.11	-4.78	-2.12	-1.56	2.66	3.55	3.11	0.89
<i>Q</i>	ZnC-Es¹³	-5.20	-4.92	-2.36	-1.65	2.56	3.55	3.06	0.99
<i>Prior</i>	<i>free base chlorins</i>								
<i>R</i>	FbC	-5.02	-4.87	-2.18	-1.68	2.69	3.34	3.02	0.65
<i>S</i>	FbC-Es¹³	-5.11	-5.01	-2.42	-1.77	2.59	3.34	2.97	0.75
<i>T</i>	FbOP	-5.19	-5.17	-2.58	-1.91	2.59	3.28	2.94	0.69

^aAll compounds contain a 10-mesityl group. Values (in eV) were obtained from DFT calculations.

^bIdentifier of data shown in Figures 4, 5 and 7.

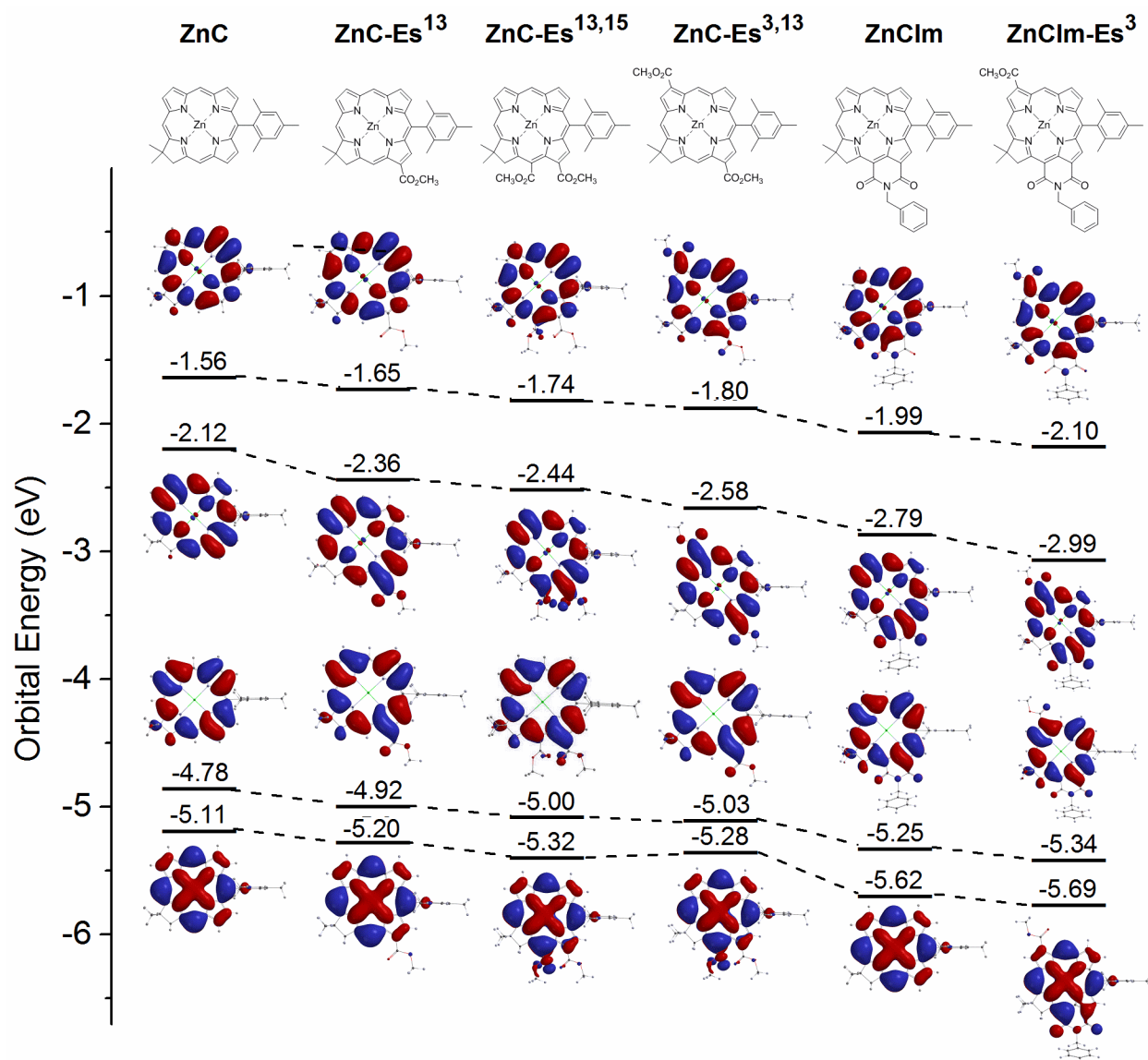


Figure 6. Comparison of four frontier MO characteristics of select zinc chlorins and zinc chlorin-imides.

According to the four-orbital model,^{1,84,85} the lowest excited states of a tetrapyrrole, those responsible for the NUV to NIR absorption spectrum, are derived from binary mixtures of the configurations derived from one-electron promotions between the four frontier MOs depicted in Figure 6 and Table 2. The Q_y and B_y states are linear combinations of [HOMO \rightarrow LUMO] and [HOMO-1 \rightarrow LUMO+1] whereas the Q_x and B_x states are linear combinations of [HOMO \rightarrow LUMO+1] and [HOMO-1 \rightarrow LUMO]. Here we focus on the Q_y state and thus the position and

intensity of the Q_y band. In this model, a change in substituents (or macrocycle type) that causes the wavelength of the Q_y band to increase will also cause the wavelength of the B_y band to move in the opposite direction. Similarly, a change in the intensity of the Q_y band is accompanied by the opposite change in B_y intensity.

The absorption spectrum is controlled by the MO energy gaps. For chlorins, because the [HOMO→LUMO] configuration contributes more to the Q_y state than the [HOMO-1 → LUMO+1] configuration, the position of the Q_y band may be expected to track the LUMO–HOMO energy gap, with the average energy of the B_y and Q_y bands reflecting the average of the LUMO–HOMO and LUMO+1 – HOMO-1 energy gaps (denoted ΔE_{avg}). The relative intensities of the Q_y and B_y bands are controlled by the extent of mixing between the [HOMO→LUMO] and [HOMO-1 → LUMO+1] configurations, and thus their relative energies (ΔE_{dif}). As ΔE_{dif} goes to zero, there is complete cancellation of the transition-dipole moments associated with these two configurations whereupon the Q_y band has zero intensity and the B_y band has all the y-polarized intensity. On the other hand, a gain in intensity of the Q_y band occurs at the expense of B_y . For most cases investigated thus far wherein substituents are at the β -pyrrole positions (e.g., 3,13-positions) of chlorins and bacteriochlorins,^{73,74,80-82,86} as ΔE_{dif} increases (because of shifts in the relative MO energies), the B_y – Q_y splitting and Q_y/B_y intensity ratio increases, affording bathochromic and hyperchromic shifts of the Q_y band and hypsochromic and hypochromic shifts of the B_y band. [Similar relationships apply to the B_x and Q_x bands and the two x-polarized one-electron configurations, but those are not a focus of the present study.] The last two columns of Table 2 list the ΔE_{avg} and ΔE_{dif} values for all the compounds under comparison.

Figure 7 graphically illustrates the connection between the energy (wavelength) of the Q_y band and the MO characteristics for the free base chlorins and chlorin-imides studied here, and representative chlorins, bacteriochlorins, and bacteriochlorin-imides studied previously. Most but not all of the data reflect 3,13-substituents. Points are included for parent and substituted synthetic oxophorbins. Figure 7A depicts trends in the energies of the frontier MOs. The LUMO has the greatest slope, followed by the HOMO-1 and LUMO+1, and then the HOMO. These trends translate in Figure 7B to a strong dependence of the Q_y energy (wavelength) on the [HOMO→LUMO] energy, and little dependence on the [HOMO-1 → LUMO+1] energy. As can be seen in the absorption spectra (Figures 1 and 3), there is a definite connection between the intensity of the Q_y band (relative to B_y) and the configurational energy gap ΔE_{dif} shown in Figure 7C. The plots in Figure 7 give insights into how changes in substituent pattern or macrocycle type (e.g., chlorin, bacteriochlorin) affect the optical properties of tetrapyrroles.

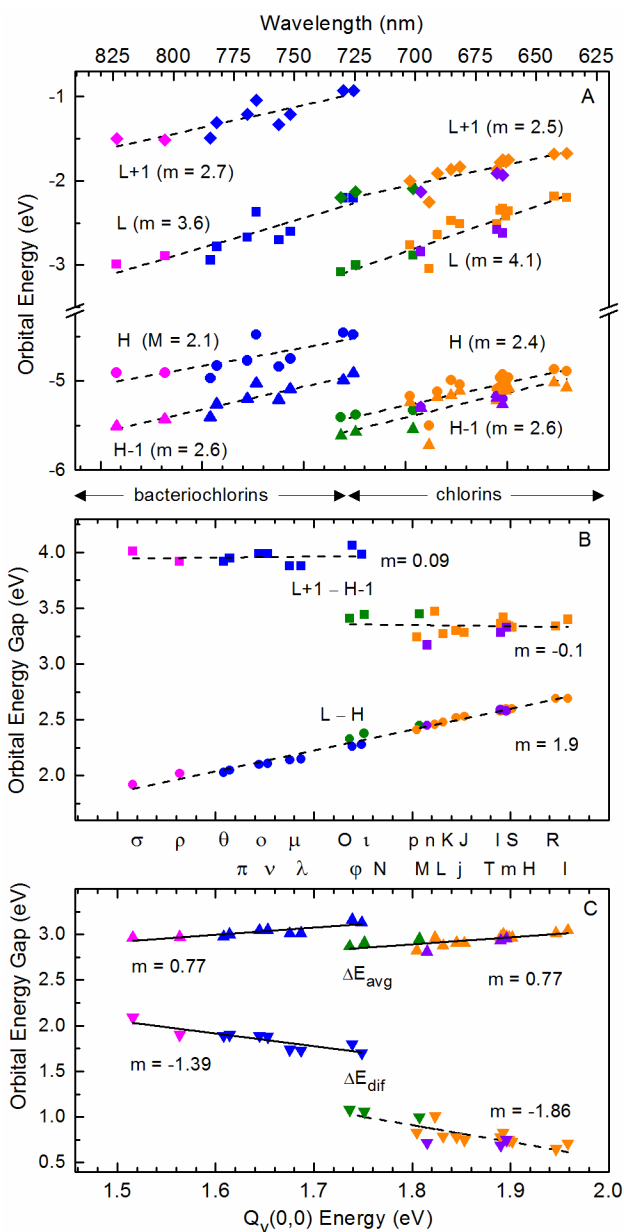


Figure 7. Frontier MO energies (A), energy gaps (B), and energy-gap averages and differences pertinent to the Q_y (and B_y) absorption bands (C) for free base chlorins (gold), chlorin-imides (green), oxophorbine (violet), bacteriochlorins (blue) and bacteriochlorin-imides (magenta). The letters above panel C identify the molecules as indicated in the legend to Figure 4. The slope of each line is given by “m”.

4. Discussion

Overview. The discussion that follows places the new results of 13- and 13,15-substituted chlorins as well as chlorin-imides (13,15 ring) in the larger framework of synthetic chlorins, bacteriochlorins, and bacteriochlorin-imides. The new work also provides additional breadth to analysis of the effects of specific substituents at specific macrocycle positions or combinations of sites. In the following, the effects of ester and benzylcarbamoyl groups at the 3- or 3,13-positions are first placed in the context of trends observed previously using a variety of common substituents at these positions on a chlorin. More specific comparisons of the properties of chlorins bearing substituents at the 13- and 3,13-positions are then given and analyzed, followed by comparisons of chlorins with substituents at the 13- and 13,15-positions. The latter two positions are the anchor points for the 13,15-imide and 13,15-anhydride rings on chlorins (with or without a 3-ester group), which leads to discussion of the new architectures containing these features. The concluding section unifies connections among photophysical properties and electronic structure spanning four classes of hydroporphyrins – chlorins, chlorin-imides, bacteriochlorins, and bacteriochlorin-imides – for which the present work provides a central bridge. Collectively, the discussion provides insights into the molecular design and tuning of red and NIR absorbing tetrapyrroles.

Effects of Ester and Benzylcarbamoyl Groups at the 3- and/or 13-Positions. The present work allows blending the effects of ester (Es) and benzylcarbamoyl (Cm) groups at the 13- and 3,13-positions into the palette of substituents used previously to tune the photophysical properties of synthetic chlorins. Key auxochromes for which photophysical consequences have been described⁸⁰⁻⁸² include the acetyl (A), formyl (F) and vinyl (V) groups found in native

(bacterio)chlorophylls as well as ethynyl (E); groups that have lesser impact than vinyl at a given macrocycle position include alkyl (methyl, ethyl) and aryl (phenyl, *p*-tolyl, mesityl) substituents.

Examination of Table 1, Figures 4 and 7 and prior data (Tables S1 and S2)⁸⁰⁻⁸² reveal that for both free base chlorins and zinc chelates, the effects of 3-, 13-, or 3,13-substituents on Q_y energy and HOMO→LUMO energy gap both follow the trend $V > Cm > E > Es > A > F$. This connection is expected because the [HOMO→LUMO] configuration contributes substantially, along with [HOMO-1→LUMO+1], to the Q_y excited state. Similarly, the I_{Q_y}/I_B peak-intensity ratio and ΔE_{dif} ([HOMO→LUMO] versus [HOMO-1→LUMO+1] configurational energy gap) generally follow the reverse trend (except E and Es are reversed for I_{Q_y}/I_B). This connection is also expected because within the four-orbital model the parallel increase in Q_y intensity and wavelength along this series derives from configurational unmixing and less destructive interference of the two transition-dipole moments. This general trend of increased absorption (and fluorescence) intensity (reflected in k_f) with substituents along the Q_y molecular axis (2,3,12,13-positions) in parallel with a bathochromic shift in Q_y (a lower energy S_1 state) is counterbalanced by the energy (wavelength) dependence of the Einstein coefficients for stimulated S_0 → S_1 absorption and spontaneous S_1 → S_0 emission,⁸⁷ which will cause a decrease in radiative rate constant as the Q_y band (S_1 state) shifts to longer wavelength (lower energy).

Effects of Combining 3- and 13-Ester Groups. Having placed the photophysical effects of the ester and benzylcarbamoyl groups in the context of the more general substituent landscape for synthetic chlorins, a closer examination of the specific effects of the common ester group is warranted. In general, the properties for the trios of chlorins always follow the trend $XC < XC-Es^{13} < XC-Es^{3,13}$ (or the reverse), where X is the free base or zinc chelate. The specific trends for the free base (zinc chelate) chlorin trios are as follows (Tables 1 and 2): (1) The Q_y

wavelength (nm) [637 (606) < 653 (627) < 677 (652)] tracks the HOMO→LUMO energy (eV) [2.69 (2.66) > 2.59 (2.56) > 2.48 (2.45)]. (2) The Q_y peak intensity relative to the Soret (B) [0.37 (0.23) < 0.53 (0.42) < 0.77 (0.50)] generally follows the radiative lifetime (k_f^{-1} , ns) obtained from the measured Φ_f and τ_s values [41 (25) < 34 (20) ~ 32 (21)], and tracks the excited-state configurational energy gap (ΔE_{dif} , eV) [0.65 (0.89) < 0.75 (0.99) < 0.79 (1.03)]. (3) Similar trends are seen in the τ_s and Φ_f values themselves (Table 1), as displayed for all the hydroporphyrins in Figure 5.

Effects of Combining 13- and 15-Ester Groups. The 13- and 15-positions are the connection points of the 13,15-imide, -anhydride, -oxophorbine, and -phorbine (annulated hydrocarbon lacking the oxo moiety) rings. Prior work has explored a number of substituents at these two positions.^{80,81} In particular, further comparisons involving ester groups are now possible that round out and extend the families started previously.

The addition of a 15-ester in addition to a 13-ester (XC-M¹⁰Es^{13,15} vs XC-M¹⁰Es¹³, where X is the free base or zinc chelate) leaves the Q_y position largely unchanged (656 nm vs 653 for the free base and 627 vs 627 nm for the zinc chelate). This finding is consistent with essentially no change in the HOMO→LUMO gap for both the free base chlorin (2.58 vs 2.59 eV) and zinc chelate (2.56 vs 2.56 eV). However, the relative Q_y absorption intensity is reduced (I_{Q_y}/I_B decreased) by about 30% (0.33 vs 0.53 for the free base, 0.29 vs 0.42 for the zinc chelate). An increase in the configurational energy difference (ΔE_{dif}) is expected and observed, albeit the difference is very small. Also reduced are the fluorescence yield (0.18 vs 0.29 for the free base, 0.20 vs 0.24 for the zinc chelate) and the singlet excited-state lifetime (6.2 vs 9.8 ns for the free base, 4.3 vs 4.8 ns for the zinc chelate).

Effects of Combining a 3-Ester Group and an Imide Ring. The incorporation of a six-membered imide ring spanning the 13,15-positions of the chlorin results in a substantial change in photophysical properties. The further addition of a 3-ester group enhances these changes. The most notable combined effect is a bathochromic shift in the Q_y band to 714 nm, which is around the short-wavelength end of the spectral region for synthetic bacteriochlorins. The effects of the imide ring and additional 3-ester group are most readily seen by comparing the properties of the trios of chlorins which generally follow the trend $XC < XCIm < XCIm-Es^3$ (or the reverse), where X is either free base or the zinc chelate. The specific trends for the free base (zinc chelate) chlorin trios are as follows: (1) The Q_y wavelength (nm) [637 (606) < 686 (660) < 714 (688)] tracks the HOMO→LUMO energy (eV) [2.69 (2.66) > 2.45 (2.46) > 2.33 (2.35)]. (2) The I_{Q_y}/I_B trend in Q_y intensity relative to the Soret (B) [0.37 (0.23) < 0.43 (0.53) < 0.71 (0.59)] does not quite track the radiative lifetime (k_f^{-1} , ns) obtained from the measured Φ_f and τ_S values [41 (25) > 33 (29) < 39 (24)], but does track the excited-state configurational energy gap (ΔE_{dif} , eV) [0.65 (0.89) < 1.00 (1.17) < 1.08 (1.24)]. Thus, the hyperchromic effect on Q_y intensity that coincides with the bathochromic shift in wavelength for chlorins **FbCIm-Es³** and **ZnCIm-Es³** follows in the four-orbital-model framework. In particular, the effect of the 13,15-imide ring and 3-ester group is to ‘unmix’ to a degree the [HOMO→LUMO] and [HOMO-1→LUMO+1] configurations.

The fluorescence yield and singlet excited-state lifetime of **FbCIm-Es³** (0.16, 6.3 ns) are only modestly reduced from those for **FbC** (0.22, 9.1 ns). Interestingly, the values for **ZnCIm-Es³** (0.18, 4.4 ns) are almost three-fold greater than those for **ZnC** (0.06, 1.5 ns). The increase in Φ_f and longer τ_S (for zinc chelates) that accompanies the shift in Q_y to lower energy resulting from the presence of the 13,15-imide ring (with or without the 3-ester group) arises in part

because for the zinc chelate there is over a three-fold decrease in the total nonradiative decay rate constant k_{nr} to $(5.4 \text{ ns})^{-1}$ from $(1.6 \text{ ns})^{-1}$. The latter effect likely stems from diminished intersystem crossing (competing with both fluorescence and internal conversion) due to the electron-withdrawing effect of the imide keto groups, which shift electron density onto the imide ring from the chlorin framework (including the nitrogens, and the central zinc when present). Such a shift will reduce the spin-orbit coupling that underlies $S_1 \rightarrow T_1$ intersystem crossing. The same effect – less probability of electrons visiting the central metal ion – likely also contributes to smaller differences in τ_S and Φ_f for the zinc chelates versus free base chlorin-imides, when compared to zinc chelates versus free base forms of simple chlorins.

Related to these observations, in general the trends in τ_S and Φ_f depicted in Figure 5 for the free base chlorins and chlorin-imides are less well defined for the zinc chelates. Because of the heavy atom effect of the central zinc ion, k_{isc} comprises a greater percentage of the total singlet decay rate ($k_f + k_{ic} + k_{isc}$) compared to the free base analogues. Thus, a change in k_f or k_{ic} induced by a change in substituents or macrocycle (chlorin-imide versus chlorin) will give a comparatively lesser effect on τ_S and Φ_f and less well-defined trends.

Such possibilities can be explored further by examination of the triplet yield (and thus k_{isc}). In this regard, such measurements for free base bacteriochlorin-imides show that k_{isc} is diminished more substantially than expected on the basis of the trends established by 3,13-substituents alone.⁷³ Furthermore, although k_{ic} for the bacteriochlorin-imides follows the trend in that value (the expected increase as Q_y moves to lower energy), k_f is off the line; the values are smaller than expected, which can be seen in Figure 5C (two magenta points). Interestingly, the k_f points for two of the chlorin-imides (Figure 5C, green) are off the trend-line in the same direction, albeit within the scatter in the data. Thus, the (bacterio)chlorin-imide motif results in

some changes in excited-state decay rate constants outside normal substituent effects. Regardless, the present studies on chlorins show that the desirable property of a bathochromic shift in Q_y band induced by the 13,15-imide ring (accentuated by the presence of a 3-ester group) either retains (free base) or enhances (zinc chelate) a long excited-state lifetime and fluorescence yield, which are useful properties for light-harvesting and photomedical applications.

5. Outlook

The studies described herein on chlorin-imides and several new sets of substituted chlorins provide a bridge that links prior work on chlorins on the one end and bacteriochlorins and bacteriochlorin-imides on the other. The *de novo* synthesis of chlorin-imides enables in-depth control over the nature of the other substituents, if any, at other sites about the perimeter of the macrocycle. To date we have focused solely on the 3-position of the chlorin-imides but the available synthetic methods enable introduction of substituents at essentially all β -pyrrole, β -pyrroline, and *meso*-positions of chlorins.^{88,89}

A number of chlorins that do not contain an imide ring but absorb at wavelengths ≥ 700 nm have been described over the years. Such chlorins contain substituents that provide extended conjugation at β -pyrrole positions,^{36,52,64,67,69} *meso*-positions,^{40,46,61,66,68} or β -pyrroline positions.^{41,46,47} Others contain substituents in the isocyclic ring.^{23,37-40,54,59,61,63,65} The majority are derived from natural chlorophylls,^{37,44,52,59,63,64,66,67,70} particularly chlorophyll *a*, whereas others have been prepared by derivatization of synthetic porphyrins, particularly 2,3,7,8,12,13,17,18-octaethylporphyrin (OEP).^{38-43,45-47,61,66} Examples of substituents include formylvinyl, dicyanovinyl, and quinonyl units. One notable subset of chlorins contains an annulated benzo ring (i.e., a benzochlorin).^{42,43,45,48-50,53,55,56,58,60,62,71} The benzochlorin derived

from OEP has long-wavelength absorption at ~ 660 nm⁹⁰ (versus ~ 645 nm for octaethylchlorin).⁹¹ In contrast with chlorins and chlorin-imides, metalation of a benzochlorin gives a bathochromic shift of the long-wavelength absorption band.^{42,55} The availability of such chlorins illustrates a variety of designs that enable longer-wavelength absorption that is not accessible with simple chlorins. On the other hand, of the (non-imide) chlorins with ≥ 700 nm absorption, some have very broad spectral features, and only a few^{55,59} have been subjected to photophysical characterization. Hence, the robustness of such designs (including wavelength tunability and synthetic tailoring) and the matching of particular chlorins to specific applications remain largely unexplored.

For the synthetic chlorin-imides, Figures 4 and 5 graphically display the connections between the energy (wavelength) of the lowest singlet excited state (Q_y) and the fluorescence yield, the singlet excited-state lifetime and the underlying radiative and total nonradiative rate constants for singlet excited-state decay. In turn, Figure 6 shows why and how certain substituents at specific sites of high electron density affect some MOs more than others. Finally, Figure 7 reveals the consequences, namely how the effects of macrocycle and associated substituent pattern affect the energies of the individual frontier MOs and as a result the MO energy gaps that dictate the energies of the excited-state configurations. These configurations dominate the NUV to NIR absorption spectra and contribute to the electronic character of the Q_y excited state and thus to its fluorescence intensity and lifetime. The connections implicit in Figures 4–7 are at the heart of the manner in which molecular design can be used to achieve desired spectral and photophysical properties of chlorins and bacteriochlorins.

Acknowledgements

This material is based upon work supported by the U.S. Department of Energy, Office of Science, Office of Basic Energy Sciences, Chemical Sciences, Geosciences and Biosciences Division, under Award Numbers DE-FG02-05ER15660 (D.F.B), DE-FG02-05ER15661 (D.H), and DE-FG02-96ER14632 (J.S.L).

References

- (1) Gouterman, M. Optical Spectra and Electronic Structure of Porphyrins and Related Rings. In *The Porphyrins*; Dolphin, D., Ed.; Academic Press: New York, 1978; Vol. 3, pp. 1–165.
- (2) Weiss, C. Electronic Absorption Spectra of Chlorophylls. In *The Porphyrins*; Dolphin, D., Ed.; Academic Press: New York, 1978; Vol. 3, pp. 211–223.
- (3) Scheer, H. An Overview of Chlorophylls and Bacteriochlorophylls: Biochemistry, Biophysics, Functions and Applications. In *Chlorophylls and Bacteriochlorophylls. Biochemistry, Biophysics, Functions and Applications*; Grimm, B., Porra, R. J., Rüdiger, W., Scheer, H., Eds.; Springer: Dordrecht, The Netherlands, 2006; Vol. 25 Advances in Photosynthesis and Respiration, pp. 1–26.
- (4) Hynninen, P. H. Chemistry of Chlorophylls: Modifications. In *Chlorophylls*; Scheer, H., Ed.; CRC Press: Boca Raton, FL, 1991; pp 145–209.
- (5) Pavlov, V. Y.; Ponomarev, G. V. Modification of the Peripheral Substituents in Chlorophylls *a* and *b* and Their Derivatives (Review). *Chem. Heterocyc. Cmpds.* **2004**, *40*, 393–425.
- (6) Conant, J. B.; Moyer, W. W. Studies in the Chlorophyll Series. III. Products of the Phase Test. *J. Am. Chem. Soc.* **1930**, *52*, 3013–3023.
- (7) Fischer, H.; Moldenhauer, O.; Süs, O. Zur Konstitution des Chlorophyll a. Über Phäophorbid, Methylphäophorbid und Chlorin e. XVI. Mitteilung: Zur Kenntnis der Chlorophylle. *Liebigs Ann. Chem.* **1931**, *486*, 107–177.
- (8) Fischer, H. Chlorophyll. *Chem. Rev.* **1937**, *20*, 41–68.
- (9) Pandey, R. K.; Bellnier, D. A.; Smith, K. M.; Dougherty, T. J. Chlorin and Porphyrin Derivatives as Potential Photosensitizers in Photodynamic Therapy. *Photochem. Photobiol.* **1991**, *53*, 65–72.
- (10) Lee, S.-J. H.; Jagerovic, N.; Smith, K. M. Use of the Chlorophyll Derivative, Purpurin-18, for Syntheses of Sensitizers for Use in Photodynamic Therapy. *J. Chem. Soc. Perkin Trans. 1* **1993**, 2369–2377.
- (11) Mironov, A. F.; Lebedeva, V. S.; Yakubovskaya, R. I.; Kazachkina, N. I.; Fomina, G. I. Chlorins with Six-Membered Imide Ring as Prospective Sensitizers for Cancer PDT. *Proc. SPIE* **1999**, *3563*, 59–67.
- (12) Zheng, G.; Potter, W. R.; Camacho, S. H.; Missert, J. R.; Wang, G.; Bellnier, D. A.; Henderson, B. W.; Rodgers, M. A. J.; Dougherty, T. J.; Pandey, R. K. Synthesis, Photophysical Properties, Tumor Uptake, and Preliminary *In Vivo* Photosensitizing

- Efficacy of a Homologous Series of 3-(1'-Alkyloxy)ethyl-3-devinylpurpurin-18-*N*-alkylimides with Variable Lipophilicity *J. Med. Chem.* **2001**, *44*, 1540–1559.
- (13) Fukuzumi, S.; Ohkubo, K.; Imahori, H.; Shao, J.; Ou, Z.; Zheng, G.; Chen, Y.; Pandey, R. K.; Fujitsuka, M.; Ito, O.; Kadish, K. M. Photochemical and Electrochemical Properties of Zinc Chlorin–C₆₀ Dyad as Compared to Corresponding Free Base Chlorin–C₆₀, Free Base Porphyrin–C₆₀, and Zinc Porphyrin–C₆₀ Dyads. *J. Am. Chem. Soc.* **2001**, *123*, 10676–10683.
- (14) Ohkubo, K.; Imahori, H.; Shao, J.; Ou, Z.; Kadish, K. M.; Chen, Y.; Zheng, G.; Pandey, R. K.; Fujitsuka, M.; Ito, O.; Fukuzumi, S. Small Reorganization Energy of Intramolecular Electron Transfer in Fullerene-Based Dyads with Short Linkage. *J. Phys. Chem. A* **2002**, *106*, 10991–10998.
- (15) Kuz'mitskii, V. A.; Knyukshto, V. N.; Gael, V. I.; Zen'kevich, E. I.; Sagun, E. I.; Pukhlikova, N. A.; Lebedeva, V. S.; Mironov, A. F. Spectral-Luminescent Properties and Electronic Structure of the Chlorin *p*₆ Derivatives with an Extended Conjugated Bond System. *J. Appl. Spectros.* **2003**, *70*, 43–53.
- (16) Mironov, A. F.; Ruziev, R. D.; Lebedeva, V. S. Synthesis and Chemical Transformations of *N*-Hydroxy and *N*-Hydroxyalkylcycloimides of Chlorin *p*₆. *Russ. J. Bioorg. Chem.* **2004**, *30*, 466–476.
- (17) Nazarova, A. I.; Feofanov, A. V.; Karmakova, T. A.; Sharonov, G. V.; Plyutinskaya, A. D.; Yakubovskaya, R. I.; Lebedeva, V. S.; Mironov, A. F.; Maurizot, J.-C.; Vigny, P. Effect of Substituents on Photochemical and Biological Properties of 13,15-*N*-Cycloimide Derivatives of Chlorin *p*₆. *Russ. J. Bioorg. Chem.* **2005**, *31*, 482–494.
- (18) Han, G.-F.; Wang, J.-J.; Qu, Y.; Shim, Y. K. Chemical Modification of Derivatives of Purpurin-18 Imide. *Chin. J. Org. Chem.* **2005**, *26*, 43–50.
- (19) Wang, J.-J.; Han, G.-F.; Wu, X.-R.; Shim, Y. K. Oxidation Reaction along Q_y Axis and Rearrangement Reaction in E-Ring of Chlorophyll-*a* and its Derivatives. *Chin. J. Org. Chem.* **2005**, *25*, 101–108.
- (20) Gryshuk, A.; Chen, Y.; Goswami, L. N.; Pandey, S.; Missert, J. R.; Ohulchanskyy, T.; Potter, W.; Prasad, P. N.; Oseroff, A.; Pandey, R. K. Structure–Activity Relationship Among Purpurinimides and Bacteriopurpurinimides: Trifluoromethyl Substituent Enhanced the Photosensitizing Efficacy. *J. Med. Chem.* **2007**, *50*, 1754–1767.
- (21) Pandey, S. K.; Zheng, X.; Morgan, J.; Missert, J. R.; Liu, T.-H.; Shibata, M.; Bellnier, D. A.; Oseroff, A. R.; Henderson, B. W.; Dougherty, T. J.; Pandey, R. K. Purpurinimide Carbohydrate Conjugates: Effect of the Position of the Carbohydrate Moiety in Photosensitizing Efficacy. *Mol. Pharm.* **2007**, *4*, 448–464.
- (22) Nechaev, A. V.; Mironov, A. F. New Amphiphilic Chlorins of the Chlorophyll *a* Series. *Russ. J. Bioorg. Chem.* **2008**, *34*, 245–251.
- (23) Liu, C.; Dobhal, M. P.; Ethirajan, M.; Missert, J. R.; Pandey, R. K.; Balasubramanian, S.; Sukumaran, D. K.; Zhang, M.; Kadish, K. M.; Ohkubo, K.; Fukuzumi, S. Highly Selective Synthesis of the Ring-B Reduced Chlorins by Ferric Chloride-Mediated Oxidation of Bacteriochlorins: Effects of the Fused Imide vs Isocyclic Ring on Photophysical and Electrochemical Properties. *J. Am. Chem. Soc.* **2008**, *130*, 14311–14323.
- (24) Goswami, L. N.; Ethirajan, M.; Dobhal, M. P.; Zhang, M.; Missert, J. R.; Shibata, M.; Kadish, K. M.; Pandey, R. K. Remarkable Features of the McMurry Reaction Conditions in Dimerization of Formyl- and 2-Formylvinylpurpurinimides. *Electrochemistry of*

- Monomeric Ni(II) Purpurinimide and the Corresponding Dyads *J. Org. Chem.* **2009**, *74*, 568–579.
- (25) Grin, M. A.; Lonin, I. S.; Lakhina, A. A.; Ol'shanskaya, E. S.; Makarov, A. I.; Sebyakin, Y. L.; Guryeve, L. Y.; Toukach, P. V.; Kononikhin, A. S.; Kuzmin, V. A.; Mironov, A. F. 1,3-Dipolar Cycloaddition in the Synthesis of Glycoconjugates of Natural Chlorins and Bacteriochlorins. *J. Porphyrins Phthalocyanines* **2009**, *13*, 336–345.
- (26) Li, J. Z.; Li, L.; Kim, J. H.; Cui, B. C.; Wang, J. J.; Shim, Y. K. Efficient Synthesis and *In Vitro* Photodynamic Anticancer Study of New Purpurinimide-Hydrazone Conjugates. *J. Porphyrins Phthalocyanines* **2011**, *15*, 264–270.
- (27) Lebedeva, V. S.; Ruziev, R. D.; Mironov, A. F. Chlorin *p*₆ Cycloimides: Synthesis, Properties and Possible Fields of Application. *Macroheterocycles* **2012**, *5*, 32–55.
- (28) Li, J. Z.; Wang, J. J.; Yoon, I.; Cui, B. C.; Shim, Y. K. Syntheses of Novel Long Wavelength Cationic Chlorins via Stereoselective Aldol-Like Condensation. *Bioorg. Med. Chem. Lett.* **2012**, *22*, 1846–1849.
- (29) Liu, R.; Yin, J.; Li, J.; Wu, J.; Chen, G.; Jin, Y.; Wang, J. Halogenation Reaction of Purpurin-18 and Synthesis of Chlorin Derivatives. *Chin. J. Org. Chem.* **2012**, *32*, 544–551.
- (30) Williams, M. P. A.; Ethirajan, M.; Ohkubo, K.; Chen, P.; Pera, P.; Morgan, J.; White, W. H., III; Shibata, M.; Fukuzumi, S.; Kadish, K. M.; Pandey, R. K. Synthesis, Photophysical, Electrochemical, Tumor-Imaging, and Phototherapeutic Properties of Purpurinimide-*N*-substituted Cyanine Dyes Joined with Variable Lengths of Linkers. *Bioconjugate Chem.* **2011**, *22*, 2283–2295.
- (31) Ethirajan, M.; Chen, P.; Ohulchanskyy, T. Y.; Goswami, L. N.; Gupta, A.; Srivatsan, A.; Dobhal, M. P.; Missert, J. R.; Prasad, P. N.; Kadish, K. M.; Pandey, R. K. Regioselective Synthesis and Photochemical and Electrochemical Studies of 20-Substituted Cyanine Dye–Purpurinimide Conjugates: Incorporation of Ni^{II} into the Conjugate Enhances its Tumor-Uptake and Fluorescence-Imaging Ability. *Chem. Eur. J.* **2013**, *19*, 6670–6684.
- (32) Ji, J.; Xia, S.; Zhao, L.; Li, J.; Qi, C.; Wang, J. Chemical Reaction of Purpurin-18 Imide and Synthesis of Chlorins Related to Chlorophyll. *Chin. J. Org. Chem.* **2013**, *33*, 1457–1464.
- (33) Cui, B. C.; Yoon, I.; Li, J. Z.; Lee, W. K.; Shim, Y. K. Synthesis and Characterization of Novel Purpurinimides as Photosensitizers for Photodynamic Therapy. *Int. J. Mol. Sci.* **2014**, *15*, 8091–8105.
- (34) Ptaszek, M.; Lahaye, D.; Krayner, M.; Muthiah, C.; Lindsey, J. S. De Novo Synthesis of Long-Wavelength Absorbing Chlorin-13,15-Dicarboximides. *J. Org. Chem.* **2010**, *75*, 1659–1673.
- (35) Muthiah, C.; Ptaszek, M.; Nguyen, T. M.; Flack, K. M.; Lindsey, J. S. Two Complementary Routes to 7-Substituted Chlorins. Partial Mimics of Chlorophyll *b*. *J. Org. Chem.* **2007**, *72*, 7736–7749.
- (36) Nichol, A. W. Formylation of Iron(III) Porphyrins and Chlorins of Natural Origin. *J. Chem. Soc. C* **1970**, 903–910.
- (37) Falk, H.; Hoornaert, G.; Isenring, H.-P.; Eschenmoser, A. Über Enolderivate der Chlorophyllreihe. Darstellung von 13²,17³-Cyclophäophorbidenolen. *Helv. Chim. Acta* **1975**, *58*, 2347–2357.
- (38) Arnold, D. P.; Gaete-Holmes, R.; Johnson, A. W.; Smith, A. R. P.; Williams, G. A. Wittig Condensation Products from Nickel *meso*-Formyl-octaethylporphyrin and –

- aetioporphyrin I and Some Cyclisation Reactions. *J. Chem. Soc. Perkin Trans. 1* **1978**, 1660–1670.
- (39) Morgan, A. R.; Tertel, N. C. Observations on the Synthesis and Spectroscopic Characteristics of Purpurins. *J. Org. Chem.* **1986**, *51*, 1347–1350.
- (40) Gunter, M. J.; Robinson, B. C. Purpurins Bearing Functionality at the 6,16-*meso*-Positions: Synthesis from 5,15-Disubstituted *meso*-[β -(Methoxycarbonyl)vinyl]porphyrins. *Aust. J. Chem.* **1990**, *43*, 1839–1860.
- (41) Chang, C.-K.; Wu, W. Derivatives of Porphyrin Useful in Photodynamic Therapy. U.S. Patent 5,064,952, 1991.
- (42) Vicente, M. G. H.; Smith, K. M. Vilsmeier Reactions of Porphyrins and Chlorins with 3-(Dimethylamino)acrolein To Give *meso*-(2-Formylvinyl)porphyrins: New Syntheses of Benzochlorins, Benzoisobacteriochlorins, and Benzobacteriochlorins and Reductive Coupling of Porphyrins and Chlorins Using Low-Valent Titanium Complexes. *J. Org. Chem.* **1991**, *56*, 4407–4418.
- (43) Skalkos, D.; Hampton, J. A. Iminium Salt Benzochlorins as Potential Photosensitizers in Photodynamic Therapy. *Med. Chem. Res.* **1992**, *2*, 276–281.
- (44) Pandey, R. K.; Shiau, F.-Y.; Sumlin, A. B.; Dougherty, T. J.; Smith, K. M. Structure/Activity Relationships Among Photosensitizers Related to Pheophorbides and Bacteriopheophorbides. *Bioorg. Med. Chem. Lett.* **1992**, *2*, 491–496.
- (45) Osuka, A.; Ikawa, Y.; Maruyama, K. Synthesis of Benzochlorin Monomer, Dimer, and Porphyrin–Benzochlorin Heterodimer from 5-Aryl- and 5,15-Diaryl-octaethylporphyrins. *Bull. Chem. Soc. Jpn.* **1992**, *65*, 3322–3330.
- (46) Robinson, B. C.; Morgan, A. R. Barbituric Acid Functionalized Porphyrins and Chlorins. *Tetrahedron Lett.* **1993**, *34*, 3711–3714.
- (47) Phadke, A. S.; Butler, C.; Robinson, B. C.; Morgan, A. R. Synthesis of New Long Red Absorbing Porphyrins: Reactions of Organolithiums on Octaethylporphyrinone. *Tetrahedron Lett.* **1993**, *34*, 6359–6362.
- (48) Boyle, R. W.; Dolphin, D. 5,15-Diphenyl-7-oxobenzochlorins. Novel Long-Wavelength Absorbing Photosensitizers for Photodynamic Therapy. *J. Chem. Soc., Chem. Commun.* **1994**, 2463–2464.
- (49) Morgan, A. R.; Gupta, S. Synthesis of Benzopurpurins, Isobacteriobenzopurpurins and Bacteriobenzopurpurins. *Tetrahedron Lett.* **1994**, *35*, 4291–4294.
- (50) Morgan, A. R.; Gupta, S. Synthesis of Benzochlorin Iminium Salts with Improved Photosensitizing Properties. *Tetrahedron Lett.* **1994**, *35*, 5347–5350.
- (51) Ma, L.; Dolphin, D. Chemical Modification of Chlorophyll *a*: Synthesis of New Regiochemically Pure Benzoporphyrin and Dibenzoporphyrin Derivatives. *Can. J. Chem.* **1997**, *75*, 262–275.
- (52) Tamiaki, H.; Kouraba, M. Synthesis of Chlorophyll-*a* Homologs by Wittig and Knoevenagel Reactions with Methyl Pyropheophorbide-*d*. *Tetrahedron* **1997**, *53*, 10677–10688.
- (53) Garbo, G. M.; Fingar, V. H.; Wieman, T. J.; Noakes, E. B., III; Haydon, P. S.; Cerrito, P. B.; Kessel, D. H.; Morgan, A. R. *In Vivo* and *In Vitro* Photodynamic Studies with Benzochlorin Iminium Salts Delivered by a Lipid Emulsion. *Photochem. Photobiol.* **1998**, *68*, 561–568.

- (54) Kozyrev, A. N.; Alderfer, J. L.; Dougherty, T. J.; Pandey, R. K. Synthesis of Verdinochlorins: A New Class of Long-Wavelength Absorbing Photosensitizers. *Chem. Commun.* **1998**, 1083–1084.
- (55) Mettath, S.; Shibata, M.; Alderfer, J. L.; Senge, M. O.; Smith, K. M.; Rein, R.; Dougherty, T. J.; Pandey, R. K. Synthesis and Spectroscopic Properties of Novel Benzochlorins Derived from Chlorophyll *a*. *J. Org. Chem.* **1998**, *63*, 1646–1656.
- (56) Johnson, C. K.; Dolphin, D. Syntheses of Chlorins Possessing Fused Nitrogen-Containing Rings. *Tetrahedron Lett.* **1998**, *39*, 4619–4622.
- (57) Beavington, R.; Burn, P. L. Bis-porphyrin Arrays. Part 1. The Synthesis of *meso*-Halophenyl Porphyrin- α -Diones. *J. Chem. Soc., Perkin Trans. 1* **1999**, 583–592.
- (58) Mettath, S.; Li, G.; Srikrishnan, T.; Mehta, R.; Grossman, Z. D.; Dougherty, T. J.; Pandey, R. K. Effect of Substituents in Directing the Formation of Benzochlorins and Isobacteriochlorins in Porphyrin and Chlorin Systems. *Org. Lett.* **1999**, *1*, 1961–1964.
- (59) Kozyrev, A. N.; Suresh, V.; Das, S.; Senge, M. O.; Shibata, M.; Dougherty, T. J.; Pandey, R. K. Syntheses and Spectroscopic Studies of Novel Chlorins with Fused Quinoxaline or Benzimidazole Ring Systems and the Related Dimers with Extended Conjugation. *Tetrahedron* **2000**, *56*, 3353–3364.
- (60) Jayaraj, K.; Gold, A.; Ball, L. M.; White, P. S. *N*-Porphyrinylamino and -amido Compounds by Addition of an Amino or Amido Nitrogen to a Porphyrin Meso Position. *Inorg. Chem.* **2000**, *39*, 3652–3664.
- (61) Robinson, B. C. Bacteriopurpurins: Synthesis from *meso*-Diacrylate Substituted Porphyrins. *Tetrahedron* **2000**, *56*, 6005–6014.
- (62) Phadke, A. S.; Robinson, B. C.; Barkigia, K. M.; Fajer, J. Synthesis of Benzochlorins and Rhodinobenzochlorins. *Tetrahedron* **2000**, *56*, 7661–7666.
- (63) Yagai, S.; Miyatake, T.; Shimono, Y.; Tamiaki, H. Supramolecular Structure of Self-assembled Synthetic Zinc-13¹-oxo-chlorins Possessing a Primary, Secondary or Tertiary Alcoholic 3¹-Hydroxyl Group: Visible Spectroscopic and Molecular Modeling Studies. *Photochem. Photobiol.* **2001**, *73*, 153–163.
- (64) Wang, J.-J.; Wu, X.-R.; Wang, L.-M.; Han, G.-F.; Shim, Y. K. Synthesis of Methyl Porphyrin-*a* Substituted at 3-Position by Benzo-heterocycle with Nitrogen Atom. *Chin. J. Org. Chem.* **2004**, *24*, 906–911.
- (65) McCarthy, J. R.; Hyland, M. A.; Brückner, C. Synthesis of Indaphyrins: *meso*-Tetraarylsecoclorin-Based Porphyrinoids Containing Direct *o*-Phenyl-to- β -Linkages. *Org. Biomol. Chem.* **2004**, *2*, 1484–1491.
- (66) Wang, J.-J.; Wu, X.-R.; Shim, Y.-K. Synthesis of δ -*meso*-Formylvinylchlorin and Benzoisobacteriochlorin by Vilsmeier Reaction with Methyl Porphyrin-*a*. *Chin. J. Chem.* **2005**, *23*, 76–80.
- (67) Sasaki, S.-I.; Kotegawa, Y.; Tamiaki, H. Trifluoroacetyl-chlorin as a New Chemosensor for Alcohol/Amine Detection. *Tetrahedron Lett.* **2006**, *47*, 4849–4852.
- (68) Wang, Y.; Wang, F.-M.; Qu, Y.; Han, G.-F.; Wang, J.-J. Synthesis of Derivatives of δ -(2-Formylvinyl)-chlorins. *Chin. J. Org. Chem.* **2007**, *27*, 391–396.
- (69) Liu, X.; Sternberg, E.; Dolphin, D. Cross-Metathesis of the Vinyl Group on Tetrapyrrolic Macrocycles: Reactivity, Selectivity, and Mechanism. *J. Org. Chem.* **2008**, *73*, 6542–6550.

- (70) Kunieda, M.; Tamiaki, H. Synthesis of Zinc 3-Hydroxymethyl-porphyrins Possessing Carbonyl Groups at the 13-and/or 15-Positions for Models of Self-Aggregative Chlorophylls in Green Photosynthetic Bacteria. *J. Org. Chem.* **2008**, *73*, 7686–7694.
- (71) Tokuji, S.; Takahashi, Y.; Shinmori, H.; Shinokubo, H.; Osuka, A. Synthesis of a Pyridine-fused Porphyrinoid: Oxopyridochlorin. *Chem. Commun.* **2009**, 1028–1030.
- (72) Wang, J. J.; Li, J. Z.; Jakus, J.; Shim, Y. K. Synthesis of Long-Wavelength Chlorins by Chemical Modification for Methyl Pyropheophorbide-*a* and their *In Vitro* Cell Viabilities. *J. Porphyrins Phthalocyanines* **2012**, *16*, 122–129.
- (73) Yang, E.; Kirmaier, C.; Krayner, M.; Taniguchi, M.; Kim, H.-J.; Diers, J. R.; Bocian, D. F.; Lindsey, J. S.; Holten, D. Photophysical Properties and Electronic Structure of Stable, Tunable Synthetic Bacteriochlorins: Extending the Features of Native Photosynthetic Pigments. *J. Phys. Chem. B* **2011**, *115*, 10801–10816.
- (74) Chen, C.-Y.; Sun, E.; Fan, D.; Taniguchi, M.; McDowell, B. E.; Yang, E.; Diers, J. R.; Bocian, D. F.; Holten, D.; Lindsey, J. S. Synthesis and Physicochemical Properties of Metallobacteriochlorins. *Inorg. Chem.* **2012**, *51*, 9443–9464.
- (75) Mass, O.; Taniguchi, M.; Ptaszek, M.; Springer, J. W.; Faries, K. M.; Diers, J. R.; Bocian, D. F.; Holten, D.; Lindsey, J. S. Structural Characteristics that Make Chlorophylls Green: Interplay of Hydrocarbon Skeleton and Substituents. *New J. Chem.* **2011**, *35*, 76–88.
- (76) Weber, G.; Teale, F. Determination of the Absolute Quantum Yield of Fluorescent Solutions. *Trans. Faraday Soc.* **1957**, *53*, 646–655.
- (77) Seybold, P. G.; Gouterman, M. Porphyrins XIII: Fluorescence Spectra and Quantum Yields. *J. Mol. Spectrosc.* **1969**, *31*, 1–13.
- (78) Gradyushko, A. T.; Sevchenko, A. N.; Solovyov, K. N.; Tsvirko, M. P. *Photochem. Photobiol.* **1970**, *11*, 387–400.
- (79) Except for molecular mechanics and semi-empirical models, the calculation methods used in Spartan '08 or '10 have been documented in: Shao, Y.; Molnar, L. F.; Jung, Y.; Kussmann, J. R.; Ochsenfeld, C.; Brown, S. T.; Gilbert, A. T. B.; Slipchenko, L. V.; Levchenko, S. V.; O'Neill, D. P.; et al. Advances in Methods and Algorithms in a Modern Quantum Chemistry Program Package. *Phys. Chem. Chem. Phys.* **2006**, *8*, 3172–3191.
- (80) Kee, H. L.; Kirmaier, C.; Tang, Q.; Diers, J. R.; Muthiah, C.; Taniguchi, M.; Laha, J. K.; Ptaszek, M.; Lindsey, J. S.; Bocian, D. F.; Holten, D. Effects of Substituents on Synthetic Analogs of Chlorophylls. Part 1: Synthesis, Vibrational Properties and Excited-State Decay Characteristics. *Photochem. Photobiol.* **2007**, *83*, 1110–1124.
- (81) Kee, H. L.; Kirmaier, C.; Tang, Q.; Diers, J. R.; Muthiah, C.; Taniguchi, M.; Laha, J. K.; Ptaszek, M.; Lindsey, J. S.; Bocian, D. F.; Holten, D. Effects of Substituents on Synthetic Analogs of Chlorophylls. Part 2: Redox Properties, Optical Spectra and Electronic Structure. *Photochem. Photobiol.* **2007**, *83*, 1125–1143.
- (82) Springer, J. W.; Faries, K. M.; Diers, J. R.; Muthiah, C.; Mass, O.; Kee, H. L.; Kirmaier, C.; Lindsey, J. S.; Bocian, D. F.; Holten, D. Effects of Substituents on Synthetic Analogs of Chlorophylls. Part 3: The Distinctive Impact of Auxochromes at the 7- versus 3-Positions. *Photochem. Photobiol.* **2012**, *88*, 651–674.
- (83) Park, J.-K.; Choe, S. J. Comparison of Different Theory Models and Basis Sets for the Calculation of FbC-M¹⁰Iso-Bn Geometry and Geometries of Chlorin-Imide and Chlorin-Isoimide Isomeric Pairs. *J. Porphyrins Phthalocyanines* **2013**, *17*, 376–383.

- (84) Gouterman, M. Study of the Effects of Substitution on the Absorption Spectra of Porphin. *J. Chem. Phys.* **1959**, *30*, 1139–1161.
- (85) Gouterman, M. Spectra of Porphyrins. *J. Mol. Spectrosc.* **1961**, *6*, 138–163.
- (86) Yuen, J.; Harris, M. A.; Liu, M.; Diers, J. R.; Kirmaier, C.; Bocian, D. F.; Lindsey, J. S.; Holten, D. Effects of Substituents on Synthetic Analogs of Chlorophylls. Part 4: How Formyl Group Location Dictates the Spectral Properties of Chlorophylls *b*, *d* and *f*. *Photochem. Photobiol.* **2015**, *91*, xxxx-xxxx (DOI:10.1111/php.12401).
- (87) Birks, J. B. *Photophysics of Aromatic Molecules*; Wiley-Interscience: London, 1970; pp. 142–192.
- (88) Aravindu, K.; Kim, H.-J.; Taniguchi, M.; Dilbeck, P. L.; Diers, J. R.; Bocian, D. F.; Holten, D.; Lindsey, J. S. Synthesis and Photophysical Properties of Chlorins Bearing 0–4 Distinct Meso-Substituents. *Photochem. Photobiol. Sci.* **2013**, *12*, 2089–2109.
- (89) Liu, M.; Ptaszek, M.; Mass, O.; Minkler, D. J.; Sommer, R. D.; Bhaumik, J.; Lindsey, J. S. Regioselective β -Pyrrolic Bromination of Hydrodipyrin–Dialkylboron Complexes Facilitates Access to Synthetic Models for Chlorophyll *f*. *New J. Chem.* **2014**, *38*, 1717–1730.
- (90) Morgan, A. R.; Skalkos, D.; Maguire, G.; Rampersaud, A.; Garbo, G.; Keck, R.; Selman, S. H. Observations on the Synthesis and *in vivo* Photodynamic Activity of Some Benzochlorins. *Photochem. Photobiol.* **1992**, *55*, 133–136.
- (91) Keegan, J. D.; Stolzenberg, A. M.; Lu, Y.-C.; Linder, R. E.; Barth, G.; Moscovitz, A.; Bunnenberg, E.; Djerassi, C. Magnetic Circular Dichroism Studies. 60. Substituent-Induced Sign Variation in the Magnetic Circular Dichroism Spectra of Reduced Porphyrins. 1. Spectra and Band Assignments. *J. Am. Chem. Soc.* **1982**, *104*, 4305–4317.

Chapter 3: Augmenting light coverage for photosynthesis through YFP-enhanced charge separation at the *Rhodobacter sphaeroides* reaction centre

Reprinted with permission from Grayson, K.J.; Faries, K.M.; Huang, X.; Qian, P.; Dilbeck, P.; Martin, E.C.; Hitchcock, A.; Vasilev, C.; Yuen, J.M.; Niedwiedzki, D.M.; Leggett, G.J.; Holten, D.; Kirmaier, C.; Hunter, C.N. (2017) Augmenting light coverage for photosynthesis through YFP-enhanced charge separation at the *Rhodobacter sphaeroides* reaction centre. *Nature Communications*, 8, 13972.

Abstract

Photosynthesis uses a limited range of the solar spectrum, so enhancing spectral coverage could improve the efficiency of light capture. Here, we show that a hybrid reaction centre (RC)/yellow fluorescent protein (YFP) complex accelerates photosynthetic growth in the bacterium *Rhodobacter sphaeroides*. The structure of the RC/YFP-light-harvesting 1 (LH1) complex shows the position of YFP attachment to RC-H, on the cytoplasmic side of the RC complex. Fluorescence lifetime microscopy of whole cells and ultrafast transient absorption spectroscopy of purified RC/YFP complexes show that the YFP-RC intermolecular distance and spectral overlap between the emission of YFP and the visible-region (Q_x) absorption bands of the RC allow energy transfer via a Förster mechanism, with an efficiency of $40 \pm 10\%$. This proof-of-principle study demonstrates the feasibility of increasing spectral coverage for harvesting light using non-native genetically-encoded light-absorbers, thereby augmenting energy transfer and trapping in photosynthesis.

1. Introduction

Photosynthesising organisms harvest only a small proportion of the visible and near-infrared radiation reaching the Earth's surface, and bacterial, algal and plant species have evolved to occupy particular spectral niches depending on the absorption of the particular chlorophyll, carotenoid, phycobilin and other pigments they synthesise^{1,2}. Several studies have explored the possibilities of expanding the spectral coverage of light harvesting and reaction centre complexes using chlorophylls³⁻⁵ or attached dye molecules⁶⁻⁸ and the biohybrid approach, which combines parts of native antennas with synthetic chromophores, provides an emerging platform technology for the creation of artificial antennas. This flexible, versatile and tailorable strategy extends solar coverage beyond natural systems. The polypeptide scaffold often chosen for such work is based on the light-harvesting LH1 complex from the photosynthetic bacterium *Rhodobacter (Rba.) sphaeroides*. The LH1 antenna consists of a circular assembly of repeating $\alpha_1\beta_1\text{BChl}_2\text{Crt}_2$ units, where each α or β polypeptide is a single transmembrane helix that binds a single bacteriochlorophyll *a* (BChl) and a carotenoid (Crt) molecule. This assembly surrounds, and donates excitation energy to, the reaction centre (RC) where charge separation occurs. The discovery that an LH1 antenna can be reconstituted from purified pigments and α/β polypeptides, plus the availability of single-site alterations and truncated versions of these polypeptides, allowed the *in vitro* self-assembly of LH1 antenna variants⁹⁻¹¹. Biohybrid antennas with enhanced spectral coverage can be assembled by creating attachment sites for synthetic chromophores that efficiently transfer energy to the BChl *a* site^{5, 12-15}. The efficiencies of energy transfer to the BChl *a* acceptor are comparable with native antennas, and current designs can accommodate up to 60 chromophores that contribute to solar light harvesting via an energy

transfer cascade. The use of unattached accessory chromophores within detergent micelles provides another route to enhance light-harvesting capability^{14, 15}.

Biohybrid architectures have great potential for producing artificial light-harvesting architectures *in vitro*, but they utilise synthetic chemistry so they cannot replicate *in vivo*. In order to create tailor-made light harvesting antennas *in vivo*, we must make use of the toolbox of proteins and pigments available in nature, or create synthetic elements that can be produced by the host organism. In the purple photosynthetic bacterium *Rba. sphaeroides*, light is harvested by the LH2 and LH1 antenna complexes and the resulting excitation energy is used to power the reduction of quinone to quinol prior to the formation of a proton gradient that powers ATP synthesis¹⁶. *Rba. sphaeroides* transfers the energy from light absorbed by B875 BChls in LH1 and B850 BChls in LH2 to the RC with near 100% quantum efficiency¹⁷⁻¹⁹. A charge separation takes place within the RC, which converts excitation energy to biochemical energy²⁰. Quinols, the eventual product of RC photochemistry, exit from the RC and traverse the LH1 ring surrounding the RC through a portal provided by the PufX polypeptide¹⁶.

As a pilot study to explore the possibility of creating artificial light-harvesting antennas *in vivo*, this work investigates the effects of incorporating the yellow fluorescent protein, YFP, as a chromophore into the *Rba. sphaeroides* photosystem. YFP is a well-studied and genetically programmable protein; the YFP variant used in this study, SYFP2, exhibits photostability, a high fluorescence quantum yield (~70 %) and a large extinction coefficient (~100,000 M⁻¹ cm⁻¹ at 515 nm)²¹. However, YFP cannot contribute usefully to the native absorption of *Rba. sphaeroides*, because the carotenoid pigments of the light-harvesting complexes absorb in the 400-550 nm range. Accordingly, we constructed a carotenoidless mutant of *Rba. sphaeroides* in order to create a baseline strain for assessing any contribution of YFP to photosynthesis. The 525 nm

emission maximum of SYFP2 has some overlap with the visible-region (Q_x) absorption band of BChl *a* in the *Rba. sphaeroides* LH1 and RC complexes, and the results of this study suggest that some of the energy absorbed by YFP migrates to the RC. This work forms the basis of future studies involving the creation of novel, tailored light-harvesting antenna complexes for increased spectral coverage of *in vivo* photosynthesis.

2. Methods

Construction of the $\Delta crtB$ deletion strain

A construct containing the upstream and downstream flanking regions of the gene was created in order to delete *crtB*. A 361 bp fragment upstream of *crtB* and the first 7 bp of the *crtB* gene flanked with *Eco*RI and *Xba*I restriction sites (underlined) was amplified using the primers crtBKOUF (5'-CCGGAATTCACATCACCATCACCACGGCG-3') and crtBKOUR (5'-GCGCTCTAGAGATCTAGGTTCTCATGAAGGTATAACCG-3'). A second fragment was amplified using the primers crtBKODF (5'GCGCTCTAGAGGCAATCATTCCGCGGCAAGC-3') and crtBKODR (5'-CCCCGCATGCGGGCTGTGGCCGAGCCCTA-3') producing a downstream flanking fragment of 363 bp which included 9 bp at the end of the *crtB* gene, flanked with *Xba*I and *Sph*I restriction sites (underlined). Following digestion with the indicated enzymes, the fragments were sequentially cloned into the same restriction sites of the suicide vector pK18mobsacB. The resulting plasmid was introduced into *E. coli* S17-1 competent cells and transferred to *Rba. sphaeroides* WT via conjugation, with first and second recombination events selected for as detailed in the Methods. Conjugative transfer of constructs from *Escherichia coli* to *Rba. sphaeroides* was performed using a modification of the method in³¹. Transconjugant *Rba. sphaeroides* colonies were selected on M22 agar plates with 25 $\mu\text{g ml}^{-1}$

kanamycin. Single colonies were grown and scaled up to an 80 ml semi-aerobic culture. The cells were serially diluted 10^{-2} , 10^{-3} and 10^{-4} onto M22 agar containing 1 % (w/v) sucrose and incubated until single colonies appeared after 4-6 days. Single colonies were replica plated onto M22 sucrose plates, with and without $25 \mu\text{g ml}^{-1}$ kanamycin. Colonies that grew on the antibiotic-free plate but not on the kanamycin plate were analysed by PCR to identify successful mutants. Transconjugants were confirmed by DNA sequencing; the modified DNA sequence at the location where *crtB* is deleted is shown in Supplementary Fig. 9.

Construction of mutant *Rhodobacter sphaeroides* strains

The RC/YFP fusion strain was created using a pk18mobsacB construct designed to fuse the gene for SYFP2²¹ to the 3' end of the *puhA* gene encoding the reaction centre H subunit. To create a C-terminal YFP fusion protein, firstly a PCR fragment was generated using primers puhAYFPUF (5'-CCGGAATTCTCGGCCGGCAAGAACCCGATCGG-3') and puhAYFPUR (5'-GCTCCTCGCCCTTGCTCACCATGGCGTATTCGGCCAGCATCGCCG-3'). This fragment contained the last 354 bp of the *puhA* ORF (excluding the stop codon), with a 5' *EcoRI* restriction site (underlined) and 3' sequence complementary to the start of the *syfp2* gene (italics).

A second PCR with primers puhAYFPFor (5'-CGGCGATGCTGGCCGAATACGCCATGGTGAGCAAGGGCGAGGAGCTGTTCAC-3') and puhAYFPRev (5'-GCGCTCTAGATCATTACTTGTACAGCTCGTCCATGCCGAGAGTGAT-3') amplified the *syfp2* ORF with 5' sequence complementary to the end of the *puhA* gene (italics) and a 3' *XbaI* restriction site (underlined). The two fragments were used as a template for overlap extension (OLE)-PCR with primers puhAYFPUF and puhAYFPRev, generating a fragment in which the end of the *puhA* gene was joined in frame with the *syfp2* gene with *EcoRI* and *XbaI* sites at the 5' and 3' ends respectively. A third fragment in which the 354 bp

immediately downstream of the *puhA* stop codon was flanked by *Xba*I and *Hind*III restriction sites (underlined) was amplified using the primers puhAYFPDF (5'-GCGCTCTAGATCCCCGCATGGCGCGGCC-3') and puhAYFPDR (5'-CCCCAAGCTTTAGGGCACCGCATAGGCCACCGC-3'). Following *Xba*I/*Hind*III digestion, the downstream fragment was cloned into the suicide vector pK18mobsacB. The resulting plasmid was opened with *Eco*RI and *Xba*I and the *puhA-sfYFP2* product cut with the same enzymes was inserted. This plasmid contained a total insert of 1428 bp. The fragments were inserted in this order as the *Xba*I site in the OLE-PCR product is blocked by overlapping *dam* methylation once inserted into a plasmid. Conjugative transfer and screening of possible mutants was performed as described for the *crtB* deletion.

Growth of *Rhodobacter sphaeroides*

Rba. sphaeroides strains were grown in M22+ medium³⁶ supplemented with 10,000 X vitamins (0.08 M nicotinic acid, 0.01 M thiamine, 7.3 mM 4aminobenzoic acid, 0.4 mM d-biotin), to a final concentration of 1 X. Liquid cultures were supplemented with 0.1% casamino acids. Single colonies were used to inoculate 10 ml starter cultures of M22 medium and grown semi-aerobically in the dark with shaking at 180 rpm at 34 °C for 48 hours. For anaerobic photosynthetic cultures, 20 ml of M22+ medium was used to dilute 10 ml of semi-aerobic culture in a 30 ml universal to the top. The culture was incubated for 48 hours. This culture was used to inoculate a 1 L Roux bottle filled with M22+ medium and grown for 24 hours. The culture was used to inoculate 8 L of M22+ medium and grown to an optical density at 680 nm (OD₆₈₀) of 3. All cultures were gently stirred using magnetic stir bars. Light was provided by 20 W MEGAMAN® CFL bulbs at 100 μmol photons s⁻¹ m⁻², measured using a LI-250A Light Meter

equipped with a LI-190 Quantum Sensor (LI-COR Biosciences). Where required, cells were pelleted by centrifugation and resuspended in 20 mM HEPES pH 8.0.

For photosynthetic growth curves, 48 hour, 10 ml semi-aerobic starter cultures were diluted to 30 ml and grown photosynthetically for 72 hours. Photosynthetically grown cells were used to inoculate 17 ml tubes to a starting OD₆₈₀ of approximately 0.15. Three tubes were grown per strain and average values and standard deviations are presented (Fig. 3). Light was provided using an array of green LEDs (520 nm emission maximum, 35 nm FWHM, 170 $\mu\text{mol photons s}^{-1} \text{m}^{-2}$ (Würth Elektronik, Germany).

Purification of RCYFP LH1 complexes

Monomeric core complexes were purified using a method adapted from³⁶. Lysozyme was added to the cell sample to a final concentration of 0.5 g l⁻¹ and incubated at 25 °C for 30 min in the dark. A small spatula of deoxyribonuclease 1 from bovine pancreas (Sigma) was added to the cells. The cells were French pressed 3 times at 18,000 psi. The cells were kept on ice throughout. Unbroken cells were removed by centrifugation at 33,000 x g at 4 °C for 25 minutes. The supernatant was applied to the top of a 15/40 % sucrose gradient followed by centrifugation for 16 hours at 65,000 x g. The intracytoplasmic membrane fraction was harvested from above the 40 % sucrose layer and pelleted by centrifugation at 125,171 x g for 2 hours and resuspended in 20 mM HEPES pH 8. The membranes were solubilised with 3 % β -dodecyl maltoside (β -DDM) for 1 hour at 4 °C with continuous stirring in the dark. The insoluble material was removed by centrifugation at 160,000 x g for 1 hour. The supernatant containing solubilised membranes was layered on top of discontinuous sucrose gradients containing 20 %, 21.25 %, 22.5 %, 23.75 %, 25 % and 50 % sucrose in 20 mM HEPES, 5 mM EDTA and 0.03 % β -DDM. Gradients were

centrifuged at 90,000 x g for 40 hours. The band containing monomeric RC/YFP-LH1 core complexes was collected.

Core complexes were purified by DEAE ion exchange and eluted with a gradient of 250 - 400 mM NaCl in 20 mM HEPES, 0.03 % β -DDM, pH 7.8. The core complex eluted at 250 mM NaCl and was subject to further purification using a Superdex 200 gel filtration column equilibrated with 10 mM NaCl 20 mM HEPES, 0.03 % β -DDM, pH 7.8. Fractions having an A_{873}/A_{280} absorbance ratio greater than 1.9 were pooled.

Purification of RCYFP complexes

Intracytoplasmic membranes were solubilised with 1% lauryl dimethyl amine oxide (LDAO) and loaded on to a DEAE Sepharose column equilibrated with 20 mM Tris-HCl, 0.1 % LDAO, pH 7.8. The column was washed with two steps of 50 mM and 100 mM NaCl and RCs were eluted with 200 mM NaCl. Eluted RCs were pooled and concentrated followed by dilution with 20 mM Tris-HCl, 0.1 % LDAO, pH 7.8. The protein was loaded on to a Q Sepharose (HiTrap QFF) column and eluted with a gradient from 0 - 400 mM NaCl. RC/YFP eluted at 300 mM NaCl and was loaded onto a Superdex 200 (GE Healthcare) gel filtration column equilibrated with 20 mM Tris-HCl, 0.1 % LDAO, 10 mM NaCl. Fractions with an A_{803}/A_{280} nm absorbance ratio of 0.73 or above were pooled.

Purification of YFP

The gene encoding SYFP2 was cloned into the vector pBBRBB-*Ppuf*₈₄₃₋₁₂₀₀²⁸ for expression in *$\Delta crtB$ Rba. sphaeroides*. Cells were grown semi-aerobically to an OD_{680} of 3 and disrupted by French pressure treatment. To remove membranes from the soluble fraction, cells were centrifuged at 125,100 x g for 2 hours and the supernatant was collected. The sample was loaded on to a DEAE Sepharose column equilibrated with 20 mM HEPES, pH 7.8. A gradient of 0 - 400

mM NaCl was run and YFP was eluted at 180 mM NaCl. YFP containing fractions were pooled and concentrated using a Centriprep (Amicon) spin concentrator followed by dilution with 20 mM HEPES, pH 7.8. The protein was loaded on to a Q Sepharose (HiTrap QFF) column and eluted with gradient of 0 - 400 mM NaCl. YFP eluted at 225 mM NaCl and was loaded onto a Superdex 200 (GE Healthcare) gel filtration column equilibrated with 1 M NaCl, 20 mM HEPES, pH 7.8.

Immunoblotting

Protein samples were separated by SDS-PAGE and transferred to a nitrocellulose membrane (Hybond ECL, Amersham) in Transfer buffer (190 mM glycine, 24 mM Tris, 20% (v/v) methanol) at a constant current of 350 mA for 1 hr at 4 °C. Following transfer, the membrane was blocked for 1 hr in Tris-buffered saline (TBS) (18 mM Tris-HCl pH 7.6 with 68 mM NaCl) with 0.2 % (w/v) Tween-20 and 5 % (w/v) skimmed milk powder, washed in TBS and then incubated with an appropriate dilution of primary antibody in TBS with 0.05 % (w/v) Tween-20 for 4-16 hr at room temperature. Anti-RCH³¹ and Anti-GFP (G1544, Sigma Aldrich) were used at dilutions of 1:5000 and 1:4000 respectively. After incubation with primary antibody the membrane was washed with TBS and then incubated with a 1:10000 dilution of secondary anti-rabbit antibody conjugated with peroxidase (Sigma Aldrich) in TBS. The membrane was washed with TBS prior to immunodetection using the AmershamTM ECLTM Western blotting analysis system (GE Healthcare Life Sciences) according to the manufacturer's instructions. Uncropped immunoblots are displayed in Supplementary Fig. 10.

Electron microscopy

Electron microscopy and single particle reconstruction of RC/YFP-LH1 complexes was performed as described previously³⁷. The detailed method was as follows. Purified RC/YFP-LH1

complexes were diluted to 0.1mg /ml. Five μ l protein solution was applied to a carbon coated 400 mesh copper EM grid, which was glow discharged 30 seconds before use. Excess protein solution was blotted by touching the edge of the grid on the surface of Whatman filter paper. After washing twice with distilled water, grids were stained with 0.75% (w/v) uranyl formate for 30 seconds. The grids were imaged using a Philips CM100 electron microscope operating under 100 kV accelerating voltage at room temperature. All micrographs were recorded with a 1K x1K Gatan Multiscan 974 CCD camera at a normal magnification of 52,000x, corresponding to 3.93 Å per pixel at specimen level with variation of under focus value from 0.5 to 2.5 μ m.

The micrographs were evaluated initially by Digitalmicrograph (Gatan, Inc.). All images showing drifting, poor staining and unsuitable under-focus were discarded. Selected images were submitted to EMAN2³⁸ for CTF correction and particle picking. 11,777 particles, each 72 x 72 pixels, were treated subsequently using the IMAGIC-5 software package³⁹. All particles were initially band-pass filtered to suppress low spatial frequencies. A soft-edged circle mask was used to remove unwanted background of the particle. The masked data were then centered and normalized for reference-free 2D classification, from which a set of characteristic classes was selected for multi-reference alignment (MRA) and multi-variant statistical analysis (MSA) classification. This procedure was iterated until a stable 2D classification was obtained. An initial model was established by assigning Euler angles to the three most different 2D classes selected from the above calculation using angular reconstitution in IMAGIC-5; this model was refined gradually by adding more 2D classes. An anchor set produced from back projection of the initial model was used to calculate the Euler angle of whole 2D class dataset, from which a new 3D model was produced. This procedure was iterated by increasing the calculation precision and decreasing the search step of the Euler angle until a stable 3D model obtained. A new

reference produced from this stable 3D model then was used for a new MSA iteration. Finally, 380 2D classes were used for generation of a 3D RC/YFP-LH1 model. The final 2D class dataset was split randomly into two halves, and two 3D models were reconstituted independently. By calculation of Fourier shell correlation (FSC) between these two 3D models, a resolution of 25.9 Å for the final model (see Supplementary Fig. 11) was estimated based on 0.5 FSC criteria⁴⁰.

Room temperature and low temperature absorbance spectra

Room temperature and 77 K absorption spectra were recorded using a Cary UV/vis spectrophotometer in the spectral range between 260 and 950 nm. For cryogenic measurements, samples suspended in a cryo-stable buffer consisting of 20 mM Tris-HCl, 80% glycerol (v/v) were cooled to 77 K in an Optistat DN-V optical cryostat manufactured by Oxford Instruments.

Low temperature spectroscopy

The absorption and excitation fluorescence spectra in Fig. 1 were recorded in a cryo-stable buffer consisting of 20 mM HEPES, 80% glycerol. Samples were cooled to 77 K as described above. Measurements were recorded on a SPEX FluoroLog spectrofluorimeter (SPEX Industries Inc.). Excitation was provided from a tungsten light source. Fluorescence excitation spectra were recorded from 400 nm to 910 nm with an emission of 915 nm, using an average of 10 individual scans. Excitation and emission slit widths of 5 nm were used. Fluorescence excitation spectra were normalised to 1 at 591 nm, data were subject to 2nd order smoothing with 5 neighbours.

Fluorescence imaging of YFP in *Rhodobacter sphaeroides*

Cells were washed three times in QH₂O then suspended in QH₂O. 15 µl of cell suspension was dropped on 30 µl of 1.5% agar film on a glass slide and sealed with DPX mountant (Sigma–Aldrich) between the glass slide and a coverslip. Fluorescence images were taken with an inverted fluorescence microscope (AxioObserverA1m, Zeiss) equipped with a Hal 100

halogen lamp, a high intensity HBO 100 mercury lamp and an ORCA-ER camera (Hamamatsu). Excitation light was first filtered by a 470/40 nm bandpass filter, then reflected by a 495 nm dichroic beam splitter to the sample through an objective (Plan-Apochromat 63x/1.40 oil objective, Zeiss). Fluorescence emission was filtered by a 520/40 nm bandpass filter before detection by the camera. Each fluorescence image was taken with a 0.1 s exposure time and 50 electron multiplication gain.

Spectral and lifetime imaging of *Rhodobacter sphaeroides*

The fluorescence emission properties of YFP in whole cells were measured on a home-built time-resolved fluorescence microscope. The inverted microscope is equipped with a spectrometer (Acton SP2558, Princeton Instruments), an electron-multiplying charge-coupled device (EMCCD) camera (ProEM 512, Princeton Instruments) and a Hybrid Detector (HPM-100-50, Becker & Hickl). The excitation light source was from a pulse supercontinuum white light laser (SC 480-10, Fianium) with a repetition rate of 40 MHz. The laser beam was focused on the sample surface, illuminating a diffraction limited spot using a 100 \times objective (PlaneFluorite, NA = 1.4, oil immersion, Olympus). The resulting fluorescence emission was detected through the spectrometer onto the EMCCD camera and the resulting fluorescence lifetime was detected through the spectrometer onto the Hybrid Detector.

During fluorescence spectral and lifetime measurements, the excitation light was filtered by a 472/30 nm bandpass filter, then reflected by a 495 nm dichroic beamsplitter to the sample. The resulting fluorescence emission was filtered by a 496 nm long-pass filter before being detected by the cameras. The fluorescence emission was captured with a slit width of 1500 μm and a grating of 150 line/mm working at a central wavelength of 550 nm in the spectrometer. Multiple measurements were performed on 8 different cells on each sample. Each fluorescence spectrum

was detected by EMCCD at an average of 3 frames with a 1 s exposure time and an electron multiplication gain of 80. Analysis was done with OriginPro.

For fluorescence lifetime measurements, the modulation of the laser was synchronized with a time-correlated single-photon counting (TCSPC) module (SPC-150, Becker & Hickl). Fluorescence lifetimes were recorded by parking the focused laser spot over one single cell, selecting a central wavelength of 550 nm by use of the monochromator and detected by the Hybrid Detector. SPCM software (Becker & Hickl) was used for the data acquisition. The families of decay curves were analysed with OriginPro and TRI2 software packages by fitting with a multiexponential decay function:

$$I(t) = \sum_{i=1}^n A_i \exp\left(\frac{-t}{\tau_i}\right) + B$$

where τ_i is the fluorescence lifetime, A_i is the fractional amplitude contribution of the i^{th} decay component, and B is the background. The quality of fit was judged on the basis of the reduced χ^2 statistic:

$$\chi^2_{\text{red}} = \frac{\sum_{k=1}^n \frac{[I(t_k) - I_c(t_k)]^2}{I(t_k)}}{n - p} = \frac{\chi^2}{n - p}$$

where $I(t_k)$ is the data at time point k , $I_c(t_k)$ is the fit at time point k , n is the number of data points and p is the number of variable fit parameters ($n-p$ = degrees of freedom). The instrument response (IRF) of the system, measured using a mirror, was approximately 0.18 ns, and the convolution of the decay curves with the IRF was taken into account when the fitting was performed.

Optical measurements on purified RC and RCYFP complexes

Photophysical measurements on RC, YFP or RC/YFP proteins in 0.1% LDAO, 10 mM Tris, 200 mM NaCl, pH 7.8 buffer were carried out at room temperature. Static absorption (Shimadzu UV-1800) and fluorescence measurements (Horiba Nanolog) employed $\sim 1 \mu\text{M}$ samples, which give $A \leq 0.1$ at λ_{exc} for fluorescence studies. The latter used 2 nm excitation and emission bandwidths, and spectra were corrected for instrument response. Fluorescence quantum yields are the average values obtained using methods: (1) an absolute method using an integrating sphere (Horiba, Quanti-Phi), and (2) a relative method using as a standard fluorescein in 0.1 M NaOH, for which $\Phi_f = 0.91$ was obtained from the average of two literature values^{41, 42}. Singlet excited-state lifetimes were determined using (1) transient absorption (TA) spectroscopy, (2) time-correlated-single-photon-counting (TCSPC) detection of fluorescence decay (instrument response function of ~ 0.2 ns), and (3) stroboscopic measurement of fluorescence decay (instrument response function of ~ 1 ns) as described previously⁴³. TA studies utilized an amplified Ti:Sapphire laser system (Spectra Physics) and Helios and Eos detection systems (Ultrafast Systems). Samples were excited with $\sim 0.5 \mu\text{J}$, ~ 100 fs 515-nm excitation pulses (at 1 KHz) focused to 1 mm diameter⁴⁴. For RC-only or RC/YFP, a spinning cell (2 mm path and 3 mm wide annulus) containing 3 mL of ~ 10 - $15 \mu\text{M}$ sample was used to prevent re-excitation of the complex while in the long-lived (1-2 s) $\text{P}^+\text{Q}_\text{B}^-$ state of the RC. A standard 2 mm path cuvette with stirring was used for YFP-only (600 uL at $\sim 15 \mu\text{M}$).

Förster calculations were performed using the measured yield of excitation energy transfer (Φ_{EET}) from excited YFP to RC to obtain the donor to acceptor distance (R) between these units. The calculations employed PhotochemCAD³², which uses the “ R_0 method” in which $\Phi_{\text{EET}} = R_0^6 / (R_0^6 + R^6)$, where $R_0^6 = (8.8 \times 10^{23}) \kappa^2 \Phi_f J \text{ n}^{-4}$ and R_0 is the distance at which $\Phi_{\text{EET}} = 0.5$.

Here, the orientation factor $\kappa^2 = 0.667$ assuming a random orientation of transition dipoles, $\Phi_f = 0.70$ (*vide infra*) is the donor (YFP) fluorescence yield, J is the spectral overlap factor (a molar absorptivity of $288,000 \text{ mM}^{-1}\text{cm}^{-1}$ at 800 nm was used for the RC⁴⁵), and n is the refractive index, for which values of 1.335, 1.45, and 1.55 were used to accommodate protein/cofactor environments ranging from buffer to pure hydrocarbon (Supplementary Figures 5, 8).

3. Results

Spectroscopy and photosynthetic growth of RCYFP strains

A baseline strain was constructed for the expression of YFP by deleting *crtB* (RSP_0270, encoding phytoene synthase) from *Rba. sphaeroides*²² (see also Fig. 9 in Methods). This manipulation abolishes the biosynthesis of carotenoids, the 450-550 nm absorption of which would otherwise eclipse YFP absorption, as shown in the absorption spectra for WT and WT RC/YFP membranes (Supplementary Fig. 1). The Δ *crtB* mutation also eradicates LH2 assembly^{23, 24} but does not affect the synthesis of the PufX polypeptide, which forms a portal for quinone traffic^{16, 25}. Although PufX is present, the carotenoidless RC-LH1-PufX complex with YFP attached will be referred to as Δ *crtB* RC/YFP-LH1. The gene encoding the YFP variant, SYFP2²¹, was fused to the 3' end of *puhA*, which encodes the reaction centre H subunit (RC-H). The placement of YFP on the periplasmic N-terminus of RC-H was ruled out as, although it would bring the YFP closer to the RC special pair and the LH1 BChls, it would have likely blocked the cytochrome *c*₂ docking site. The result of constructing *puhA-SYFP2* is a fusion protein with YFP on the C-terminus of RC-H, located on the cytoplasmic side of the complex. Immunoblotting with antibodies specific for the RC-H subunit or YFP showed the presence of a signal at 54.9 kDa corresponding to the expected size of a RC-H/YFP fusion (Fig. 1a). Room

temperature absorption spectra of intracytoplasmic membranes (ICM) prepared from photosynthetically grown $\Delta crtB$ RC/YFP-LH1 show the YFP peak at 517 nm, which is shifted to 519 nm at 77 K (Fig. 1b,c). Fluorescence excitation spectra of ICM prepared from $\Delta crtB$ RC/YFP-LH1 recorded at 77 K exhibit a feature at 519 nm corresponding to energy transfer from YFP (Fig. 1d).

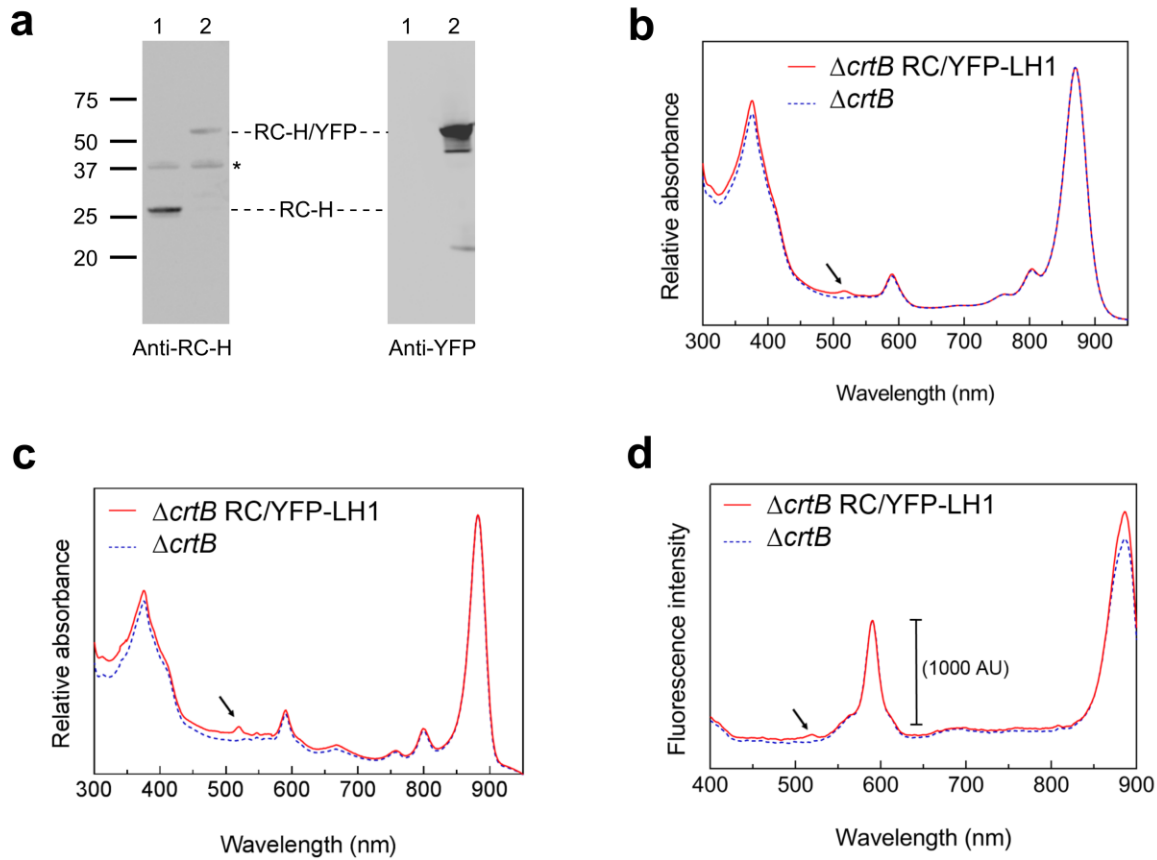


Figure 1. Immunoblotting and spectroscopic analysis of $\Delta crtB$ RC/YFP-LH1 intracytoplasmic membranes. (a) Immunoblotting with antibodies for the RC-H subunit and, separately, to YFP showing the synthesis of an RC-H/YFP polypeptide in *Rba. sphaeroides*. The asterisk indicates a non-specific signal from the RC-H antibodies. The numbers to the left of the anti-RC-H blot show the positions of protein standards, in kDa. (b) Room temperature and (c) 77 K absorption spectra of membranes purified from $\Delta crtB$ (blue, dashed) and $\Delta crtB$ RC/YFP-LH1 (orange) normalised to 870 nm (b) or 880 nm (c). $\Delta crtB$ RC/YFP-LH1 has a peak at 517 nm corresponding to YFP (indicated by arrow); this peak is shifted to 519 nm at 77 K. (d) Fluorescence excitation spectra of membranes with emission monitored at 910 nm show that YFP (peak indicated by arrow) contributes to emission at 910 nm.

Photosynthetic growth from absorption of light by YFP

The 400-550 nm carotenoid absorption of light-harvesting LH1 and LH2 complexes overwhelms the absorption of RC-attached YFP (Supplementary Fig. 1), so WT and WT RC/YFP-LH1 strains grow at the same rate under illumination by white light (Supplementary Fig. 2). Nevertheless, the 525 nm emission maximum of SYFP2 has some overlap with the visible-region (Q_x) absorption band of BChl *a* in the *Rba.sphaeroides* LH1 and RC complexes, so growth tests were conducted to find out if energy absorbed by YFP could migrate to RC-LH1 complexes *in vivo*. The carotenoidless $\Delta crtB$ mutant of *Rba. sphaeroides* provides the ideal baseline strain for growth rate experiments; the $\Delta crtB$ and $\Delta crtB$ RC/YFP-LH1 strains were grown in white light (100 $\mu\text{mol photons s}^{-1} \text{ m}^{-2}$), under which conditions both strains are able to grow autotrophically. The LH2-minus positive control (carotenoids+RC-LH1-PufX), chosen because the other two strains also lack LH2 due to the $\Delta crtB$ mutation, shows strong photosynthetic growth (Fig. 2a, green). Allowing for the ~30 hour lag delaying the onset of photosynthetic growth the subsequent difference between the green and blue growth curves shows that under white light illumination the $\Delta crtB$ culture is light-limited by approximately 50 %. This effect arises because the absence of carotenoids impairs the light-absorbing capacity of the LH1 antenna, thereby limiting turnover at the RCs. After ~30 hours the growth of $\Delta crtB$ RC/YFP-LH1 cultures began to outpace the control $\Delta crtB$ strain, providing evidence for *in vivo* energy transfer from YFP to the RC-LH1-PufX complex (Fig. 2a). In an additional growth test, an LED light source (520 nm emission maximum, 35 nm full-width-at-half-maximum FWHM) was used to direct excitation energy specifically to YFP. The difference between the positive control (carotenoids+RC-LH1-PufX; green line) and $\Delta crtB$ strains (no carotenoids, red/blue lines) in Fig 2c shows that both $\Delta crtB$ and $\Delta crtB$ RC/YFP-LH1 are growing at sub-saturating light intensities. Illumination of

carotenoid-less cultures by green LEDs barely allows native BChl pigments to contribute towards light harvesting. Comparison of the green and blue growth curves in Fig. 2c suggests that RC turnover in the $\Delta crtB$ strain runs at only ~10 % of its potential capacity so the addition of a 520 nm-absorbing chromophore to the $\Delta crtB$ strain might be expected to be beneficial, as long as the absorbed energy can transfer to photosystem components. The emission of the green LEDs (depicted by the white region in Fig. 2b) is well matched to the absorption band of purified and RC-attached YFP, and the $\Delta crtB$ RC/YFP-LH1 strain (Fig. 2c, red) grows faster than $\Delta crtB$ under these experimental conditions. In contrast, the $\Delta crtB$ negative control absorbed enough energy to sustain only very weak photosynthetic growth (Fig. 2c, blue).

The inset in Fig. 2c shows that the growth conditions supplied sufficient oxygen for maturation of the YFP chromophore in the $\Delta crtB$ RC/YFP-LH1 strain. Thus, the data presented in Figure 2 provide further evidence for light absorption by YFP and transfer of excitation energy to the RC to drive photosynthesis and cell division. However, the absence of carotenoids in the $\Delta crtB$ strain used for this work could have created a need for photoprotective pigments, and it has been suggested that fluorescent proteins can play a photoprotective role^{26, 27}. To confirm that the superior growth rate of the $\Delta crtB$ RC/YFP-LH1 strain (versus the $\Delta crtB$ negative control) was due to YFP energy transfer and not photoprotection (which could favour an increased growth rate), the expression plasmid pBBRBB YFP, based on pBBRBB-*Ppuf*₈₄₃₋₁₂₀₀²⁸, was used to make cytoplasmic YFP in *Rba. sphaeroides* $\Delta crtB$, which is free of any attachment to membrane proteins. Photosynthetic growth curves for high light cultures show that the presence of free YFP in the cytoplasm confers no benefit on $\Delta crtB$ pBBRBB YFP (Supplementary Fig. 3) , which grows at the same slow rate as $\Delta crtB$. The effectiveness of this plasmid expression system for YFP synthesis in *Rba. sphaeroides* was verified by the subsequent purification of YFP from this

strain, which was used as a control for the static and time-resolved fluorescence measurements.

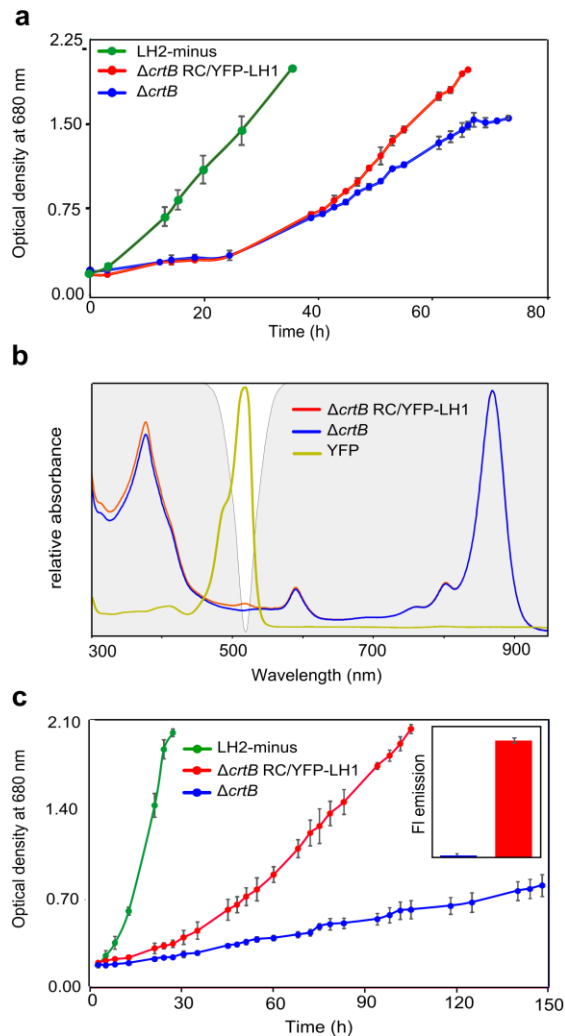


Figure 2. Photosynthetic growth curve analysis of $\Delta crtB$ RC/YFP-LH1. (a) Light was provided using Megaman CFL bulbs at an intensity of $100 \mu\text{mol photons s}^{-1} \text{m}^{-2}$. Photosynthetic growth curves are shown for $\Delta crtB$ RC/YFP-LH1 (red circles) and $\Delta crtB$ (blue circles); a carotenoid-containing LH2-minus strain (green circles) is included as a positive control. (b) Superposition of the absorption of $\Delta crtB$, $\Delta crtB$ RC/YFP-LH1 and purified YFP onto the emission output of the LEDs used for the photosynthetic growth rate experiment in (c). $\Delta crtB$ is shown in blue, $\Delta crtB$ RC/YFP-LH1 in red and purified YFP in yellow; the spectra are normalised to their maximum values. The emission of the green LEDs (520 nm emission maximum, 35 nm FWHM) is indicated by the white region on the grey background. (c) Photosynthetic growth curves of $\Delta crtB$ RC/YFP-LH1 (red circles) and $\Delta crtB$ (blue circles) under green LEDs. A carotenoid-containing LH2-minus strain (green circles) is included as an additional control. Error bars indicate the standard deviation from the mean; $n=3$. Each growth curve is representative of at least three independent experiments. The inset shows a quantification of YFP fluorescence, normalised for equal numbers of cells, showing that there was sufficient oxygen for maturation of the YFP chromophore.

Structural model of the RCYFP LH1 complex

In order to visualise the attachment of YFP to the RC-H subunit, the RC/YFP-LH1 complex was purified from ICM prepared from photosynthetically grown cells, as described in the Methods. Following sucrose density gradient centrifugation, ion exchange chromatography and gel filtration the final complex was reasonably pure, as judged by the A875:A280 nm absorbance ratio of 1.92 and the presence of only five main bands (the PufX polypeptide stains poorly²⁹) in a Coomassie-stained SDS-PAGE gel (Supplementary Fig. 4).

Purified RC/YFP-LH1 complexes were adsorbed onto the pre-coated carbon film on a copper grid and negatively stained; Fig. 3a shows typical raw data with some single particles showing an additional density, indicated by white arrows in the inset to Fig. 3a. Then 11,777 particles were selected for further analysis; Fig. 3b shows examples of averaged reference-free 2D classes and Fig. 3c, d show the reconstructed model of the RC/YFP-LH1 complex viewed from the cytoplasmic side of the membrane and in the plane of the membrane, respectively. This model is based on half of the structure of the dimeric RC-LH1-PufX core complex^{29, 30}; the extra density apparent in some of the single particles and image classes and seen in the final reconstruction arises from YFP, which clearly protrudes from the side of the complex.

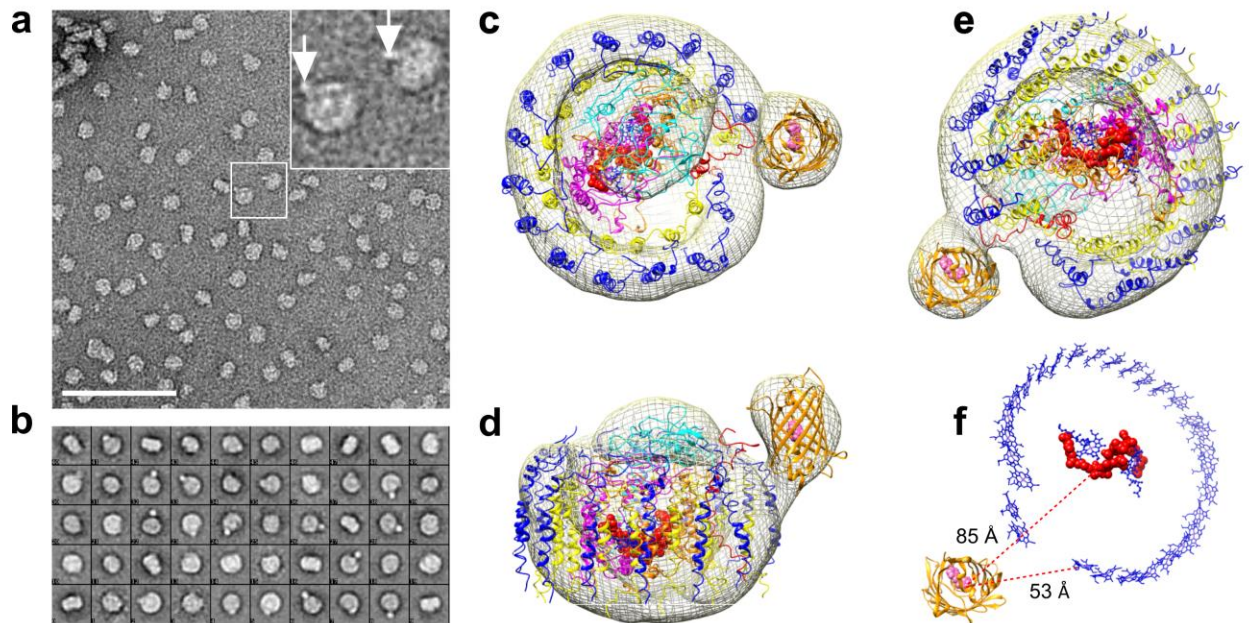


Figure 3. Electron microscopy and 3D reconstruction of the RC/YFP-LH1 complex. (a) Electron micrograph of purified, negatively stained RC/YFP-LH1 complexes; the two complexes in the central white box are enlarged in the inset, with white arrows indicating the density arising from YFP. The scale bar represents 100 nm. (b) Gallery of 40 selected 2D averaged classes; the box size is 28 x 28 nm. 11,777 particles were used for reconstruction of the 3D model. (c-f) The reconstructed model of the RC/YFP-LH1 complex at 29 Å resolution; the diagram shows the electron density (grey mesh), and the following subunits: LH1 β (blue), LH1 α (yellow), PufX (red), RC-M (magenta), RC-H (cyan) and RC-L (orange). YFP is in gold. The RC special pair of BChls is shown in red. The structural model is viewed from (c) the cytoplasmic side of the membrane, (d) the plane of the membrane, (e) the periplasmic side, (f) the periplasmic side of the complex, showing only YFP and the LH1 and RC pigments. The dashed red lines show the distances between the YFP chromophore, the RC special pair BChls (red) and LH1 BChls (blue).

YFP fluorescence lifetimes in *Rhodobacter sphaeroides* cells

A home-built microscope³¹ was used to image fluorescence from YFP, both in the free state in $\Delta crtB$ pBBRBB YFP cells, and attached to RC-H in the $\Delta crtB$ RC/YFP-LH1 strain; the $\Delta crtB$ strain was included as a negative control. The images in Fig. 4a,c show the YFP emission from YFP in the RC-attached and free states, respectively. Fig. 4d shows fluorescence emission spectra, each recorded on a single cell; the shapes of the spectra match those for purified YFP and RC/YFP-LH1 samples in Fig. 5b. No conclusions can be drawn from the amplitudes, which

reflect the relative abundance of YFP in the free and attached states in these particular cells, as well as the fluorescence yield arising from coupling to acceptors in the RC/YFP-LH1 complex. As expected, no signal was observed in cells of the control $\Delta crtB$ mutant, (Fig. 4b, and 4d, black trace). Fluorescence lifetimes of YFP in the whole cell samples were recorded in order to detect any quenching that would indicate Förster resonance energy transfer (FRET) from the YFP to an acceptor molecule (Fig. 4e and Table 1). The YFP fluorescence signal from $\Delta crtB$ pBBRBB YFP, which is an average taken from 8 cells, has a bi-exponential decay (Fig. 4e, black points and fitted curve) which gives an amplitude weighted average lifetime of 2.3 ns. When YFP is attached to RCs in $\Delta crtB$ RC/YFP-LH1 cells the lifetimes of both the short- and long-lived components are significantly shorter (Fig. 4e, red points), with an average lifetime of 1.21 ns. These amplitude-weighted average lifetimes (Table 1) and Equation 1 were used to calculate a FRET efficiency (Φ_{EET}) for energy transfer between YFP and the RC-LH1 complex of ~ 0.48 . Fig. 3f shows the distances between the YFP chromophore and the RC special pair BChls, and between YFP and the nearest LH1 B875 BChl, based on the structural model of the RC/YFP-LH1 complex in Fig. 3c-d. These distances, of $\sim 85 \text{ \AA}$ and $\sim 53 \text{ \AA}$, respectively, are both within the range for FRET, although they suggest that the most likely route for energy migration to the RC is via the LH1 BChls.

Equation 1.
$$\Phi_{\text{EET}} = 1 - \frac{\tau_{\text{YFP-RC}}}{\tau_{\text{YFP}}}$$

In order to examine this point in more detail we used Förster theory to estimate the distance between the YFP chromophore and acceptor pigments in the RC-LH1 complex, on the basis of the 0.48 value for Φ_{EET} determined from the whole cell fluorescence lifetime measurements. The calculations employed PhotochemCad³² using three values of the refractive index (1.335, 1.45, and 1.55) to accommodate latitude in the polarity of the cofactor/protein environments

(Supplementary Fig. 5). The calculations return a YFP to acceptor distance of 43 to 48 Å, in good agreement with the structural model in Fig. 3f which gives a 53 Å distance between YFP and the nearest LH1 BChl.

Table 1. YFP lifetimes measured for $\Delta crtB$ RC/YFP-LH1 and $\Delta crtB$ pBBRBB-YFP whole cells. The values of amplitudes and lifetimes presented are the mean and standard error, n=8. The fluorescence decay curves shown in Fig. 5e were analysed using OriginPro and TRI2 software packages. A_1 and A_2 are the amplitude contributions of the long- and short-lived components, τ_1 and τ_2 are the lifetimes of each component, and τ_{av} is the amplitude-weighted lifetime.

Sample	A_1	τ_1 [ns]	A_2	τ_2 [ns]	τ_{av} [ns]
$\Delta crtB$ RC/YFP-LH1	0.49 ± 0.18	1.76 ± 0.28	0.51 ± 0.18	0.57 ± 0.26	1.2
$\Delta crtB$ pBBRBB-YFP	0.65 ± 0.14	3.15 ± 0.39	0.35 ± 0.14	0.83 ± 0.16	2.3

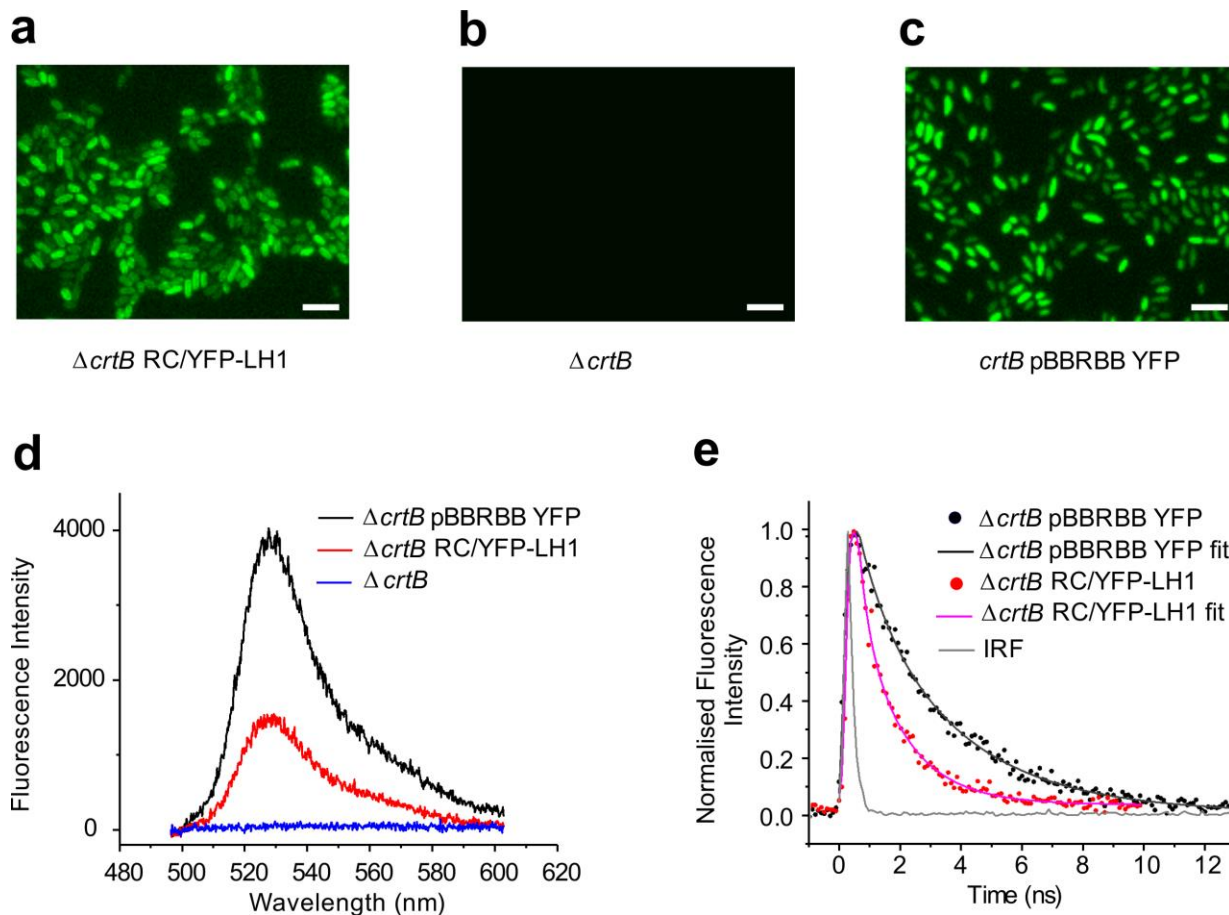


Figure 4. Spectral and lifetime imaging of YFP in $\Delta crtB$ RC/YFP-LH1 and $\Delta crtB$ pBBRBB-YFP whole cells. (a-c) Fluorescence images of whole cells of $\Delta crtB$ RC/YFP-LH1, $\Delta crtB$ and $\Delta crtB$ pBBRBB-YFP cells when excited at 495 nm. (d) Fluorescence emission spectra, each recorded on a single cell. (e) Fluorescence lifetime decay curves recorded at a central wavelength of 550 nm. The best fits, displayed as blue and red lines, were achieved using a double-exponential decay function. The measured instrument response (IRF) of the system was approximately 0.18 ns and taken into account during fitting. Scalebars represent 5 μ M.

RCYFP fluorescence quantum yield and excited-state lifetime

Having shown that YFP is a donor of excitation energy to YFP/RC-LH1 complexes *in vivo*, we set out to construct the simplest system for examining the characteristics of a coupled YFP/energy trapping complex. Accordingly, RC/YFP complexes with no surrounding LH1 antenna were purified from carotenoid-less intracytoplasmic membranes. Supplementary Fig. 6

shows the outcome of the purification, which yielded complexes free of LH1; Fig. 5a shows the clearly visible YFP absorption at 514 nm (black arrow), which is not present in the RC control. YFP was purified from *Rba. sphaeroides* $\Delta crtB$ pBBRBB-YFP (Supplementary Fig. 7), to act as a control for the fluorescence decay measurements.

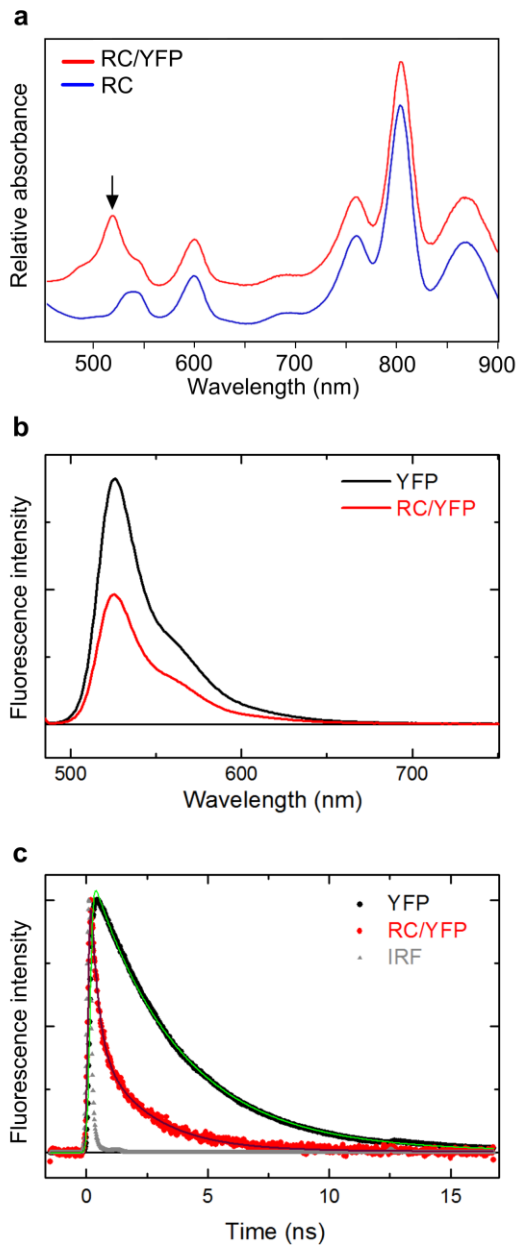


Figure 5. Spectroscopic analysis of purified RC/YFP complexes. (a) Room temperature absorption spectra of control RC complexes purified from the $\Delta crtB$ strain and RC/YFP complexes purified from the $\Delta crtB$ RC/YFP-LH1 strain. The arrow indicates the absorption maximum of YFP at 514 nm. (b) Fluorescence spectra of purified YFP (YFP-only; dashed red line) and the RC/YFP complex (solid black line) normalized to the absorbance at $\lambda_{exc} = 486$ nm. (c) Normalized fluorescence decay (at 550 nm using $\lambda_{exc} = 515$ nm) and fits (using two exponentials plus a constant) of YFP-only (open red circles) and RC/YFP (closed black circles) obtained via TCSPC.

The yield of excitation energy transfer (Φ_{EET}) from excited YFP (YFP*) to the RC is determined from changes in the photophysical properties of YFP – fluorescence intensity (I_f), fluorescence quantum yield (Φ_f), or singlet excited-state lifetime (τ_s) – in the presence versus absence of the RC. The YFP* \rightarrow RC energy-transfer process provides an additional decay pathway for YFP* when the RC is present, resulting in a reduction in the measured parameter χ (I_f , Φ_f , τ_s) so that $\Phi_{\text{EET}} = 1 - \chi_{\text{YFP-RC}} / \chi_{\text{YFP}}$. YFP* \rightarrow RC energy flow was initially measured using static and time-resolved fluorescence spectroscopy. A significant reduction in integrated YFP fluorescence intensity for RC/YFP (Fig. 5b, solid black line) versus YFP-only (red dashed line) gives $\Phi_{\text{EET}} = 0.47$. Similarly, as expected based on the simple fluorescence-intensity reduction, the Φ_f of YFP in RC/YFP is lower than in YFP-only as measured relative to a standard (0.40 versus 0.76) or with an integrating sphere (0.27 versus 0.64), giving Φ_{EET} values of 0.47 and 0.58, respectively. Finally, time-resolved studies of the YFP fluorescence decay in RC/YFP versus YFP-only by time correlated single photon counting (TCSPC; Fig. 5c, black and red traces) give τ_s of 2.0 and 3.6 ns, and a value for $\Phi_{\text{EET}} = 0.44$. Analogous YFP fluorescence decays obtained with a stroboscopic method (not shown) give τ_s of 1.8 and 2.6 ns and thus $\Phi_{\text{EET}} = 0.31$.

The Φ_{EET} values obtained by probing the various photophysical parameters using different techniques are in good agreement and give an average $\Phi_{\text{EET}} = 0.4 \pm 0.1$. Similarly the YFP* lifetimes in the RC/YFP complex from the various time-resolved studies (2.2, 2.0, 1.8 ns) are in good agreement, with an average $\tau_s = 2.0 \pm 0.2$ ns. These values give a time constant (inverse of the rate constant) for YFP* \rightarrow RC energy transfer of $(2.0 \text{ ns})/0.4 = 5 \text{ ns}$ (Fig. 5c).

As in Supplementary Fig. 5, the measured $\Phi_{\text{EET}} = 0.4$ was used to estimate the effective distance between the YFP chromophore and the RC cofactors using Förster theory and the photophysical parameters for the energy donor (YFP) and acceptor (RC) given in the Methods section

(Supplementary Fig. 8). The calculations return a spectral-overlap integral of $J = 2.96 \times 10^{-13} \text{ cm}^6$, a Förster radius of $R_0 = 53\text{--}58 \text{ \AA}$, and a YFP to RC distance of 56 to 62 \AA . The discrepancy between this and the 85 \AA distance in Fig. 3d are discussed later.

Ultrafast transient absorption spectroscopy of RCYFP

Ultrafast transient absorption (TA) spectroscopy was used to measure the τ_s of YFP, and to demonstrate $\text{YFP}^* \rightarrow \text{RC}$ energy transfer from the ‘growing in’ of key RC features (absorption bleaching or stimulated emission) associated with formation of the excited primary donor (P^*), which initiates the charge-separation sequence in the RC. Fig. 6a shows representative TA spectra in the near-infrared region for the isolated RC (RC-only) sample, with 515 nm excitation directed at the YFP chromophore. The spectral evolution at early times (dashed lines) arises primarily from decay of P^* stimulated emission centred at $\sim 910 \text{ nm}$, with little change in the bleaching of the ground state absorption band of P centred at $\sim 865 \text{ nm}$. After P^* decay (solid lines) by charge separation, the P bleach persists because P is oxidized (P^+) and remains so and in the same amount during the entire charge-separation sequence, namely $\text{P}^* \rightarrow \text{P}^+\text{H}_\text{A}^- \rightarrow \text{P}^+\text{Q}_\text{A}^- \rightarrow \text{P}^+\text{Q}_\text{B}^-$. This process proceeds with essentially unity quantum yield; charge recombination $\text{P}^+\text{Q}_\text{B}^- \rightarrow \text{P}$ occurs on the time scale of $\sim 1\text{--}10$ seconds (Fig. 6c). Kinetic profiles at 850 nm and 910 nm were fit to two exponentials plus a constant, giving average time constants of 3.9 ps and 306 ps, nicely matching typical wild-type RC P^* ($\sim 4 \text{ ps}$) and $\text{P}^+\text{H}_\text{A}^-$ ($\sim 250 \text{ ps}$) lifetimes³³. As expected, the change in ΔAbs at 850 nm with time is small (nonzero because H_A^- in $\text{P}^+\text{H}_\text{A}^-$ and the other states differ in the size of a small absorption opposing the P bleach) and remains virtually constant from $\sim 1 \text{ ns}$ to past $\sim 60 \text{ ns}$, the longest time shown (Fig. 7, blue triangles).

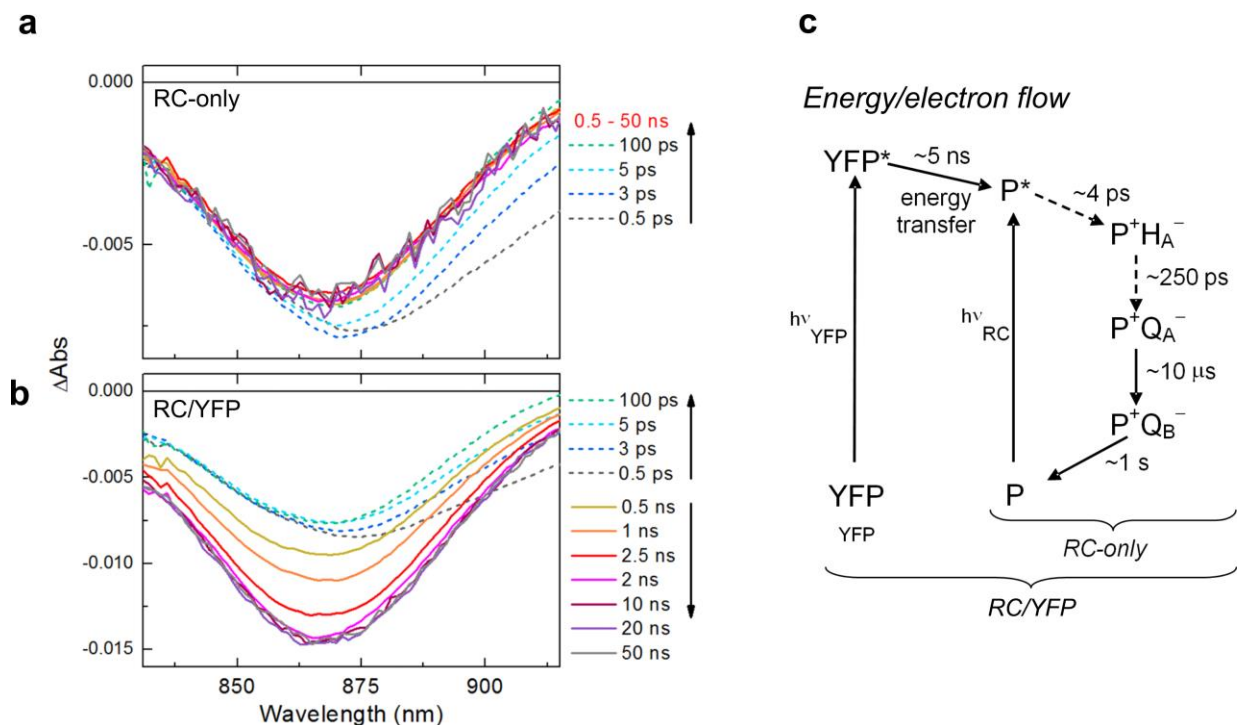


Figure 6. Transient absorption spectra of P-bleaching (~ 865 nm) and P* stimulated emission (~ 910 nm) for RC-only and RC/YFP samples with 515 nm excitation into the YFP absorption band. The dashed lines indicate absorbance changes due to P* (and decay to P⁺H_A⁻ and P⁺Q_A⁻) upon direct excitation (at 515 nm) of the RC-only sample (**a**) and in RC/YFP, for which YFP is primarily excited by the flash (**b**). Note the difference in vertical scales for (**a**) and (**b**), such that the amplitude of the absorbance changes in at early times (dashed) due to direct excitation of the RC are the same in (**a**) and (**b**) because the samples have approximately the same concentration. (**c**) Dynamics of energy flow from YFP* to the RC in RC/YFP followed by charge separation in the RC (in both RC/YFP and RC-only).

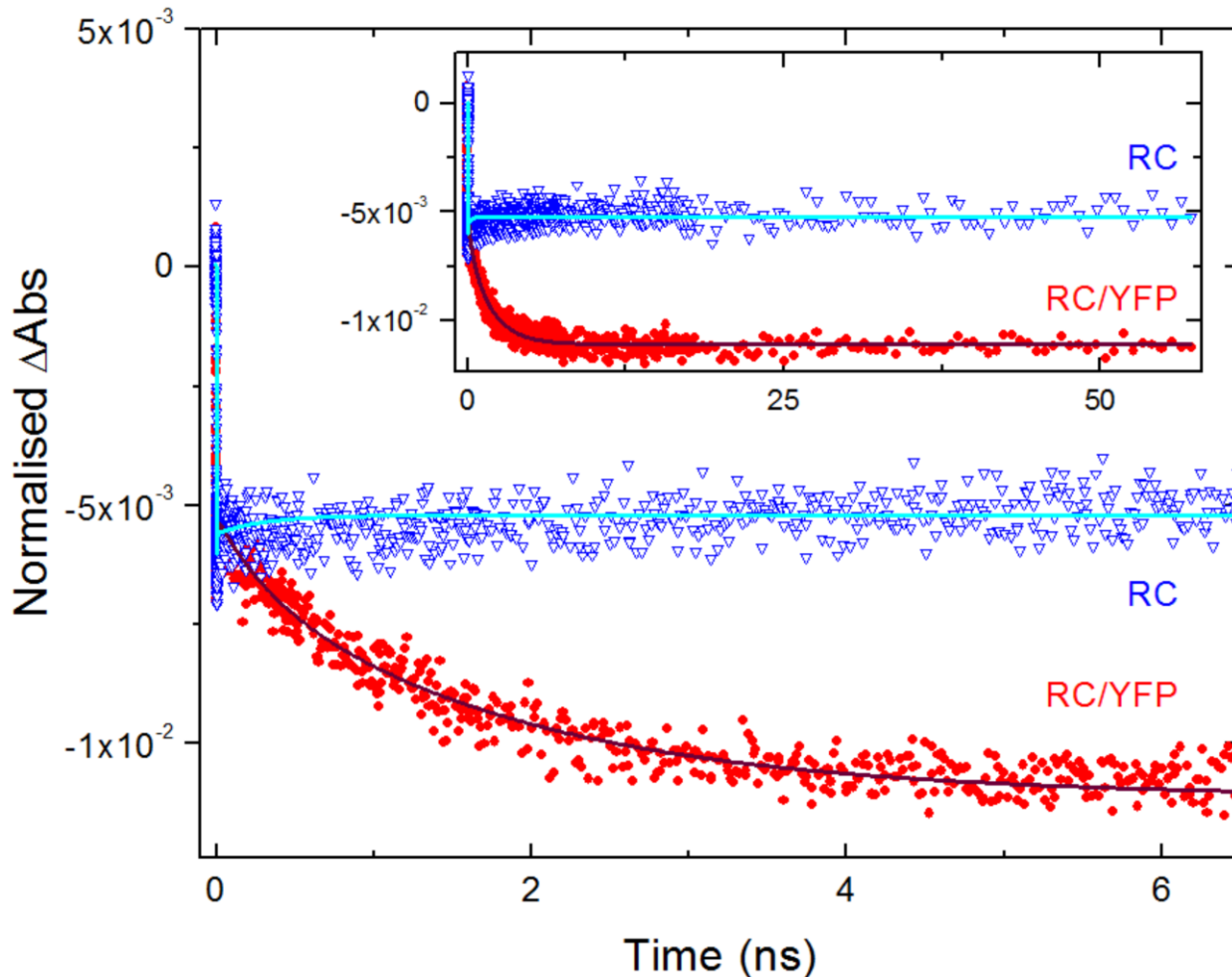


Figure 7. Kinetic profiles and fits for evolution of RC P-bleaching at 850 nm for RC/YFP and RC-only, with 515 nm excitation of YFP. The signals were normalized at the P absorbance maximum at 867 nm. RC/YFP data (black, filled circles) was fit to three exponentials plus a constant (solid grey line) and RC-only data (blue, open triangles) to two exponentials plus a constant (solid green line).

TA spectra for the RC/YFP sample at early times (Fig. 6b, dashed lines) give spectral changes with time constants (5.3 and 331 ps) that closely resemble those for RC-only as a result of unavoidable direct RC excitation in a small fraction of the sample. However, at later times (>100 ps), the P bleaching at ~865 nm triples in magnitude and P* stimulated emission at ~910 nm reappears (Fig. 6b, solid lines). These signals arise unambiguously from YFP* → RC energy transfer on the nanosecond timescale, which is in marked contrast to the data for RC-only after a few hundred picoseconds (Fig. 6a). For RC/YFP, kinetic profiles at 850 nm (Fig. 7, black circles)

and 910 nm were fit to three exponentials plus a constant to account for the RC P^* and $P^+H_A^-$ lifetimes plus a (rise) component reflecting the YFP* lifetime, which includes $YFP^* \rightarrow RC$ energy transfer. The τ_s for YFP* in the RC/YFP complex was determined to be 1.8 ns at 850 nm (Fig. 7, black circles), 2.1 ns at 910 nm from the growth of the RC signals, and 2.4 ns from the decay of YFP stimulated emission at 560 nm (data not shown), giving an average of 2.2 ns. The YFP stimulated-emission decay at 560 nm in the YFP-only sample gives $\tau_s = 3.4$ ns. The YFP* decay in the presence/absence of the RC gives an energy-transfer yield of $\Phi_{EET} = 0.35$.

4. Discussion

Photosynthetic organisms – plants, algae, cyanobacteria, purple bacteria - are demonstrably successful in occupying their particular spectral niches but there is scope nevertheless for enhancing the spectral coverage of photosynthesis, by augmenting the absorption of chlorophyll, carotenoid and phycobilin pigments normally employed for absorbing light. For example, some synthetic biology applications could require the design and construction of bacteria for light-powered bioreactors that could utilise a greater range of wavelengths than naturally-evolved photosynthetic bacteria. Thus arises the challenge of constructing modified antennas; the light-harvesting complexes found in photosynthetic organisms are flexible and diverse, providing a basis for the design of artificial light-harvesting constructs with a broad spectral coverage and the ability to transfer the resulting energy to a RC-like site with high efficiency.

Antenna modification *in vitro* can be achieved by attaching highly-absorbing dye molecules to purified complexes, thereby filling gaps in the native absorption spectrum. These biohybrid complexes exhibit efficient energy transfer from attached chromophores to native pigments, and by attaching several chromophores it has been possible to create energy transfer relays^{5, 12-15}.

Attaching up to nine Alexa Fluor 647 molecules to the LH2 complex from *Rhodospseudomonas acidophila* strain 10050 enhanced its light harvesting functions by occupying a vacant spectral region from 600-700 nm⁸. Dutta *et al.*⁶ have shown that DNA-templated dye molecules can be attached to *Rba. sphaeroides* RCs *in vitro*; the spectral range of these dyes complemented the native absorption of the RCs, and dye-RC energy transfer was observed, with efficiencies ranging from 42-83%. In another study, Alexa Fluor dyes were attached directly to the periplasmic face of the RC and dye-RC energy transfer efficiencies of 52-70% were obtained⁷.

The present study was performed to determine whether light harvesting and energy transfer could be augmented *in vivo* by genetically modifying a photosystem complex so that it carries an extra chromophore. Photosystems normally contain many tens of pigments that feed absorbed energy into RC traps, and the attachment of YFP to the RC adds an extra chromophore to the 'photosynthetic unit', in a spectral region already occupied by carotenoids. Thus, it was necessary for this pilot study to make some prior alterations to the bacterial chassis by eliminating the LH2 antenna and carotenoids clearing space, in spectral terms, to allow assessment of any contribution from YFP.

In this study we have shown that YFP, when fused to the RC of *Rba. sphaeroides*, is able to transfer electronic excitation energy to the native RC. This process has been observed at three levels; in bacterial cultures, in single cells, and in purified complexes (Fig. 1, 2, 4-7). Attachment of YFP to the RC increases the photosynthetic growth rate of a carotenoidless mutant of *Rba. sphaeroides* (compared with a control strain with no YFP) when YFP-specific illumination is used. Although the most straightforward explanation of this result is energy transfer from YFP to LH1 and RC pigments (supported by the static and time-resolved microscopy and spectroscopy) we checked for the possibility that YFP mitigates the photosensitivity of the carotenoidless $\Delta crtB$

background strain^{34, 35} since it has been proposed that fluorescent proteins may have a photoprotective function^{26, 27}. We found that the $\Delta crtB$ pBBRBB-YFP control strain with cytosolic YFP present, unattached to the RC, did not grow significantly faster than $\Delta crtB$ and therefore we discount any photoprotective effect of YFP.

We attributed differences in growth rates between carotenoid-containing and carotenoid-less strains (Fig. 2) to the lack of appropriate pigments for absorbing light at 520 nm and show that the attachment of YFP to RCs partly alleviates this problem. Other factors could potentially contribute to the relatively slow growth of carotenoid-less strains, such as destabilisation of the photosynthetic apparatus or susceptibility to photodamage. We have shown that only the assembly of the LH2 antenna is affected by inactivation of carotenoid biosynthesis²²⁻²⁵; thus, we genetically removed LH2 complexes in the positive control so all strains could be compared on an equal basis in terms of antenna composition. In terms of photodamage, respiration by these photoheterotrophic bacteria during illumination alleviates phototoxic effects in carotenoid-less mutants. Thus, under white light illumination, even the $\Delta crtB$ mutant achieves good rates of photosynthetic growth even with respect to the carotenoid-containing positive control.

Direct observation of YFP→ RC-LH1 energy transfer in whole cells, visualised using fluorescence lifetime microscopy (Fig. 4), is consistent with the increased photosynthetic growth rate of $\Delta crtB$ RCH-YFP compared to $\Delta crtB$ (Fig. 2a-c); the *in vivo* efficiency of energy transfer, Φ_{EET} , was calculated to be 0.48. In order to discover a structural basis for *in vivo* energy transfer, we used single particle reconstruction to obtain a structural model of the RC/YFP-LH1 complex (Fig. 3). The use of negative stain limited the resolution of the structural model to ~ 26 Å, but the presence of YFP was evident from the outset, even in raw images, and the final structural model clearly shows a density that can be confidently assigned to YFP. The staining procedure could

affect the perceived orientation of YFP with respect to the rest of the complex; we used over 11,000 particles for calculating the structural model so Fig. 3 shows an averaged orientation of YFP. The use of cryo-EM would produce a better quality structural model, which would also allow a more precise estimate of the distance between the YFP chromophore and the RC special pair. Nevertheless, the low resolution data are sufficient for a calculation of an ~ 85 Å distance between the YFP chromophore and the RC special pair and 53 Å to the nearest LH1 B875 BChl (Fig. 3f). Our energy transfer data provide another way to estimate distances and Förster calculations (Supplementary Fig. 5) show that the acceptor of excitation energy lies 43-48 Å from the YFP donor, consistent with our 53 Å estimate from the structure of the RC/YFP-LH1 complex. Thus, the most likely route for energy transfer from YFP to the RC *in vivo* is via the LH1 BChls.

In order to make a minimal energy transfer unit free of LH1, we purified a RC/YFP complex and quantified its energy transfer dynamics using static and time-resolved absorption and fluorescence spectroscopy. The TA measurements for the RC/YFP complexes (Figs. 7, 8) show an additional ~ 1.8 ns component indicating $\text{YFP}^* \rightarrow \text{RC}$ energy transfer, which is not seen in the RC-only control complex. The energy-transfer yield, Φ_{EET} , was calculated to be 0.35. Measurements of fluorescence yields for RC/YFP and YFP-only by two methods gave 0.47 and 0.58, and fluorescence lifetimes for RC/YFP-RC versus YFP-only using two different methods gave $\Phi_{\text{EET}} = 0.44$ and 0.31. The average value for Φ_{EET} is 0.4 ± 0.1 . We calculated a 5 ns time constant for $\text{YFP}^* \rightarrow \text{RC}$ energy transfer and a YFP to RC special pair distance of 56 to 62 Å (Supplementary Fig. 8), significantly lower than the 85 Å estimate from the RC/YFP-LH1 structure (Fig. 3f). There is a likely structural basis for this apparent discrepancy; the region connecting the YFP and RC-H could accommodate some movement of the YFP in the absence

of LH1, allowing YFP to move nearer to the RC “special pair” BChls (P) and resulting in more efficient energy transfer. This possible change in YFP position, caused by the absence of LH1, is depicted in Fig. 8. The YFP-RC distance of 45 Å measured from this model is shorter than calculated from energy transfer data, but the model represents the minimum possible YFP-RC distance and in practice the YFP likely does not approach the RC so closely, not least because some detergent molecules likely surround the central part of the RC complex.

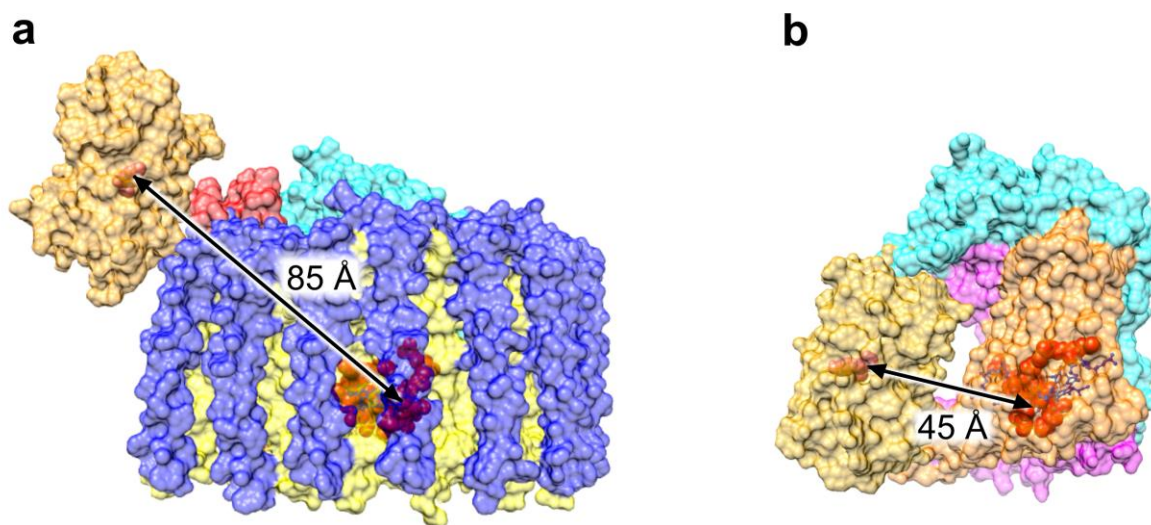


Figure 8. Modelling of the effect of LH1 removal on the position of YFP and the energy transfer distances. (a), The RC/YFP-LH1 complex shown is adapted from the data in Fig. 3. The subunits are: LH1β (blue), LH1α (yellow), PufX (red), RC-M (magenta), RC-H (cyan) and RC-L (orange). YFP is in gold, with its chromophore in orange. The RC special pair of BChls is shown in red. The 85 Å distance between the YFP chromophore and the RC BChl dimer in (a) is shown to shorten when the surrounding LH1 complex is removed during purification of the RC, down to a minimum of 45 Å in (b).

In summary, this proof-of-principle study opens up possibilities for the creation of new energy-trapping photosynthetic pathways; we show that translational fusions of genetically-encoded light-absorbers and antenna or RC complexes can augment energy transfer and trapping in photosynthesis.

Acknowledgments

This work was supported as part of the Photosynthetic Antenna Research Center (PARC), an Energy Frontier Research Center funded by the U.S. Department of Energy, Office of Science, Office of Basic Energy Sciences under Award Number DE-SC 0001035. PARC supported photophysical studies of RC/YFP, YFP, and RC complexes (P.D., J.M.Y., D.M.N., C. K., K.J.G.), and fluorescence lifetime studies of whole cells (X.H., C.V.) with support for X.H., P.D., C.V., Y.M.M., D.M.M., and partial support for C.N.H. C.N.H. also acknowledges financial support from Advanced Award 338895 from the European Research Council. C.N.H. and A.H. acknowledge financial support from the Biotechnology and Biological Sciences Research Council (BBSRC UK), award number BB/G021546/1. K.J.G. was supported by a doctoral studentship from the Engineering and Physical Sciences Research Council (EPSRC UK), and gratefully acknowledges a Scientific Exchange award from PARC; G.J.L. thanks the EPSRC (grant EP/I012060/1) for financial support. K.M.F. was supported by the National Science Foundation Graduate Research Fellowship under grant DGE-1143954. The authors are grateful to Dr Amanda Brindley and Dr David Mothersole for useful discussions.

References

1. Blankenship, R. E. *et al.* Comparing photosynthetic and photovoltaic efficiencies and recognizing the potential for improvement. *Science* **332**, 805-809 (2011).
2. Slouf, V. *et al.* Photoprotection in a purple phototrophic bacterium mediated by oxygen-dependent alteration of carotenoid excited-state properties. *Proc. Natl. Acad. Sci. USA* **109**, 8570-8575 (2012).
3. Herek, J.L. *et al.* B800→B850 energy transfer mechanism in bacterial LH2 complexes investigated by B800 pigment exchange. *Biophys. J.* **78**, 2590–2596 (2000).
4. Gundlach, K., Werwie, M., Wiegand, S. & Paulsen, H. Filling the “green gap” of the major light-harvesting chlorophyll *a/b* complex by covalent attachment of Rhodamine Red. *BBA-Bioenergetics* **1787**, 1499-1504 (2009).
5. Reddy, K. R. *et al.* Palette of lipophilic bacteriochlorins for construction of biohybrid light-harvesting architectures. *Chem. Sci.* **4**, 2036-2053 (2013).
6. Dutta, P. K. *et al.* A DNA-directed light-harvesting/reaction center system. *J. Am. Chem. Soc.* **136**, 16618–16625 (2014).

7. Dutta, P. K. *et al.* Reengineering the optical absorption cross-section of photosynthetic reaction centers. *J. Am. Chem. Soc.* **136**, 4599-4604 (2014).
8. Yoneda, Y. *et al.* Extension of light-harvesting ability of photosynthetic light-harvesting complex 2 (LH2) through ultrafast energy transfer from covalently attached artificial chromophores. *J. Am. Chem. Soc.* **137**, 13121–13129 (2015).
9. Meadows, K. A. *et al.* Enzymatic and chemical cleavage of the core light-harvesting polypeptides of photosynthetic bacteria - determination of the minimal polypeptide size and structure required for subunit and light-harvesting complex-formation. *Biochemistry* **34**, 1559-1574 (1995).
10. Meadows, K. A., Parkes-Loach, P. S., Kehoe, J. W. & Loach, P. A. Reconstitution of core light-harvesting complexes of photosynthetic bacteria using chemically synthesized polypeptides. 1. Minimal requirements for subunit formation. *Biochemistry* **37**, 3411-3417 (1998).
11. Kehoe, J. W., Meadows, K. A., Parkes-Loach, P. S. & Loach, P. A. Reconstitution of core light-harvesting complexes of photosynthetic bacteria using chemically synthesized polypeptides. 2. Determination of structural features that stabilize complex formation and their implications for the structure of the subunit complex. *Biochemistry* **37**, 3418-3428 (1998).
12. Springer, J. W. *et al.* Biohybrid photosynthetic antenna complexes for enhanced light-harvesting. *J. Am. Chem. Soc.* **134**, 4589-4599 (2012).
13. Harris, M. A. *et al.* Integration of multiple chromophores with native photosynthetic antennas to enhance solar energy capture and delivery. *Chem. Sci.* **4**, 3924-3933 (2013).
14. Harris, M. A. *et al.* Versatile design of biohybrid light-harvesting architectures to tune location, density, and spectral coverage of attached synthetic chromophores for enhanced energy capture. *Photosynth. Res.* **121**, 35-48 (2014).
15. Harris, M. A. *et al.* Enhanced light harvesting capacity by micellar assembly of free accessory chromophores and LH1-like antennas. *Photochem. Photobiol.* **90**, 1264-1276.
16. Cartron, M.L. *et al.* Integration of energy and electron transfer processes in the photosynthetic membrane of *Rhodobacter sphaeroides*. *BBA-Bioenergetics* **1837**, 1769-1780 (2014).
17. Sener, M. K., Olsen, J. D., Hunter, C. N. & Schulten, K. Atomic-level structural and functional model of a bacterial photosynthetic membrane vesicle. *P. Natl. Acad. Sci. USA* **104**, 15723-15728 (2007).
18. Sener, M. *et al.* Structural model and excitonic properties of the dimeric RC-LH1-Pufx complex from *Rhodobacter sphaeroides*. *Chem. Phys.* **357**, 188-197 (2009).
19. Sener, M. K. & Schulten, K. From atomic-level structure to supramolecular organization in the photosynthetic unit of purple bacteria. In: *The Purple Phototrophic Bacteria* (Hunter, C.N., Daldal, F., Thurnauer, M.C. and Beatty, J.T., eds) pp 275-294 (2009) Springer, The Netherlands.
20. Cardona, T., Sedoud, A., Cox, N., & Rutherford A.W. Charge separation in photosystem II: A comparative and evolutionary overview. *Biochim. Biophys. Acta* **1817**, 26–43 (2012).
21. Kremers, G. J., Goedhart, J., van Munster, E. B. & Gadella, T. W. J. Cyan and yellow super fluorescent proteins with improved brightness, protein folding, and FRET forster radius. *Biochemistry* **45**, 6570-6580 (2006).

22. Chi, S.C. *et al.* Assembly of functional photosystem complexes in *Rhodobacter sphaeroides* incorporating carotenoids from the spirilloxanthin pathway. *Biochim. Biophys. Acta.* **1847**, 189-201 (2015).
23. Lang, H.P. & Hunter, C.N. The relationship between carotenoid biosynthesis and the assembly of the light harvesting LH2 complex in *Rhodobacter sphaeroides*. *Biochem. J.* **298**, 197-205 (1994).
24. Lang, H.P., Cogdell, R.J., Takaichi, S. & Hunter, C.N. Complete DNA sequence, specific Tn5 insertion map, and gene assignment of the carotenoid biosynthesis pathway of *Rhodobacter sphaeroides*. *J. Bacteriol.* **177**, 2064-2073 (1995).
25. Ng, I. W., *et al.* Carotenoids are essential for normal levels of dimerisation of the RC-LH1-PufX core complex of *Rhodobacter sphaeroides*: characterisation of R-26 as a *crtB* (phytoene synthase) mutant. *Biochim. Biophys Acta* **1807**, 1056-1063 (2011).
26. Kawaguti, S. On the physiology of reefs corals VI. Study on the pigments. *Palao Tropical Biological Station Studies Tokyo* **2**, 617-673 (1944).
27. Salih, A., Larkum, A., Cox, G., Kuhl, M. & Hoegh-Guldberg, O. Fluorescent pigments in corals are photoprotective. *Nature* **408**, 850-853 (2000).
28. Tikh, I. B., Held, M. & Schmidt-Dannert, C. Biobrick™ compatible vector system for protein expression in *Rhodobacter sphaeroides*. *Appl. Microbiol. Biot.* **98**, 3111-3119 (2014).
29. Qian, P. *et al.* The 3-D structure of the *Rhodobacter sphaeroides* RC-LH1-PufX complex: dimerization and quinone channels promoted by PufX. *Biochemistry* **52**, 7575-7585 (2013).
30. Qian, P., Bullough, P.A. & Hunter, C.N. 3-D reconstruction of a membrane-bending complex: the RC-LH1-PufX core dimer of *Rhodobacter sphaeroides*. *J. Biol. Chem.* **283**, 14002-14011 (2008).
31. Mothersole, D.J. *et al.* PucC and LhaA direct efficient assembly of the light-harvesting complexes in *Rhodobacter sphaeroides*. *Mol. Microbiol.* **99**, 307-327 (2016).
32. Du, H., Fuh, R.-C. A., Li, J., Corkan, L. A. & Lindsey J. S. PhotochemCAD: A computer-aided design and research tool in photochemistry and photobiology. *Photochem. Photobiol.* **68**, 141–142 (1998).
33. Kirmaier, C. & Holten, D. Primary photochemistry of reaction centers from the photosynthetic purple bacteria, *Photosynth. Res.* **13**, 225-260 (1987).
34. Clayton, R. K. & Smith, C. *Rhodopseudomonas spheroides* - high catalase and bluegreen double mutants. *Biochem. Bioph. Res. Co.* **3**, 143-145 (1960).
35. Cogdell, R. J. & Frank, H. A. How carotenoids function in photosynthetic bacteria. *Biochim. Biophys. Acta* **895**, 63-79 (1987).
36. Qian, P., Hunter, C. N. & Bullough, P. A. The 8.5 Å projection structure of the core RC-LH1-PufX dimer of *Rhodobacter sphaeroides*. *J. Mol. Biol.* **349**, 948-960 (2005).
37. Majumder, E. L-W. *et al.* Supramolecular organization of photosynthetic complexes in membranes of *Roseiflexus castenholzii*. *Photosynth. Res.* **127**, 117-130 (2016).
38. Tang, G., *et al.* EMAN2. An extensible image processing suite for electron microscopy. *J. Struct. Biol.* **157**, 38-46 (2007)
39. van Heel, M., Harauz, G., Orlova, E. V., Schmidt, R., and Schatz, M. A new generation of the IMAGIC-5 image processing system. *J. Struct. Biol.* **116**, 17–24 (1996).
40. van Heel, M., and Schatz, M. Fourier shell correlation threshold criteria. *J. Struct. Biol.* **151**, 250 –262 (2005).
41. Brannon, J. H. & Magde, D. Absolute quantum yield determination by thermal blooming fluorescein. *J. Phys. Chem.* **82**, 705-709 (1978).

42. Magde, D., Wong, R. & Seybold, P. G. Fluorescence quantum yields and their relation to lifetimes of Rhodamine 6G and Fluorescein in nine solvents: improved absolute standards for quantum yields, *Photochem. Photobiol.* **75**, 327-334 (2002).
43. Sahin, T. *et al.* Self-assembled light-harvesting system from chromophores in lipid vesicles *J. Phys. Chem. B.* **119**, 10231-10243 (2015).
44. Kressel, L. *et al.* High yield of secondary B-side electron transfer in mutant *Rhodobacter capsulatus* reaction centers. *Biochim. Biophys. Acta* **1937**, 1892-1903 (2014).
45. Straley S. C., Parson W. W., Mauzerall D. C. & Clayton, R. K. Pigment content and molar extinction coefficient of the primary electron donor. *Biochim. Biophys. Acta* **305**, 597-609 (1973).

Chapter 4: High Yield of Secondary B-side Electron Transfer in Mutant *Rhodobacter capsulatus* Reaction Centers

Reprinted with permission from Kressel, L.; Faries, K.M.; Wander, M.J.; Zogzas, C.E.; Mejdrich, R.J.; Hanson, D.K.; Holten, D.; Laible, P.D.; Kirmaier, C. (2014) High yield of secondary B-side electron transfer in mutant *Rhodobacter capsulatus* reaction centers. *Biochimica et Biophysica Acta* 1837, 1892-1903.

Abstract

From the crystal structures of reaction centers (RCs) from purple photosynthetic bacteria, two pathways for electron transfer (ET) are apparent but only one pathway (the A side) operates in the native protein-cofactor complex. Partial activation of the B-side pathway has unveiled the true inefficiencies of ET processes on that side in comparison to analogous reactions on the A side. Of significance are the relative rate constants for forward ET and the competing charge recombination reactions. On the B side, these rate constants are nearly equal for the secondary charge-separation step (ET from bacteriopheophytin to quinone), relegating the yield of this process to <50%. Herein we report efforts to optimize this step. In surveying all possible residues at position 131 in the M subunit, we discovered that when glutamic acid replaces the native valine the efficiency of the secondary ET is nearly two-fold higher than in the wild-type RC. The positive effect of M131 Glu is likely due to formation of a hydrogen bond with the ring-V keto group of the B-side bacteriopheophytin leading to stabilization of the charge-separated state involving this cofactor. This change slows charge recombination by roughly a factor of two and affords the improved yield of the desired forward ET to the B-side quinone terminal acceptor.

1. Introduction

The bacterial photosynthetic reaction center (RC) is a transmembrane protein-cofactor complex that converts light energy into chemical potential for use in cellular processes. Of the three protein subunits (L, M and H), homologous L and M comprise an integral core and bind a bacteriochlorophyll (BChl) dimer (P) that is the primary electron donor, two monomeric BChls (B), two monomeric bacteriopheophytins (H) and two quinones (Q). These cofactors are arranged in two branches (A and B) in pseudo- C_2 symmetry (Fig. 1A).¹⁻⁴ Despite the similarity between the branches, in the wild-type (WT) RC only the A-side cofactors participate in rapid multi-step electron transfer (ET) that results in nearly quantitative formation of $P^+Q_A^-$ from P^* in less than a nanosecond. Subsequent $P^+Q_A^- \rightarrow P^+Q_B^-$ ET occurs on the microsecond timescale.

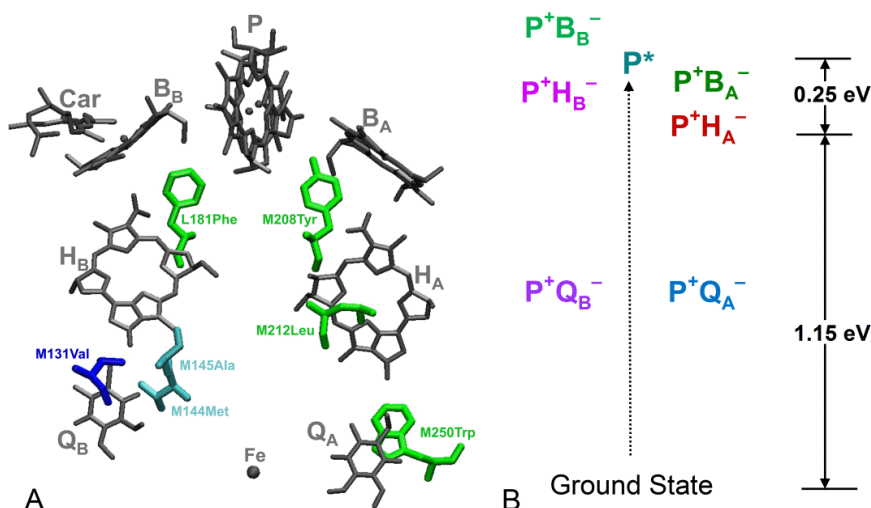


Figure 1. (A) Positions of the substituted amino acids relative to the cofactors in the RC, from the *Rb. sphaeroides* crystal structure 1PCR.⁴ Native amino acids are shown. Sites that comprise the YFHV background mutations are in green. The M131 site that was subject to extensive mutation here is in blue. The M144 and M145 sites also studied here are in cyan. See Table 1 for additional details. (B) Model free energy diagram for WT RCs.

Site-directed mutagenesis has been used with great success over the last 25 years to explore the factors responsible for unidirectional A-side ET in the RC. Mutant RCs that perform B-side charge separation – albeit generally in low yield – have enriched our understanding of the mechanism of primary A-side charge separation and framed views of how ET from P* to the B-side cofactors is normally suppressed.⁵⁻²⁵ The general working model (Fig. 1B) is that the P⁺B_A⁻ state is positioned between P* and P⁺H_A⁻ supporting two initial ET steps, P* → P⁺B_A⁻ → P⁺H_A⁻, that occur on the ~0.5 to ~5 ps timescale.²⁶⁻³⁶ On the B side, P* → P⁺H_B⁻ ET is much slower (~100-200 ps) with P⁺B_B⁻ thought to be higher in free energy than P* and supporting ET by a superexchange mechanism. Distinctions also exist between the intrinsic properties of P⁺H_A⁻ and P⁺H_B⁻. P⁺H_A⁻ → P⁺Q_A⁻ ET occurs in 200 ps. In the absence of ET, P⁺H_A⁻ lives for 10-20 ns and decays by charge recombination (CR) to form the ground and triplet excited states.^{28,34} In comparison, P⁺H_B⁻ → P⁺Q_B⁻ ET is much slower (~4 ns time constant) and P⁺H_B⁻ has a shorter intrinsic lifetime (~3 ns).²³ This combination results in ~45% yield of P⁺H_B⁻ → P⁺Q_B⁻ ET compared to 100% formation of P⁺Q_A⁻ on the A side. Therefore, even if a high yield of P* conversion to P⁺H_B⁻ is achieved in a mutant, translation of that increase through to a high yield of P⁺Q_B⁻ is not assured. To achieve this end, the mutant RC would also require changes that increase the rate constant for P⁺H_B⁻ → P⁺Q_B⁻ ET and/or reduce the rate constant for P⁺H_B⁻ CR.

We have adopted a directed molecular evolution approach to engineering the RC to enable efficient B-branch ET that employs *Rhodobacter (Rb.) capsulatus* and rapid, efficient, semi-random methods for constructing RC mutants. This is coupled to a high-throughput millisecond screening assay (ms assay) that measures the yield of P⁺Q_B⁻ formed solely via the B-branch cofactors.³⁷ In this work we report on two groups of mutant RCs, seeking mutations that

increase the rate of $P^+H_B^- \rightarrow P^+Q_B^-$ ET and/or decrease the rates of the competing CR processes of $P^+H_B^-$. The first mutant set targets residue M131 near H_B (Fig. 1A), where a Val is the native amino acid in *Rb. capsulatus* (Thr in *Rb. sphaeroides*). All amino acids were substituted at M131 (“saturation mutagenesis”), mutants denoted V(M131)X. The motivation for exploring M131 is that the C_2 symmetry-related residue on the A side is a Glu (at L104) that forms a hydrogen bond with H_A^1 and previous work has suggested that an Asp at M131 (or at M133 in *Rb. sphaeroides*) forms a hydrogen bond to H_B .^{10,25,38,39} The second group couples substitution of all 20 amino acids at M131 with mutations of M144Met to Ile and M145Ala to Ser (designated “IS”). Residues M144-145 are located somewhat between H_B and Q_B (Fig. 1A) and the IS substitutions were identified by Youvan and coworkers in a photocompetent phenotypic revertant of a strain carrying multiple-site mutations in the Q_B binding pocket.^{40,41}

We find an increased yield of $P^+Q_B^-$ from B-side ET in RCs carrying amino acid substitutions at M131, for the IS pair alone, and for some substitutions at M131 paired with the IS mutations. Of these, five mutants were selected for further investigation of ET to and between the B-side cofactors using ultrafast transient absorption (TA) spectroscopy in order to determine the origin of improved $P^+Q_B^-$ production. Among the selected mutants, we find that the yields of initial $P^* \rightarrow P^+H_B^-$ ET are essentially identical and the relative higher/lower yields of $P^+Q_B^-$ derive from a rebalancing of the rate constants for the competing $P^+H_B^- \rightarrow P^+Q_B^-$ ET and $P^+H_B^-$ CR processes.

2. Materials and Methods

2.1. Preparation of Mutants and RCs. The V(M131)X and V(M131)X+IS mutations were created in derivatives of a specifically engineered expression plasmid,

pBBRKW2HTsLsM.³⁷ This plasmid contains strategically-placed unique restriction enzyme sites in the L and M genes that enable rapid cassette-based mutagenesis of regions near the RC cofactors. Each V(M131)X mutation was carried on a cassette flanked by *EcoRV* and *XmaI* restriction enzyme sites and the M(M144)I-A(M145)S mutations were carried on a fragment bearing *XmaI* and *AflIII* ends. In a small subset of mutant plasmids, a synthetic cassette encoding the native Trp residue at M250 was used to replace a region flanked by unique *NheI* and *NcoI* sites. All mutations were verified by sequencing of candidate plasmids. RCs were expressed in *Rb. capsulatus* host strain U43 following conjugal transfer of mutant plasmids. RC expression screening and RC purification followed methods described previously.³⁷ Purified RCs were suspended in 10 mM Tris (pH 7.8), 0.1% Deriphat 160-C for all spectroscopic experiments.

2.2. Millisecond Screening Assay. The $P^+Q_B^-$ yield in the mutant RCs was determined using a dedicated apparatus of local design that allows studies spanning $\sim 100 \mu\text{s}$ to $\sim 5 \text{ min}$.³⁷ Samples, $\sim 100 \mu\text{l}$ in volume and having $A_{865\text{nm}} = 0.05 \pm 0.005$ in a 2 mm pathlength, were arrayed and screened in 96-well plates. RCs were excited with a single $\sim 7 \text{ ns}$ excitation flash at 532 nm (provided by a Q-switched Nd:YAG laser) and the magnitude and decay of bleaching of the ground state absorbance of P were probed at 850 nm (provided by a continuous-wave diode laser). As controls, RCs from WT and the YFHV mutant (defined in Section 3.1) were included on every screening plate. The WT RC provides the reference of $\sim 100\%$ $P^+Q_B^-$ formation (from $P^+Q_A^-$) and the YFHV RC gives $\sim 22\%$ yield of $P^+Q_B^-$ formation via B-side ET.

2.3. Ultrafast Transient Absorption (TA) Spectroscopy. Ultrafast TA experiments employed $\sim 130 \text{ fs}$ excitation and white light probe flashes at 10 Hz and an apparatus described previously.⁸ Data were acquired in an $\sim 220\text{-nm}$ spectral window. For experiments that probed 480-700 nm, RCs had $A_{865\text{nm}} = \sim 0.9\text{-}1.0$ (2 mm pathlength). Experiments probing 830-1050 nm

utilized RCs with $A_{865\text{nm}} = \sim 0.5\text{-}0.6$ (2 mm pathlength). To ensure that fresh sample was excited on each laser flash, 2.0-2.5 mls of RCs were flowed rapidly through a 2 mm path-length cell and an ice-cooled ($\sim 10^\circ\text{C}$) reservoir.

2.4. Extended-Timescale Ultrafast TA Measurements. TA measurements on the ~ 0.5 ns to 450 μs timescale utilized 1 KHz, ~ 130 -fs excitation flashes at 865 nm provided by an amplified (Spitfire Ace) Ti:sapphire (MaiTai) laser system (Spectra Physics) coupled to a Topaz (Light Conversion) optical parametric amplifier. An EOS detection system (Ultrafast Systems Inc.) provided ~ 1 ns white light probe light flashes that are slaved to the 1 KHz clock of the ultrafast laser system. The instrument response function (if viewed as a Gaussian) of the EOS detection system is ~ 0.5 ns. TA spectra (400-800 nm window) were averaged into “bins” (100 ps minimum width) with 450 μs being the longest delay time possible at a 1 KHz repetition rate. RC samples used for these experiments were stirred rapidly and contained terbutryn (tb), a competitive inhibitor of Q_B binding. In particular, 10-13 μL of a 40 mM tb stock solution in ethanol was added to 0.40-0.50 mls of ~ 25 μM RCs to obtain a final concentration of ~ 1 mM tb ($\sim 40:1$ ratio of tb:RCs), keeping the ethanol concentration at $\leq 3\%$. Steady-state oxidation of the samples during the 1 KHz experiments was prevented by adding ~ 2.5 μL of 400 mM ascorbic acid stock to give a final concentration of 2 mM.

2.5. Spectrochemical Redox Measurements. The P/P^+ midpoint potentials of selected mutant RCs were determined as described previously.⁴²

3. Results and Discussion

3.1. Mutant RCs. The V(M131)X and V(M131)X+IS mutants bear a core set of mutations (Fig. 1A; Table 1) that have been shown previously to enhance B-side ET at the

expense of A-side ET.^{8,15,37} In the “YFHV” and “YFH” mutants that were used as templates for the insertion of the mutations at M131 and/or at M144-145, Y denotes change of the native Phe at L181 to Tyr (near B_B) and F denotes substitution of the native symmetry-related M208 Tyr to Phe (near B_A). The H designation indicates substitution of the native Leu at M212

Table 1. Key Mutant RC Designations.*

RC	Mutations
WT	none
YFHV	F(L181)Y-Y(M208)F-L(M212)H-W(M250)V
ISYFHV	M(M144)I-A(M145)S-YFHV
E+YFHV	V(M131)E-YFHV
E+ISYFHV	V(M131)E-ISYFHV
I+YFHV	V(M131)I-YFHV
I+ISYFHV	V(M131)I-ISYFHV

*L(M212)H results in incorporation of a BChl (denoted β) in place of H_A; W(M250)V results in the absence of Q_A from the RC.

(near H_A) with His, resulting in incorporation of a BChl (denoted β) in place of H_A,⁴³ allowing unambiguous spectroscopic resolution of P⁺H_B⁻ Q_X bleaching^{5,8,15} in mutants chosen from the ms assay for more in-depth studies. For RCs in Deriphat/Tris, the combination of the YFH mutations provides ~40% P* → P⁺H_B⁻ ET, along with ~50% yield of P* → P⁺ β ⁻ and ~10% P* internal conversion to the ground state.⁴⁴ The same is true of the YFHV RC, where the V designation refers to replacement of Trp at M250 by Val, a substitution that prevents RCs from incorporating Q_A.^{45,46} Of the 19 possible V(M131)X+YFHV mutants, two did not produce RCs (Q and Y). Six V(M131)X+ISYFHV mutants also failed to produce RCs (P, L, A, S, F, and R).

3.2. Ground State Absorption Spectra of Mutant RCs. Ground state spectra of the isolated RCs are shown in Fig. 2A and 2B. The P absorbances near 865 nm are relatively similar among the mutants, while some differences exist in the Q_X and Q_Y absorbance regions of H_B. At first glance, spectra of purified RCs containing K and Y substitutions at M131 (in the ISYFHV

background) appear to indicate that these RCs may lack H_B since there is no resolved 760-nm peak (Fig. 2A). In fact, the Q_y absorption of this cofactor has been red-shifted and is not resolved from the Q_y absorption of β near 780 nm.⁴³ The spectra of RCs containing the H and W substitutions at M131 in combination with ISYFHV have a similar appearance, but to a lesser degree (not shown). In the M131X+YFHV mutants, red-shifted Q_y absorptions for H_B are noted in the RCs carrying K, H, W, F, and R substitutions (Fig. 2A). Less pronounced are analogous spectral shifts in the set of mutants that were chosen, based on the ms assay results presented below (Section 3.3), for extensive spectroscopic characterization (Fig. 2B). Here, the substitution of E or I at M131 has limited influence on the Q_y absorption of H_B and can be seen to red-shift its Q_x absorption; this shift is more pronounced in the YFHV background relative to the ISYFHV background.

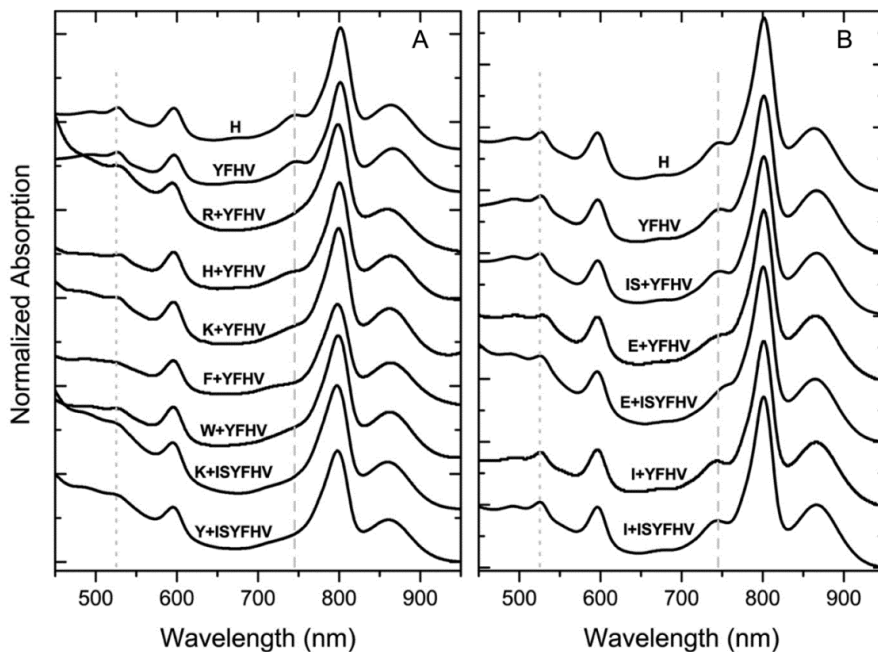


Figure 2. Ground state spectra of selected RC complexes carrying mutations in the vicinity of H_B and a core mutations (YFHV; Table 1). The spectrum of the H mutant carrying the L(M212)H substitution is given in both parts for comparison purposes. Spectra of the mutant RC studied in detailed in this work are given in part B. Regions that shift with amino acid substitution are indicated by dashed (Q_y region) or dotted (Q_x region) lines.

3.3. $P^+Q_B^-$ Yields Determined from the Millisecond Screening Assay. The ms screening results for the yield of formation of $P^+Q_B^-$ in the sets of V(M131)X+YFHV and V(M131)X+ISYFHV mutant RCs are shown in Fig. 3 along with WT, YFHV, and W(M250)V controls. Because the mutant RCs do not bind Q_A (again, owing to the presence of the W(M250)V mutation; Table 1) the only long-lived charge-separated state that can be present is $P^+Q_B^-$ formed via B-side ET.³⁷ The WT RC screened in the ms-assay provides the control of 100% formation of $P^+Q_B^-$ via A-side charge separation and $P^+Q_A^- \rightarrow P^+Q_B^-$ ET. The orange-filled bars in Fig. 3 give the results for RCs carrying 17 amino acids at M131 in the YFHV background. Glu at M131 (mutant E+YFHV, left-most orange bar) significantly improves the yield of $P^+Q_B^-$ compared to the native Val (control sample YFHV, yellow bar). The Asn, Gly, Asp and Ile substitutions are also better than or comparable to the native Val in promoting B-branch formation of $P^+Q_B^-$, and several other amino acids rank just slightly below Val in supporting

B-side

ET.

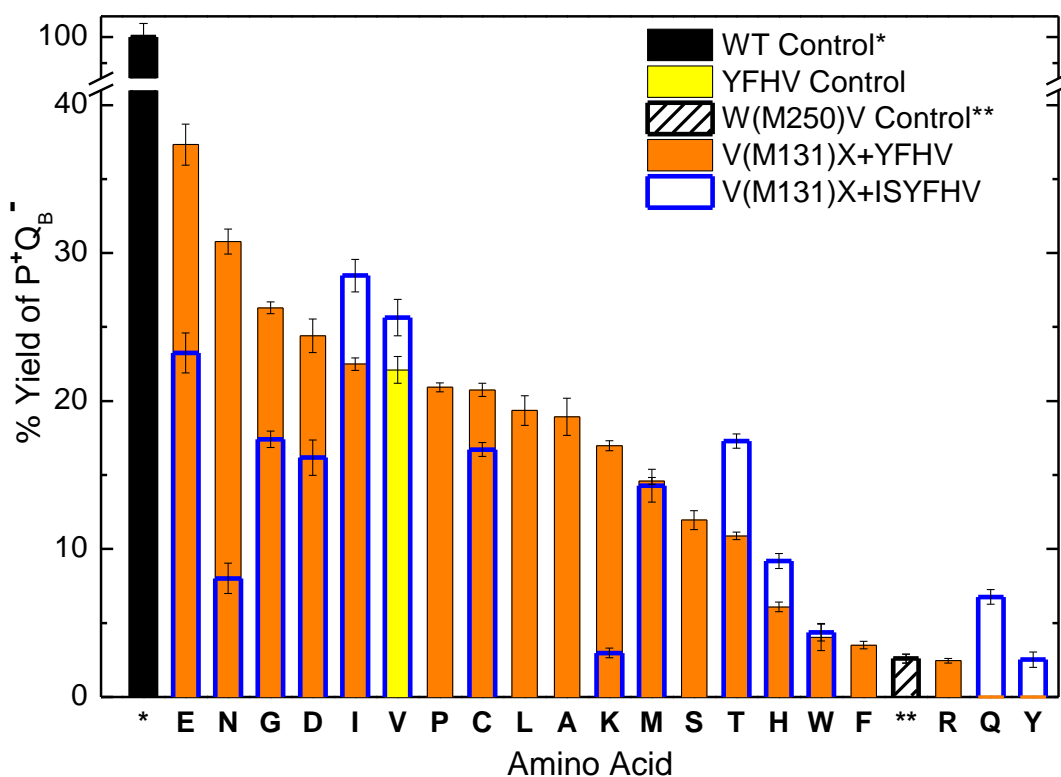


Figure 3.
 $P^+Q_B^-$ yields
in the

V(M131)X+YFHV (orange bars) and V(M131)X+ISYFHV (blue outline bars) mutant RCs relative to controls WT (solid black bar), YFHV (solid yellow bar) and W(M250)V (black-hashed bar) obtained from the millisecond screening assay. In the WT RC, $P^+Q_B^-$ forms in 100% yield via initial A-side charge separation and $P^+Q_A^- \rightarrow P^+Q_B^-$ ET.

The blue-outlined (open) bars in Fig. 3 show the results of screening 15 amino acid substitutions at M131 in a background where the IS pair of mutations [M(M144)I+A(M145)S] has been added to YFHV. Compared to YFHV, the assay indicates that a higher yield of $P^+Q_B^-$ is obtained in the ISYFHV mutant RC. The same comparison holds for adding the IS mutations to the V(M131)I+YFHV construct to give mutant I+ISYFHV. For a given residue at M131, the $P^+Q_B^-$ yield goes down upon addition of the IS substitutions in about half of the cases and goes

up or stays the same in half. For the four top performing residues at M131 (E, N, G, D), addition of the IS substitutions results in significantly lower $P^+Q_B^-$ yield.

3.4 Millisecond Assay Considerations.

3.4.1 Photochemical Recycling. In the ms assay, it is possible for ‘recycling’ of the RC photochemistry to occur when fast (ps-ns timescale) CR processes return RCs to the ground state, which can then be re-excited during the 7-ns excitation flash. For example, upon excitation $P^+\beta^-$ is formed on the A side in ~50% yield in the YFHV background (Fig. 4A). The lifetime of $P^+\beta^-$ in the absence of Q_A is ~ 1 ns^{43,47,48} providing the opportunity for recycling. RCs that return to the ground state via P^* internal conversion (~10% yield for YFHV; Fig 4A) may also be re-excited. Ultrafast studies have revealed that in many mutant RCs there is an ~30% ‘inactive’ fraction/population of P^* (discussed in Section 3.5.2) wherein P^* decays to the ground state via internal conversion in 100-200 ps; a fraction of these RCs may not be inactive on a subsequent excitation event. Because of recycling via any of these avenues, it is thus possible to obtain higher yields of charge separation in the ms assay than obtained from experiments employing ultrashort ps-fs laser flashes.

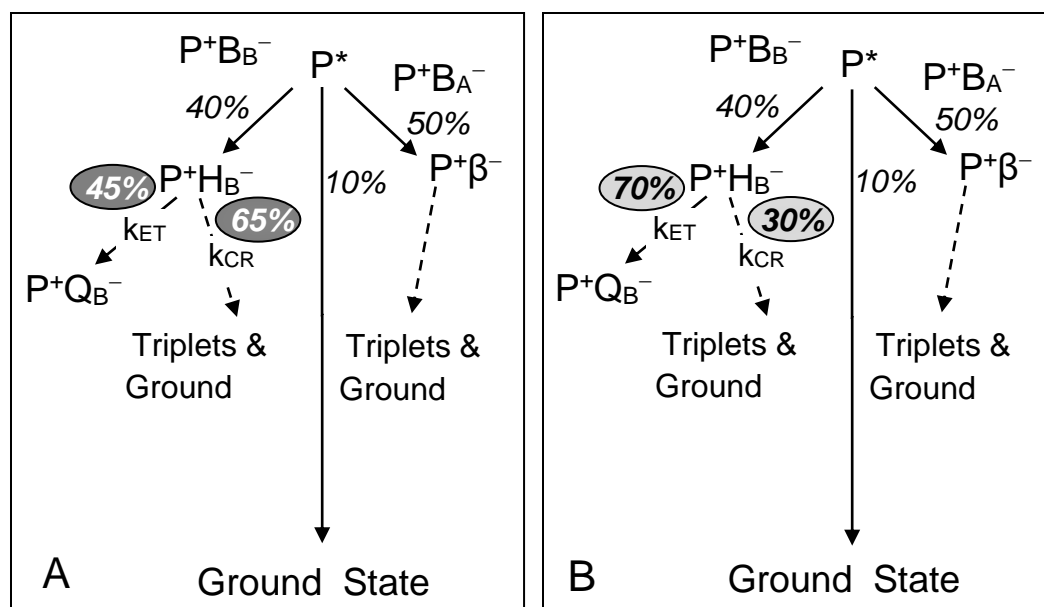


Figure 4. Simplified schematic of processes observed in this study. (A) Photochemical scheme for the YFHV template RC. The yields in percent pertain to individual branching points as indicated and as currently estimated from this and previous work on YFHV RCs. (B) Photochemical scheme for the E+YFHV RC with increased yield of forward secondary ET. See the text and Equations 1-3 for definitions of k_{ET} and k_{CR} .

Based on the inventory of mutants screened to date and results presented here, our current assessment is that the general relative ordering of the yield of $P^+Q_B^-$ in mutant RCs is assayed reliably by the ms screen with recycling adding no more than ~10% to the measured $P^+Q_B^-$ yields. The W(M250)V mutant (Fig. 3) is a negative control that lacks Q_A but is otherwise WT. It should give no or only a very small yield of $P^+Q_B^-$ (due to a few percent inherent B-side yield, recycling, or residual Q_A content). In general, mutants with the lowest yields of $P^+Q_B^-$ formation have the greatest potential to be recycled, meaning that the poorest mutants may in fact have

even lower actual $P^+Q_B^-$ yields than indicated. Conversely, the mutants with the highest yields are the least affected by recycling.

3.4.2 Q_B Occupancy. In the WT RC, after receiving two electrons from successive A-side charge-separation events and acquiring two protons, Q_B migrates out of the complex as the quinol Q_BH_2 . Unlike its tightly-bound counterpart Q_A , Q_B binding is labile by natural design. We have determined that WT and YFHV control RCs have $\geq 90\%$ occupancy of the Q_B site as prepared via our standard methods (Section 3.5.5). All the mutant RCs are purified similarly and the ms assay is performed on all RCs “as is” with the view that if a mutant exhibits a low yield of B-side formation of $P^+Q_B^-$, it is not considered a “hit” in our quick ms screening assay.

In optimizing and understanding our assay, however, we have explored the extent to which adding either UQ_4 or UQ_6 under variety of conditions might increase the $P^+Q_B^-$ yield compared to the same RC with no UQ additions (i.e., prepared “as is”). In *Rb. capsulatus* RCs, both the Q_A and Q_B sites are occupied by ubiquinone-10 (UQ_{10}) molecules which have ten repeating isoprenyl units attached to the functional headgroup; UQ_4 and UQ_6 have correspondingly fewer isoprenyl units attached to the same headgroup. A sampling of mutants has been used for this effort (ones reported here, previously, or as yet unpublished). Most of this effort has involved use of UQ_6 . To date, we have not been able to discover consistent conditions for UQ_6 addition that lead to appreciable increase in magnitude of the $P^+Q_B^-$ signal in the ms assay. Nor would such readily be expected given differences in positions of mutation. In some cases, there is evidence that added quinone (UQ_4 especially) may bind in the Q_A pocket, which leads to a very undesirable false positive effect in the ms assay ($P^+Q_B^-$ that derives from ET to Q_A and subsequent ET from Q_A to Q_B).

Clearly lack of change in the amplitude of $P^+Q_B^-$ formation upon addition of quinone cannot distinguish between whether an RC has full Q_B occupancy to start with or whether the occupancy is low and exogenous quinone fails to be incorporated under the conditions tested. Depending on the site(s) of the mutation(s), knowledge of the exact occupancy of the Q_B site is needed for those mutants that score high in the ms assay and are investigated further in ultrafast studies. Such is the case here and determinations of Q_B occupancy for a subset of six mutants will be described below (Section 3.5.5) in the context of data analysis to determine the rates and yields of $P^+H_B^- \rightarrow P^+Q_B^-$ ET.

3.5 Ultrafast Spectroscopic Analysis of the Six Mutant RCs. Based on the ms assay results, six mutant RCs were selected for ultrafast TA studies: YFHV (the starting template mutant), ISYFHV, E+YFHV, E+ISYFHV, I+YFHV and I+ISYFHV (Table 1). The yield of $P^+Q_B^-$ in all five of the new mutants is about the same as or larger than found for YFHV (Fig 3). The ultrafast measurements confirm this basic result and unravel changes to the properties of the B-side charge-separated states that lead to the E+YFHV mutant producing the most $P^+Q_B^-$. Analysis of the ultrafast measurements requires the considerations presented in the following subsections that ultimately lead (Section 3.5.6) to the conclusion that mutations described here that result in an enhanced yield of $P^+Q_B^-$ primarily do so by slowing $P^+H_B^-$ CR.

3.5.1. General Model for RC Photochemistry. In the simplest picture (Fig. 4A), mutation(s) may alter the competition of processes/rates at two branching points to afford a higher yield of $P^+Q_B^-$. One possibility is that initial P^* decay produces relatively more $P^+H_B^-$ compared to P^* decay by internal conversion or by ET to the A side to form $P^+\beta^-$. The second is a more favorable biasing of $P^+H_B^- \rightarrow P^+Q_B^-$ ET over $P^+H_B^-$ CR to form the ground state or triplet excited states. For simplicity, we define k_{ET} as the rate constant for $P^+H_B^- \rightarrow P^+Q_B^-$ ET

and τ_{ET} as the associated time constant (Eq. 1). We define k_{CR} as the “effective rate constant” for the combination of all other processes by which $P^+H_B^-$ decays by CR, where τ_{CR} is the associated time constant (the ‘CR lifetime’) for the decay of the state in the absence of ET (Eq. 2). When $P^+H_B^-$ can decay by both ET and CR (i.e., when Q_B is present), the lifetime of the state (τ_{HB}) is given by Eq. 3 and the associated yields by Eqs. 4 and 5.

$$\tau_{ET} = 1/k_{ET} = 1/(\tau_{HB}^{-1} - \tau_{CR}^{-1}) \quad (1)$$

$$\tau_{CR} = 1/k_{CR} \quad (2)$$

$$\tau_{HB} = 1/k_{HB} = 1/(k_{CR} + k_{ET}) \quad (3)$$

$$\phi_{ET} = k_{ET} \cdot \tau_{HB} \quad (4)$$

$$\phi_{CR} = k_{CR} \cdot \tau_{HB} \quad (5)$$

In RCs with native A-side cofactors, the routes by which $P^+H_A^-$ decays in the absence of ET to Q_A include spin rephasing in the initially produced singlet form of the $P^+H_A^-$ radical-pair state (i.e., $[P^+H_A^-]^1$) to produce the triplet radical pair (i.e., $[P^+H_A^-]^3$) and subsequent collapse (by CR) to give the triplet excited state of P (denoted P^R) in parallel to the decay of the singlet radical pair (by CR) to the ground state. Fig. 5 shows (potential) analogous processes for the B-side state $P^+H_B^-$ as well as for $P^+\beta^-$ on the A side. Analysis of the complex decay pathways and kinetics for the radical-pair states is beyond the scope of this work. However, we will show data indicating triplet excited state formation that support the model of the radical-pair dynamics depicted in Fig. 5. Otherwise, our results and discussion are framed in terms of Fig. 4A, a simplified form of Fig. 5, in order to focus on general trends and differences found in the competition between k_{ET} and k_{CR} among the six mutants under study.

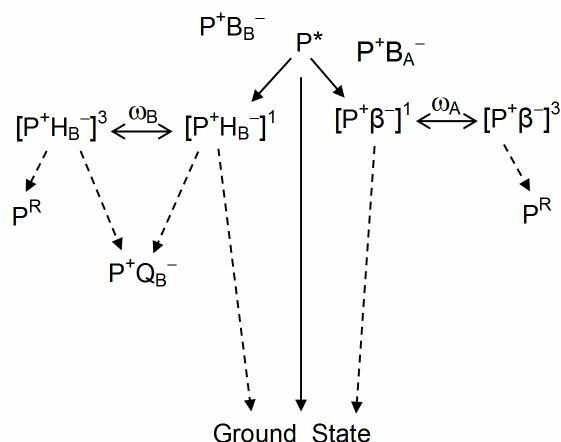


Figure 5. An elaborated scheme of processes observed in this study for the YFHV RC that includes spin rephasing and formation of the triplet radical pair and subsequent formation of the triplet excited state of P denoted P^R .

The relative free energies of the charge-separated states in WT RCs shown in Fig. 1B reflect a generally agreed-upon model derived in part from indirect measurements. One readily measured value that affects the free energies of the states relative to P^* is the P/P^+ midpoint potential. Previous work has shown that, compared to a Phe, a Tyr at either L181 or M208 lowers the P/P^+ midpoint potential by ~ 25 mV.⁴⁹ Swapping FY for YF at L181/M208 in the YFH RC results in only a ~ 10 mV lower P redox potential compared to WT (Table 2), in agreement with prior studies on the YF mutant.⁴⁹ Since M131, M144 and M145 are not located near P, we expect that among the mutants reported here, the redox potential of P will (1) not vary significantly, and (2) not be significantly different than WT. For the five new selected mutants, the P/P^+ midpoint potentials vary between 466 ± 5 mV and 475 ± 2 mV averaging only ~ 15 mV lower than 488 ± 8 mV for WT (Table 2, column 2). These values are consistent with the YF-swap and only minor additional effects upon residue changes at M131 (E or I) or at M144-M145 (IS pair). Thus, for the six mutants chosen for ultrafast studies, the basic model in Fig. 4 is

reasonably adopted. The V(M131)E mutation likely lowers the free energy of $P^+H_B^-$ by 50-100 mV (discussed in Section 3.5.6).

Table 2. Properties of WT and Selected Mutant RCs.^a

Sample	P Oxidation Potential	Q _B Occupancy (%)
WT	488 ± 8	94
YFH	478 ± 5	92
ISYFH	475 ± 2	90
E+YFH	469 ± 1	67
E+ISYFH	466 ± 5	47
I+YFH	471 ± 7	91
I+ISYFH	469 ± 5	78

^a Error bars on the oxidation potentials are obtained from replicate ($N \geq 2$) measurements. The Q_B occupancy has an error of ±5% of the reported value. Mutant nomenclature as given in Table 1.

3.5.2. $P^* \rightarrow P^+H_B^-$ Charge Separation. Fig. 6 shows ultrafast TA spectra in the visible (parts A and C) and near-infrared (parts B and D) regions for RCs containing the ISYFH and E+ISYFH mutations. The TA spectra acquired 0.5 ps after excitation are identical to those obtained for WT and are assigned to P^* . In the near infrared, the P^* spectrum features bleaching of the long-wavelength absorption band of P at 865 nm and stimulated emission from P^* extending to ~1000 nm. For all six mutants, the P^* stimulated emission decay kinetics fit well to a function consisting of the instrument response plus two exponentials plus a constant. Representative data and fits are shown in the insets to panels B and D in Fig. 6. The fits can be generally summarized as revealing (1) a shorter component (~70% amplitude) ranging between 20 and 30 ps and (2) a longer component (~30% amplitude) ranging between 150 and 300 ps. For each mutant, values returned by the fits are given in Table 3, columns 2-5. In the visible region, bleaching of the Q_x band of H_B at ~530 nm in the mutant RCs develops with a time constant also in the range of 20-30 ps (Table 4, column 2), in very good agreement with the

shorter of the two stimulated emission decay components (Table 3, column 2). On the other hand, the appearance (development) of bleaching of the 530 nm band of H_B does not contain a clear ~ 200 ps component.

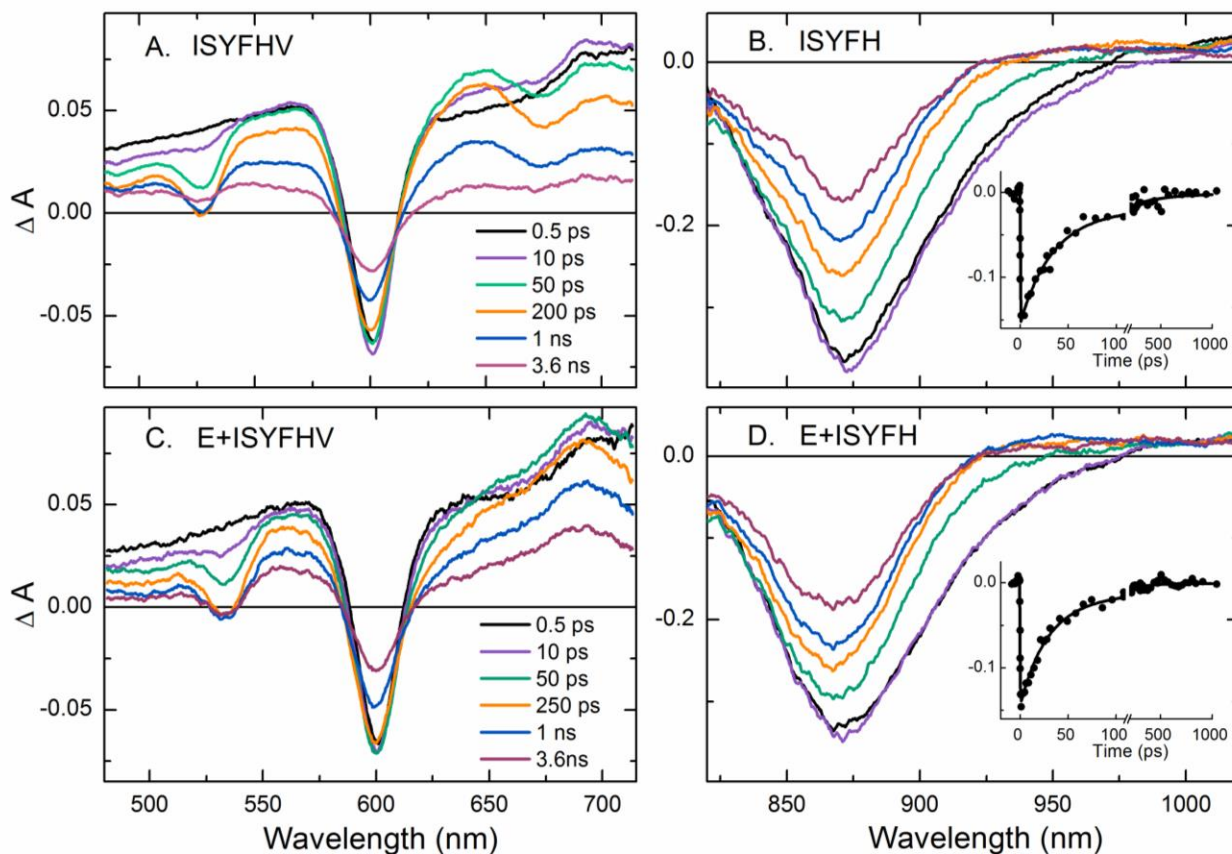


Figure 6. TA spectra and kinetics for RCs containing the ISYFH (A and B) and E+ISYFH (C and D) mutations. The Q_x region data (A and C) were acquired at the times indicated following a 130-fs, 850-nm excitation flash. The listed times for the traces in (A) also apply to (B) and those for (C) also apply to (D). In (B) and (D) the TA spectra were acquired using 130-fs, 590-nm excitation flashes. The insets in (B) and (D) show the data (filled circles) averaged in a 10-nm interval centered on the stimulated emission isosbestic point at ~ 910 nm. The solid lines are a fit to the instrument response function plus two exponentials plus a constant. The presence/absence of the W(M250)V mutation has no effect on the early photochemical events.

Table 3. P* Lifetimes and Relative Populations Determined from Stimulated Emission Decay.^a

Sample ^b	τ_{P^*} 'Active' (ps)	'Active' Fraction	τ_{P^*} 'Inactive' (ps)	'Inactive' Fraction
YFH ^c	32	0.65	210	0.35
ISYFH	32	0.81	307	0.19
E+YFH	30	0.84	154	0.16
E+ISYFH	27	0.80	159	0.20
I+YFH	23	0.73	220	0.27
I+ISYFH	27	0.74	178	0.26

^a The time constants have a typical error of $\pm 10\%$ of the reported value.

^b Nomenclature for RC mutations as given in Table 1, except that these experiments were done on mutants that do not contain the W(M250)V mutant that prevents binding of Q_A. ^c Taken from ref [8].

Table 4. P* lifetime, P⁺H_B⁻ Yield and Position of the Q_x band of H_B in Mutants.^a

Sample ^b	P* Lifetime Active Fraction (ps)	Yield of P ⁺ H _B ⁻ (%)	H _B Q _x Bleaching (nm)
YFHV	27	46	528
ISYFHV	28	31	527
E+YFHV	29	38	534
E+ISYFHV	27	34	533
I+YFHV	23	40	527
I+ISYFHV	20	37	527

^a Results pertain to the P* photochemically 'active' fraction. The time constants and yields have a typical error of $\pm 10\%$ of the reported value.

^b Nomenclature for RC mutations as given in Table 1.

Thus, the ~200-ps component found here, as found previously in many mutants, does not appear to be associated with (appreciable) charge separation but rather (primarily) with P* internal conversion to the ground state. Underscoring this analysis is a mutant in which no charge separation takes place at all and P* decays solely by internal conversion with a time constant of ~200 ps (in Deriphath; ~100 ps in LDAO).²¹ These observations are the basis of a

model we have developed of ‘active’ and ‘inactive’ populations (fractions) of P*. These populations are present in ~70:30 active:inactive ratio in many (but not all) of the YF-containing mutants we have studied to date and other mutants as well.^{25,44,50} These mutants have in common attempts to raise the free energy of P⁺B_A⁻ (ideally placing it above P*) and lower that of P⁺B_B⁻ (ideally positioning it below P*), thereby narrowing the span of the free energies of P* and the charge-separated states and making the photochemistry more sensitive to static/dynamic effects of the protein.

The presence of a nominally inactive P* population adds a facet of complexity (another fitting component) to the data analysis procedures. With all six mutants having similar P* lifetimes in the active fraction of ~20 to ~30 ps, similar yields of P⁺H_B⁻ in the active fraction are expected. Such is found, averaging to 38% yield of P⁺H_B⁻ in the active fraction (Table 4, column 3). This value is in good agreement with those reported previously for YFH and YFHV RCs.^{8,44} The results presented in this section thus show that initial P* → P⁺H_B⁻ ET takes place with nearly equal time constants (~70 ps) and yields (~40%) in the six mutants. (Note that this description is with respect to the P* active fraction, which will be the focus of the results and discussions from this point on, unless otherwise noted.) These results imply that the differences in P⁺Q_B⁻ yield found in the ms assay are rooted nearly entirely in the competition between P⁺H_B⁻ → P⁺Q_B⁻ ET versus P⁺H_B⁻ CR in the mutants, as discussed below (Section 3.5.6).

3.5.3 Evidence that Glu (M131) forms a Hydrogen Bond with H_B. Fig. 7A compares matched (to the same P* amplitude at 0.5 ps) TA spectra for the six mutants. The spectra in Fig. 7A were acquired at a delay time (~200 ps) that is equal to roughly seven 1/e multiples of the lifetime of P* in the ~70% “active” fraction and two 1/e multiples of the lifetime of the ~30% “inactive” P*. Except for the two mutants carrying the V(M131)E mutation, the spectra in Fig.

7A are essentially identical to those we have reported previously at analogous delay times for YFH and YFHV RCs.^{8,12,37} Since $P^+H_B^-$ lives for several nanoseconds (Section 3.5.6) these spectra largely – but not uniquely – reflect the TA spectrum of $P^+H_B^-$. There is a small contribution of the TA spectrum of P^* (from the inactive P^* fraction) plus TA changes due to $P^+\beta^-$ that forms on the A side in the active fraction in ~50% yield (Fig. 4). The contribution of $P^+\beta^-$ (bleaching at ~600 nm and a broad anion band between 620 and 720 nm^{43,47}) “washes out” the features of a true $P^+H_B^-$ spectrum at wavelengths longer than ~610 nm that have been documented in prior studies.²¹ However, the hallmark features of $P^+H_B^-$ are readily distinguished in Fig. 7A. For the YFHV, ISYFHV, I+YFHV and I+ISYFHV RCs, bleaching of the Q_x ground state absorption of H_B occurs at 527 nm (compared to the bleaching of H_A at 542-543 nm in WT) along with a relatively narrow H_B anion absorption at ~640 nm (compared to a broad absorption band for H_A at ~665 nm in WT).

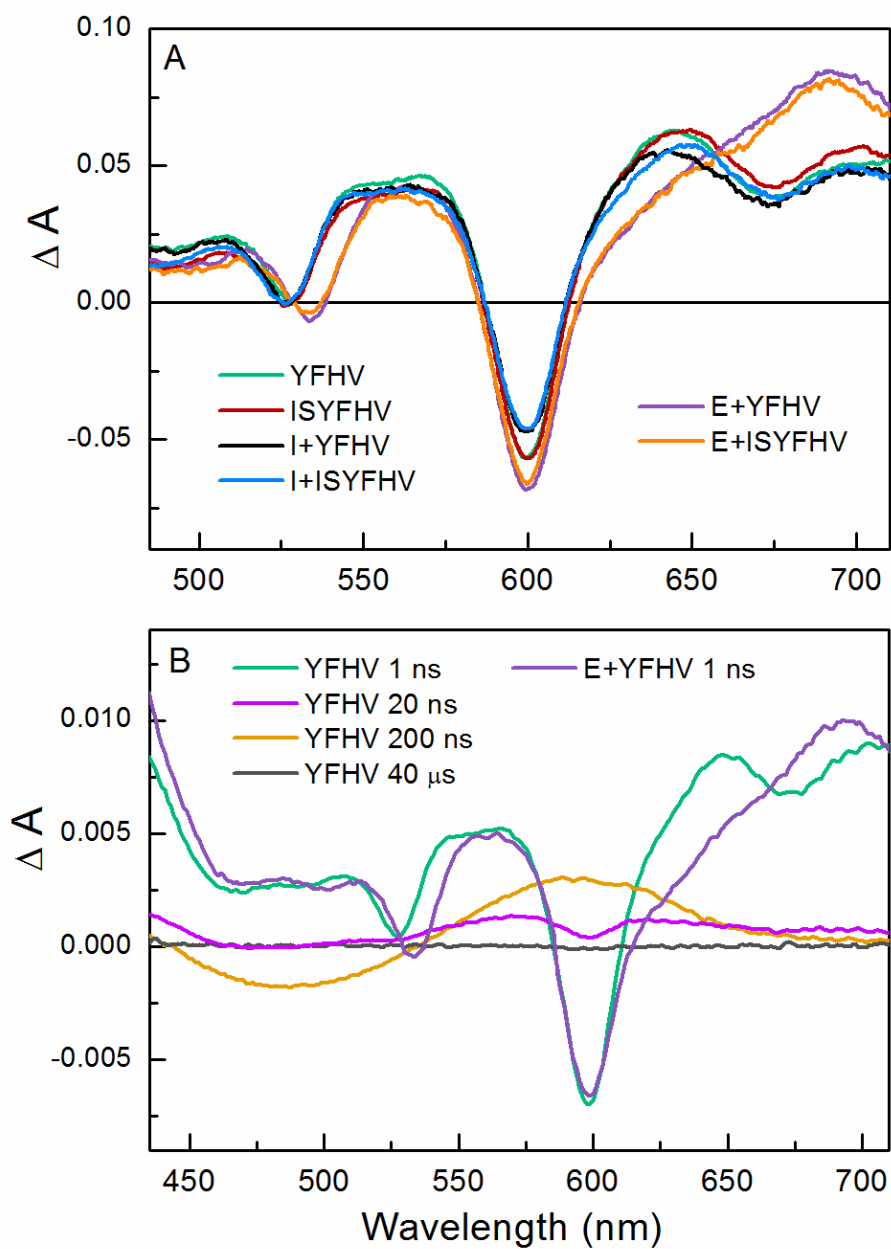


Figure 7. (A) TA spectra of state $P^+H_B^-$ (plus a contribution of $P^+\beta^-$) comparing the ground state Q_x band bleaching and anion absorption features of H_B . The spectra were taken at roughly equivalent delay times ranging from 190-250 ps obtained using the ultrafast TA spectrometer. (B) TA spectra acquired on the ns to μ s timescales following a 130-fs flash at 865 nm. The spectra at 1 ns for YFHV and E+YFHV are for state $P^+H_B^-$ (plus a contribution of $P^+\beta^-$). The spectrum at 20 ns can be assigned to the triplet excited state P^R and the spectrum at 200 ns to the triplet excited state of the carotenoid (formed by energy transfer from P^R), which has a lifetime of 4.5 μ s and thus has decayed completely by 40 μ s.

The TA spectra of E+YFHV and E+ISYFHV RCs clearly differ from the spectra of the other four RCs. Both RCs containing the V(M131)E mutation reveal a 6-7 nm red shift in Q_x band of H_B , with the bleaching at 533-534 nm rather than 527 nm. The anion band absorption is positioned near 690 nm, also clearly red-shifted compared to the other four mutants. Similar but smaller shifts of these features have been reported previously for mutants with an Asp at M131, and these changes assigned to formation of a hydrogen bond between M131Asp and the ring-V keto group of H_B .^{10,25} The same assertion can be made regarding the Glu substitution at M131 in the E+YFHV and E+ISYFHV mutants studied here. Interesting comparisons can be made concerning H_A and the C_2 symmetry-related residue Glu L104 on the A pathway. Glu L104 forms a hydrogen bond with H_A , which has a Q_x band at 542 nm and an anion band at 665 nm. Replacement of L104Glu by Leu removes this hydrogen bond and blue shifts the Q_x band of H_A , but not fully to the position of H_B at 527-528 nm.^{51,52} (Functionally, replacing the A-side L104 Glu with Leu lengthens the time constant for $P^+H_A^- \rightarrow P^+Q_A^-$ ET only slightly with no reduction of yield of $P^+Q_A^-$ reported.⁵¹) Likewise, formation of a (putative) hydrogen bond between Glu or Asp at M131 and H_B does not reposition the Q_x absorption of H_B to that of H_A at 542-543 nm. Rather, in *Rb. capsulatus*, these two situations – the ring-V keto group of non-hydrogen bonded H_A and the ring-V keto group of glutamic acid-hydrogen bonded H_B – meet in the middle between 530 and 535 nm. Clearly one can invoke participation of water molecules and other differences in the local environments and global electrostatics experienced by these pigments that could affect the strengths of the hydrogen bonds⁵³ and/or other interactions as the causes of differences in the electronic structures and spectra of H_A and H_B .

3.5.4 $P^+H_B^-$ Decay Pathways in the Absence of Q_B . The $P^+H_B^-$ CR pathways and dynamics were probed via ultrafast studies of the six mutant RCs to which terbutryn had been

added to displace Q_B . Representative time-resolved spectra obtained using the EOS spectrometer are shown in Fig. 7B for the YFHV and E+YFHV mutants. The spectra acquired at 1 ns are largely that of $P^+H_B^-$ and have features that agree with those seen in the ~ 200 ps spectra in Fig. 7A obtained using standard ultrafast techniques. In particular, the V(M131)E mutation causes a red-shift in the position of both the H_B Q_x bleaching and peak of the H_B^- anion band compared to the positions of these features for the YFHV mutant.

The time evolution of the spectra in Fig. 7B not only give a measure of the $P^+H_B^-$ lifetime in the absence of ET (~ 4 -9 ns; Section 3.5.6) but also follow the decay pathways of $P^+H_B^-$ at longer times for the YFHV mutant. At 20 ns, the H_B bleaching at 530 nm and the H_B anion band have substantially decayed as has most of the combined P and β Q_x bleaching at ~ 600 nm. The 20-ns spectrum is similar to that reported previously for the triplet excited state of P (denoted P^R) in WT RCs, which forms from $P^+H_A^-$ when ET from H_A to Q_A is blocked,⁵⁴ as described above (Section 3.5.1; Fig. 5). State P^R likely forms in the YFHV mutant at least in part via spin rephasing and CR from $P^+H_B^-$ and perhaps via similar events involving $P^+\beta^-$ on the A pathway. In the YFHV mutant, state P^R has a lifetime of ~ 100 ns and decays primarily by energy transfer to the carotenoid molecule situated near B_B (Fig. 1A), again analogous to what happens in WT RCs. The spectrum at 200 ns is assigned largely to Car^T (carotenoid triplet) and shows the expected derivative-like shape.^{55,56} Car^T has an ~ 4.5 μ s lifetime, again agreeing well with the WT RC carotenoid triplet state lifetime measured previously.^{55,56} Generally similar results are found for the other five mutants investigated in detail. Further assessment of the spin rephasing events in the $P^+H_B^-$ and $P^+\beta^-$ radical pair states (Figs. 4 and 5) in the mutants is beyond the scope of this work.

3.5.5 Q_B Occupancy in the Six Mutant RCs. Knowledge of the Q_B occupancy in the six selected mutants is a required element for determination of k_{ET} and k_{CR} (Fig. 4) via the ultrafast studies. These rate constants are readily obtained from the lifetime of $P^+H_B^-$ in the presence and in the absence of Q_B (Eqs. 1-3). Determining the $P^+H_B^-$ lifetime in the presence of Q_B requires RCs in which the Q_B site is fully occupied or that we know and correct for the fraction of RCs in which Q_B is absent.

The Q_B occupancy can be assayed by the yield of $P^+Q_B^-$ formed via ET from $P^+Q_A^-$. The mutant RCs constructed for this study lack Q_A due to the presence of the W(M250)V mutation. To restore the WT Q_A binding site, allowing determination of the extent of Q_B occupancy, derivatives of the six mutant RCs under detail study were prepared in which cassette-based mutagenesis was used to restore the native Trp residue at M250 (mutants designated E+YFH, I+YFH, ISYFH, E+ISYFH, I+ISYFH); the YFH mutant was already in hand from previous work. RCs with the native Trp at M250 are expected to contain Q_A .

$P^+Q_A^- \rightarrow P^+Q_B^-$ ET occurs with a time constant on the order of 1-100 μ s and $P^+Q_B^-$ formed in this way (i.e., from the A side) decays primarily with a time constant of ~ 0.7 s (albeit in a pH-dependent manner along with a small-amplitude longer phase).^{57,58} If the Q_B site is not fully occupied, $P^+Q_A^-$ in the Q_B -less fraction will decay by CR to the ground state with a time constant of 100-200 ms.⁵⁹ To determine the fraction of each RC sample that is Q_B -less, the P-bleaching recovery for E+YFH, I+YFH, ISYFH, E+ISYFH, I+ISYFH, YFH, and WT RCs were assayed (using the ms screening apparatus) for detection of a 100-200 ms component. Fig. 8 shows representative data for YFH and E+ISYFH, each time profile being the average of two replications spaced ~ 10 min apart to allow time for excited RCs to fully recover to the ground state between excitation flashes. The data in the insets of Fig. 8 show very little of the 100-200

ms component for YFH (high occupancy of the Q_B site) and a significant 100-200 ms phase for E+ISYFH (some loss of Q_B).

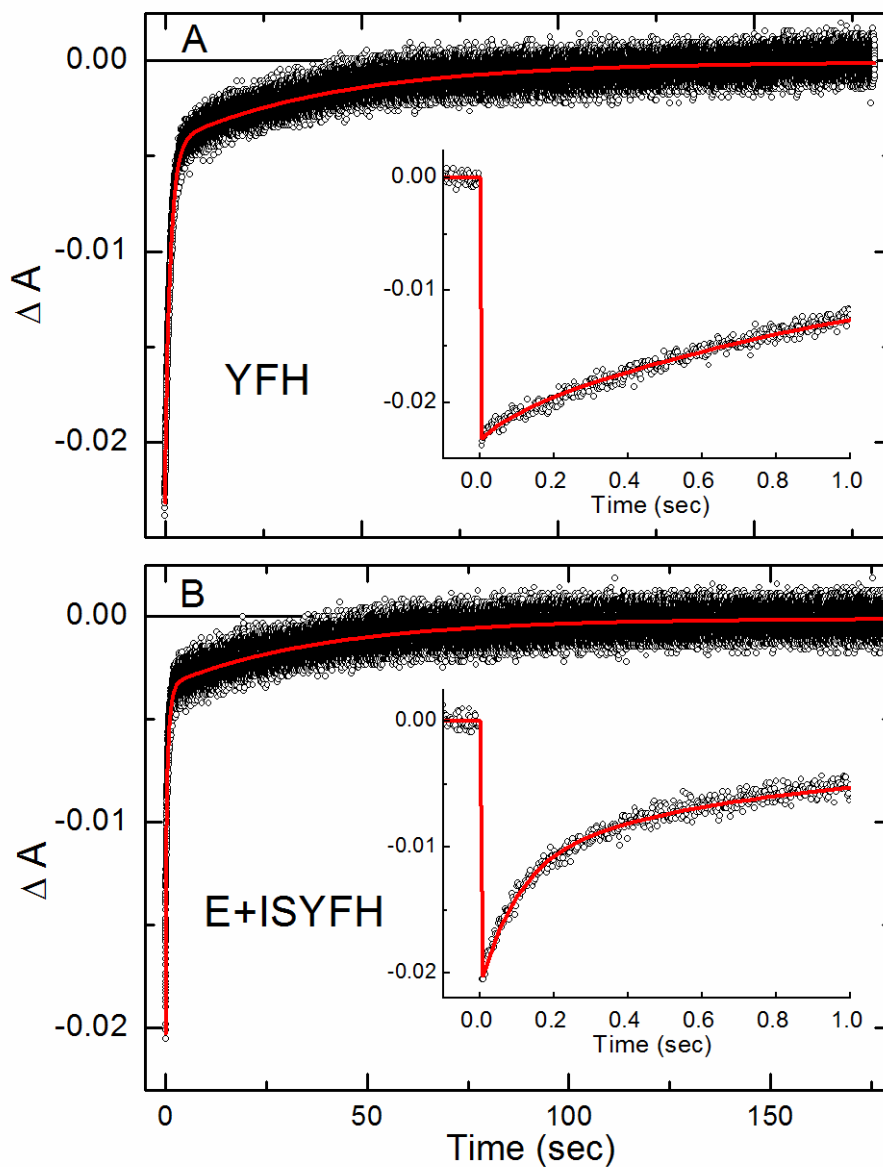


Figure 8. P-bleaching decay profile (open circles) at 850 nm for the YFH (A) and E+ISYFH (B) RCs following excitation with a 7-ns 532-nm excitation flash. The insets show the data on an expanded scale. The solid line is a fit to a function containing three exponentials. The amplitude of the 100-200 ms component is 8% in YFH and 53% in E+ISYFH and reflects the fraction of RCs in which Q_B is absent.

The Q_B occupancy was quantitated by fitting the P-bleaching decay profiles (e.g., Fig. 8) for each of the six mutants to a function containing three exponentials and a constant. Two components had a range of 1.0-1.5 s and 30-40 s that give consistently good fits for the bi-exponential decay of $P^+Q_B^-$. The third exponential reflects the 100-200 ms decay of $P^+Q_A^-$. For samples such as E+ISYFH with a significant Q_B -less fraction, the fits return a time constant of ~150 ms with this component being a free fitting parameter. In the case of E+ISYFH (Fig. 8B), the fits returned a relative amplitude of 0.53 for this component, indicating 47% Q_B occupancy. For samples such as YFH with very high Q_B occupancy, the fits would typically not reliably find such a low-amplitude phase so the time constant of the third component was fixed at 150 ms and the associated amplitude simply fit, yielding $\geq 90\%$ Q_B occupancy in all such cases (Table 2).

3.5.6 Rates and Yields of $P^+H_B^-$ Decay via Electron Transfer versus Charge Recombination. The rate of $P^+H_B^- \rightarrow P^+Q_B^-$ ET (k_{ET} in Fig. 4A and 4B) and what we term the “effective rate” of $P^+H_B^-$ CR (k_{CR}) were determined from the $P^+H_B^-$ lifetime in the presence of Q_B (τ_{HB}) and in the absence of Q_B (τ_{CR}) (Eqs. 1-3). Kinetic profiles for appearance and disappearance of bleaching of the Q_x band of H_B in all six mutants in the presence (red open circles) and absence (blue solid circles) of the Q_B -displacing terbutryn are given in Fig. 9. The H_B Q_x bleaching is at ~527 nm for YFHV, ISYFHV, I+YFHV and I+ISYFHV and is shifted to ~534 nm for E+YFHV and E+ISYFHV (see Fig. 7A). As discussed above (Section 3.5.2), as $P^+H_B^-$ forms, bleaching of the Q_x band of H_B develops with a time constant of 20-30 ps (again, reflecting the P^* lifetime in the “active” fraction) in all six mutants. This signal manifests as the initial fast decrease in absorbance (i.e., appearance of bleaching) in all the kinetic traces in Fig. 9. As $P^+H_B^-$ decays, the bleaching of the Q_x band of H_B decays on the several nanosecond timescale.

Simple visual inspection of Fig. 9 shows (1) a faster $P^+H_B^-$ decay in all mutant RCs in the presence of Q_B than in its absence, and (2) much slower $P^+H_B^-$ decay for the two mutant RCs containing Glu at M131 (parts C and D). The first point reflects the obvious fact that $P^+H_B^- \rightarrow P^+Q_B^-$ ET can and does occur in the samples that contain Q_B but cannot occur when this process is inhibited by terbutryn. The second point is particularly apparent for the samples lacking Q_B (containing terbutryn) and qualitatively indicates that the putative hydrogen bond between H_B and Glu (M131) increases the value of τ_{CR} (and decreases k_{CR}). The second point is a major finding of this work – that the replacement of the native Val with Glu at M131 significantly slows $P^+H_B^-$ CR.

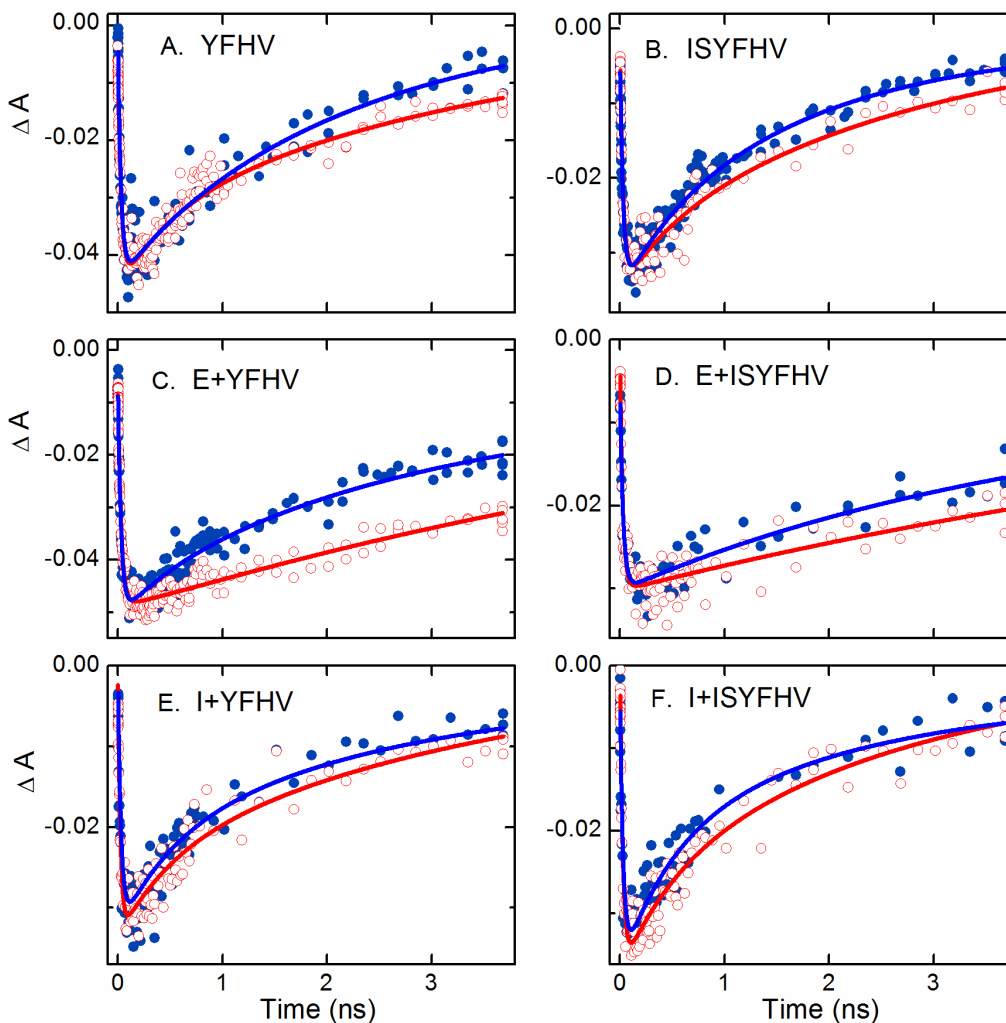


Figure 9. Representative data (open and closed circles) and non-linear fits (solid lines), of the appearance and decay of bleaching of the Q_x band of H_B (with respect to the featureless 560-570 nm transient absorption; Fig. 7A) acquired with Q_B present at the occupancies obtained via our standard RC purification protocols (blue) and with Q_B displaced by terbutryn (red).

Quantifying these observations rests on obtaining the values of τ_{HB} ($P^+H_B^-$ lifetime when Q_B is present) and τ_{CR} ($P^+H_B^-$ lifetime in the absence of Q_B) and from them τ_{ET} (Eq. 1). Determining these lifetimes has complications arising from (1) the difficult timescale involved for ultrafast TA measurements including the limited time span (~ 3.5 ns, Fig. 9), (2) the above-noted presence of a fraction of Q_B -less RCs in some samples, and (3) the presence of other

lifetime components (e.g., decay of $P^+\beta^-$) on the same general timescale. Methodical data analysis was required to address these issues and obtain the most reliable values for comparison of the six mutant RCs. For each mutant RC, two steps to obtain τ_{CR} and τ_{HB} were performed as follows.

First, for an RC to which terbutryn has been added, the time profile of the Q_x bleaching measured by ultrafast TA (i.e., each red trace in Fig. 9) was fit with a multi-exponential function to account for the 20-30-ps decay of P^* (and formation of $P^+H_B^-$), the target decay of $P^+H_B^-$, and the simultaneous decay of other states on this timescale ($P^+\beta^-$ on the A side and P^* in the inactive population). The red lines through the Q_x time-profile data in Fig. 9 reflect a typical fit for each of the six mutants. Similar fitting was done for the decay of the H_B anion band at ~640 nm (for YFHV, ISYFHV, I+YFHV and I-ISYFHV) or 690 nm (for E+YFHV and E-ISYFHV). The decay profiles in the same two wavelength regions (Q_x bleaching and anion absorption) acquired by the EOS measurements provided a second type of data set with an extended time range. These data were fit similarly to a multi-exponential function that accounted for decay of the same states on the 0.1 to 100 ns time scale and the evolution of P^R and Car^T extending to many microseconds. The resulting best-fit values for the $P^+H_B^-$ lifetime when only CR can occur (τ_{CR}) from the two wavelength regions and the two types of data sets (“standard” ultrafast TA extending to 3.5 ns and ultrafast EOS measurements extending to many microseconds) were averaged. The resultant value is given in Table 5, column 2.

Table 5. $P^+H_B^-$ Lifetimes and $P^+H_B^- \rightarrow P^+Q_B^-$ ET Yields (Φ_{ET})^a

Sample ^b	$P^+H_B^-$ τ_{CR} (ns) ^c	$P^+H_B^-$ τ_{HB} (ns) ^d	$P^+H_B^- \rightarrow P^+Q_B^-$ τ_{ET} (ns) ^e	$P^+H_B^- \rightarrow P^+Q_B^-$ Φ_{ET}	$P^+H_B^-$ charge recombination Φ_{CR}
YFHV	4.0	2.2	4.9	0.45	0.55
ISYFHV	3.7	1.6	2.8	0.57	0.43
E+YFHV	9.0	2.5	3.5	0.72	0.28
E+ISYFHV	9.0	3.2	5.0	0.64	0.36
I+YFHV	4.0	1.9	3.6	0.52	0.48
I+ISYFHV	3.6	2.1	5.0	0.42	0.58

^a The measured time constants in columns 2 and 3 have an error of $\pm 20\%$ of the values listed.

^b Nomenclature for RC mutations as given in Table 1. ^c Measured lifetime of $P^+H_B^-$ in RCs with terbutryn replacing Q_B (Eq. 2). ^d Measured lifetime of $P^+H_B^-$ in RCs with Q_B present (Eq. 3).

^e Time constant for $P^+H_B^- \rightarrow P^+Q_B^-$ ET calculated from the values in columns 2 and 3 (Eq. 1).

In the second step, the ultrafast TA data acquired for each mutant RC in its “as purified” condition were also fit using a multi-exponential function (blue lines, Fig. 9). Here the fitting function included an additional component accounting for the fraction of Q_B -less RCs in each sample. The time constant of this component was fixed at the τ_{CR} value derived above (Table 5, column 2) and its amplitude was fixed according to the fraction of Q_B -less RCs (Table 2, column 3). The values of τ_{HB} so determined from the decay of bleaching of the Q_x band of H_B and for the decay of the H_B anion band were averaged (Table 5, column 3). The time constant for $P^+H_B^- \rightarrow P^+Q_B^-$ ET (τ_{ET} ; Eq. 1) and the associated yields for ET (Φ_{ET} ; Eq. 4) and $P^+H_B^-$ CR (Φ_{CR} ; Eq. 5) were then calculated (Table 5, columns 4, 5 and 6).

These results confirm what is apparent from examination of the raw data sets in Fig. 9 – that the inherent lifetime of $P^+H_B^-$ (decay only by CR; τ_{CR}) in the two mutants carrying the Glu substitution at M131 (E+YFHV and E+ISYFHV) is about two-fold longer compared to the four mutants that have Ile or the native Val at M131 (~9 ns versus ~4 ns). This relatively long ~9 ns ‘CR lifetime’ of $P^+H_B^-$ is striking and closer to the 10-20 ns lifetime of $P^+H_A^-$ in the absence of

ET to Q_A . The calculated τ_{ET} , the time constant for $P^+H_B^- \rightarrow P^+Q_B^-$ ET, for the six mutants ranges between 2.8 and 5.0 ns with no clear pattern in relation to the mutations.

Comparing the mutants, it is clear that a Glu at M131 results in a significantly higher yield of $P^+H_B^- \rightarrow P^+Q_B^-$ ET than occurs when Ile or the native Val is at this position. In fact, on an absolute basis, substitution of a Glu at M131 results in a remarkable ~70% yield for this ET process (Fig. 4B), still below the roughly 100% attained on the native A side for the analogous reaction, but very high. The data in Table 5 indicate that a major, if not *the* major, origin of this result may be the hydrogen bond apparently created between M131E and H_B and significant attendant slowing of the CR processes of $P^+H_B^-$, thus allowing $P^+H_B^- \rightarrow P^+Q_B^-$ ET to compete more successfully. This result can be anticipated to be obtained in the case of other amino acid substitutions at M131 that form a hydrogen bond to H_B such as Asp and possibly Lys or His.

Many laboratories have reported significant effects on spectral, redox, photophysical, and ET properties of RC cofactors caused by the addition or removal of hydrogen bonds. Based on calculations on hydrogen bonding to the ring-V group of bacteriopheophytin, and the effects of adding/removing hydrogen bonds to P in the RC,⁶⁰⁻⁶² the addition of a hydrogen bond to H_B is expected to lower the free energy of $P^+H_B^-$ (stabilize the state) by as much as ~100 mV. This shift could affect the rate of CR in a number of ways, as has been discussed previously for $P^+H_B^-$ -decay^{12,23} and for $P^+H_A^-$ decay^{28,63-67} or $P^+\beta^-$ decay^{43,47,48} on the A side. Such studies suggest that the manner in which the free energy position of $P^+H_B^-$ affects its CR rate is likely more complex than simply the free energy gap from the ground state and thus the position on the (Marcus) rate versus free energy curve. Instead this CR process, like the decay of $P^+H_A^-$ or $P^+\beta^-$ on the A side, likely involves thermal and/or quantum mechanical mixing with a higher energy state (e.g., $P^+B_B^-$) that has an inherently faster deactivation rate. The effects on ET versus CR on

the A and B branches will not parallel exactly owing to specific differences, including generally higher free energies of analogous charge-separated states on the B side versus the A side, different free energy spacing of the states, and different reorganization energies.

The decrease in the rate constant for CR and increase in the yield of ET due to the V(M131)E mutation is also accompanied by an apparent partial loss of Q_B , at least under our normal RC purification protocols. At first glance these two effects would seem to offset each other in progress towards the goal of attaining the highest possible yield of B-side charge separation to produce $P^+Q_B^-$. Yet, these results may not reflect the level of occupancy of the Q_B site when the RC is present in its native membrane environment.

3.6. Conclusions. Time-resolved spectroscopy encompassing 15 orders of magnitude was used to characterize excited-state, charge-separation and charge-recombination dynamics in a set of six RCs bearing mutations near H_B and/or Q_B . These mutant RCs are found to have similar P^* lifetimes and yields of initial B-side $P^* \rightarrow P^+H_B^-$ charge separation. However, the mutations elicit varying effects on the CR lifetime of $P^+H_B^-$, the rates and yield of $P^+H_B^- \rightarrow P^+Q_B^-$ ET, and Q_B binding. Specifically, we have shown that mutation of the native Val at M131 to a Glu most likely results in formation of a hydrogen bond between the introduced Glu and H_B , as inferred from the red-shifted position of the Q_x band and anion band of H_B . Additionally, we find that a Glu at M131 slows the CR processes of $P^+H_B^-$ by a factor of two and thus boosts the yield of $P^+H_B^- \rightarrow P^+Q_B^-$ ET to ~70%.

This study shows that the balance between ET to produce $P^+Q_B^-$ and unwanted CR can be markedly improved by a single amino acid change. Interestingly, the substitution with greatest effect uncovered via saturation mutagenesis in a directed-evolution and fast-screening approach is the incorporation near H_B of a Glu at M131. This site is related by pseudo C_2 -symmetry to

L104 that houses Glu near the photoactive H_A in the native RC. It is noteworthy that such a symmetry effect should not be viewed as an expected norm, given the many differences between the A and B sides when viewed locally or globally. For example, in a prior study focused on the first step of B-side charge separation (branched decay of P^*), random mutation of sites near B_B revealed that substitutions with the greatest impact on initial ET to the B side were ionizable or polar residues.³⁷ Some of these residues would have been the least favored choices based on current knowledge of A-side (or B-side) architecture using a traditional site-directed approach generating select mutants one at a time. Thus, the results described herein add to those of prior work on B-side transmembrane charge separation and represent another step towards attaining a fundamental molecular-level understanding of how intricate differences in protein-cofactor interactions on the A- versus B-sides of the RC underlie differences in functionality. Such knowledge will be useful for the design of efficient, bioinspired multistep ET sequences for solar-energy conversion.

Acknowledgements

This work was supported by grant DE-FG-02-09ER16116 (to CK, DH and PL) from DOE Office of Basic Energy Sciences, Division of Chemical Sciences, Geosciences, and Biosciences. Argonne, a U.S. Department of Energy Office of Science laboratory, is operated under Contract No. DE-AC02-06CH11357. KF was supported by the National Science Foundation Graduate Research Fellowship under Grant No. DGE-1143954. CEZ and RJM were participants in DOE-sponsored summer internship programs for undergraduate students.

References

- (1) Deisenhofer, J.; Epp, O.; Miki, K.; Huber, R.; Michel, H. Structure of the Protein Subunits in the Photosynthetic Reaction Center from *Rhodospseudomonas viridis* at 3 Å Resolution. *Nature* **1985**, *318*, 618-624.
- (2) Allen, J. P.; Feher, G.; Yeates, T. O.; Komiya, H.; Rees, D. C. Structure of the Reaction Center from *Rhodobacter sphaeroides* R-26: The Cofactors. *Proc. Natl. Acad. Sci. U.S.A.* **1987**, *84*, 5730-5734.
- (3) Chang, C.-H.; El-Kabbani, O.; Tiede, D. M.; Norris, J. R.; Schiffer, M. The Structure of the Membrane-Bound Photosynthetic Reaction Center from *Rhodobacter sphaeroides* R-26. *Proc. Natl. Acad. Sci. U.S.A.* **1991**, *30*, 5352-5360.
- (4) Ermler, U.; Fritsch, G.; Buchanan, S. K.; Michel, H. Structure of the Photosynthetic Reaction Centre from *Rhodobacter sphaeroides* at 2.65 Å Resolution: Cofactors and Protein-Cofactor Interactions. *Structure* **1994**, *2*, 925-936.
- (5) Heller, B. A.; Holten, D.; Kirmaier, C. Control of Electron Transfer to the L-side Versus the M-side of the Photosynthetic Reaction Center. *Science* **1995**, *269*, 940-945.
- (6) Kirmaier, C.; Weems, D.; Holten, D. M-side Electron Transfer in Reaction Center Mutants with a Lysine near the Nonphotoactive B Bacteriochlorophyll. *Biochemistry* **1999**, *38*, 11516-11530.
- (7) Katilius, E.; Turanchik, T.; Lin, S.; Taguchi, A. K. W.; Woodbury, N. W. B-Side Electron Transfer in a *Rhodobacter sphaeroides* Reaction Center Mutant in Which the B-Side Monomer Bacteriochlorophyll is Replaced with Bacteriopheophytin. *J. Phys. Chem. B* **1999**, *103*, 7386-7389.
- (8) Kirmaier, C.; He, C.; Holten, D. Manipulating the Direction of Electron Transfer in the Bacterial Reaction Center by Swapping Phe for Tyr Near BChl_M (L181) and Tyr for Phe Near BChl_L (M208). *Biochemistry* **2001**, *40*, 12132-12139.
- (9) Kirmaier, C.; Laible, P. D.; Czarnecki, K.; Hata, A. N.; Hanson, D. K.; Bocian, D. F.; Holten, D. Comparison of M-side Electron Transfer in *Rb. sphaeroides* and *Rb. capsulatus* Reaction Centers. *J. Phys. Chem. B* **2002**, *106*, 1799-1808.
- (10) Kirmaier, C.; Cua, A.; He, C.; Holten, D.; Bocian, D. F. Probing M-Branch Electron Transfer and Cofactor Environment in the Bacterial Photosynthetic Reaction Center by the Addition of a Hydrogen Bond to the M-side Bacteriopheophytin. *J. Phys. Chem. B* **2002**, *106*, 495-503.
- (11) de Boer, A. L.; Neerken, S.; de Wijn, R.; Permentier, H. P.; Gast, P.; Vijgenboom, E.; Hoff, A. J. B-branch electron transfer in reaction centers of *Rhodobacter sphaeroides* assessed with site-directed mutagenesis. *Photosynth. Res.* **2002**, *71*, 221-239.
- (12) Kirmaier, C.; Laible, P. D.; Hanson, D. K.; Holten, D. B-side Charge Separation in Bacterial Photosynthetic Reaction Centers: Nanosecond-Timescale Electron Transfer from H_B⁻ to Q_B. *Biochemistry* **2003**, *42*, 2016-2024.
- (13) Katilius, E.; Babendure, J. L.; Katiliene, Z.; Lin, S.; Taguchi, A. K.; Woodbury, N. W. Manipulations of the B-Side Charge-Separated States' Energetics in the *Rhodobacter sphaeroides* Reaction Center. *J. Phys. Chem. B* **2003**, *107*, 12029-12034.
- (14) Wakeham, M. C.; Goodwin, M. G.; McKibbin, C.; Jones, M. R. Photoaccumulation of the P⁺Q_B⁻ radical pair state in purple bacterial reaction centres that lack the Q_A ubiquinone. *Febs Lett* **2003**, *540*, 234-240.

- (15) Kirmaier, C.; Laible, P. D.; Hanson, D. K.; Holten, D. B-side electron transfer to form $P^+H_B^-$ in reaction centers from the F(L181)Y/Y(M208)F mutant of *Rhodobacter capsulatus*. *J. Phys. Chem. B* **2004**, *108*, 11827-11832.
- (16) Wakeham, M. C.; Breton, J.; Nabedryk, E.; Jones, M. R. Formation of a semiquinone at the Q_B site by A- or B-branch electron transfer in the reaction center from *Rhodobacter sphaeroides*. *Biochemistry* **2004**, *43*, 4755-4763.
- (17) Breton, J.; Wakeham, M. C.; Fyfe, P. K.; Jones, M. R.; Nabedryk, E. Characterization of the bonding interactions of $Q(B)$ upon photoreduction via A-branch or B-branch electron transfer in mutant reaction centers from *Rhodobacter sphaeroides*. *Biochimica et Biophysica Acta* **2004**, *1656*, 127-138.
- (18) Wakeham, M. C.; Jones, M. R. Rewiring Photosynthesis: Engineering Wrong-Way Electron Transfer in the Purple Bacterial Reaction Center. *Biochem Soc T* **2005**, *133*, 851-857.
- (19) Frolov, D.; Wakeham, M. C.; Andrizhiyevskaya, E. G.; Jones, M. R.; van Grondelle, R. Investigation of B-branch electron transfer by femtosecond time resolved spectroscopy in a *Rhodobacter sphaeroides* reaction centre that lacks the Q_A ubiquinone. *Biochim. Biophys. Acta* **2005**, *1707*, 189-198.
- (20) Paddock, M. L.; Chang, C.; Xu, Q.; Abresch, E. C.; Axelrod, H. L.; Feher, G.; Okamura, M. Y. Quinone (Q_B) reduction by B-branch electron transfer in mutant bacterial reaction centers from *Rhodobacter sphaeroides*: Quantum efficiency and X-ray structure. *Biochemistry* **2005**, *44*, 6920-6928.
- (21) Chuang, J. I.; Boxer, S. G.; Holten, D.; Kirmaier, C. High yield of M-side electron transfer in mutants of *Rhodobacter capsulatus* reaction centers lacking the L-side bacteriopheophytin. *Biochemistry* **2006**, *45*, 3845-3851.
- (22) Paddock, M. L.; Flores, M.; Isaacson, R.; Chang, C.; Abresch, E. C.; Selvaduray, P.; Okamura, M. Y. Trapped conformational states of semiquinone ($D(+center dot)Q(B)(-center dot)$) formed by B-Branch electron transfer at low temperature in *Rhodobacter sphaeroides* reaction centers. *Biochemistry* **2006**, *45*, 14032-14042.
- (23) Kee, H. L.; Laible, P. D.; Bautista, J. A.; Hanson, D. K.; Holten, D.; Kirmaier, C. Determination of the rate and yield of B-side quinone reduction in *Rhodobacter capsulatus* reaction centers. *Biochemistry* **2006**, *45*, 7314-7322.
- (24) Carter, B.; Boxer, S. G.; Holten, D.; Kirmaier, C. Trapping the $P^+B_L^-$ Initial Intermediate State of Charge Separation in Photosynthetic Reaction Centers from *Rhodobacter capsulatus*. *Biochemistry* **2009**, *48*, 2571-2573.
- (25) Carter, B.; Boxer, S. G.; Holten, D.; Kirmaier, C. Photochemistry of a Bacterial Photosynthetic Reaction Center Missing the Initial Bacteriochlorophyll Electron Acceptor. *J. Phys. Chem. B* **2012**, *116*, 9971-9982.
- (26) Parson, W. W.; Chu, Z. T.; Warshel, A. Electrostatic Control of Charge Separation in Bacterial Photosynthesis. *Biochim. Biophys. Acta* **1990**, *1017*, 251-272.
- (27) Arlt, T.; Schmidt, S.; Kaiser, W.; Lauterwasser, C.; Meyer, M.; Scheer, H.; Zinth, W. The Accessory Bacteriochlorophyll: A Real Electron Carrier in Primary Photosynthesis. *Proc. Natl. Acad. Sci. U.S.A.* **1993**, *90*, 11757-11761.
- (28) Woodbury, N. W.; Peloquin, J. M.; Alden, R. G.; Lin, X.; Lin, S.; Taguchi, A. K. W.; Williams, J. C.; Allen, J. P. Relationship between Thermodynamics and Mechanism during Photoinduced Charge Separation in Reaction Centers from *Rhodobacter sphaeroides*. *Biochemistry* **1994**, *33*, 8101-8112.

- (29) Bixon, M.; Jortner, J.; Michel-Beyerle, M. E. A Kinetic Analysis of the Primary Charge Separation in Bacterial Photosynthesis. Energy Gaps and Static Heterogeneity. *Chem. Phys.* **1995**, *197*, 389-404.
- (30) Alden, R. G.; Parson, W. W.; Chu, Z. T.; Warshel, A. Orientation of the OH Dipole of Tyrosine (M)210 and Its Effect on Electrostatic Energies in Photosynthetic Bacterial Reaction Centers. *J. Phys. Chem.* **1996**, *100*, 16761-16770.
- (31) Gunner, M. R.; Nicholls, A.; Honig, B. Electrostatic Potentials in *Rhodospseudomonas viridis* Reaction Centers: Implications for the Driving Force and Directionality of Electron Transfer. *J. Phys. Chem.* **1996**, *100*, 4277-4291.
- (32) Holzwarth, A. R.; Muller, M. G. Energetics and Kinetics of Radical Pairs in Reaction Centers from *Rhodobacter Sphaeroides*. A Femtosecond Transient Absorption Study. *Biochemistry* **1996**, *35*, 11802-11831.
- (33) Shuvalov, V. A.; Yakovlev, A. G. Energy level of P+B⁻ with respect to P* found from recombination fluorescence measurements in pheophytin modified reaction centers. *Biol Membrane* **1998**, *15*, 455-460.
- (34) Hartwich, G.; Lossau, H.; Michel-Beyerle, M. E.; Ogrodnik, A. Nonexponential fluorescence decay in reaction centers of *Rhodobacter sphaeroides* reflecting dispersive charge separation up to 1 ns. *J. Phys. Chem. B* **1998**, *102*, 3815-3820.
- (35) Zinth, W.; Wachtveitl, J. The first picoseconds in bacterial photosynthesis - Ultrafast electron transfer for the efficient conversion of light energy. *Chemphyschem* **2005**, *6*, 871-880.
- (36) Kakitani, Y.; Hou, A.; Miyasako, Y.; Koyama, Y.; Nagae, H. Rates of the initial two steps of electron transfer in reaction centers from *Rhodobacter sphaeroides* as determined by singular-value decomposition followed by global fitting. *Chem. Phys. Lett.* **2010**, *492*, 142-149.
- (37) Faries, K. M.; Kressel, L. L.; Wander, M. J.; Holten, D.; Laible, P. D.; Kirmaier, C.; Hanson, D. K. High Throughput Engineering to Revitalize a Vestigial Electron Transfer Pathway in Bacterial Photosynthetic Reaction Centers. *J. Biol. Chem.* **2012**, *287*, 8507-8514.
- (38) Nabedryk, E.; Allen, J. P.; Taguchi, A. K. W.; Williams, J. C.; Woodbury, N. W.; Breton, J. Fourier-Transform Infrared Study of the Primary Electron-Donor in Chromatophores of *Rhodobacter sphaeroides* with Reaction Centers Genetically-Modified at Residue-M160 and Residue-L131. *Biochemistry* **1993**, *32*, 13879-13885.
- (39) Muh, F.; Williams, J. C.; Allen, J. P.; Lubitz, W. A Conformational Change of the Photoactive Bacteriopheophytin in Reaction Centers from *Rhodobacter sphaeroides*. *Biochemistry* **1998**, *37*, 13066-13074.
- (40) Coleman, W. J.; Youvan, D. C. Atavistic Reaction-Center. *Nature* **1993**, *366*, 517-518.
- (41) Bylina, E. J.; Jovine, R. V. M.; Youvan, D. C. A Genetic System for Rapidly Assessing Herbicides That Compete for the Quinone Binding-Site of Photosynthetic Reaction Centers. *Bio-Technology* **1989**, *7*, 69-74.
- (42) Saggi, M.; Carter, B.; Zhou, X.; Faries, K. M.; Cegelski, L.; Holten, D.; Boxer, S. G.; Kirmaier, C. Putative Hydrogen Bond to Tyrosine M208 in Photosynthetic Reaction Centers from *Rhodobacter capsulatus* Significantly Slows Primary Charge Separation. *J. Phys. Chem. B* **2014**, in press: DOI 10.1021/jp503422c.

- (43) Kirmaier, C.; Gaul, D.; DeBey, R.; Holten, D.; Schenck, C. C. Charge Separation in a Reaction Center Incorporating Bacteriochlorophyll in Place of Photoactive Bacteriopheophytin. *Science* **1991**, *251*, 922-927.
- (44) Kirmaier, C.; Laible, P. D.; Hinden, E.; Hanson, D. K.; Holten, D. Detergent Effects on Primary Charge Separation in Wild-Type and Mutant *Rhodobacter capsulatus* Reaction Centers. *Chem. Phys.* **2003**, *294*, 305-318.
- (45) Laible, P. D.; Kirmaier, C.; Udawatte, C. S. M.; Hofman, S. J.; Holten, D.; Hanson, D. K. Quinone Reduction via Secondary B-branch Electron Transfer in Mutant Bacterial Reaction Centers. *Biochemistry* **2003**, *42*, 1718-1730.
- (46) Coleman, W. J.; Bylina, E. J.; Aumeier, W.; Siegl, J.; Eberl, U.; Heckmann, R.; Ogrodnik, A.; Michel-Beyerle, M. E.; Youvan, D. C. Influence of Mutagenic Replacements of Tryptophan M250 on Electron Transfer Rates Involving Primary Quinone in Reaction Centers of *Rhodobacter capsulatus*. In *Structure and Function of Bacterial Photosynthetic Reaction Centers*; Michel-Beyerle, M. E., Ed.; Springer-Verlag: New York, 1990; pp 273-281.
- (47) Heller, B. A.; Holten, D.; Kirmaier, C. Effects of Asp Residues Near the L-side Pigments in Bacterial Reaction Centers. *Biochemistry* **1996**, *35*, 15418-15427.
- (48) Kirmaier, C.; Laporte, L.; Schenck, C. C.; Holten, D. The Nature and Dynamics of the Charge-Separated Intermediate in Reaction Centers in Which Bacteriochlorophyll Replaces the Photoactive Bacteriopheophytin .2. The Rates and Yields of Charge Separation and Recombination. *J. Phys. Chem.* **1995**, *99*, 8910-8917.
- (49) Jia, Y.; DiMagno, T. J.; Chan, C.-K.; Wang, Z.; Du, M.; Hanson, D. K.; Schiffer, M.; Norris, J. R.; Fleming, G. R.; Popov, M. S. Primary Charge Separation in Mutant Reaction Centers of *Rhodobacter capsulatus*. *J. Phys. Chem.* **1993**, *97*, 13180-13191.
- (50) Chuang, J. I.; Boxer, S. G.; Holten, D.; Kirmaier, C. Temperature Dependence of Electron Transfer to the M-side Bacteriopheophytin in *Rhodobacter capsulatus* Reaction Centers. *J. Phys. Chem. B* **2008**, *112*, 5487-5499.
- (51) Bylina, E. J.; Kirmaier, C.; McDowell, L. M.; Holten, D.; Youvan, D. C. Influence of an Amino Acid Residue on the Optical Properties and Electron Transfer Dynamics of a Photosynthetic Reaction Center Complex. *Nature* **1988**, *336*, 182-184.
- (52) Kirmaier, C.; Laporte, L.; Schenck, C. C.; Holten, D. The Nature and Dynamics of the Charge-Separated Intermediate in Reaction Centers in Which Bacteriochlorophyll Replaces the Photoactive Bacteriopheophytin .1. Spectral Characterization of the Transient State. *J. Phys. Chem.* **1995**, *99*, 8903-8909.
- (53) Palaniappan, V.; Bocian, D. Resonance Raman Spectroscopic Evidence for Dielectric Asymmetry in Bacterial Photosynthetic Reaction Centers. *J. Am. Chem. Soc.* **1995**, *117*, 3647-3648.
- (54) Parson, W. W.; Clayton, R. K.; Cogdell, R. J. Excited States of Photosynthetic Reaction Centers at Low Redox Potentials. *Biochimica et Biophysica Acta* **1975**, *387*, 265-278.
- (55) Monger, T. G.; Cogdell, R. J.; Parson, W. W. Triplet-States of Bacteriochlorophyll and Carotenoids in Chromatophores of Photosynthetic Bacteria. *Biochim. Biophys. Acta* **1976**, *449*, 136-153.
- (56) Arellano, J. B.; Melo, T. B.; Fyfe, P. K.; Cogdell, R. J.; Naqvi, K. R. Multichannel flash spectroscopy of the reaction centers of wild-type and mutant *Rhodobacter sphaeroides*: Bacteriochlorophyll(B)-mediated interaction between the carotenoid triplet and the special pair. *Photochem. Photobiol.* **2004**, *79*, 68-75.

- (57) Kleinfeld, D.; Okamura, M. Y.; Feher, G. Electron Transfer in Reaction Centers of *Rhodospseudomonas sphaeroides*. I. Determination of the Charge Recombination Pathway of $D^+Q_AQ_B^-$ and Free Energy and Kinetic Relations Between the Acceptor States $Q_A^-Q_B$ and $Q_AQ_B^-$. *Biochim. Biophys. Acta* **1984**, *766*, 126-140.
- (58) Sebban, P.; Maroti, P.; Hanson, D. K. Electron and Proton-Transfer to the Quinones in Bacterial Photosynthetic Reaction Centers - Insight from Combined Approaches of Molecular Genetics and Biophysics. *Biochimie* **1995**, *77*, 677-694.
- (59) Arata, H.; Parson, W. W. Delayed Fluorescence from Rhodospseudomonas-Sphaeroides Reaction Centers - Enthalpy and Free-Energy Changes Accompanying Electron-Transfer from P-870 to Quinones. *Biochim. Biophys. Acta* **1981**, *638*, 201-209.
- (60) Michel-Beyerle, M. E.; Plato, M.; Deisenhofer, J.; Michel, H.; Bixon, M.; Jortner, J. Unidirectionality of Charge Separation in Reaction Centers of Photosynthetic Bacteria. *Biochim. Biophys. Acta* **1988**, *932*, 52-70.
- (61) Allen, J. P.; Williams, J. C. Relationship Between the Oxidation Potential of the Bacteriochlorophyll Dimer and Electron Transfer in Photosynthetic Reaction Centers. *J Bioenerg Biomembr* **1995**, *27*, 275-283.
- (62) Ivancich, A.; Artz, K.; Williams, J. C.; Allen, J. P.; Mattioli, T. A. Effects of Hydrogen Bonds on the Redox Potential and Electronic Structure of the Bacterial Primary Electron Donor. *Biochemistry* **1998**, *37*, 11812-11820.
- (63) Gibasiewicz, K.; Pajzderska, M.; Potter, J. A.; Fyfe, P. K.; Dobek, A.; Brettel, K.; Jones, M. R. Mechanism of Recombination of the $P^+H_A^-$ Radical Pair in Mutant *Rhodobacter sphaeroides* Reaction Centers with Modified Free Energy Gaps Between $P^+B_A^-$ and $P^+H_A^-$. *J. Phys. Chem. B* **2011**, *115*, 13037-13050.
- (64) Gibasiewicz, K.; Pajzderska, M.; Dobek, A.; Karolczak, J.; Burdzinski, G.; Brettel, K.; Jones, M. R. Analysis of the temperature-dependence of $P^+H_A^-$ charge recombination in the *Rhodobacter sphaeroides* reaction center suggests nanosecond temperature-independent protein relaxation. *Phys Chem Chem Phys* **2013**, *15*, 16321-16333.
- (65) Woodbury, N. W.; Parson, W. W. Nanosecond Fluorescence from Isolated Photosynthetic Reaction Centers of *Rhodospseudomonas sphaeroides*. *Biochim. Biophys. Acta* **1984**, *767*, 345-361.
- (66) Tang, C.-K.; Williams, J. C.; Taguchi, A. K. W.; Allen, J. P.; Woodbury, N. W. $P^+H_A^-$ Charge Recombination Rate Constant in *Rhodobacter sphaeroides* Reaction Centers is Independent of P/P^+ Midpoint Potential. *Biochemistry* **1999**, *38*, 8794-8799.
- (67) Laporte, L.; McDowell, L. M.; Kirmaier, C.; Schenck, C. C.; Holten, D. Insights into the Factors Controlling the Rates of the Deactivation Processes That Compete with Charge Separation in Photosynthetic Reaction Centers. *Chem. Phys.* **1993**, *176*, 615-629.

Chapter 5: Optimizing Multi-Step B-side Charge Separation in Photosynthetic Reaction Centers from *Rhodobacter capsulatus*

Reprinted with permission from Faries, K.M.; Kressel, L. L.; Dylla, N.P.; Wander, M.J.; Hanson, D.K.; Holten, D.; Laible, P.D.; Kirmaier, C. (2016) Optimizing multi-step B-side charge separation in photosynthetic reaction centers from *Rhodobacter capsulatus*. *Biochimica et Biophysica Acta, Bioenergetics*, 1857, 150-159.

Abstract

Using high-throughput methods for mutagenesis, protein isolation and charge-separation functionality, we have assayed 40 *Rhodobacter capsulatus* reaction center (RC) mutants for their $P^+Q_B^-$ yield (P is a dimer of bacteriochlorophylls and Q is a ubiquinone) as produced using the normally inactive B-side cofactors B_B and H_B (where B is a bacteriochlorophyll and H is a bacteriopheophytin). Two sets of mutants explore all possible residues at M131 (M polypeptide, native residue Val near H_B) in tandem with either a fixed His or a fixed Asn at L181 (L polypeptide, native residue Phe near B_B). A third set of mutants explores all possible residues at L181 with a fixed Glu at M131 that can form a hydrogen bond to H_B . For each set of mutants, the results of a rapid millisecond screening assay that probes the yield of $P^+Q_B^-$ are compared among that set and to the other mutants reported here or previously. For a sub-set of eight mutants, the rate constants and yields of the individual B-side electron transfer processes are determined via transient absorption measurements spanning 100 fs to 50 μ s. The resulting ranking of mutants for their yield of $P^+Q_B^-$ from ultrafast experiments is in good agreement with that obtained from the millisecond screening assay, further validating the efficient, high-throughput screen for B-side transmembrane charge separation. Results from mutants that individually show progress toward optimization of $P^+H_B^- \rightarrow P^+Q_B^-$ electron transfer or initial $P^* \rightarrow P^+H_B^-$ conversion highlight unmet challenges of optimizing both processes simultaneously.

1. Introduction

Electron transfer (ET) in wild-type (WT) photosynthetic bacterial reaction centers (RCs) proceeds with near unity yield in successive steps from the excited state of a dimer (P) of bacteriochlorophylls (BChl or B) to A-side cofactors B_A , H_A and Q_A , which are a BChl, a bacteriopheophytin (BPh or H) and a quinone (Q), respectively (Figure 1). These cofactors are embedded in macroscopic mirror-image L- and M- polypeptides, both having five alpha helices that span the photosynthetic membrane [1-4]. Conversion of P^* to $P^+Q_A^-$ is complete in less than a nanosecond and is followed by $P^+Q_A^- \rightarrow P^+Q_B^-$ ET on the microsecond timescale. Two rounds of A-side charge separation followed by ET to Q_B and proton uptake convert Q_B to a quinol that diffuses out of the RC. Electron transfer from P^* to the normally inactive H_B cofactor was first obtained more than two decades ago. In the time since, mutants have both improved on the initially obtained very low yield of $P^* \rightarrow P^+H_B^-$ ET and demonstrated $P^+H_B^- \rightarrow P^+Q_B^-$ ET [5-27]. However, replicating the efficiency of A-side charge separation is still a significant challenge.

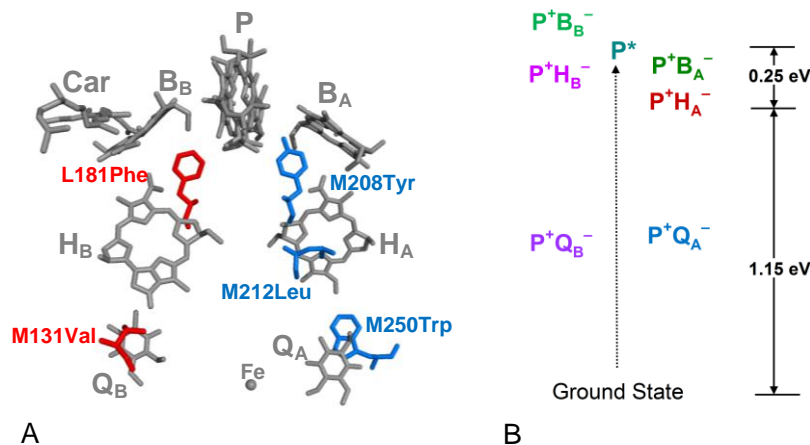


Figure 1. (A) Arrangement of *R. capsulatus* RC cofactors (gray) based on the *R. sphaeroides* RC crystal structure (PDB code 1RG5). The native amino acids in red were subject to saturation mutagenesis while the amino acids in blue are sites of background mutations common to all RCs studied in this work: (M208Tyr → Phe, M212Leu → His, M250Trp → Val). (B) Working model for the free energies of the charge separated states in WT RCs.

We have developed streamlined semi-random mutagenesis to obtain greater numbers of *Rhodobacter (R.) capsulatus* mutant RCs that are competent in overall B-side $P^* \rightarrow P^+Q_B^-$ charge separation coupled with an efficient spectroscopic assay that screens the mutants on the millisecond-timescale for their yield of $P^+Q_B^-$ as obtained solely via B-side charge separation [28, 29]. The normal course of A-side reduction of Q_B is defeated by a platform W(M250)V mutation (native Trp changed to a Val), which prevents binding of quinone in the Q_A pocket (Figure 1A) [30]. (See Table 1 for nomenclature.) In RCs bearing this “V” mutation, $P^+Q_B^-$ is obtained via ET from P^* to the B-side cofactors perforce. Two other background mutations denoted “F” and “H” are employed. The first indicates replacement of Tyr M208 with Phe. Much theoretical and experimental work has indicated that the native Tyr at M208 (Figure 1B) is key in facilitating initial A-side charge separation by poising the free energy of $P^+B_A^-$ between that of P^* and $P^+H_A^-$ [27, 31, 32]. A Phe at this position results in a reduced yield of $P^+H_A^-$ [6]. With the “H” mutation, a His replaces Leu at M212. This results in incorporation of a BChl [33], denoted β , in place of H_A and makes spectroscopic quantitation of H_B reduction in the 530-550 nm window straightforward because overlapping absorption changes due to ET to H_A or bandshifts associated with H_A are eliminated.

Table 1. Nomenclature of Mutant RCs.

Name ^a	Mutations
WT	None
V(M131)X+NFHV	X = all possible amino acids; NFHV as below
V(M131)X+HFHV	X = all possible amino acids; HFHV as below
E+F(L181)X+FHV	X = all possible amino acids; E and FHV as below
YFHV	F(L181)Y-Y(M208)F-L(M212)H-W(M250)V
E+YFHV	V(M131)E-YFHV
NFHV	F(L181)N-Y(M208)F-L(M212)H-W(M250)V
E+NFHV	V(M131)E-NFHV
HFHV	F(L181)H-Y(M208)F-L(M212)H-W(M250)V
E+HFHV	V(M131)E-HFHV
FHV	Y(M208)F-L(M212)H-W(M250)V
E+FHV	V(M131)E-FHV

^a The L(M212)H mutation, denoted “H”, results in incorporation of a BChl (β) in place of H_A. The W(M250)V mutation, denoted “V”, results in the absence of Q_A from the RC.

An earlier set of mutants explored saturation mutagenesis to replace the conserved Phe at L181, which is the symmetry-related residue of the key Tyr M208 (Figure 1A) [28]. A Tyr at L181 enhances ET to the B side though not nearly as effectively as does Tyr M208 on the A-side [6]. Screening the F(L181)X+FHV set of mutants distinguished amino acids His, Asn, Asp, Gln, Tyr and Glu (1st to 6th ordering) as supporting the highest yield of P⁺Q_B⁻ formation. The prospect that the yield of P* \rightarrow P⁺H_B⁻ conversion follows the same order was largely confirmed by ultrafast spectroscopic studies that ranked His > Asn > Asp > Tyr for yield of P⁺H_B⁻. (RCs bearing the Gln and Glu substitutions were not examined.)

A subsequent mutant set tested saturation replacement of M131 (Figure 1A), which is a Val in WT RCs [29]. M131Val is related by C₂-symmetry to L104Glu on the A-side that forms a hydrogen bond to the 13¹-keto group of H_A. Earlier work showed that an Asp at M131 can form a hydrogen bond to H_B [11, 34, 35] and, in some cases, increase the yield of P⁺H_B⁻ by about a factor of two [26]. Our ms-assay screen for the P⁺Q_B⁻ yield in the V(M131)X+YFHV mutant set revealed that Glu at M131 is the superior amino acid at this position with Asp also among a

group four amino acids (Glu, Asn, Gly and Asp) that are better than the native Val [29]. Ultrafast studies on the V(M131)E+YFHV mutant found no significant effect on the yield of $P^* \rightarrow P^+H_B^-$, but an ~50% increase in the yield of $P^+H_B^- \rightarrow P^+Q_B^-$. This was shown to be largely due to a longer overall (effective) time constant for the competing charge recombination (CR) processes of $P^+H_B^-$ ($\tau_{CR} = 1/k_{CR}$ in Figure 2) from ~4 ns to ~9 ns with only a small change in the time constant for $P^+H_B^- \rightarrow P^+Q_B^-$ ET ($\tau_{HQ} = 1/k_{HQ}$ in Figure 2). For comparison, the corresponding $P^+H_A^-$ CR lifetime (i.e., the $P^+H_A^-$ lifetime in the absence of ET to Q_A) is ~10 ns or ~20 ns depending on whether Q_A is absent or pre-reduced, respectively.

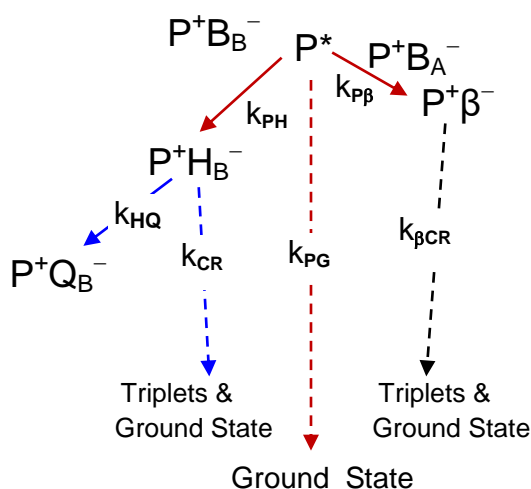


Figure 2. Competing decay pathways of P^* (red) and $P^+H_B^-$ (blue) that are targets for engineering to achieve the highest possible yield of $P^+Q_B^-$ via the B-side cofactors. Q_A is absent by experimental design except where noted.

The studies here build on this foundation with $P^+Q_B^-$ ms-screening assays and ultrafast transient absorption (TA) measurements on three new sets of mutants with combined variations at L181 and M131 (Table 1): V(M131)X+NFHV, V(M131)X+HFHV and E+F(L181)X+FHV where E is V(M131)E. In each case “X” indicates substitution of all possible amino acids (19 new mutants each set). The first two of the mutant sets have an Asn or a His, respectively, at

L181, which we identified as the two best residues at L181 from screening the F(L181)X+FHV mutants, as described above. If the previously-conferred advantages are additive, the mutant with Glu at M131 and Asn at L181 and the mutant with Glu at M131 and His at L181 are two candidates for which the overall yield of $P^* \rightarrow P^+Q_B^-$ could approach 50%. The third mutant set examines the strategy of fixing Glu at M131 and exploring all possible residues at L181. These three mutant sets are only a sampling of the 400 possible pairings at M131 and L181, but the 57 new variants have built-in biases toward higher yields of the B-side ET reactions as informed by the results from prior rounds of saturation mutagenesis at these sites.

2. Material and Methods

The procedures used in this work have been described elsewhere [28, 29]. The *R. capsulatus* mutants derive from rapid, cassette-based saturation mutagenesis at either M131 or L181 in combination with additional fixed mutations, primarily Y(M208)F, L(M212)H and W(M250)V, as described above. Three mutant sets and eight individual mutants whose photochemistry is examined are defined in Table 1. RCs were expressed in *R. capsulatus* strain U43 from a plasmid that yields RC-only (antenna-less) membranes, and RC protein was purified via robotically-assisted standard techniques. For all experiments, RCs were in buffer comprised of 10 mM Tris (pH 7.8) and 0.1% Deriphat 160-C. The mutant RCs were arrayed in black 96-well clear- and flat-bottomed plates and assayed for their yields of $P^+Q_B^-$ relative to WT and other control RCs at 295 K. The assay utilizes 7-ns excitation flashes at 532 nm and continuous probing at 850 nm provided by a diode laser.

A subset of eight mutants was subject to further characterization. This included determining the oxidation potential of P/P^+ and occupancy of the Q_B site. The latter is required for full analysis of the TA measurements. To determine the Q_B occupancy, a parallel set of

mutants absent the W(M250)V mutation was generated, i.e. the analogous set of mutants in which Q_A is bound. The Q_A -containing variants at 295K were excited with 7-ns flashes at 532 nm and bleaching of P's band at 850 nm was assayed for the relative magnitudes of a "fast" ~ 100 ms component and much slower multi-second components associated with the lifetime of $P^+Q_B^-$. (This assay for Q_B content is the best that can be done, though insensitive to possible effects of Q_A on binding of or reactivity of Q_B .) The fast ~ 100 ms component is associated with $P^+Q_A^- \rightarrow$ ground state CR in those RCs in which Q_B is absent and the relative magnitude of this component determines the fraction of Q_B -less RCs. This fraction is taken into account in fitting the ns-timescale $P^+H_B^-$ decay kinetics.

Initial charge separation proceeding from P^* in the eight mutants was examined by ultrafast TA measurements utilizing ~ 100 fs pump/probe flashes from a laser system operating at 10 Hz. RCs were held at 285K in an ice-cooled reservoir and flowed through a 2 mm pathlength cell. The ns-timescale lifetime of $P^+H_B^-$ was measured using a 1 kHz, ultrafast (~ 100 fs) excitation laser source (Spectra Physics) coupled to TA detection instrumentation (Ultrafast Systems) that employs ~ 1 ns white-light probe flashes, has time-point resolution of ~ 100 ps, and can probe to a delay time of ~ 450 μ s. To measure the $P^+H_B^-$ lifetime in the absence of ET to Q_B , terbutryn (tb) was added to the RCs to a final concentration of $\sim 25:1$ (tb:RC). In an expansion of the technique compared to our prior report, the kHz system and a spinning sample cell (with ~ 2 mm pathlength) were used for measurement of the $P^+H_B^-$ lifetime at 295 K in RCs in which Q_B is present.

3. Results

3.1. Millisecond Screening Assay of the Yield of $P^+Q_B^-$

Of the 57 mutants made, RCs could be purified from 40 of them: 10 from the V(M131)X+NFHV set, 13 from V(M131)X+HFHV and 17 from E+F(L181)X+FHV. The ground state spectra are given in Figure S1. Figure 3A compares the results of the ms-screening assay of the V(M131)X+NFHV mutants (blue bars) and the V(M131)X+HFHV mutants (red bars) for their relative yields of $P^+Q_B^-$. The assay result for another new mutant, E+FHV (solid green bar), is also given along with the controls WT, YFHV, E+YFHV, NFHV, HFHV, FHV and V. Figure 3A indicates that among all these mutants the yield of $P^+Q_B^-$ is highest in E+YFHV, which result was also obtained for the V(M131)X+YFHV mutant set [29]. Also as obtained previously, FHV and V [W(M250)V mutant] have among the lowest yields of $P^+Q_B^-$. Based on the result that adding M131Glu to YFHV improves the yield of $P^+Q_B^-$ formation (compare solid orange bar for E+YFHV and orange striped bar for YFHV), the same could be anticipated for E+FHV compared to FHV. Such result is seen in Figure 3A (compare solid green bar for E+FHV with green striped bar for FHV). On the other hand, addition of M131Glu does not improve the $P^+Q_B^-$ yield for NFHV or HFHV. In fact, no residue screened at M131 improves the $P^+Q_B^-$ yield compared to the native Val in the parent mutants NFHV and HFHV.

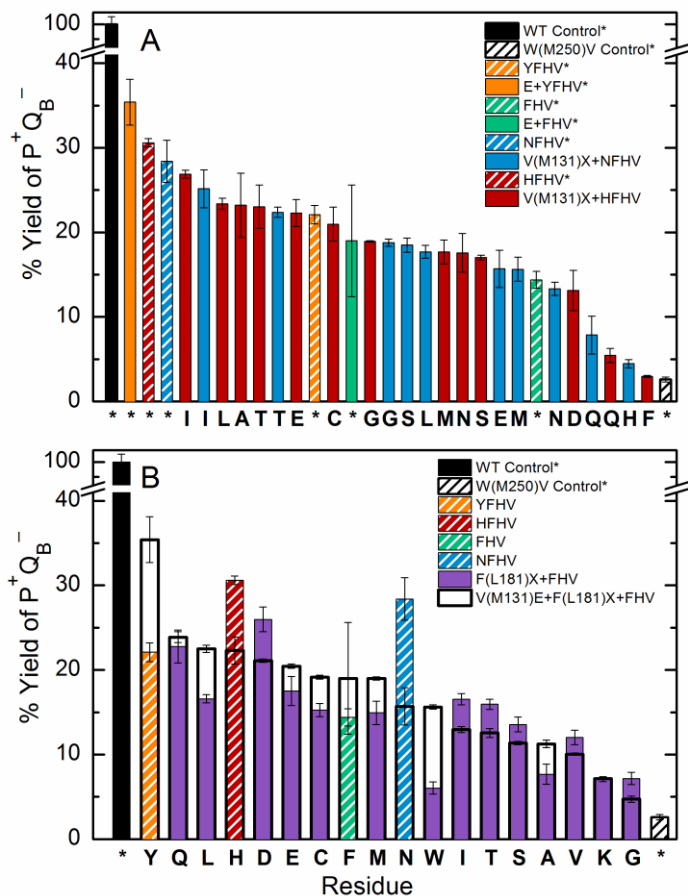


Figure 3. $P^+Q_B^-$ yields in mutant RCs relative to WT as determined via a rapid millisecond screening assay that utilizes 7-ns excitation flashes. The bars for the V(M131)E+F(L181)X+FHV mutant set are open (unfilled) bars outlined in black and allow for comparison to the respective F(L181)X+FHV mutant (colored bars) that lacks the V(M131)E mutation.

The third mutant set fixes Glu at M131 and tests whether a residue other than Tyr at L181 improves on the $P^+Q_B^-$ yield observed in the E+YFHV mutant (black outline bars in Figure 3B). No other substitution at L181 was found to be more effective than Tyr. The comparison violet bars in Figure 3B are the screening results for mutant set F(L181)X+FHV [29].

In order to confirm and understand the origin of the higher $P^+Q_B^-$ yield in E+YFHV compared to YFHV, ultrafast spectroscopy was used to measure the rate constants and yields of

the B-side charge separation steps $P^* \rightarrow P^+H_B^- \rightarrow P^+Q_B^-$ [29]. It was shown that the primary effect of the Glu at M131 in E+YFHV compared to YFHV is a slowing of the combined CR processes of $P^+H_B^-$ (k_{CR} in Figure 2) that competes with forward ET $P^+H_B^- \rightarrow P^+Q_B^-$ (k_{HQ}). From the new mutants, we chose three more pairings to further investigate the effect of a Glu at M131. One pair is FHV and E+FHV, again where the ms-assay indicates that a Glu at M131 results in a higher $P^+Q_B^-$ yield (Figure 3). The other two pairs are E+NFHV with NFHV and E+HFHV with HFHV. These pairs are also of interest from the standpoint that HFHV and NFHV are the two best residues in the ms-screen of F(L181)X+FHV mutants. (Compare the red dashed bar for HFHV and blue dashed bar for NFHV with the purple bars for the other F(L181)X+FHV mutants in Figure 3B). Also, in Figure 3A HFHV and NFHV are the next two highest ranking mutants after E+YFHV, making them of interest also in their own right and of course as being “primed” for addition of M131Glu. However, the ms-assay reveals that Glu at M131 confers no advantage in these two cases, differing from the pairs based on YFHV and FHV.

3.2. Cofactor Content and Properties of Selected Mutants

Ground state spectra of the eight mutants selected for further study and WT are shown in Figure 4. The β -phenotype (H_A replaced with a BChl) is apparent, with significantly reduced absorption in the ~ 750 - 760 nm Q_y region of BPh and increased absorption in the ~ 780 - 800 nm Q_y region of BChl compared to WT. In the Q_x region, the ~ 542 nm band of H_A in WT is absent in the mutants with concomitant increased absorption in the 590-600 BChl manifold. The Q_x band of H_B (also the Q_x band of H_A in WT) is convolved with 500-550 nm absorption bands of the carotenoid. Nonetheless, the addition of Glu at M131 results in a clear red shift of the Q_x

absorption profile of H_B . The position of the Q_x band of H_B in each mutant is given in Figure 4 as determined from the ultrafast measurements in Section 3.4. For each of the four mutant pairings, the addition of M131Glu results in a 5-8 nm red shift of the Q_x band of H_B and appears to cause a slight broadening of the Q_y band of H_B . The red shift of the Q_x band is consistent with formation of a hydrogen bond between Glu at M131 and the 13¹-keto group of H_B [11, 26, 34, 35].

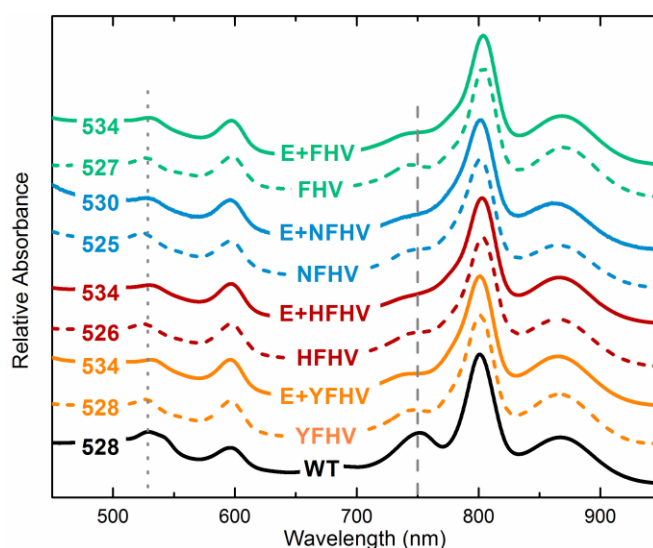


Figure 4. Ground state absorption spectra of select mutant RCs. The vertical gray lines at 528 nm (dotted) and 750 nm (dashed) are visual guides. The numbers on the left indicate the position of the Q_x absorption band of H_B in each mutant as determined from ultrafast measurements.

Table 2 reports the P/P^+ oxidation potentials and Q_B occupancies in the six new mutants along with those for WT, YFHV and E+YFHV. Within each pair (with and without Glu at M131), the P oxidation potentials are the same within experimental error, an expected result given that M131 is some distance from P . The template F substitution (native Tyr at M208 replaced with Phe) raises the P oxidation potential a small amount compared to WT, while replacing Phe L181 with Tyr lowers the P oxidation potential by ~ 20 meV and replacement with Asn or His by 30-40 meV. Other things being equal, lowering the P oxidation potential should

result in a corresponding lowering of the free energy of each of the charge separated states with respect to P*.

Table 2. Properties of WT and Selected Mutant RCs.^a

Sample	P Oxidation Potential (mV) ^b	Q _B Occupancy (%) ^c
WT	491 ± 8	98
YFH	474 ± 5	97
E+YFH	469 ± 1	78
NFH	452 ± 3	99
E+NFH	460 ± 6	69
HFH	457 ± 5	99
E+HFH	455 ± 2	80
FH	499 ± 4	91
E+FH	489 ± 3	64

^aNecessarily, measurements are made on on the mutant versions that lack W(M250)V; i.e., the mutants contain Q_A.

^bError bars on the oxidation potentials are obtained from replicate (N ≥ 2) measurements.

^cThe Q_B occupancy has an error of ±5% of the reported value.

Q_B is a labile cofactor by nature and upon assaying the Q_B content of the YFH and E+YFH mutants it was found that the V(M131)E mutation results in diminished binding of ubiquinone in the Q_B site [29]. The Q_B occupancy of mutants is determined by TA spectroscopy via the relative magnitude of an ~150 ms kinetics component that will manifest in the decay kinetics of P⁺Q_A⁻, reflecting P⁺Q_A⁻ → ground state in those RCs in which Q_B is absent. Hence the Q_B occupancy is determined using mutants that contain Q_A – i.e., a set of mutants in which the W(M250)V mutation is *not* present. Figure S2 shows the data used to determine the Q_B occupancy for the six Q_A-containing variants NFH, E+NFH, HFH, E+HFH, FH and E+FH. The Q_B occupancies of these and WT and YFH are given in Table 2. The parameters associated with the decay kinetics are given in Table S1. While WT and mutants YFH, NFH, HFH and FH have

~100% Q_B occupancy, the variants with the V(M131)E mutation have Q_B occupancies of ~65-80%. These results are required for fitting the ultrafast kinetic data (Section 3.4).

3.3. P^* Decay Pathways and the Rate and Yield of $P^* \rightarrow P^+H_B^-$

Figure 5 shows TA spectra in the visible and the near-infrared regions for NFHV (panels A and B) and E+NFHV (panels C and D). Analogous results for the HFHV and E+HFHV pair are given in Figure S3, and for the FHV and E+FHV in Figure S4. The insets in parts B and D show data and fits of the decay kinetics of the P^* stimulated emission averaged over an ~10 nm interval (generally ~910-920 nm) that is centered where $\Delta A = 0$ in the TA difference spectra at long times (≥ 1 ns). This approach isolates, as best as possible, the P^* stimulated emission kinetics from contributions of absorption changes due to bleaching of P and absorption by P^+ and the anions of H_B and β . The P^* decay kinetics are known to be heterogeneous even for WT RCs and the lines in panels B and D are fits of the data to the convolution of an instrument response with two exponentials plus a constant. (As expected, the fits return ~0 for the value of the constant reflecting the spectral/temporal isosbestic point.)

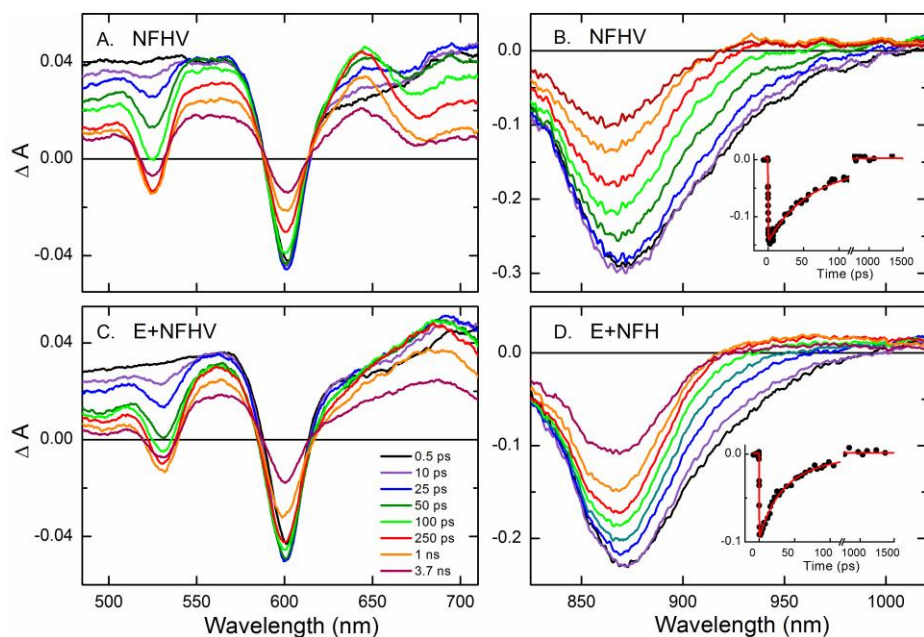


Figure 5. TA spectra and kinetics for NFHV (A and B) and E+NFHV (C and D, except that for panel D the variant without the V mutation was used due to sample limitation). The spectra were obtained at the times indicated (panel C) following an ~130-fs excitation flash at either 860 nm (panels A and C) or 590 nm (panels B and D). The insets in (B) and (D) show the data (filled circles) averaged in a 10-nm interval centered on the stimulated emission isosbestic point at ~920 nm. The solid red lines are the fit of the data to the convolution of the instrument response with two exponentials plus a constant.

The values of the time constants and their relative amplitudes for P* decay in the eight mutants are given in Table 3. Four of the mutants display an ~15-35% component with an ~200 ps lifetime as found for other mutants as well [26, 29, 36, 37]. The time constant for internal conversion P* → ground state, k_{PG} in Figure 2, is known to be ~200 ps for RCs in Deriphat from work on a number of mutant RCs but most particularly one in which P* decays solely by internal conversion [23, 38, 39]. This correlation, plus the finding that the kinetics for the appearance of bleaching of the Q_x band of H_B (see below and Table 4, column 2) generally matches well that of the shorter P* stimulated emission time constant, is the basis for a model of a (mainly) “inactive” population of RCs in many mutants. In other words, this is a fraction of RCs in which little charge separation appears to take place following excitation. In some cases where a second P* fraction having a lifetime substantially smaller than 200 ps was observed it was suggested that these may be performing charge separation to some extent also [26]. A distribution of time constants (non-single exponential P* decay kinetics) for initial charge separation even in WT RCs has been described by many workers (as summarized in ref [27]). The extent to which either or both of these models may apply to the E+NFHV and E+HFHV mutants is unclear at present. Interestingly, and perhaps not coincidentally, these two mutants have the two shortest active-fraction P* lifetimes and the largest percentage (~50%) of the fraction with a longer P* lifetime (the mainly “inactive” fraction). The quite long P* lifetime of the second component in the FHV and E+FHV mutants, compared to the ~200 ps typically found for P* internal conversion, is an interesting result for which we have no explanation other than reflecting changes in the environment of P.

Table 3. P* Lifetimes and Relative Populations Determined from Heterogeneous Stimulated Emission Decay.^a

Sample	“Active” τ_P (ps) ^b	Active Fraction	“Inactive” τ_P (ps) ^b	Inactive Fraction
YFH ^{c,d}	32	0.65	210	0.35
E+YFH ^d	30	0.85	200	0.15
NFHV	53	0.72	201	0.28
E+NFH ^d	24	0.52	74	0.48
HFHV	41	0.71	244	0.29
E+HFH ^d	17	0.47	72	0.53
FHV	131	0.70	628	0.30
E+FHV	129	0.80	403	0.20

^a The active population refers to RCs in which ET from P* occurs and the inactive population refers to RCs in which P* decays to the ground state only (or nearly so).

^b The time constants have a typical error of $\pm 10\%$ of the reported value.

^c Taken from ref [29].

^d Due to sample constraints, P* lifetimes were measured in four cases on the mutant variant that has Q_A (i.e., the W(M250)V mutation is absent).

Table 4. Properties of the Photochemically Productive RC Population.^a

Sample	P* lifetime τ_P (ps)	H _B Q _x band position (nm)	P ⁺ H _B ⁻ Yield Φ_{HB}	τ_{PH} (ps) ^b
YFHV	28	528	0.46	65
E+YFHV	23	534	0.38	70
NFHV	36	525	0.56	79
E+NFHV	19	530	0.69	31
HFHV	39	526	0.56	71
E+HFHV	17	534	0.65	26
FHV	80	527	0.16	659
E+FHV	47	534	0.24	367

^a Results pertain to the photochemically “active” P* population in the sample, i.e., the fraction of RCs in which ET from P* occurs. The time constants and yields have typical errors of $\pm 10\%$ of the reported values.

^b Time constant for ET from P* to H_B where $\tau_{PH} = 1/k_{PH}$; see Figure 2. These values were calculated using a P* lifetime that is the average of the value in column 2 (determined via the appearance of Q_x bleaching) and the value in column 2 of Table 3 (determined by decay of stimulated emission in the “active” fraction).

As P* decays, bleaching of the Q_x absorption band of H_B near 530 nm grows in along with absorption features of the anion of H_B between 620 and 700 nm (Figure 5 parts A and C).

Bleaching of H_B near 530 nm is resolved unambiguously since H_A is not present in these RCs. The kinetics associated with the appearance and the subsequent decay of bleaching of the Q_x band of H_B give the P^* lifetime and $P^+H_B^-$ lifetime, respectively (in the active fraction). The data fitting and analysis procedures that give these two lifetimes have been described [29] and involve fitting data acquired using two different TA systems (see Section 2) that together probe about eight orders of magnitude (~ 0.1 ps to 50 μ s). Most of the complexity of the multi-exponential fitting relates to determining the $P^+H_B^-$ lifetime (see Section 3.4). Typical results for the P^* lifetime returned from the fits are given in Table 4, column 2. These results generally are in good agreement with the values given in Table 3 for the P^* lifetimes in the active fraction as measured by stimulated emission decay. The small yield of ET to H_B in the case of the FHV and E+FHV RCs probably contributes to the larger uncertainty in the time constants measured for both P^* stimulated emission and the Q_x bleaching of H_B .

Figure 6 shows TA spectra acquired at ~ 8 multiples of the respective P^* (active fraction) lifetime for the eight mutants. The V(M131)E mutation results in an ~ 7 nm red shift of the bleaching of the Q_x band of H_B as well as an ~ 50 nm red shift of the apparent H_B anion absorption maximum, from near 640 nm (mutants with the native Val at M131) to near 690 nm for the mutants with Glu at M131. This is consistent with prior results for mutants having an Asp or Glu at M131 [11, 26, 29, 34, 35] and formation of a hydrogen bond to H_B , which was the intended goal. The position of the Q_x band of H_B in each of the mutants as determined from spectra such as those in Figure 6 is noted on Figure 4 and in column 3 of Table 4. The absorption changes due to $P^+\beta^-$ formed on the A-side also contribute to the raw data in Figure 6, with β^- adding to the magnitude of the 600-nm (BChl) bleaching and adding a relatively broader, more featureless and smaller BChl anion absorption profile between 620-720 nm. For the FHV

mutant, with the lowest yield of B-side ET, this spectral region is more heavily weighted to the absorption changes due to the anion of β ; however, the FHV and E+FHV comparison still reveals a red shift of the transient absorption profile between 620-720 nm as well as a clear red shift of the position of Q_x bleaching of H_B .

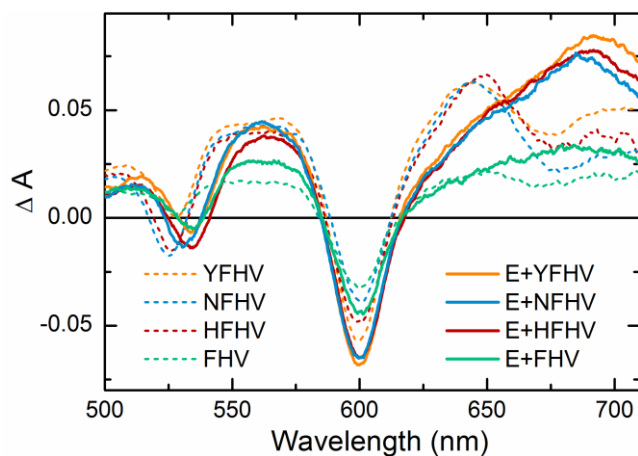


Figure. 6. TA spectra of mutant RCs comparing the positions of Q_x bleaching and anion absorption of H_B ; absorption changes due to $P^+\beta^-$ are also present. The spectra shown were acquired at ~ 700 ps for the FHV and E+FHV mutants and 200-350 ps for the others in order to feature the maximum Q_x bleaching and anion absorption features of H_B .

The yield of $P^* \rightarrow P^+H_B^-$ ET in each of the mutants was determined from the ratio of the maximal magnitude of Q_x bleaching of H_B at the respective peak bleaching wavelength to the maximal magnitude of P^* bleaching at ~ 600 nm (see e.g., 0.5 ps P^* spectrum in Figure 5 parts A and C), factoring out the contribution to the 600-nm bleaching by the P^* inactive fraction in each mutant. The resulting values for the yield of $P^* \rightarrow P^+H_B^-$ ET in the active fraction, denoted Φ_{HB} , are given in Table 4 column 4. From this yield and the active fraction P^* lifetime, the time constant for $P^* \rightarrow P^+H_B^-$ ET, τ_{PH} , was determined (Table 4 column 5).

3.4 $P^+H_B^-$ Decay Pathways and the Rate and Yield of $P^+H_B^- \rightarrow P^+Q_B^-$

The experimental and data-fitting methodologies for determining the rate constant and yield of $P^+H_B^- \rightarrow P^+Q_B^-$ ET (k_{HQ} in Figure 2) and the rate constant and yield of the combined $P^+H_B^-$ CR processes (k_{CR} in Figure 2) have been described [25, 29]. At their simplest, one need only determine the lifetime of $P^+H_B^-$ in the presence and in the absence of Q_B . To this end, TA data were acquired to a delay time of 50 μ s under both of the two relevant conditions (RCs with tb added, which displaces Q_B , and RCs with no tb addition). Representative TA spectra spanning ~1 ns to 50 μ s are shown in Figure 7A for the HFHV mutant. As noted above, the combined $P^+H_B^-$ CR processes are distilled into a simple k_{CR} in our fitting model in Figure 2. However, decay of $P^+H_B^-$ is more complex (see Figure S5), with the initial singlet form of $P^+H_B^-$ decaying in part to the triplet form of the radical pair state. This in turn can decay to give P^R , the triplet excited state of P (e.g., 20 ns spectrum, Figure 7A). P^R has a lifetime of ~100 ns, largely reflecting energy transfer to give the triplet excited state of the carotenoid (e.g., 200 ns spectrum, Figure 7A) which lives for 2-3 μ s. The triplet form of $P^+H_B^-$ can also decay via ET to Q_B to give $P^+Q_B^-$, a process we do not include explicitly in our analysis. For simplicity, the “rate constant” denoted here as k_{CR} , or time constant τ_{CR} , reflects a combination of the processes by which $P^+H_B^-$ decays other than by ET to Q_B , at its simplest a combination of decay to the ground state and decay to P^R .

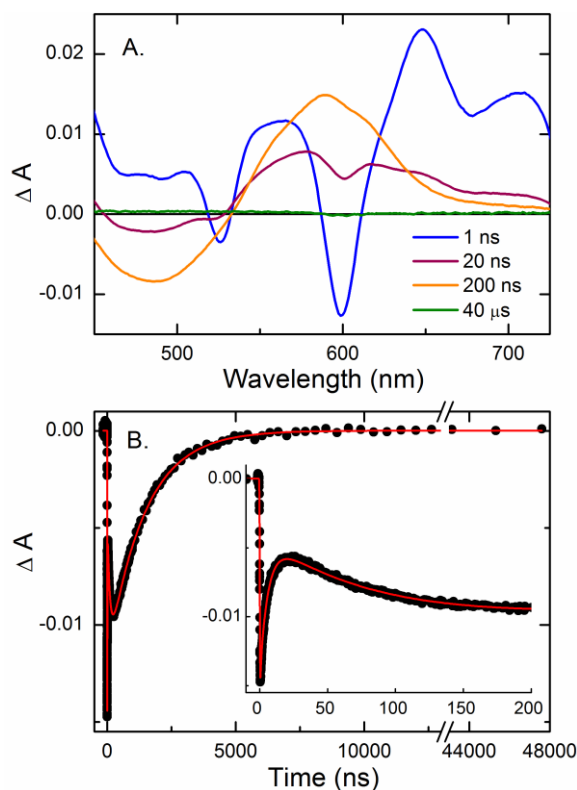


Figure 7. Representative spectral and kinetic data acquired on the timescale of a few ns to a few μ s following 100-fs excitation flashes at 865 nm. A: TA spectra for the HFHV mutant with no additions (i.e., no added tb). B: Kinetics of the TA data for the HFHV mutant averaged over a 10-nm interval centered at the maximal H_B bleaching, from which the TA data averaged between \sim 550 and 560 nm is subtracted (i.e., the latter is used as a reference region as described previously [29]).

The $P^+H_B^-$ CR lifetime, τ_{CR} , was thus determined from fitting the decay kinetics of $P^+H_B^-$ in RCs to which terbutryn was added to displace Q_B , to a convolution of the instrument response with four exponentials plus a constant. The four exponentials are associated with the \sim 1 ns lifetime of $P^+\beta^-$ (formed on the A-side), the $P^+H_B^-$ CR lifetime ($\tau_{CR} = 1/k_{CR}$) and the P^R (\sim 100 ns) and car^T (\sim 2-3 μ s) lifetimes. (The P^R and car^T lifetimes are given in Table S1.) Figure 7B shows representative data and fit for the HFHV mutant. The fit values for τ_{CR} in the eight

mutants range from about 3 to 10 ns (Table 5, column 2). Analogous analysis was carried out for the unblocked (no tb added) RCs except that for the four mutants bearing the M131E mutation, a fifth exponential was added to the fitting function with its value fixed at that determined for τ_{CR} for the respective mutant and an amplitude fixed according to the inherent Q_B occupancy in Table 2. This fifth component thus takes into account the fraction of RCs in which Q_B is not present in the mutants bearing M131Glu. Distinctions between the data and fits over the first 25 ns (of the 50 μ s time course probed) for all eight mutants under the two conditions (with/without added tb) are readily apparent in Figure S6. The results for the $P^+H_B^-$ lifetime in RCs with Q_B present are given in column 3 of Table 5. Column 4 gives the value for τ_{HQ} calculated from the values in columns 2 and 3 of Table 5. The yields of $P^+H_B^-$ ET and CR are given in columns 5 and 6, respectively, calculated from the time constants in columns 2 and 4.

The results in Table 5 indicate that the fastest rates of $P^+H_B^- \rightarrow P^+Q_B^-$ ET, corresponding time constants ranging between about 6 and 7 ns, are found for the YFHV, E+YFHV, FHV and E+FHV mutants. This ET process is three or more times slower in the NFHV, E+NFHV, HFHV and E+HFHV mutants, where the time constants are between about 20 and 60 ns. There is less difference between the time constants for CR amongst the eight mutants, but E+YFHV has the longest τ_{CR} of ~10 ns. Only in E+YFHV is the yield of ET (~57%) clearly larger than that of CR (~43%). In earlier work, we reported that the branching at this step in B-side charge separation for E+YFHV was ~70% ET and ~30% CR, which results came from analysis of ultrafast TA data acquired on a much more limited timescale (longest time point in the kinetics for RCs containing Q_B was only 4 ns compared to 50 μ s here). However, E+YFHV was the superior mutant relative to the others in our prior report and the same result is obtained here. The competition between ET and CR clearly greatly favors CR for the NFHV and E+NFHV pair,

and similarly HFHV and E+HFHV. For these four RCs, the CR lifetimes range from ~6-9 ns and the time constants for ET range from ~20-60 ns, resulting in $P^+H_B^- \rightarrow P^+Q_B^-$ ET yields of only ~15-30%. For the YFHV, E+YFHV, FHV and E+FHV mutants the $P^+H_B^- \rightarrow P^+Q_B^-$ ET yields are clearly larger, ranging between ~40-55%. A more general discussion encompassing the full sequence of $P^* \rightarrow P^+H_B^- \rightarrow P^+Q_B^-$ conversion follows in the next Section.

Table 5. $P^+H_B^-$ Lifetimes and $P^+H_B^- \rightarrow P^+Q_B^-$ ET Yields (Φ_{QB}).^a

Sample ^b	$P^+H_B^-$ τ_{CR} (ns) ^c	$P^+H_B^-$ τ_{HB} (ns) ^d	$P^+H_B^- \rightarrow P^+Q_B^-$ τ_{HQ} (ns) ^e	$P^+H_B^- \rightarrow P^+Q_B^-$ Yield (Φ_{QB}) ^f	$P^+H_B^-$ Yield (Φ_{CR})
YFHV	4.6	2.9	7.5	0.38	0.62
E+YFHV	10.3	4.4	7.6	0.57	0.43
NFHV	6.5	4.9	20.8	0.24	0.76
E+NFHV	7.0	5.2	20.6	0.25	0.75
HFHV	9.2	6.5	21.4	0.30	0.70
E+HFHV	8.0	7.0	56.0	0.13	0.87
FHV	3.7	2.3	5.9	0.39	0.61
E+FHV	7.3	3.7	7.6	0.49	0.51

^a The time constants in columns 2 and 3 have an error of $\pm 20\%$ of the values listed.

^b Nomenclature for RC mutations as given in Table 1.

^c Lifetime of $P^+H_B^-$ in RCs with terbutryn replacing Q_B : $\tau_{CR} = 1/k_{CR}$ in Figure 2.

^d Lifetime of $P^+H_B^-$ in RCs with Q_B present (after taking into account any Q_B -less RCs).

^e Time constant for $P^+H_B^- \rightarrow P^+Q_B^-$ ET calculated from the values in columns 2 and 3:

$$\tau_{HQ} = 1/k_{HQ} = 1/[(1/\tau_{HB}) - (1/\tau_{CR})].$$

^f $\Phi_{QB} = k_{HQ}/(k_{HQ}+k_{CR})$

4. Discussion

Forty new mutants that harbor combinations of amino acids at residues L181 and M131 have been evaluated via a ms-screening assay for their relative yields of $P^+Q_B^-$ produced by B-side charge separation. Ultrafast studies on a subset of eight mutants provided the rate constants and yields of the individual B-side ET and CR reactions that take place out to 50 μ s. The latter aspect of the work serves dual purposes. One is to understand specific effects that the mutations have on the various B-side steps of competing charge separation and charge recombination reactions that overall determine the yield of $P^* \rightarrow P^+Q_B^-$ conversion. Second, the ultrafast studies on a subset of mutants serve as an independent assay that ideally reconciles with the results of the much simpler and far less time consuming ms-assay (and vice versa).

Previous ms-screening of the L(181)X+FHV mutant set identified NFHV and HFHV as having the largest yields of $P^+Q_B^-$ (Figure 3B) and preliminary ultrafast measurements indicated that in both of these mutants there is a higher yield of $P^* \rightarrow P^+H_B^-$ ET compared to that found in the YFHV mutant [29]. The ultrafast measurements undertaken here determine an ~56% yield of $P^* \rightarrow P^+H_B^-$ ET for both NFHV and HFHV in the “active” P^* fraction of RCs, compared to 46% for YFHV (Table 4, column 4). Taking into account the percentage of the “active” P^* fraction present in these samples (Table 3, column 3), one can calculate that the $P^+H_B^-$ yield expected to be obtained upon probing the “entire” sample in both NFHV and in HFHV is 40%, again both besting 30% for YFHV. The ultrafast measurements thus provide insight that is consistent with, and in fact is the main contributing factor for, NFHV and HFHV having among the higher overall $P^+Q_B^-$ yields as found by the ms-assay (Figure 3B and ref 29).

The NFHV and HFHV mutants were thus logical choices as platforms to build toward a high-yield B-side ET mutant and M131 was a logical target for saturation mutagenesis. Substitution of an Asp at M131 has been utilized in several studies to make a hydrogen bond to H_B and in some cases results in a two-fold increase in the yield of $P^+H_B^-$ [11, 26, 34, 35]. In our earlier screen of the V(M131)X+YFHV mutants we found that both Glu and Asp had favorable outcomes on the $P^+Q_B^-$ yield, with Glu being the better of the two [29]. Ultrafast studies revealed that the most significant difference between the E+YFHV and YFHV mutants is that the Glu at M131 slows by over a factor of two the combination of CR processes by which $P^+H_B^-$ decays to the ground or triplet states, having a lesser effect on the rate of $P^+H_B^- \rightarrow P^+Q_B^-$ ET (slowed by ~10%).

These findings motivated our ms-screen of all possible residues at M131 in the NFHV and HFHV backgrounds. Unlike the case for E+YFHV compared to YFHV, the ms-assay determines for both the NFHV and E+NFHV pair and the HFHV and E+HFHV pair that addition of Glu results in a lower yield of $P^+Q_B^-$ (Figure 3). In fact, the ms-assay indicates that the native Val residue at M131 provides in the highest yield of B-side ET for both the NFHV and HFHV mutants. On the other hand, the ms-assay indicates that M131Glu added to FHV results in a significantly larger yield of $P^+Q_B^-$, mirroring the relationship between the E+YFHV and YFHV pair.

Each of these four pair-wise comparisons of either an increased or decreased yield of $P^+Q_B^-$ upon addition of Glu at M131 is verified by the ultrafast measurements. Table 6 gives the yields of $P^+Q_B^-$ as determined by both methods, the ms-assay and the ultrafast-assay. The mutants are ordered in column 1 according to the ms-assay $P^+Q_B^-$ yields (given in column 2) from highest yield of $P^+Q_B^-$ (35% found for the E+YFHV mutant) to lowest yield of $P^+Q_B^-$ (4%

for the FHV mutant). Column 3 lists the yield of $P^+Q_B^-$ that is obtained from the series ultrafast experiments. For each mutant, the yield in column 3 is the product of three terms: 1) the percentage of “ET-active” P^* in the sample; 2) the yield of $P^* \rightarrow P^+H_B^-$ ET in the active fraction of RCs; and 3) the yield of $P^+H_B^- \rightarrow P^+Q_B^-$ ET. For example, for the E+YFHV mutant, the $P^+Q_B^-$ yield of 18% is the product of, respectively, 0.85 (Table 3, column 3), 0.38 (Table 4, column 4), and 0.57 (Table 5 column 5). The results in Table 6 show that both techniques, the ms-assay and the ultrafast measurements, determine that addition of a Glu at M131 to YFHV and to FHV results in an increase in the overall amount of $P^+Q_B^-$ that is formed, while the opposite is true for addition of Glu at M131 to NFHV and HFHV.

Table 6. Comparison of Results for $P^+Q_B^-$ Yield.

Mutant	ms-assay ^a	ultrafast ^b
E+YFHV	35	18
HFHV	30	12
NFHV	28	10
E+HFHV	22	4
YFHV	21	11
E+FHV	18	9
E+NFHV	16	9
FHV	14	4

^aPercent yield relative to WT as determined by the ms-assay using 7-ns excitation flashes.

^bPercent yield as determined by ultrafast TA following an ~100 fs excitation flash.

This is a good agreement of results for these eight mutants as determined by two wholly different methods, both of which have significant and different sources of error. For example, the dominant error source for the ms-assay likely is “recycling” of the photochemistry during the 7-ns excitation flash. In brief, recycling refers to the process by which an excited RC can return

to the ground state (e.g., by ~200 ps internal conversion or by ~1 ns P^+B^- CR, for example) and then be re-excited and produce $P^+Q_B^-$ on a second, third, etc. cycle during the 7-ns flash. This and other potential error sources for the ms-assay have been described elsewhere [29]. The $P^+Q_B^-$ yields determined by the ultrafast measurements come from multiplying together three terms, each of which derives from a lengthy and complex data analysis (Sections 3.3 and 3.4), with errors propagating throughout. Additionally, for all of these mutants, B-side production of $P^+Q_B^-$ is still in low yield making the cumulative error more significant.

In addition to both assays indicating that addition of M131Glu has a positive effect on the yield of $P^+Q_B^-$ when added to YFHV and FHV and a negative effect when added to NFHV and HFHV, they order the eight mutants as to their yield of $P^+Q_B^-$ fairly similarly. As seen in Table 6, E+YFHV is the best mutant and HFHV second best for both measurements. Ignoring for the moment the E+HFHV mutant, NFHV and YFHV fall next in line. Below these come E+FHV and E+NFHV, with FHV last. The E+HFHV mutant is the one out of the eight mutants with least consistency between the results of the ms-assay and the ultrafast measurements, for which we have no explanation at present. A final note regarding the summary in Table 6 is that “recycling” might be viewed cautiously as of some value with these low-yield mutants, possibly amplifying the differences between them giving in effect a larger dynamic range to the results.

A host of mutants has been studied in the past thirty years since the crystal structure of the RC was reported, most of these, of course, aimed at understanding ET on the A-side of the RC. Mutational effects have been interpreted usually qualitatively and indirectly in terms of changes in the free energies of the A-side charge separated states and consequences on the rate constants and yields of the A-side ET and CR reactions. A much smaller literature exists to this purpose for the B side of the RC. Some points we can take from the present study begin with the

observation that the oxidation potential of P in the NFHV, HFHV, E+NFHV and E+HFHV is 30-40 meV lower than for WT and the FHV mutant (Table 2). Other things being equal, this lowers all the charge separated states in free energy relative to P* by the respective amount. This would be expected to lower P⁺B_B⁻, making it closer to P* though probably not lower than P* (Figure 2) given the estimates of a ~100-200 meV gap between these two states in WT. A Tyr at L181 has a smaller effect on the P/P⁺ potential. Additionally, a Tyr at either L181 or M208 is known/thought to lower the free energy of the P⁺B⁻ state via a stabilizing interaction with the respective B_B or B_A molecule. For all six mutants with either a Tyr, Asn or His at L181, the rate of P* → P⁺H_B⁻ ET is clearly much larger than when an F is present (Table 4) lending qualitative, consistent insight to these considerations regarding P* → P⁺H_B⁻ conversion.

For the E+NFHV and E+HFHV mutants, the respective ~31 ps and ~26 ps time constants for P* → P⁺H_B⁻ ET are among the fastest attained to date. Correspondingly, in E+NFHV and E+HFHV, the yield of ET to H_B is very high, approaching 70% in the active fraction. For both of these mutants, the P* lifetime in the so-called “inactive” fraction is ~70 ps, which indicates this P* fraction contributes somewhat to production of P⁺H_B⁻. (Again, we have ignored this possibility in the analysis presented above; Section 3.3) The data in Table 3 suggest that the M131Glu mutation is a contributing factor to the high yields of P* → P⁺H_B⁻ ET in the E+NFHV and E+HFHV RCs, since the corresponding NFHV and HFHV mutants have lower yields and larger time constants for P* → P⁺H_B⁻ conversion. The hydrogen bond to H_A provided by the symmetry-related Glu at L104 on the A-side is typically considered to lower the free energy of P⁺H_A⁻ by as much as ~100 meV (by stabilizing the H_A anion). Clearly among the eight mutants studied here, the E+NFHV and E+HFHV mutational combinations have resulted in the most favorable conditions for P* → P⁺H_B⁻ ET. Unfortunately, these two mutants and the parent

NFHV and HFHV mutants, which likely have the smallest free energy gap between $P^+H_B^-$ and $P^+Q_B^-$, have the slowest $P^+H_B^- \rightarrow P^+Q_B^-$ ET of the eight mutants.

A high yield of ET at any step requires that the competing CR (or other) reactions are much slower in comparison. The CR lifetime of $P^+H_A^-$ is 10-20 ns, against 200 ps $P^+H_A^- \rightarrow P^+Q_B^-$ ET. In RCs with β on the A-side, the $P^+\beta^-$ CR lifetime is ~ 1 ns, even though the free energy of this state is (expected to be) higher by ~ 200 meV compared to that of $P^+H_A^-$. This would place $P^+\beta^-$ further from the ground state yielding slower CR based on a traditional Marcus inverted region argument. The counter-intuitive shorter $P^+\beta^-$ CR lifetime has been argued to reflect that $P^+\beta^-$ and $P^+B_A^-$ are close in free energy providing better mixing of these states and more facile deactivation to the ground state driven by the $P^+B_A^-$ contribution (with shorter distance between electron and hole) [33, 40, 41]. This has similarly been discussed for $P^+H_A^-$ on the A side [42-47] and for $P^+H_B^-$ on the B side [14, 25, 29]. Looking to the $P^+H_B^-$ CR lifetimes presented in Table 5 for similar or other trends, one might have expected that for each mutant pair, the variant with the Glu at M131 would have longer CR lifetime. This is found for three of the four pairs. Interestingly, the E+YFHV mutant – the mutant that provided much motivation for this study – has the longest $P^+H_B^-$ CR lifetime.

Observations and interpretations such as these and others mentioned earlier reflect changes to the free energies of the states. Additionally, many other effects of mutations can be catalogued, such as structural changes that affect distance between cofactors or their orientation, changes in the ionization state of residues and the presence of bound detergent, lipid or water molecules. All of these have been posited over the years as affecting various RC processes. Recently, the presence or absence of bound water molecules in a hydrogen bond network involving B_A has been shown to have significant impact on initial $P^* \rightarrow P^+H_A^-$ conversion [48-

53]. Finally we note that the Q_B and Q_A pockets are dissimilar with the latter being very hydrophobic and likely contributing only a relatively small re-organization energy upon $P^+H_A^- \rightarrow P^+Q_A^-$ ET. Such is not likely to be the case for $P^+H_B^- \rightarrow P^+Q_B^-$ considering the numerous polar residues in the Q_B binding pocket, making the A-side template less relevant for guidance in optimizing this B-side ET reaction.

In conclusion, the present study has explored three new sets of mutants that combine saturation mutagenesis near either B_B or H_B with other fixed substitutions identified as enhancing B-side ET in prior rounds of mutagenesis and screening. Forty new mutants RCs were screened by a relatively fast and simple millisecond timescale assay for $P^+Q_B^-$ as obtained solely by B-side ET. Eight of these mutants were subject to ultrafast time-resolved studies. From the latter studies, rate constants and yields of the competing ET and CR processes at both the primary and secondary stages of charge separation were determined. In mutants showing increased B-side activity, charge recombination was slowed to favor ET to the B-side quinone. The results of the ultrafast studies confirm that the ms-screen – which requires much less time, effort and material – provides the correct relative ordering of the yields of $P^+Q_B^-$ among the eight mutants. The combined results clearly show that the road to achieving a high yield of $P^+Q_B^-$ formed via the B side is not as simple as combining mutations that might be discovered to favor individual ET steps, nor would this generally be expected. Therefore, continued use of high-throughput mutagenesis and rapid screening techniques are critical for identifying RCs that perform efficient charge separation utilizing the B-side cofactors. Insights gained further elucidate the molecular underpinnings of photosynthetic reaction center function and critical factors that can be applied to bioinspired architectures for solar energy conversion.

Acknowledgements

This work was supported by the U. S. Department of Energy, Office of Science, Office of Basic Energy Sciences under grant DE-SC0002036 (to CK and DH) and associated Argonne-FWP (to PL). Argonne, a U.S. Department of Energy Office of Science laboratory, is operated under Contract No. DE-AC02-06CH11357. KF was supported by the National Science Foundation Graduate Research Fellowship under grant DGE-1143954.

References

- [1] J. Deisenhofer, O. Epp, K. Miki, R. Huber, H. Michel, Structure of the Protein Subunits in the Photosynthetic Reaction Center from *Rhodospseudomonas viridis* at 3 Å Resolution, *Nature*, 318 (1985) 618-624.
- [2] J.P. Allen, G. Feher, T.O. Yeates, H. Komiya, D.C. Rees, Structure of the Reaction Center from *Rhodobacter sphaeroides* R-26: The Cofactors, *Proc. Natl. Acad. Sci. U.S.A.*, 84 (1987) 5730-5734.
- [3] C.-H. Chang, O. El-Kabbani, D.M. Tiede, J.R. Norris, M. Schiffer, The Structure of the Membrane-Bound Photosynthetic Reaction Center from *Rhodobacter sphaeroides* R-26, *Proc. Natl. Acad. Sci. U.S.A.*, 30 (1991) 5352-5360.
- [4] U. Ermler, G. Fritsch, S.K. Buchanan, H. Michel, Structure of the Photosynthetic Reaction Centre from *Rhodobacter sphaeroides* at 2.65 Å Resolution: Cofactors and Protein-Cofactor Interactions, *Structure*, 2 (1994) 925-936.
- [5] B. Robert, M. Lutz, D.M. Tiede, Selective Photochemical Reduction of Either of the Two Bacteriopheophytins in Reaction Centers of Rps. *Sphaeroides* R-26, *Febs Lett*, 183 (1985) 326-330.
- [6] B.A. Heller, D. Holten, C. Kirmaier, Control of Electron Transfer to the L-side Versus the M-side of the Photosynthetic Reaction Center, *Science*, 269 (1995) 940-945.
- [7] C. Kirmaier, D. Weems, D. Holten, M-side Electron Transfer in Reaction Center Mutants with a Lysine near the Nonphotoactive Bacteriochlorophyll, *Biochemistry*, 38 (1999) 11516-11530.
- [8] E. Katilius, T. Turanchik, S. Lin, A.K.W. Taguchi, N.W. Woodbury, B-Side Electron Transfer in a *Rhodobacter sphaeroides* Reaction Center Mutant in Which the B-Side Monomer Bacteriochlorophyll is Replaced with Bacteriopheophytin, *J. Phys. Chem. B*, 103 (1999) 7386-7389.
- [9] C. Kirmaier, C. He, D. Holten, Manipulating the Direction of Electron Transfer in the Bacterial Reaction Center by Swapping Phe for Tyr Near BChl_M (L181) and Tyr for Phe Near BChl_L (M208), *Biochemistry*, 40 (2001) 12132-12139.
- [10] C. Kirmaier, P.D. Laible, K. Czarnecki, A.N. Hata, D.K. Hanson, D.F. Bocian, D. Holten, Comparison of M-side Electron Transfer in *Rb. sphaeroides* and *Rb. capsulatus* Reaction Centers, *J. Phys. Chem. B*, 106 (2002) 1799-1808.
- [11] C. Kirmaier, A. Cua, C. He, D. Holten, D.F. Bocian, Probing M-Branch Electron Transfer and Cofactor Environment in the Bacterial Photosynthetic Reaction Center by the Addition

- of a Hydrogen Bond to the M-side Bacteriopheophytin, *J. Phys. Chem. B*, 106 (2002) 495-503.
- [12] A.L. de Boer, S. Neerken, R. de Wijn, H.P. Permentier, P. Gast, E. Vijgenboom, A.J. Hoff, B-branch electron transfer in reaction centers of *Rhodobacter sphaeroides* assessed with site-directed mutagenesis, *Photosynth. Res.*, 71 (2002) 221-239.
- [13] A.L. de Boer, S. Neerken, R. de Wijn, H.P. Permentier, P. Gast, E. Vijgenboom, A.J. Hoff, High Yield of B-Branch Electron Transfer in a Quadruple Reaction Center Mutant of the Photosynthetic Bacterium *Rhodobacter sphaeroides*, *Biochemistry*, 41 (2002) 3081-3088.
- [14] C. Kirmaier, P.D. Laible, D.K. Hanson, D. Holten, B-side Charge Separation in Bacterial Photosynthetic Reaction Centers: Nanosecond-Timescale Electron Transfer from H_B^- to Q_B , *Biochemistry*, 42 (2003) 2016-2024.
- [15] E. Katilius, J.L. Babendure, Z. Katiliene, S. Lin, A.K. Taguchi, N.W. Woodbury, Manipulations of the B-Side Charge-Separated States' Energetics in the *Rhodobacter sphaeroides* Reaction Center, *J. Phys. Chem. B*, 107 (2003) 12029-12034.
- [16] M.C. Wakeham, M.G. Goodwin, C. McKibbin, M.R. Jones, Photoaccumulation of the $P^+Q_B^-$ radical pair state in purple bacterial reaction centres that lack the Q_A ubiquinone, *Febs Lett*, 540 (2003) 234-240.
- [17] C. Kirmaier, P.D. Laible, D.K. Hanson, D. Holten, B-side electron transfer to form $P^+H_B^-$ in reaction centers from the F(L181)Y/Y(M208)F mutant of *Rhodobacter capsulatus*, *J. Phys. Chem. B*, 108 (2004) 11827-11832.
- [18] M.C. Wakeham, J. Breton, E. Nabedryk, M.R. Jones, Formation of a semiquinone at the Q_B site by A- or B-branch electron transfer in the reaction center from *Rhodobacter sphaeroides*, *Biochemistry*, 43 (2004) 4755-4763.
- [19] J. Breton, M.C. Wakeham, P.K. Fyfe, M.R. Jones, E. Nabedryk, Characterization of the bonding interactions of $Q(B)$ upon photoreduction via A-branch or B-branch electron transfer in mutant reaction centers from *Rhodobacter sphaeroides*, *Biochimica et Biophysica Acta*, 1656 (2004) 127-138.
- [20] M.C. Wakeham, M.R. Jones, Rewiring Photosynthesis: Engineering Wrong-Way Electron Transfer in the Purple Bacterial Reaction Center, *Biochem Soc T*, 133 (2005) 851-857.
- [21] D. Frolov, M.C. Wakeham, E.G. Andrizhiyevskaya, M.R. Jones, R. van Grondelle, Investigation of B-branch electron transfer by femtosecond time resolved spectroscopy in a *Rhodobacter sphaeroides* reaction centre that lacks the Q_A ubiquinone, *Biochim. Biophys. Acta*, 1707 (2005) 189-198.
- [22] M.L. Paddock, C. Chang, Q. Xu, E.C. Abresch, H.L. Axelrod, G. Feher, M.Y. Okamura, Quinone (Q_B) reduction by B-branch electron transfer in mutant bacterial reaction centers from *Rhodobacter sphaeroides*: Quantum efficiency and X-ray structure, *Biochemistry*, 44 (2005) 6920-6928.
- [23] J.I. Chuang, S.G. Boxer, D. Holten, C. Kirmaier, High yield of M-side electron transfer in mutants of *Rhodobacter capsulatus* reaction centers lacking the L-side bacteriopheophytin, *Biochemistry*, 45 (2006) 3845-3851.
- [24] M.L. Paddock, M. Flores, R. Isaacson, C. Chang, E.C. Abresch, P. Selvaduray, M.Y. Okamura, Trapped conformational states of semiquinone ($D(+center dot)Q(B)(-center dot)$) formed by B-Branch electron transfer at low temperature in *Rhodobacter sphaeroides* reaction centers, *Biochemistry*, 45 (2006) 14032-14042.

- [25] H.L. Kee, P.D. Laible, J.A. Bautista, D.K. Hanson, D. Holten, C. Kirmaier, Determination of the rate and yield of B-side quinone reduction in *Rhodobacter capsulatus* reaction centers, *Biochemistry*, 45 (2006) 7314-7322.
- [26] B. Carter, S.G. Boxer, D. Holten, C. Kirmaier, Photochemistry of a Bacterial Photosynthetic Reaction Center Missing the Initial Bacteriochlorophyll Electron Acceptor, *J. Phys. Chem. B*, 116 (2012) 9971-9982.
- [27] M. Saggi, B. Carter, X. Zhou, K. Faries, L. Cegelski, D. Holten, S.G. Boxer, C. Kirmaier, Putative Hydrogen Bond to Tyrosine M208 in Photosynthetic Reaction Centers from *Rhodobacter capsulatus* Significantly Slows Primary Charge Separation, *J. Phys. Chem. B*, 118 (2014) 6721-6732.
- [28] K.M. Faries, L.L. Kressel, M.J. Wander, D. Holten, P.D. Laible, C. Kirmaier, D.K. Hanson, High Throughput Engineering to Revitalize a Vestigial Electron Transfer Pathway in Bacterial Photosynthetic Reaction Centers, *J. Biol. Chem.*, 287 (2012) 8507-8514.
- [29] L. Kressel, K.M. Faries, M.J. Wander, C.E. Zogzas, R.J. Mejdrich, D.K. Hanson, D. Holten, P.D. Laible, C. Kirmaier, High yield of secondary B-side electron transfer in mutant *Rhodobacter capsulatus* reaction centers, *Biochim. Biophys. Acta.*, 1837 (2014) 1892-1903.
- [30] W.J. Coleman, E.J. Bylina, W. Aumeier, J. Siegl, U. Eberl, R. Heckmann, A. Ogrodnik, M.E. Michel-Beyerle, D.C. Youvan, Influence of Mutagenic Replacements of Tryptophan M250 on Electron Transfer Rates Involving Primary Quinone in Reaction Centers of *Rhodobacter capsulatus*, in: M.E. Michel-Beyerle (Ed.) *Structure and Function of Bacterial Photosynthetic Reaction Centers*, Springer-Verlag, New York, 1990, pp. 273-281.
- [31] W.W. Parson, Z.T. Chu, A. Warshel, Electrostatic Control of Charge Separation in Bacterial Photosynthesis, *Biochim. Biophys. Acta*, 1017 (1990) 251-272.
- [32] R.G. Alden, W.W. Parson, Z.T. Chu, A. Warshel, Orientation of the OH Dipole of Tyrosine (M)210 and Its Effect on Electrostatic Energies in Photosynthetic Bacterial Reaction Centers, *J. Phys. Chem.*, 100 (1996) 16761-16770.
- [33] C. Kirmaier, D. Gaul, R. DeBey, D. Holten, C.C. Schenck, Charge Separation in a Reaction Center Incorporating Bacteriochlorophyll in Place of Photoactive Bacteriopheophytin, *Science*, 251 (1991) 922-927.
- [34] E. Nabedryk, J.P. Allen, A.K.W. Taguchi, J.C. Williams, N.W. Woodbury, J. Breton, Fourier-Transform Infrared Study of the Primary Electron-Donor in Chromatophores of *Rhodobacter sphaeroides* with Reaction Centers Genetically-Modified at Residue-M160 and Residue-L131, *Biochemistry*, 32 (1993) 13879-13885.
- [35] F. Muh, J.C. Williams, J.P. Allen, W. Lubitz, A Conformational Change of the Photoactive Bacteriopheophytin in Reaction Centers from *Rhodobacter sphaeroides*, *Biochemistry*, 37 (1998) 13066-13074.
- [36] C. Kirmaier, P.D. Laible, E. Hinden, D.K. Hanson, D. Holten, Detergent Effects on Primary Charge Separation in Wild-Type and Mutant *Rhodobacter capsulatus* Reaction Centers, *Chem. Phys.*, 294 (2003) 305-318.
- [37] C. Kirmaier, D. Holten, Low-Temperature Studies of Electron Transfer to the M Side of YFH Reaction Centers from *Rhodobacter capsulatus*, *J. Phys. Chem. B*, 113 (2009) 1132-1142.
- [38] J. Breton, J.L. Martin, J.C. Lambry, S.J. Robles, D.C. Youvan, Ground State and Femtosecond Transient Absorption Spectroscopy of a Mutant of *Rhodobacter capsulatus* which Lacks the Initial Electron Acceptor Bacteriopheophytin, in: M.E. Michel-Beyerle

- (Ed.) Structure and Function of Bacterial Photosynthetic Reaction Centers, Springer-Verlag, New York, **1990**, pp. 293-302.
- [39] J.I. Chuang, S.G. Boxer, D. Holten, C. Kirmaier, Temperature Dependence of Electron Transfer to the M-side Bacteriopheophytin in *Rhodobacter capsulatus* Reaction Centers, *J. Phys. Chem. B*, 112 (2008) 5487-5499.
- [40] B.A. Heller, D. Holten, C. Kirmaier, Effects of Asp Residues Near the L-side Pigments in Bacterial Reaction Centers, *Biochemistry*, 35 (1996) 15418-15427.
- [41] C. Kirmaier, L. Laporte, C.C. Schenck, D. Holten, The Nature and Dynamics of the Charge-Separated Intermediate in Reaction Centers in Which Bacteriochlorophyll Replaces the Photoactive Bacteriopheophytin .2. The Rates and Yields of Charge Separation and Recombination, *J. Phys. Chem.*, 99 (1995) 8910-8917.
- [42] L. Laporte, L.M. McDowell, C. Kirmaier, C.C. Schenck, D. Holten, Insights into the Factors Controlling the Rates of the Deactivation Processes That Compete with Charge Separation in Photosynthetic Reaction Centers, *Chem. Phys.*, 176 (1993) 615-629.
- [43] N.W. Woodbury, J.M. Peloquin, R.G. Alden, X. Lin, S. Lin, A.K.W. Taguchi, J.C. Williams, J.P. Allen, Relationship between Thermodynamics and Mechanism during Photoinduced Charge Separation in Reaction Centers from *Rhodobacter Sphaeroides*, *Biochemistry*, 33 (1994) 8101-8112.
- [44] A. Ivancich, K. Artz, J.C. Williams, J.P. Allen, T.A. Mattioli, Effects of Hydrogen Bonds on the Redox Potential and Electronic Structure of the Bacterial Primary Electron Donor, *Biochemistry*, 37 (1998) 11812-11820.
- [45] C.-K. Tang, J.C. Williams, A.K.W. Taguchi, J.P. Allen, N.W. Woodbury, $P^+H_A^-$ Charge Recombination Rate Constant in *Rhodobacter sphaeroides* Reaction Centers is Independent of P/P^+ Midpoint Potential, *Biochemistry*, 38 (1999) 8794-8799.
- [46] K. Gibasiewicz, M. Pajzderska, J.A. Potter, P.K. Fyfe, A. Dobek, K. Brettel, M.R. Jones, Mechanism of Recombination of the $P^+H_A^-$ Radical Pair in Mutant *Rhodobacter sphaeroides* Reaction Centers with Modified Free Energy Gaps Between $P^+B_A^-$ and $P^+H_A^-$, *J. Phys. Chem. B*, 115 (2011) 13037-13050.
- [47] K. Gibasiewicz, M. Pajzderska, A. Dobek, J. Karolczak, G. Burdzinski, K. Brettel, M.R. Jones, Analysis of the temperature-dependence of $P^+H_A^-$ charge recombination in the *Rhodobacter sphaeroides* reaction center suggests nanosecond temperature-independent protein relaxation, *Phys Chem Chem Phys*, 15 (2013) 16321-16333.
- [48] P.K. Fyfe, J.R. Ridge, K.E. McAuley, R.J. Cogdell, N.W. Isaacs, M.R. Jones, Structural Consequences of the Replacement of Glucine M203 with Aspartic Acid in the Reaction Center from *Rhodobacter sphaeroides*, *Biochemistry*, 39 (2000) 5953-5960.
- [49] A.G. Yakovlev, L.G. Vasilieva, A.Y. Shkuropatov, T.I. Bolgarina, V.A. Shkuropatova, V.A. Shuvalov, Mechanism of charge separation and stabilization of separated charges in reaction centers of *Chloroflexus aurantiacus* and of YM210W(L) mutants of *Rhodobacter sphaeroides* excited by 20 fs pulses at 90 K, *J Phys Chem A*, 107 (2003) 8330-8338.
- [50] A.G. Yakovlev, M.R. Jones, J.A. Potter, P.K. Fyfe, L.G. Vasilieva, A.Y. Shkuropatov, V.A. Shuvalov, Primary charge separation between P^* and B_A : Electron-transfer pathways in native and mutant GM203L bacterial reaction centers, *Chem. Phys.*, 319 (2005) 297-307.
- [51] N. Ivashin, S. Larsson, Trapped water molecule in the charge separation of a bacterial reaction center, *J. Phys. Chem. B*, 112 (2008) 12124-12133.

- [52] A.G. Yakovlev, A.Y. Khmel'nitsky, V.A. Shuvalov, Femtosecond charge separation in dry films of reaction centers of *Rhodobacter sphaeroides* and *Chloroflexus aurantiacus*, *Biochemistry-Moscow*, 77 (2012) 444-455.
- [53] N.V. Ivashin, E.E. Shchupak, Mechanism by which a single water molecule affects primary charge separation kinetics in a bacterial photosynthetic reaction center of *Rhodobacter sphaeroides*, *Opt. Spectrosc.*, 113 (2012) 474-486.

Chapter 6: Species Differences in Unlocking B-side Electron Transfer in Bacterial Reaction Centers

Reprinted with permission from Dylla, N.P.; **Faries, K.M.**; Wyllie, R.M.; Swenson, A.M.; Hanson, D.K.; Holten, D.; Kirmaier, C.; Laible, P.D. (2016) Species differences in unlocking B-side electron transfer in bacterial reaction centers. *FEBS Letters*, 590, 2515-2526.

Abstract

The structure of the bacterial photosynthetic reaction center (RC) reveals symmetry-related electron transfer (ET) pathways but only one path is used in native RCs. Analogous mutations have been made in two *Rhodobacter* (*R.*) species. A glutamic acid at position 133 in the M subunit increases transmembrane charge separation via the naturally inactive (B-side) path through impacts on primary ET in mutant *R. sphaeroides* RCs. Prior work showed that the analogous substitution in the *R. capsulatus* RC also increases B-side activity, but mainly affects secondary ET. The overall yields of transmembrane ET are similar but enabled in fundamentally different ways.

1. Introduction

Photosynthetic organisms convert light into chemical energy using transmembrane complexes known as reaction centers (RCs). They are comprised of three subunits – L, M, and H (Fig. 1A) – and cofactors that include bacteriochlorophylls (P, B), bacteriopheophytins (H), and quinones (Q). Structures of RCs from purple, non-sulfur bacteria, first reported 30 years ago [1,2], reveal a striking axis of approximate C_2 symmetry that relates the homologous L and M chains and two paths of electron transfer (ET) cofactors (Fig. 1B). Earlier functional studies had established that only one of them, the so-called A side, supports ET (reviewed in [3]); the other is possibly vestigial. Since then, many studies have sought to determine the means to activate the B-side ET pathway, with limited success (reviewed in [4]).

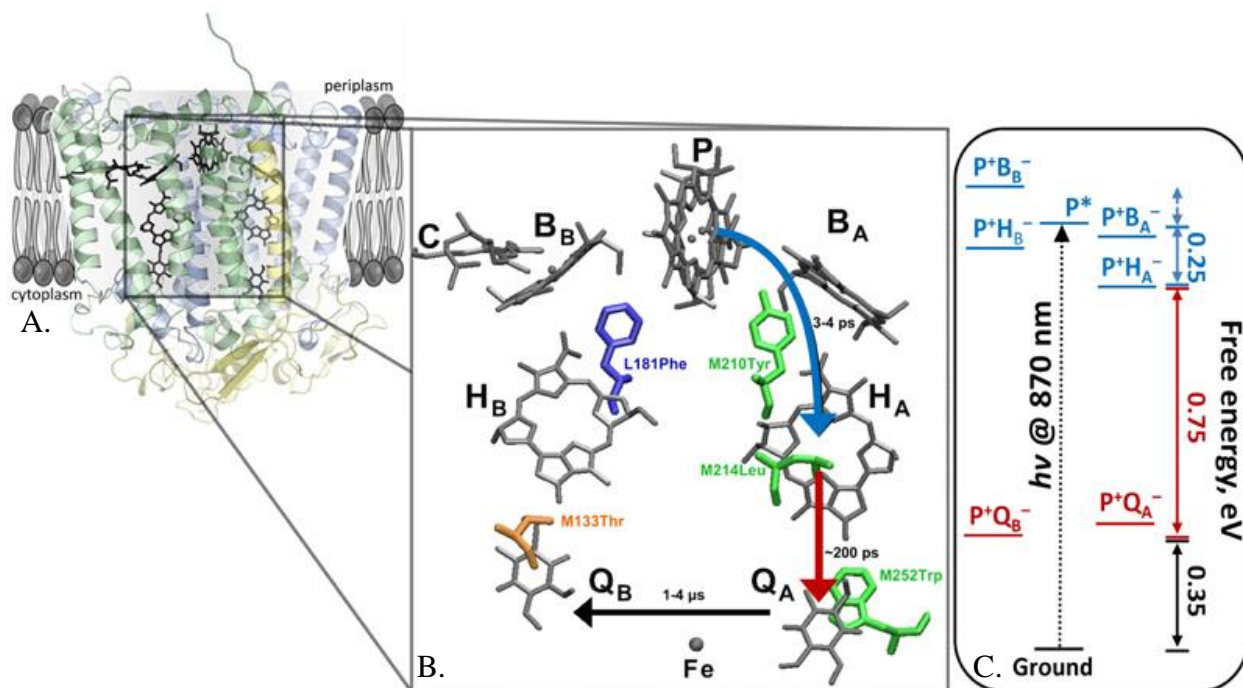


Figure 1. The structure of the bacterial RC. (panel A) The membrane localization and orientation of the three subunits (L, blue; M, green; and H, yellow); (panel B) Cofactors (gray) and the A-side ET pathway (from P^* to $P^+Q_B^-$) in wild-type *Rhodobacter* RCs, from the crystal structure of the *R. sphaeroides* RC (PDB code 1PCR; [8]). The cofactors include a specialized dimer of bacteriochlorophylls (P) that serves as the primary electron donor, two bacteriochlorophyll monomers (B_A and B_B), two bacteriopheophytins (H_A and H_B), and two quinones (Q_A and Q_B); a carotenoid (C) positioned between P and B_B serves as protection against oxidative radicals. This pathway is split into primary (blue; $P^* \rightarrow P^+H_A^-$) and secondary (red; $P^+H_A^- \rightarrow P^+Q_A^-$) ET steps. The positions of the amino acids substituted in this study relative to the cofactors are shown for reference (green comprise the core set of targeted residues: M210Tyr, M214Leu, and M252Trp; blue represents residue L181Phe that was subjected to saturation mutagenesis; and M133Thr is shown in orange); and (panel C) model free-energy diagram for WT RCs (charge-separated states involved in primary ET, blue; states involved in secondary ET, red).

The *Rhodobacter (R.) capsulatus* RC was the initial vehicle for investigating structure/function relationships since it was the first for which a genetic system was developed [5]. It shares a high degree of sequence similarity with the RC of *R. sphaeroides*, whose crystal structure is known [1,6-8]. RCs from *R. capsulatus* have continued to lead discovery of the delicate balance of protein-cofactor interactions that can support ET via the B-side path. As a means to identify variants that are competent in the reduction of Q_B via sole activity of the B-side ET cofactors, streamlined mutagenesis and protein purification strategies have been developed [9-11].

In this study, we describe construction of a similar mutagenesis platform for the *R. sphaeroides* RC and use it to provide new insight and/or complementary validation of structure-function relationships that dictate rates and directionality of ET in RCs. The *R. sphaeroides* mutants generated and investigated here bear a ‘core’ set of mutations (“FHV”; Table 1) that have been shown previously to enhance B-side ET at the expense of A-side ET (Fig. 1; [10,12,13]). The W(M252)V mutation prevents binding of the A-side quinone, Q_A [14,15], thus, any quinone reduction that is observed in RCs with the “V” mutation is obtained solely via ET from the primary donor (P^*) to the B-side cofactors (Fig. 1B). The L(M214)H (“H”) mutation results in incorporation of a bacteriochlorophyll [16], denoted β , in place of H_A . This substitution provides a clear spectroscopic window in which to observe ET to H_B . A conserved C_2 asymmetry is represented by residues L181Phe (near P and B_B ; Fig. 1) and M210Tyr (near P and B_A). Much work supports the model that the native Tyr at M210 lowers the free energy of the charge-separated state $P^+B_A^-$ while a Phe at L181 on the B side provides no parallel effect on the free energy of $P^+B_B^-$ (Fig. 1C; [17-21]). Reversal of this asymmetry hinders ET to the A side (M210“F”) and promotes ET to the B side (L181“Y”) [12,22,23].

Table 1. Rationale for choice of substitutions employed in this study.

Mutation	Designation	Desired Effect(s)
F(L181)Y	Y	Mimic A-side WT residue [†] M210Tyr to increase ET to H _B
Y(M208)F	F	Mimic B-Side WT residue L181Phe to decrease ET to H _A
[†]Y(M210)F		
V(M131)E	E	Mimic A-side WT residue L104Glu to increase ET from H _B to Q _B and decrease P ⁺ H _B ⁻ charge recombination
[†]T(M133)E		
L(M212)H	H	Replace H _A with a bacteriochlorophyll to decrease A-side ET
[†]L(M214)H		
W(M250)V	V	Block binding of Q _A , eliminating Q _B reduction from A pathway
[†]W(M252)V		
F(L181)X	--	Identify residues that might favor B-side ET to H _B via saturation mutagenesis

[†]The *R. sphaeroides* M subunit contains two additional amino acids, as reflected in numbering of these homologous residues.

Another conserved C₂ asymmetry is represented by residue M133 in *R. sphaeroides* (M131 in *R. capsulatus*), positioned between H_B and Q_B (Fig. 1B), which mirrors the A-side residue L104Glu known to form a hydrogen bond with H_A [24]. Previous work has shown that Asp or Glu substituted at M133/M131 can form a hydrogen bond with H_B [25-28], promoting its reduction. The combination of the V(M131)E (“E”) substitution with the ‘core’ FHV and YFHV mutations in the *R. capsulatus* RC has resulted in large increases in yields of B-side ET [9,11].

The ‘E+FHV’ and ‘E+YFHV’ mutants have now been constructed in the *R. sphaeroides* RC, and the L181 site has been targeted for saturation mutagenesis in the FHV and E+FHV backgrounds. Effects of the mutations on B-side ET are compared with the effects of the analogous mutations in RCs of *R. capsulatus*. Previously such comparison studies of analogous

mutants from these two species have revealed lower (typically about twofold) initial B-side activity in the *R. sphaeroides* analog [4,29-31]. Here, in sharp contrast, a case is revealed where the B-side path is activated to a larger extent in *R. sphaeroides* RCs. Thus, key residues are found to unlock the B-side pathway differentially in RCs of related species.

2. Materials and Methods

Plasmids and strains used in this study are described in Table S1. Mutant *R. capsulatus* RCs have been described previously [10]. *R. sphaeroides* mutants were constructed within a new expression plasmid that was developed for high-throughput RC mutagenesis in this species. Its features are summarized in Figure 2 and Tables S2 and S3. Mutant RCs were expressed in *R. sphaeroides* host strain Δ rshI [32], a new transformable strain enabled by alteration of genes involved in restriction/modification (details of design and construction of expression plasmid and host strain are found in the Supporting Information). RCs of *R. sphaeroides* that are produced from the new expression plasmid in Δ rshI reside in an antennaeless, ‘RC-only’ membrane that is required for solubilization and subsequent purification of multiply-mutated variants with the mild detergent Deriphat 160C; these conditions favor maximal retention of quinone binding.

The T(M133)E+FHV and T(M133)E+YFHV mutants were constructed by replacement of the WT region F (Fig. 2; Table S2) with a synthetic cassette (Eurofins). For saturation mutagenesis of the L181 site in both the FHV and T(M133)E+FHV backgrounds, a set of oligonucleotides encoding all 20 amino acids was designed that replaced the WT segment containing region D (Fig. 2; Table S2). Q_A-containing variants of selected mutant RCs were made by insertion of a segment carrying the WT Trp residue at M252 (region O; Fig. 2; Table S2). In all cases, candidate plasmids isolated from *E. coli* transformants (DH5 α or *E. cloni*) were

screened using restriction fragment analysis and sequenced. Mutant plasmids were transferred to expression host Δ rshI via electroporation (2500 V, 25 °F, 400 Ω ; 2 mm cuvette; [33]).

E. coli strains were propagated on LB or 2xTY media. *R. sphaeroides* strains were cultured on ^GYCC (YCC medium [34] containing an additional 1 g/L of yeast extract, pH 7.1) under semi-aerobic, chemoheterotrophic conditions in the dark (2 L medium in a 2.8 L baffled Fernbach flask, 125 rpm, silicone sponge closures, 33°C). Plasmids were selected with kanamycin (Km; 30 μ g/ml), gentamicin (Gm; 12 μ g/ml for *E. coli*; 24 μ g/ml for *R. sphaeroides*) or tetracycline (Tc; 15 μ g/ml for *E. coli*; 1 μ g/ml for *R. sphaeroides*).

Culture volumes of expression strains (2-12 L) varied depending upon levels of RCs that could be isolated. When cultures neared stationary phase, cells were harvested, lysed and frozen. Membrane proteins were solubilized and RCs were purified in the presence of Deriphat 160C as described previously [10,30], in the absence of separating membranes from the soluble fraction by ultracentrifugation. The imidazole eluant was removed using a PD-10 desalting column (GE Healthcare). The RCs were concentrated to $A_{860\text{nm}}$ of 2.5 in a spin concentrator (50 kDa cutoff filter; Millipore).

Ground-state spectra, millisecond (ms) screening assays, ultrafast transient absorption (TA) experiments, and measurements of Q_B site occupancy followed procedures reported earlier [11]. Specifically, a 100-fs, 1 KHz laser system (Spectra Physics) with Helios or EOS spectrometers (Ultrafast Systems) were used for TA experiments. RC samples were held in a standard 2 mm path cuvette and stirred. Other conditions as described previously [9].

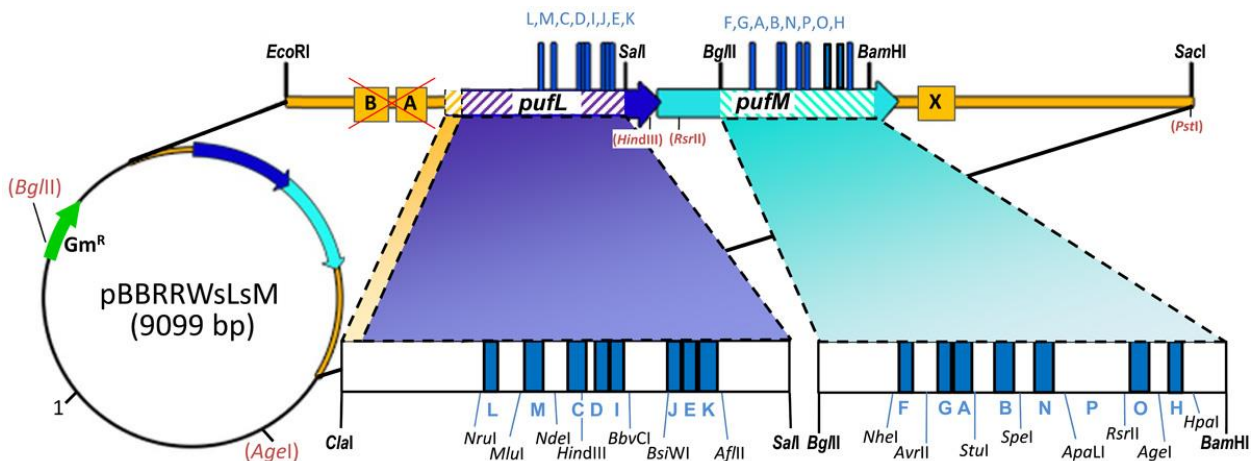


Figure 2. Engineered expression vector for RC mutagenesis in *R. sphaeroides*. Segments of the L and M genes targeted for mutagenesis (striped regions and Table S2) are flanked by unique restriction sites that facilitate the insertions of oligonucleotide cassettes encoding one or more substitutions. In addition to seven sites removed previously from broad-host-range vector pBBR1MCS-2 [10], five restriction sites (red, in parentheses) in this new plasmid were removed to enable the cassette-based mutagenesis approach (Table S3). To disable synthesis of the LHI antenna complex, the *pufB* and *pufA* genes were replaced by a synthetic cassette.

3. Results

The effectiveness of the V(M131)E substitution in promoting B-side activity was probed by constructing analogous mutants of the *R. sphaeroides* RC – T(M133)E+FHV and T(M133)E+YFHV – and by characterizing the primary ET reactions (Fig. 1B,C; reactions originating from P*) using ultrafast TA spectroscopy. Fig. 3 compares spectra recorded in the visible region for the FHV and E+FHV mutants of *R. sphaeroides* to those of the analogous and previously reported mutants of *R. capsulatus*. Fig. 4 similarly compares the results for the YFHV and E+YFHV mutant RCs of *R. sphaeroides* and *R. capsulatus*. The 0.6 ps spectrum in each panel is due to the excited state of the primary donor (P*). It displays bleaching of the 600-

nm ground-state band of P and absorption features of P* (to the red and the blue of this bleach). At subsequent times, the bleaching of the Q_x absorption band of H_B (at 527-535 nm; dotted lines) increases as P* decays, reflecting formation of P⁺H_B⁻. The yields of P⁺H_B⁻ were obtained from integrating the maximal Q_x bleaching of H_B ([9]; Table 2). The T(M133)E mutation had a profound effect of the yields of P⁺H_B⁻ when added to both the FHV and YFHV backgrounds in the *R. sphaeroides* RC, to a larger degree than that seen for the analogous V(M131)E substitution in *R. capsulatus* RCs. The largest yield of P⁺H_B⁻ (59%) is observed for the E+YFHV mutant of the *R. sphaeroides* RC.

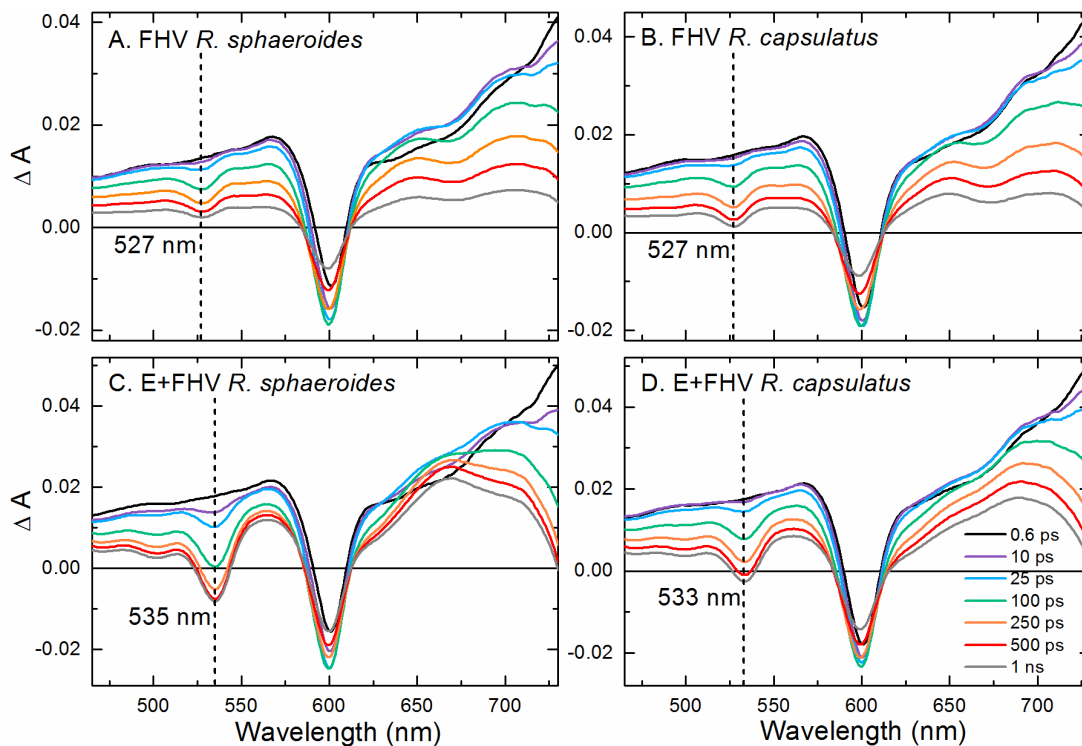


Figure 3. TA spectra obtained 0.6 ps to 1 ns after a ~100-fs excitation flash at 865 nm for *R. sphaeroides* (panels A and C) and *R. capsulatus* (panels B and D) mutant RC samples in the FHV background without (panels A and B) and with (panels C and D) the V/T(M131/M133)E mutation.

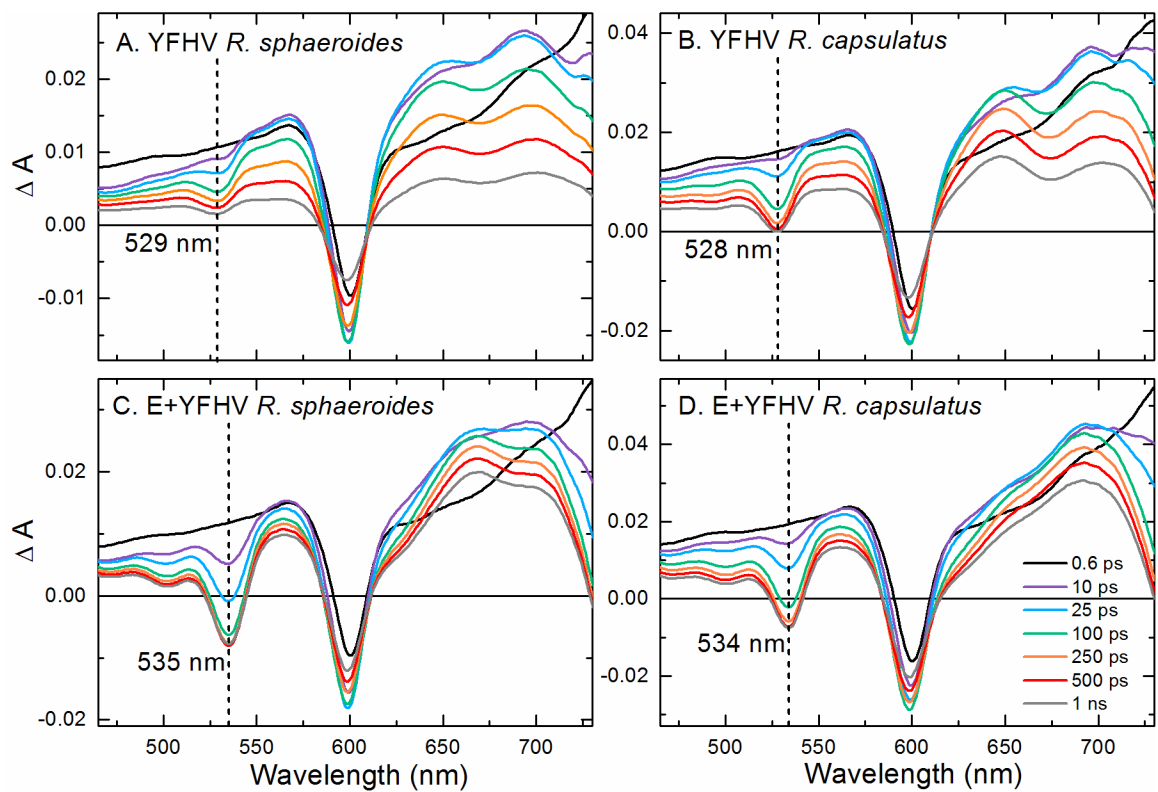


Figure 4. TA spectra obtained 0.6 ps to 1 ns after a ~100-fs excitation flash at 865 nm for *R. sphaeroides* (panels A and C) and *R. capsulatus* (panels B and D) mutant RC samples in the YFHV background without (panels A and B) and with (panels C and D) the V/T(M131/M133)E mutation.

Table 2. Yields, time constants, and transient spectral features of select mutant RCs^a.

Sample	Species	P* Lifetime ^b (ps)	P* Decay Fraction ^c	P ⁺ H _B ⁻ Yield (%) ^d	Position of H _B Bleach (nm)	P ⁺ H _B ⁻ τ _{CR} (ns) ^e	Q _B Occupancy ^f (%)
FHV	<i>R. capsulatus</i>	29	0.62	9	527	6.6	91
	<i>R. sphaeroides</i>	36	0.57	10	527	7.2	95
E+FHV	<i>R. capsulatus</i>	66	0.57	20	533	11.0	64
	<i>R. sphaeroides</i>	31	0.60	41	535	7.3	96
YFHV	<i>R. capsulatus</i>	31	0.79	25	528	4.5	97
	<i>R. sphaeroides</i>	14	0.86	19	529	5.0	100
E+YFHV	<i>R. capsulatus</i>	28	0.80	42	534	11.2	78
	<i>R. sphaeroides</i>	16	0.94	59	535	8.5	99

^aQ_B occupancy and P⁺Q_B⁻ yields are ~100% in WT RCs of both species.

^bAmplitude-weighted lifetime from two fast components (typically ~4-10 ps and ~20-50 ps).

^cFraction of the P* decay in the two fast components versus the slower component (~130-250 ps).

^dP⁺H_B⁻ yields have errors of ±10%.

^eThe reported value for the P⁺H_B⁻ τ_{CR} time constant has a typical error of ±10%.

^fThe reported value for the Q_B occupancy has an error of ± 5%.

Consistent with previous findings for the V(M131)E mutation in *R. capsulatus* [9,11], the Q_x bleach of H_B shows a shift to longer wavelength in *R. sphaeroides* RCs carrying the T(M133)E mutation (to ~535 nm from ~527 nm; Figs. 3,4 and Table 2) when compared to RCs with the native residue. Spectral shifts of the H_B anion (transient absorption of H_B⁻) attributable to the T(M133)E mutation are also resolved. These differences are most pronounced in the 1 ns spectra in Figs. 3,4 (gray), also seen in Figs. S6, S7 (black). With the addition of the T(M133)E mutation to either FHV or YFHV RCs, H_B⁻ absorption shifts to ~665 nm from ~650 nm in *R. sphaeroides*; they shift even more dramatically to the red (>690 nm) in the V(M131)E-

containing *R. capsulatus* mutant RCs. Determination of the exact position of this spectral feature is complicated by its spectral overlap with the absorption of β^- and the varying relative yields of the β and H_B anions in these mutants.

In contrast to the striking improvements in B-side activity observed with the T(M133)E substitution in the *R. sphaeroides* RC are the results obtained for the F(L181)Y substitution when comparing the FHV and YFHV mutant RCs. B-side activity is enhanced by the Y mutation, but only marginally in comparison. Yields of $P^+H_B^-$ improved by 9% and 18% in the FHV and E+FHV backgrounds, respectively, in *R. sphaeroides*, and by 16% and 22% in the corresponding mutants of *R. capsulatus*. The Tyr substitution at L181 had the greatest relative effect in *R. capsulatus* with respect to $P^+H_B^-$ yields (Table 2).

The P^* decays in these eight mutants (Table 2) are multi-exponential. The P^* lifetimes given in Table 2 are amplitude-weighted values comprised of the two shortest components [9]. Together these account for most of the P^* stimulated emission decay profile when fit to a 3-exponential function (the remainder is described by a ~130-250 ps component. Notably, the P^* decay tends to be faster in the *R. sphaeroides* mutants. Further, in the E+YFHV mutant of *R. sphaeroides*, the two fastest components account for 94% of P^* decay, almost eliminating the long component that reflects P^* internal conversion to the ground state.

To explore the T(M133)E in a larger number of *R. sphaeroides* RCs, the ms screening assay [10] was used to survey two sets of mutants – F(L181)X+FHV and T(M133)E+F(L181)X+FHV – for their ability to produce $P^+Q_B^-$. For the F(L181)X+FHV set, 17 new mutant RCs were examined; fifteen new mutant RCs were assayed for the T(M133)E+F(L181)X+FHV set. As seen in Fig. 5A, for about two-thirds of the *R. sphaeroides* RCs, the yields of B-side ET are substantially larger in the M133E+L181X+FHV mutant than in

the corresponding variant having the native Thr at M133. The highest yield of $P^+Q_B^-$ occurs for the mutant having Tyr at L181 in the E+FHV background.

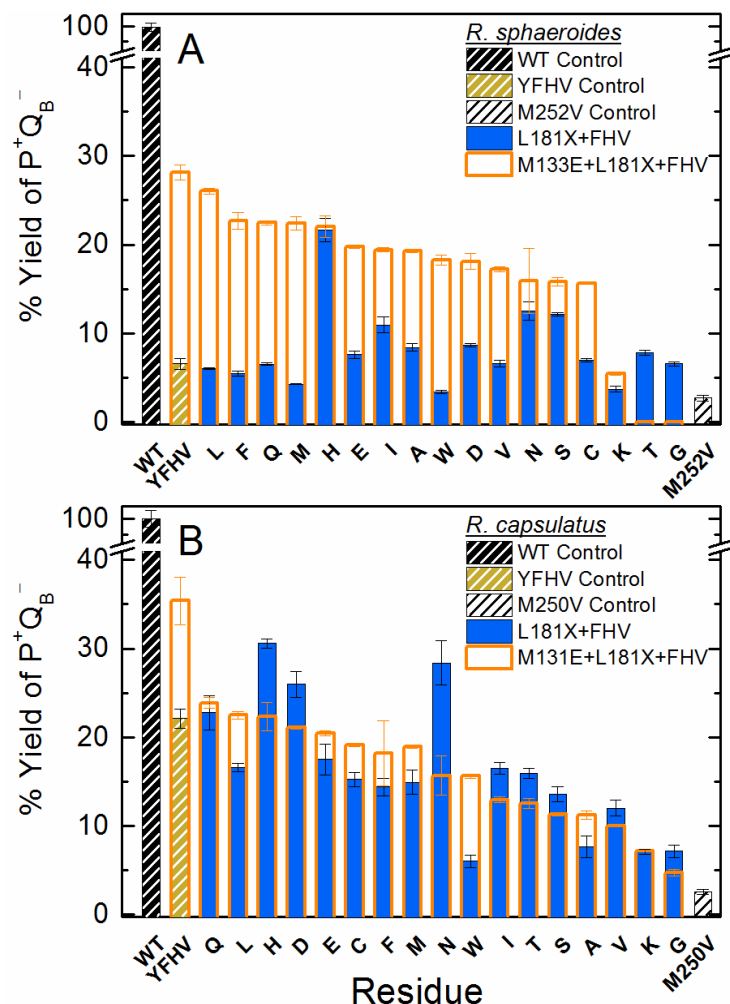


Figure 5. $P^+Q_B^-$ yields obtained for *R. sphaeroides* (panel A) and *R. capsulatus* (panel B and [10,11]) mutant RCs (as compared to WT, black bars) following a 7-ns, 532 nm excitation flash utilized by the millisecond screening assay [10]. Filled, blue bars represent mutants with the F(L181)X+FHV background. Unfilled, orange bars represent mutants with the V/T(M131/M133)E mutation, in addition to the F(L181)X+FHV background. RCs of both species carrying the P or R substitutions could not be purified; in addition, RCs carrying the G or T substitutions in the T(M133)E+FHV background of *R. sphaeroides* could not be purified.

This observation is contrasted by analogous sets of *R. capsulatus* mutants (Fig. 5B) where, in general, the efficacy of M131E substitution is smaller. This observation stems in some part from the negative impact of the V(M131)E mutation on binding of Q_B ([9]; Table 2; Fig. S5). The degree of occupancy of the Q_B site was determined for the four T(M133)E-containing mutant *R. sphaeroides* RCs that were characterized more comprehensively. The Q_B assay requires RCs in which Q_A is present; for these four mutants, variants were constructed in which the WT Q_A binding site was regenerated. The results for Q_B occupancy in mutant RCs of both species are given in Table 2 (see also Fig. S5). Unlike the *R. capsulatus* mutant RCs, the two *R. sphaeroides* RCs with the T(M133)E substitution retain quantitative binding of Q_B (within our ability to measure it). A clear conclusion from Fig. 5 is that the M133E mutation in *R. sphaeroides* RC strongly enhances the yield of B-side charge separation.

The highest yields of P⁺Q_B⁻ in the four *R. sphaeroides* mutant RCs selected for comprehensive characterization are approximately half that of P⁺H_B⁻, thus efficiencies of secondary ET (P⁺H_B⁻ → P⁺Q_B⁻) in these mutant RCs approach 50% at best. The rates of forward ET to Q_B are known to be on a par with the rate of charge recombination of P⁺H_B⁻ → ground state in the *R. capsulatus* RC [9] and a similar outcome is observed here. The time constant of the charge recombination process P⁺H_B⁻ → ground state was measured for the four *R. sphaeroides* mutants studied in more detail (using samples to which terbutryn was added to displace Q_B) and range from ~5 to ~9 ns (Table 2). The results indicate that P⁺H_B⁻ charge recombination in the *R. sphaeroides* RC may be somewhat less sensitive to a Glu at M133 than the analogous *R. capsulatus* mutants where a more significant slowing of this process is obtained (as long as 11 ns; Table 2).

4. Discussion

The symmetrical arrangement of cofactors of the bacterial RC (Fig. 1A,B) has proven to be a general architecture that is preserved in the photosynthetic apparatus of cyanobacteria, algae and higher plants – photosystems I [35,36] and II [37-41]. In type I RCs (e.g., photosystem I), both sets of cofactors are active to produce reduced quinones with relative activities of the A- and B-branches varying depending on the organism or conditions [42-56]. In type II RCs (e.g., purple bacterial RCs and photosystem II), ET to the B cofactors is quantitatively suppressed (e.g., [57]).

Since the crystal structure of the bacterial RC was reported in 1985 [2], an array of biophysical and biochemical techniques has been applied to numerous mutant RCs to determine the basis of the functional asymmetry by which only one set of cofactors is used for ET. It is clear that the protein modulates the redox properties, spatial arrangement, and extent of electronic coupling of the cofactors. However, the specifics of how amino acid side chains fine-tune the functional properties of individual cofactors are still under-explored in both energetic and structural terms. Advances in genetic systems empowered by synthetic biology have enabled higher-throughput approaches to the study of structure/function relationships.

The mutagenesis system employed here utilizes synthetic oligonucleotide cassettes. This strategy circumvents the difficulties in site-directed mutagenesis that are imposed by the high degree of sequence similarity between the *pufL* and *pufM* genes (especially in highly-conserved regions that surround the cofactors). This design can be adapted to plate-based methods (as done here), allowing rapid discovery of effective substitutions and facile iteration of them into next-generation mutant RCs.

Directional cloning of cassettes (Fig. 2; Table S2) required a broad-host-range expression plasmid that was significantly downsized and engineered as compared to the one constructed

previously for mutagenesis of the *R. sphaeroides pufL* and *pufM* genes [58]. The yield of RCs expressed from the new, partially-synthetic plasmid have been up to four times greater than the yield obtained from the original one. This result may be due to differences in plasmid copy number and/or (i) codon preferences, (ii) unexpected changes in transcript stability, or (iii) modification of regulatory elements that occurred as a result of the engineering that was required. A significant time savings (of up to a week in the process of constructing a set of mutants) was also afforded by the construction of Δ rshI – a transformable, *R. sphaeroides* expression host strain.

We have exploited these advances here to compare parallel *R. sphaeroides* and *R. capsulatus* mutant RCs. Dissimilarities in the detailed functioning of RCs with the *Rhodobacter* genus have long been noted, especially between *R. sphaeroides* and *R. capsulatus* RCs. These differences are remarkable given that the complexes have identical cofactors and share high sequence similarities, especially in the residues of the transmembrane L and M chains that interact with the cofactors. For the small sampling of analogous mutants in which yields of B-side ET have been compared previously, the *R. sphaeroides* versions show about a two-fold smaller yield of ET to the B side than the *R. capsulatus* analogs, the origin of which is not completely understood [29-31]. Other noted differences in the properties and functioning of these complexes include their sensitivities to detergent. The 865-nm absorption band of P in the *R. capsulatus* RC shifts to ~850 nm in positively charged detergents [59], and Q_B binding is more labile in detergent-purified RCs of *R. capsulatus* [59,60]. Different residues are involved in the delivery of protons to the Q_B anions [61,62], resulting in a species-specific profile of phenotypic revertants that arise from selections for photocompetence in Q_B-site mutants [62,63]. RCs of the two species also differ in their interactions with periplasmic cytochrome *c*₂ [64].

Activity of the B-side ET path is increased by different amounts via differing mechanisms in RCs of *R. capsulatus* and *R. sphaeroides* carrying substitutions of analogous residues. The extent to which the effect of the F(L181)Y substitution is larger in *R. capsulatus* whereas the Glu substitution near H_B is far superior in *R. sphaeroides* is emphasized in Fig. 6. Mutants are positioned on the scale relative to P⁺H_B⁻ yields with *R. capsulatus* RCs on the left and *R. sphaeroides* RCs on the right. In both species, the effects of Tyr and Glu substitutions are cumulative with respect to the overall yields of P⁺Q_B⁻. The yield of P⁺H_B⁻ in the E+YFHV mutant of *R. sphaeroides* (59%) is second only to that found (~70%) in a *R. capsulatus* mutant RC that bears a helix swap (over a dozen amino acid changes) and binds no cofactor in the H_A site [65,66]. While a detailed description of the photophysics of P* decay and primary charge separation is beyond the scope of this work, an interesting point can be made that relates the YFHV and E+YFHV mutants. For these RCs, the P* lifetime (Table 2) in the *R. sphaeroides* variant is about one-half that found in the *R. capsulatus* version. This correlates well, as it should (other things being equal), with about a factor of two larger yield of P⁺H_B⁻ in the *R. sphaeroides* variant compared to *R. capsulatus*.

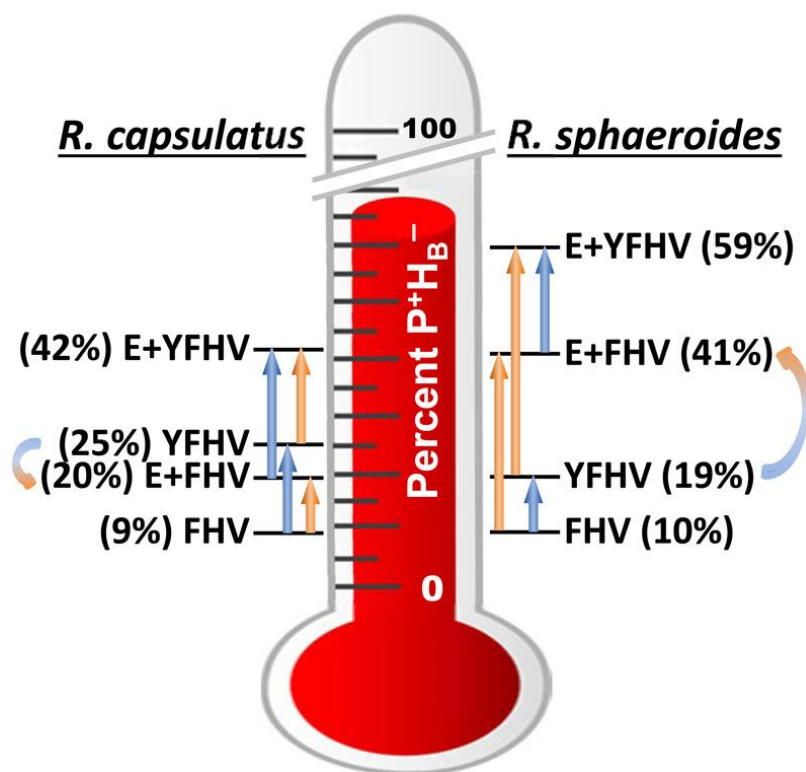


Figure 6. Comparison of increases (arrows) in $P^+H_B^-$ yields as a result of the E substitution at M131/M133, orange, or the Y substitution at L181, blue, in RCs of both *Rhodospirillum rubrum* species.

The red shifts in the positions of the Q_X bleachings of H_B and its anion in the transient spectra of RCs carrying the M133E/M131E substitutions (Figs. 3,4) indicate formation of a hydrogen bond between the Glu and the ring V keto group of H_B , analogous to that formed between L104Glu and H_A at the symmetry-related position in the WT RC [24]. This hydrogen bond is expected to lower of the free energy of $P^+H_B^-$ (Fig. 1C by an estimated 50- 100 meV). This substitution can also influence the observed yield of secondary $P^+H_B^- \rightarrow P^+Q_B^-$ ET by (1)

affecting the binding of Q_B and/or (2) changing the balance between forward ET to Q_B and non-productive charge recombination $P^+H_B^- \rightarrow$ ground state. Quinone retention is reduced in M131E-containing RCs of *R. capsulatus* (~70%, Table 2); however, quinones are quantitatively retained in the parallel subset of four M133E-containing mutant RCs of *R. sphaeroides* (Table 2, Fig. S5). The $P^+H_B^-$ charge recombination lifetime is increased by factors of 1.7 and 2.5 upon addition of M131E to the FHV and YFHV backgrounds, respectively, of *R. capsulatus*, resulting in increased overall $P^+Q_B^-$ yields [9]. However, for the analogous *R. sphaeroides* mutants, the influence of M133E on the secondary $P^+H_B^- \rightarrow P^+Q_B^-$ ET step is more modest (increased the charge recombination lifetimes by factors of 1.1 and 1.7, respectively, in the FHV and YFHV backgrounds). Determination of the time constant for $P^+H_B^- \rightarrow P^+Q_B^-$ forward ET for these *R. sphaeroides* mutants will be undertaken in future work, but it is expected that this forward ET time constant will also be on the order of a few nanoseconds based on the ms screening assay results (Fig. 5A).

The effectiveness of the Glu substitution at M133 in *R. sphaeroides* was rather surprising. However, it is noted that the consequences of these substitutions are likely multifaceted. The free-energy gaps between P^* and the charge-separated states involving B_A , H_A , B_B , and H_B are relatively small (≤ 200 meV; Fig. 1B). When these modest free-energy gaps are diminished even further (or the ordering of the states is reversed) as a consequence of genetic manipulation, the results can be dramatic. The results obtained here indicate a general strong positive effect of M133Glu in the set of L181X mutants of *R. sphaeroides*. This is a perfect example of how a single amino acid can have global effect, in this case presumably lowering the free energy of $P^+H_B^-$ significantly enough to be an advantage for virtually any amino acid at L181. In order for the T(M133)E mutation to have improved B-side yields as much as observed in the *R.*

sphaeroides RCs, it must have increased the rate of primary B-side ET, decreased the rate of primary A-side ET, decreased the fraction of ‘inactive’ RCs [11], and/or decreased the rate of internal P* deactivation. It is also intriguing to consider that the different magnitude of the effects observed when comparing the V(M131)E substitution in *R. capsulatus* to the T(M133)E substitution in *R. sphaeroides* might be explained in terms of the removal of a silencing effect of the threonine on the normally inactive B path. A polar threonine may interact with H_B in ways that are completely different than the hydrophobic valine. Indeed, the V(M131)T substitution reduced B-side ET in the YFHV background of *R. capsulatus* RCs [11]. Unlike the strictly conserved L181Phe, there is a greater degree of variability (e.g., V, T, M, A, and I) at the M133/M131 site in related photosynthetic bacteria.

In conclusion, the details of the operation of an evolutionarily-silenced ET pathway are being elucidated by an approach that generates and screens a large number of structural variants rapidly. Many of the steps in the process can be semi-automated, enabling functional scrutiny of a transmembrane protein-cofactor complex at an accelerated pace. These strategies are now available in two related species and allow the effects of mutations to be compared – and possibly validated – across genera. Using these parallel systems, we have uncovered two residues in *Rhodobacter* RCs that unlock B-pathway ET in two species in different ways. In both species, the F(L181)Y mutation likely lowers the free energy of the P⁺B_B⁻ state and allows the B path to be energetically available/accessible for ET. Similar effects of the F(L181)Y substitution are observed in both species but the relative mixing of states involved in primary ET allows for F(L181)Y-induced B-branch activity to be more pronounced in *R. capsulatus* RCs. In contrast, the T/V(M133/M131)E mutation does little to aid secondary ET in *R. sphaeroides* but assists greatly in *R. capsulatus*. It elicits its primary influence on state P⁺H_B⁻, dramatically increasing

yields of $P^+H_B^-$ in *R. sphaeroides* and slowing $P^+H_B^-$ charge recombination in *R. capsulatus*; its effects on primary ET are most pronounced for *R. sphaeroides*. The effects of the F(L181)Y and V/T(M131/M133)E substitutions are additive in both species. The yield of $P^+H_B^-$ is 42% and 59% in the ‘double mutants’ of *R. capsulatus* and *R. sphaeroides*, respectively, among the highest that have been observed. The differential nature of the effects of the mutations, especially the Glu substitution, is surprising. Residues within the membrane-localized central core of the RC – especially those that are internal to the two branches of cofactors (Fig. 1A,B) – are highly conserved and any natural amino acid variability must retain the functional role of the side chain. The conservation of the core is especially important to retain A-side function; it, however, may be equally important to maintain B-side dysfunction. Such information will be used iteratively toward the ultimate goal of realizing a strain that grows photosynthetically via the sole activity of B-pathway cofactors of the RC.

Acknowledgements

This work was supported by the U. S. Department of Energy, Office of Science, Office of Basic Energy Sciences under grant DE-SC0002036 (to CK and DH) and associated Field Work Proposal (to PDL). Argonne, a U.S. Department of Energy Office of Science laboratory, is operated under Contract No. DE-AC02-06CH11357. KMF was supported by National Science Foundation Graduate Research Fellowship grant DGE-1143954. RMW was supported in part by the U.S. Department of Energy, Office of Science, Office of Workforce Development for Teachers and Scientists under the Science Undergraduate Laboratory Internship Program.

References

- [1] Allen, J.P., Feher, G., Yeates, T.O., Komiyama, H. and Rees, D.C. (1987). Structure of the reaction center from *Rhodobacter sphaeroides* R-26: the protein subunits. Proc Natl Acad Sci U S A 84, 6162-6.
- [2] Deisenhofer, J., Epp, O., Miki, K., Huber, R. and Michel, H. (1985). Structure of the protein subunits in the photosynthetic reaction center from *Rhodospseudomonas viridis* at 3 Å resolution. Nature 318, 618-624.
- [3] Kirmaier, C. and Holten, D. (1987). Primary photochemistry of reaction centers from the photosynthetic purple bacteria. Photosynthesis Research 13, 225-260.
- [4] Wakeham, M.C. and Jones, M.R. (2005). Rewiring photosynthesis: engineering wrong-way electron transfer in the purple bacterial reaction centre. Biochemical Society Transactions 33, 851-7.
- [5] Youvan, D.C., Ismail, S. and Bylina, E.J. (1985). Chromosomal deletion and plasmid complementation of the photosynthetic reaction center and light-harvesting genes from *Rhodospseudomonas capsulata*. Gene 33, 19-30.
- [6] Allen, J.P., Feher, G., Yeates, T.O., Komiyama, H. and Rees, D.C. (1987). Structure of the reaction center from *Rhodobacter sphaeroides* R-26: the cofactors. Proc Natl Acad Sci U S A 84, 5730-4.
- [7] Chang, C.H., el-Kabbani, O., Tiede, D., Norris, J. and Schiffer, M. (1991). Structure of the membrane-bound protein photosynthetic reaction center from *Rhodobacter sphaeroides*. Biochemistry 30, 5352-60.
- [8] Ermler, U., Fritsch, G., Buchanan, S.K. and Michel, H. (1994). Structure of the photosynthetic reaction centre from *Rhodobacter sphaeroides* at 2.65 Å resolution: cofactor and protein-cofactor interactions. Structure 2, 925-936.
- [9] Faries, K.M., Kressel, L.L., Dylla, N.P., Wander, M.J., Hanson, D.K., Holten, D., Laible, P.D. and Kirmaier, C. (2016). Optimizing multi-step B-side charge separation in photosynthetic reaction centers from *Rhodobacter capsulatus*. Biochim Biophys Acta 1857, 150-9.
- [10] Faries, K.M., Kressel, L.L., Wander, M.J., Holten, D., Laible, P.D., Kirmaier, C. and Hanson, D.K. (2012). High throughput engineering to revitalize a vestigial electron transfer pathway in bacterial photosynthetic reaction centers. The Journal of biological chemistry 287, 8507-14.
- [11] Kressel, L. et al. (2014). High yield of secondary B-side electron transfer in mutant *Rhodobacter capsulatus* reaction centers. Biochimica et Biophysica Acta 1837, 1892-903.
- [12] Kirmaier, C., He, C. and Holten, D. (2001). Manipulating the direction of electron transfer in the bacterial reaction center by swapping Phe for Tyr near BChl(M) (L181) and Tyr for Phe near BChl(L) (M208). Biochemistry 40, 12132-12139.
- [13] Kirmaier, C., Laible, P.D., Hanson, D.K. and Holten, D. (2004). B-side electron transfer to form P+HB- in reaction centers from the F(L181)Y/Y(M208)F mutant of *Rhodobacter capsulatus*. Journal of Physical Chemistry B 108, 11827-11832.
- [14] Coleman, W.J. et al. (1990) Influence of mutagenic replacements of tryptophan M250 on electron transfer rates involving primary quinone in reaction centers of *Rhodobacter capsulatus*. In Structure and Function of Bacterial Photosynthetic Reaction Centers (Michel-Beyerle, M.E., ed.), pp. 273-281. Springer-Verlag, New York.
- [15] Stilz, H.U., Finkle, U., Holzappel, W., Lauterwasser, C., Zinth, W. and Oesterhelt, D. (1994). Influence of M subunit Thr222 and Trp252 on quinone binding and electron transfer

- in *Rhodobacter sphaeroides* reaction centres. *European Journal of Biochemistry* 223, 233-242.
- [16] Kirmaier, C., Gaul, D., DeBey, R., Holten, D. and Schenck, C.C. (1991). Charge separation in a reaction center incorporating bacteriochlorophyll for photoactive bacteriopheophytin. *Science* 251, 922-927.
- [17] Alden, R.G., Parson, W.W., Chu, Z.T. and Warshel, A. (1996). Orientation of the OH dipole of tyrosine (M)210 and its effect on electrostatic energies in photosynthetic bacterial reaction centers. *J. Phys. Chem.* 100, 16761-16770.
- [18] Beekman, L.M.P., van Stokkum, I.H.M., Monshouwer, R., Rijnders, A.J., McGlynn, P., Visschers, R.W., Jones, M.R. and van Grondelle, R. (1996). Primary electron transfer in membrane-bound reaction centers with mutations at the M210 position. *J Phys. Chem.* 100, 7256-7268.
- [19] Finkle, C., Lauterwasser, C., Zinth, W., Gray, K.A. and Oesterhelt, D. (1990). Role of tyrosine M210 in the initial charge separation of reaction centers of *Rhodobacter sphaeroides*. *Biochemistry* 29, 8517-8521.
- [20] Gray, K.A., Farchaus, J.W., Wachtveitl, J., Breton, J., Finkle, U., Lauterwasser, C., Zinth, W. and Oesterhelt, D. (1990) The role of tryosine M210 in the initial charge separation in the reaction center of *Rhodobacter sphaeroides*. In *Structure and Function of Bacterial Photosynthetic Reaction Centers* (Michel-Beyerle, M.E., ed.^eds), pp. 251-264. Springer-Verlag, New York.
- [21] Nagarajan, V., Parson, W.W., Gaul, D. and Schenck, C. (1990). Effect of specific mutations of tyrosine-(M)210 on the primary photosynthetic electron-transfer process in *Rhodobacter sphaeroides*. *Proceedings of the National Academy of Sciences USA* 87, 7888-7892.
- [22] Gunner, M.R., Nicholls, A. and Honig, B. (1996). Electrostatic potentials in *Rhodospseudomonas viridis* reaction centers: implications for the driving force and directionality of electron transfer. *Journal of Physical Chemistry* 100, 4277-4291.
- [23] Parson, W.W., Chu, Z.-T. and Warshel, A. (1990). Electrostatic control of charge separation in bacterial photosynthesis. *Biochimica et Biophysica Acta* 1017, 251-272.
- [24] Bylina, E.J., Kirmaier, C., McDowell, L., Holten, D. and Youvan, D.C. (1988). Influence of an amino-acid residue on the optical properties and electron transfer dynamics of a photosynthetic reaction centre complex. *Nature* 336, 182-184.
- [25] Carter, B., Boxer, S.G., Holten, D. and Kirmaier, C. (2012). Photochemistry of a bacterial photosynthetic reaction Center missing the initial bacteriochlorophyll electron acceptor. *Journal of Physical Chemistry B* 116, 9971-9982.
- [26] Katilius, E., Babendure, J.L., Katiliene, Z., Lin, S., Taguchi, A.K.W. and Woodbury, N.W. (2003). Manipulations of the B-side charge-separated states' energetics in the *Rhodobacter sphaeroides* reaction center. *Journal of Physical Chemistry B* 107, 12029-12034.
- [27] Kirmaier, C., Cua, A., He, C.Y., Holten, D. and Bocian, D.F. (2002). Probing M-branch electron transfer and cofactor environment in the bacterial photosynthetic reaction center by addition of a hydrogen bond to the M-side bacteriopheophytin. *Journal of Physical Chemistry B* 106, 495-503.
- [28] Muh, F., Williams, J.C., Allen, J.P. and Lubitz, W. (1998). A conformational change of the photoactive bacteriopheophytin in reaction centers from *Rhodobacter sphaeroides*. *Biochemistry* 37, 13066-13074.

- [29] de Boer, A.L., Neerken, S., de Wijn, R., Permentier, H.P., Gast, P., Vijgenboom, E. and Hoff, A.J. (2002). B-branch electron transfer in reaction centers of *Rhodobacter sphaeroides* assessed with site-directed mutagenesis. *Photosynthesis Research* 71, 221-239.
- [30] Kirmaier, C., Laible, P.D., Czarnecki, K., Hata, A.N., Hanson, D.K., Bocian, D.F. and Holten, D. (2002). Comparison of M-side electron transfer in *R. sphaeroides* and *R. capsulatus* reaction centers. *Journal of Physical Chemistry B* 106, 1799-1808.
- [31] Paddock, M.L., Chang, C., Xu, Q., Abresch, E.C., Axelrod, H.L., Feher, G. and Okamura, M.Y. (2005). Quinone (QB) reduction by B-branch electron transfer in mutant bacterial reaction centers from *Rhodobacter sphaeroides*: quantum efficiency and X-ray structure. *Biochemistry* 44, 6920-8.
- [32] Laible, P.D. and Hanson, D.K. (2012) Transformable *Rhodobacter* strains, methods for producing transformable *Rhodobacter* strains (USPTO; full utility submitted September 30.)
- [33] Koch, H.G., Hwang, O. and Daldal, F. (1998). Isolation and characterization of *Rhodobacter capsulatus* mutants affected in cytochrome cbb3 oxidase activity. *J Bacteriol* 180, 969-78.
- [34] Taguchi, A.K., Stocker, J.W., Alden, R.G., Causgrove, T.P., Peloquin, J.M., Boxer, S.G. and Woodbury, N.W. (1992). Biochemical characterization and electron-transfer reactions of *sym1*, a *Rhodobacter capsulatus* reaction center symmetry mutant which affects the initial electron donor. *Biochemistry* 31, 10345-55.
- [35] Ben-Shem, A., Frolow, F. and Nelson, N. (2003). Crystal structure of plant photosystem I. *Nature* 426, 630-5.
- [36] Jordan, P., Fromme, P., Witt, H.T., Klukas, O., Saenger, W. and Krauss, N. (2001). Three-dimensional structure of cyanobacterial photosystem I at 2.5 Å resolution. *Nature* 411, 909-17.
- [37] Barber, J., Ferreira, K., Maghlaoui, K. and Iwata, S. (2004). Structural model of the oxygen-evolving centre of photosystem II with mechanistic implications. *Physical Chemistry Chemical Physics* 6, 4737-4742.
- [38] Ferreira, K.N., Iverson, T.M., Maghlaoui, K., Barber, J. and Iwata, S. (2004). Architecture of the photosynthetic oxygen-evolving center. *Science* 303, 1831-8.
- [39] Komiya, H., Yeates, T.O., Rees, D.C., Allen, J.P. and Feher, G. (1988). Structure of the reaction center from *Rhodobacter sphaeroides* R-26 and 2.4.1: symmetry relations and sequence comparisons between different species. *Proc Natl Acad Sci U S A* 85, 9012-6.
- [40] Umena, Y., Kawakami, K., Shen, J.R. and Kamiya, N. (2011). Crystal structure of oxygen-evolving photosystem II at a resolution of 1.9 Å. *Nature* 473, 55-U65.
- [41] Zouni, A., Witt, H.T., Kern, J., Fromme, P., Krauss, N., Saenger, W. and Orth, P. (2001). Crystal structure of photosystem II from *Synechococcus elongatus* at 3.8 Å resolution. *Nature* 409, 739-43.
- [42] Bautista, J.A., Rappaport, F., Guergova-Kuras, M., Cohen, R.O., Golbeck, J.H., Wang, J.Y., Beal, D. and Diner, B.A. (2005). Biochemical and biophysical characterization of photosystem I from phytoene desaturase and xi-carotene desaturase deletion mutants of *Synechocystis sp* PCC 6803. *Journal of Biological Chemistry* 280, 20030-20041.
- [43] Dashdorj, N., Xu, W., Cohen, R.O., Golbeck, J.H. and Savikhin, S. (2005). Asymmetric electron transfer in cyanobacterial Photosystem I: charge separation and secondary electron transfer dynamics of mutations near the primary electron acceptor A0. *Biophysical Journal* 88, 1238-49.

- [44] Di Donato, M., Stahl, A.D., van Stokkum, I.H.M., van Grondelle, R. and Groot, M.L. (2011). Cofactors involved in light-driven charge separation in photosystem I identified by subpicosecond infrared spectroscopy. *Biochemistry* 50, 480-490.
- [45] Fairclough, W.V., Forsyth, A., Evans, M.C.W., Rigby, S.E.J., Purton, S. and Heathcote, P. (2003). Bidirectional electron transfer in photosystem I: electron transfer on the PsaA side is not essential for phototrophic growth in *Chlamydomonas*. *Biochimica et Biophysica Acta-Bioenergetics* 1606, 43-55.
- [46] Giera, W., Ramesh, V.M., Webber, A.N., van Stokkum, I., van Grondelle, R. and Gibasiewicz, K. (2010). Effect of the P700 pre-oxidation and point mutations near A(0) on the reversibility of the primary charge separation in Photosystem I from *Chlamydomonas reinhardtii*. *Biochimica et Biophysica Acta-Bioenergetics* 1797, 106-112.
- [47] Guergova-Kuras, M., Boudreaux, B., Joliot, A., Joliot, P. and Redding, K. (2001). Evidence for two active branches for electron transfer in photosystem I. *Proceedings of the National Academy of Sciences USA* 98, 4437-42.
- [48] Holzwarth, A.R., Muller, M.G., Niklas, J. and Lubitz, W. (2006). Ultrafast transient absorption studies on Photosystem I reaction centers from *Chlamydomonas reinhardtii*. 2: Mutations near the P700 reaction center chlorophylls provide new insight into the nature of the primary electron donor. *Biophysical Journal* 90, 552-565.
- [49] Joliot, P. and Joliot, A. (1999). In vivo analysis of the electron transfer within photosystem I: are the two phylloquinones involved? *Biochemistry* 38, 11130-6.
- [50] Li, Y.J. et al. (2006). Directing electron transfer within photosystem I by breaking H-bonds in the cofactor branches. *Proceedings of the National Academy of Sciences of the United States of America* 103, 2144-2149.
- [51] Muller, M.G., Slavov, C., Luthra, R., Redding, K.E. and Holzwarth, A.R. (2010). Independent initiation of primary electron transfer in the two branches of the photosystem I reaction center. *Proceedings of the National Academy of Sciences of the United States of America* 107, 4123-4128.
- [52] Poluektov, O.G., Paschenko, S.V., Utschig, L.M., Lakshmi, K.V. and Thurnauer, M.C. (2005). Bidirectional electron transfer in photosystem I: Direct evidence from high-frequency time-resolved EPR spectroscopy. *Journal of the American Chemical Society* 127, 11910-11911.
- [53] Ramesh, V.M., Gibasiewicz, K., Lin, S., Bingham, S.E. and Webber, A.N. (2004). Bidirectional electron transfer in photosystem I: accumulation of A0⁻ in A-side or B-side mutants of the axial ligand to chlorophyll A0. *Biochemistry* 43, 1369-75.
- [54] Santabarbara, S., Jasaitis, A., Byrdin, M., Gu, F.F., Rappaport, F. and Redding, K. (2008). Additive effect of mutations affecting the rate of phylloquinone reoxidation and directionality of electron transfer within photosystem I. *Photochemistry and Photobiology* 84, 1381-1387.
- [55] Santabarbara, S., Kuprov, I., Fairclough, W.V., Purton, S., Hore, P.J., Heathcote, P. and Evans, M.C.W. (2005). Bidirectional electron transfer in photosystem I: Determination of two distances between P(700)(+) and A(1)(-) in spin-correlated radical pairs. *Biochemistry* 44, 2119-2128.
- [56] Santabarbara, S., Kuprov, I., Poluektov, O., Casal, A., Russell, C.A., Purton, S. and Evans, M.C.W. (2010). Directionality of electron-transfer reactions in photosystem I of prokaryotes: universality of the bidirectional electron-transfer model. *Journal of Physical Chemistry B* 114, 15158-15171.

- [57] Kellogg, E.C., Kolaczowski, S., Wasielewski, M.R. and Tiede, D.M. (1989). Measurement of the extent of electron transfer to the bacteriopheophytin in the M-subunit in reaction centers of *Rhodospseudomonas viridis*. *Photosynthesis Research* 22, 47-59.
- [58] Pokkuluri, P.R., Laible, P.D., Deng, Y.L., Wong, T.N., Hanson, D.K. and Schiffer, M. (2002). The structure of a mutant photosynthetic reaction center shows unexpected changes in main chain orientations and quinone position. *Biochemistry* 41, 5998-6007.
- [59] Wang, S., Lin, S., Woodbury, N.W. and Allen, J.P. (1994). Comparative study of reaction centers from purple photosynthetic bacteria: isolation and spectroscopy. *Photosynthesis Research* 42, 203-215.
- [60] Prince, R.C. and Youvan, D.C. (1987). Isolation and spectroscopic properties of photochemical reaction centers from *Rhodobacter capsulatus*. *Biochimica et Biophysica Acta* 890, 286-291.
- [61] Baciou, L., Bylina, E.J. and Sebban, P. (1993). Study of wild type and genetically modified reaction centers from *Rhodobacter capsulatus*: structural comparison with *Rhodospseudomonas viridis* and *Rhodobacter sphaeroides*. *Biophysical Journal* 65, 652-660.
- [62] Sebban, P., Maróti, P. and Hanson, D.K. (1995). Electron and proton-transfer to the quinones in bacterial photosynthetic reaction centers -- insight from combined approaches of molecular genetics and biophysics. *Biochimie* 77, 677-694.
- [63] Okamura, M.Y., Paddock, M.L., Graige, M.S. and Feher, G. (2000). Proton and electron transfer in bacterial reaction centers. *Biochimica et Biophysica Acta* 1458, 148-163.
- [64] Daldal, F., Cheng, S., Applebaum, J., Davidson, E. and Prince, R.C. (1986). Cytochrome c(2) is not essential for photosynthetic growth of *Rhodospseudomonas capsulata*. *Proceedings of the National Academy of Sciences of the United States of America* 83, 2012-6.
- [65] Chuang, J.I., Boxer, S.G., Holten, D. and Kirmaier, C. (2006). High yield of M-side electron transfer in mutants of *Rhodobacter capsulatus* reaction centers lacking the L-side bacteriopheophytin. *Biochemistry* 45, 3845-51.
- [66] Chuang, J.I., Boxer, S.G., Holten, D. and Kirmaier, C. (2008). Temperature dependence of electron transfer to the M-side bacteriopheophytin in *Rhodobacter capsulatus* reaction centers. *J Phys Chem B* 112, 5487-99.
- [67] Kovach, M.E., Elzer, P.H., Hill, D.S., Robertson, G.T., Farris, M.A., Roop II, R.M. and Peterson, K.M. (1995). Four new derivatives of the broad-host-range cloning vector pBBR1MCS, carrying different antibiotic-resistance cassettes. *Gene* 166, 175-176.
- [68] Marx, C.J. and Lidstrom, M.E. (2002). Broad-host-range *cre-lox* system for antibiotic marker recycling in gram-negative bacteria. *Biotechniques* 33, 1062-7.
- [69] Simon, R., Priefer, U. and Puhler, A. (1983). A broad host range mobilization system for *in vivo* genetic engineering: Transposon mutagenesis in gram negative bacteria. *Bio/Technology* 1, 37-45.
- [70] Scott, H.N., Laible, P.D. and Hanson, D.K. (2003). Sequences of versatile broad-host-range vectors of the RK2 family. *Plasmid* 50, 74-79.
- [71] Lee, J.K., Kiley, P.J. and Kaplan, S. (1989). Post-transcriptional control of *puc* operon expression of B800-850 light-harvesting complex formation in *Rhodobacter sphaeroides*. *J. Bacteriol.* 171, 3391-3405.
- [72] Laible, P.D., Kirmaier, C., Udawatte, C.S., Hofman, S.J., Holten, D. and Hanson, D.K. (2003). Quinone reduction via secondary B-branch electron transfer in mutant bacterial reaction centers. *Biochemistry* 42, 1718-30.

Chapter 7: Manipulating the energetics and rates of electron transfer in *Rhodobacter capsulatus* reaction centers with asymmetric pigment content

Reprinted with permission from Faries, K.M.; Dylla, N.P.; Hanson, D.K.; Holten, D.; Laible P.D.; Kirmaier, C. (2017) Manipulating the energetics and rates of electron transfer in *Rhodobacter capsulatus* reaction centers with asymmetric pigment content. *Journal of Physical Chemistry B*, *121*, 6989-7004.

Abstract

Seemingly redundant parallel pathways for electron transfer (ET) – comprised of identical sets of cofactors – are a cornerstone feature of photosynthetic reaction centers (RCs) involved in light-energy conversion. In native bacterial RCs, both the A and B branches house one bacteriochlorophyll (BChl) and one bacteriopheophytin (BPh), but the A branch is used exclusively. Described herein are results obtained for two *Rhodobacter capsulatus* RCs with an unnaturally high degree of cofactor asymmetry – two BPh on the RC's B side and two BChl on the A side. These pigment changes derive, respectively, from the His(M180)Leu mutation [a BPh (Φ_B) replaces the B-side BChl (B_B)], and the Leu(M212)His mutation [a BChl (β_A) replaces the A-side BPh (H_A)]. Additionally, Tyr(M208)Phe was employed to disfavor ET to the A branch and in one mutant Val(M131)Glu creates a hydrogen bond to H_B to enhance ET to H_B . In both Φ_B mutants, the decay kinetics of the excited primary ET donor (P^*) resolve three populations with lifetimes of ~9 ps (50-60%), ~40 ps (10-20%) and ~200 ps (20-30%), with $P^+\Phi_B^-$ formed predominately from the 9-ps fraction. The 50-60% yield of $P^+\Phi_B^-$ is the highest yet observed for a Φ_B -containing RC. The results provide insight into factors needed for efficient multi-step ET.

1. Introduction

Reaction center (RC) protein-cofactor complexes of photosynthetic organisms convert light energy to chemical energy via fast stepwise electron transfer (ET) reactions that result in charge separation across a membrane. The homologous L- and M-protein subunits of RCs from purple bacteria such as *Rhodobacter (R.) capsulatus* and *R. sphaeroides* house a dimer (P) of two bacteriochlorophylls (BChl), two BChl monomers (B_A and B_B), two bacteriopheophytin (BPh) monomers (H_A and H_B), two quinones (Q_A and Q_B), a carotenoid (Car) and an iron atom (Fe). Despite structural pseudo C_2 -symmetry (Figure 1A) that relates both the cofactors and the L and M subunits,¹⁻⁵ charge separation in the wild-type (WT) RC occurs with near unity yield and in less than a nanosecond solely via the A-side cofactors.

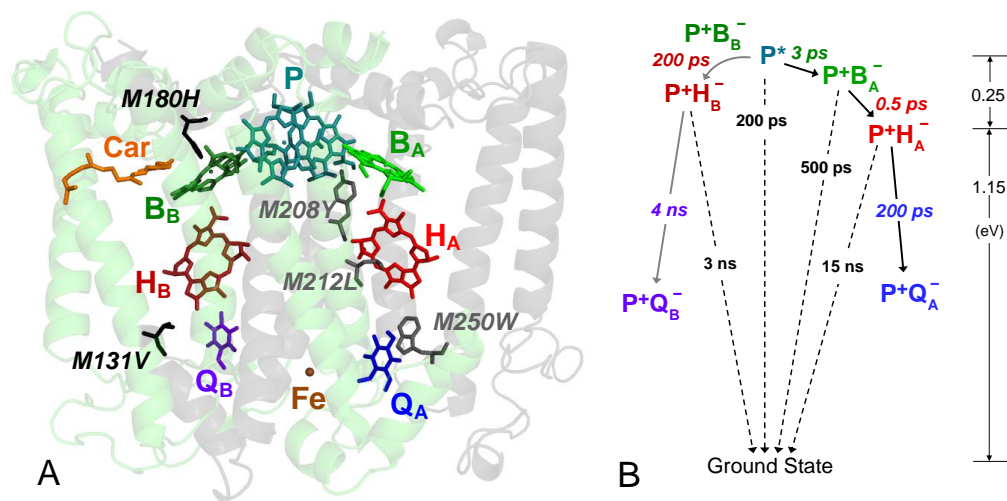


Figure 1. (A) Wild-type RC cofactors, L (gray) and M (green) protein subunits and amino acid residues targeted for mutagenesis in this work. The A-side (gray) and B-side (black) mutations and their effects are given in Table 1. This diagram is based on the *R. sphaeroides* crystal structure (1pcr). The H subunit of the RC is not shown. The pseudo C_2 symmetry axis runs from P to the non-heme iron. (B) Model of the free energies of charge-separated states and rates of various processes for wild-type RCs.

The free energies of the WT RC charge-separated states and the very fast rates and high yields of A-side ET compared to both the slow competing A-side charge-recombination reactions

and slow B-side ET have been addressed for three decades and are summarized in Figure 1B. A number of early studies indicated that $P^+H_A^-$ is 200-300 meV below P^* in free energy,⁶⁻⁹ and both experiments and calculations place $P^+B_A^-$ 50-100 meV below P^* in free energy.⁹⁻¹⁷ A conserved Tyr residue near B_A (M208 in *R. capsulatus*, M210 in *R. sphaeroides*) is critical in poising the free energy of $P^+B_A^-$, while on the B side the conserved symmetry-related residue near B_B is Phe(L181).^{10,17,18} ET to H_B was initially achieved in the *R. capsulatus* RC via mutagenesis aimed at destabilizing $P^+B_A^-$ (by placement of an Asp near B_A ^{19,20}) and significantly improved by swapping Tyr(M208)/Phe(L181) to Phe(M208)/Tyr(L181).¹⁸ Studies on *R. sphaeroides* mutant RCs in which B_B is replaced by a BPh (denoted Φ_B) gave important insight into the relative free energies of P^* , $P^+B_B^-$ and $P^+H_B^-$.²¹⁻²⁴ This pigment cofactor change results from mutation of the native His ligand of B_B (residue M182 in *R. sphaeroides*) to a Leu. Ultrafast spectroscopic measurements on the *R. sphaeroides* Φ_B mutant found that P^* decays in ~3 ps to give $P^+H_A^-$ in ~65% yield and $P^+\Phi_B^-$ in ~35% yield. Subsequent B-side $P^+\Phi_B^- \rightarrow P^+H_B^-$ ET was not observed. Rather, $P^+\Phi_B^-$ was found to have a ~200 ps lifetime and to decay via charge recombination yielding the ground state. Thus, in the *R. sphaeroides* Φ_B mutant, $P^+\Phi_B^-$ is thought to be lower in free energy than $P^+H_B^-$, and remains the case even when a hydrogen bond is added to H_B via an introduced Asp at M133.²⁴ A later study of a Φ_B -containing RC bearing additional mutations that hinder ET to the A side found evidence for a mixture of $P^+\Phi_B^-$ and $P^+H_B^-$ at 10 K.²⁵ Coupled with the *in vitro* differences in redox properties of BChl and BPh (BPh ~150-300 meV easier to reduce than BChl²⁶⁻²⁹), these studies clearly provide a model for the free energies of the B-side charge-separated states relative to each other and to P^* in WT, such as in Figure 1B.

Over the last two decades, many mutant RCs have been generated that can perform B-side ET from P^* to H_B . Using streamlined methods for mutagenesis and protein purification along with a fast photochemical assay, in recent years we have screened several hundred *R. capsulatus* mutants (and more recently some *R. sphaeroides* mutants) for their ability to produce $P^+Q_B^-$ via ET to the B-side cofactors.³⁰⁻³³ In a number of *R. capsulatus* mutants $P^* \rightarrow P^+H_B^-$ ET is coaxed to 30-40% yield. This is achieved, in part, by building in mutations that slow competing A-side ET, typically replacing the key Tyr(M208) with a Phe. Mutations are also incorporated to enhance B-side ET, such as replacing the analogous Phe(L181) with Tyr or Val(M131) with Glu. To date we have little evidence for achieving B-side $P^* \rightarrow P^+H_B^-$ charge separation in a step-wise fashion involving B_B analogous to the function of B_A in formation of $P^+H_A^-$ on the native A side (Figure 1B). Rather, B-side initial charge separation is slower (tens to hundreds of ps) presumably utilizing B_B via a superexchange mechanism to produce $P^+H_B^-$. However, in a recent set of *R. sphaeroides* mutants we found even higher yield of ET to H_B – nearly 60% in one case with kinetics that suggest some contribution of a two-step ET mechanism.³³ In contrast, previous work has found the opposite, that the B-side ET yield is about a factor of two higher for certain mutations in *R. capsulatus* compared to the *R. sphaeroides* version.³⁴ These differences in primary ET for the two species plus the fact that all the prior mutants that contain Φ_B were prepared in *R. sphaeroides* suggested that construction of Φ_B -containing mutants in *R. capsulatus* should be informative.

Thus, in this work the H(M180)L mutation in the *R. capsulatus* RC has been examined for its potential utility in giving the $B_B \rightarrow \Phi_B$ pigment swap and eliciting B-side ET to H_B and thence to Q_B . Additionally, the RCs investigated bear three core mutations, “F β_{AV} ” (Table 1). Changing the native Tyr(M208) near B_A to Phe (the “F” mutation) slows initial A-side ET and

strongly biases ET towards the B side by destabilizing $P^+B_A^-$. The “ β_A ” mutation – L(M212)H – replaces H_A with a BChl further decreasing A-side ET and the “V” mutation – W(M250)V – blocks binding of Q_A , thus preventing any reduction of Q_B from A-side ET. We show here that the H(M180)L mutation in *R. capsulatus* produces the Φ_B phenotype and gives a 50% yield of $P^+\Phi_B^-$ in the Φ_B -F β_{AV} mutant. Further we show that the yield of $P^+\Phi_B^-$ is increased to 60% in the E Φ_B -F β_{AV} via addition of the Val(M131)Glu substitution that creates a hydrogen bond to H_B and lowers the free energy of $P^+H_B^-$. However, the low yields of $P^+H_B^-$ (2% for Φ_B -F β_{AV} and 6% for E Φ_B -F β_{AV}) that are obtained suggest that $P^+\Phi_B^-$ is not poised in free energy between P^* and $P^+H_B^-$, at least in the major population of RCs for either mutant. Small yields of $P^+Q_B^-$ (4% for E Φ_B -F β_{AV}) are also observed. These and other results are presented and discussed.

Table 1. Substitutions in *R. capsulatus* RCs.

Mutation	Designation	Target Effect(s) on Cofactors
V(M131)E	E	- Form hydrogen bond to ring V keto group of H_B^a - Mimic hydrogen bond to H_A provided by Glu(L104)
H(M180)L	Φ_B	- Replace B_B with a BPh (denoted Φ_B) ^b
Y(M208)F	F	- Decrease rate and yield of ET to the A side ^c
L(M212)H	β_A	- Replace H_A with a BChl (denoted β_A) ^b - Allow better spectral resolution of H_B and Φ_B - Decrease ET to the A side
W(M250)V	V	- Prevent binding of Q_A - Eliminate Q_B reduction from the A side

^aThe hydrogen bond is expected to lower $P^+H_B^-$ in free energy by ~50-100 meV.

^bBPh is easier to reduce than BChl by ~150-300 meV *in vitro*. Thus, from the L(M212H) mutation, state $P^+\beta_A^-$ is expected to be higher in free energy than $P^+H_A^-$. Analogously, from the H(M180)L mutation, $P^+\Phi_B^-$ is expected to be lower in free energy than $P^+B_B^-$.

^cCalculations indicate that the Y(M208)F substitution raises the free energy $P^+B_A^-$ by as much as ~200 meV, of which 10-40 meV is an effect on the oxidation potential of P.¹⁰

2. Materials and Methods

Mutagenesis and RC Purification. The mutant RCs derive from a cassette-based mutagenesis strategy. Platform expression plasmid pBBRKW2HTsLsM³⁰ was engineered further to facilitate construction of the mutants described herein. A silent *Bsi*WI site was introduced into region B³⁰ of the synthetic M gene (encoding residues M167-185) by incorporation of a cassette flanked by *Ppu*MI and *Xmn*I sites. With the *Bsi*WI site in place, a 106 bp segment encompassed the 3' portion of region B and all of region N (residues M186-209). This segment was synthesized as two cassettes – “left” and “right” – that share a central 9-base

overlap and carry *Bsi*WI or *Blp*I cohesive ends, respectively. The left cassette surrounds the M180 site while the right cassette carries other sites (e.g., M208) to be targeted in combination with substitutions at M180. The left and right cassettes were inserted via three-way ligation into *Bsi*WI/*Blp*I-digested plasmids carrying the L(M212)H-W(M250)V or V(M131)E-L(M212)H-W(M250)V mutations. Candidate plasmids were screened for the gain of a silent *Bse*RI site; all mutations were verified by sequencing. Following conjugal transfer from *E. coli* donor S17-1, RCs encoded by these plasmids were expressed in *R. capsulatus* strain U43 yielding RC-only (antennaless) membranes. RCs were purified as described previously.^{32,33}

Determination of Pigment Cofactor Content. The ratio of the BChl and BPh cofactors was determined by extracting the pigments into acetone:methanol (7:2 v:v) as described previously,³⁵ with small modifications to allow extractions to be performed on small volume (~7 μ l) aliquots of ~70 μ M RCs diluted into 150 μ L of solvent. A wash step (using an additional 150 μ l of solvent) similar to that described previously³⁵ was employed for samples whose pellets exhibited a distinct pink/purple color following centrifugation of the extracts. The expected values of the BChl/BPh pigment ratio for the mutants under study are 5.0 (β -type pigment content of 5 BChl and 1 BPh) or 2.0 (WT- or Φ_B -type pigment content of 4 BChl and 2 BPh). Intermediate values indicate RC mixed pigment content and/or incomplete pigment extraction. The fraction (x) of RCs containing Φ_B in a given sample can be determined from the pigment ratio via (Equation 1):

$$\text{BChl/BPh ratio} = 5.0(1 - x) + 2.0(x) \quad (1)$$

Where x is the fraction of the sample containing Φ_B . This encompasses a range of values of only 3, with the bounds determined by an upper limit of 5.0 (β -type pigment content) and a lower limit of 2.0 (WT or Φ_B type pigment content).

Millisecond Assay for $P^+Q_B^-$ Formation. Details of the millisecond (ms) screening apparatus that assays $P^+Q_B^-$ formation following a single 7-ns, 532-nm excitation flash have been described previously.³⁰⁻³³ Here, we have advanced this instrumentation with addition of an alternate excitation source – a laser that outputs 15-ps pulses at 10 Hz (Leopard; Continuum). An external shutter under control of home-built electronics extracts a single, on-demand 15-ps pulse that is used for single-shot excitation of RCs in the assay. All measurements were done at room temperature using $\sim 2 \mu\text{M}$ RCs (in 10 mM Tris, 0.1% Deriphat buffer pH 7.8) arrayed in a clear-bottomed, 96-well plate (black-walled to avoid light exposure of RCs not under interrogation). Freshly thawed RCs were used in separate runs that assayed the yield of $P^+Q_B^-$ formed following sub-saturating, 7-ns, 532-nm excitation and following sub-saturating, 15-ps, 532-nm excitation. For both the 7-ns and 15-ps assays, the reported $P^+Q_B^-$ yields are the average of two replicates of single-shot excitations. Each RC sample was dark-adapted for 1-2 hrs between successive interrogations.

Femtosecond to Microsecond Transient Absorption Spectroscopy. Ultrafast transient absorption (TA) measurements utilized a 1-KHz amplified Ti:Sapphire laser system (Spectra Physics) and Helios and EOS detection spectrometers (Ultrafast Systems) described previously.³² RC samples [$\sim 20 \mu\text{M}$ RCs, sodium ascorbate (100x) and terbutryn (25x)] were vigorously stirred in a 2-mm pathlength cell and excited with ~ 100 fs flashes at 865 nm for visible region probing or 590 nm for near-infrared (NIR) region probing. Resultant Helios scans (spanning several ps before excitation to 7 ns) and EOS scans (spanning several ns before excitation to 40 μs) were dechirped (Surface Xplorer X4, Ultrafast Systems) and combined (OriginPro 2016, OriginLab; custom routines) to give final datasets that spanned seven orders of magnitude in time, from before $t = 0$ to 40 μs .

TA data were analyzed by an iterative combination of fitting locally (specific key wavelengths) and globally (entire spectral/temporal data sets) using OriginPro 2016 custom routines as well as Surface Explorer, which utilizes a singular-value-decomposition (SVD) based global analysis, and CarpetView V1.1.8 (Light Conversion), which allows fitting to various models (parallel, serial, custom serial/branched). The time profiles were fit (globally and at all wavelengths independently) to the convolution of the pump/probe pulses with a sum of exponentials plus a constant (the latter found to be near zero at 40 μ s for all RCs studied here). As needed for each mutant RC, the number of exponentials varied to accommodate up to three P* decay components and the lifetimes of P⁺ β _A⁻/P⁺H_A⁻, P⁺ Φ _B⁻, P⁺H_B⁻, triplet P (P^R) and triplet carotenoid (Car^T). Shown below and in the Supporting Information are spectra at select times that reveal the evolution of these states as well as three types of spectra from global analysis: (1) decay associated difference spectra (DADS), which are spectra of the pre-exponential factors (A₁, A₂, ..., A_n, C) from fits to independent exponentials [A₁exp(-t/ τ ₁) + A₂exp(-t/ τ ₂)...+ A_nexp(-t/ τ _n)+C]; (2) evolution associated difference spectra (EADS) in which a sequential model (A₁ → A₂ → ... A_n → C) is assumed and each A_n is the product of a concentration, a relative extinction coefficient (amplitude) and a term that depends on the time/rate constants of all the terms; and (3) species associated difference spectra (SADS) that assume a specific kinetic model with various parallel, branched and sequential steps. The model assumed is the minimum for the mutant RCs and includes three populations of P*, each of which can decay with various yields (associated with the competing rate/time constants) by electron transfer to the A side, the B side or to the ground state by internal conversion. The charge-separated states then can decay with the competing rate/time constants to form the next product state (such as the triplet excited state of P, P^R, for decay of P⁺H_B⁻) or by charge recombination to give the ground state. More details

are given along with the presentation and analysis of the results. It is found in all cases that the time constants obtained from fits of the time evolution at key wavelengths for decay/growth of the various states/species (e.g., associated with bleaching of the usually distinct ground state absorption bands of the molecules involved) are in good agreement with those obtained from global analysis of entire data sets in both the visible and NIR spectral regions.

3. Results and Discussion

Ground State Spectra and RC Pigment Cofactor Content. The ground state absorption spectra of the *R. capsulatus* Φ_B -F β_A V and E Φ_B -F β_A V mutants are shown in Figure 2A and compared to those of some previously reported mutant RCs used for controls. The two Φ_B mutants were obtained in low yields with a co-purifying component absorbing mainly between ~280 nm and 550 nm. The absorption spectrum of this component is given in Figure S1 and has been subtracted from the spectra of the Φ_B -F β_A V and E Φ_B -F β_A V mutants shown in Figure 2. The F and V mutations (Table 1) are optically silent in the visible-NIR spectral region shown and the spectrum of the V mutant (Figure 2A, black) is identical to that of WT RCs (not shown). The β_A and Φ_B mutations alter the pigment content of the RC. Spectra of the β_A V (purple), F β_A V (light green), and E-F β_A V (dark green) control mutants bear the well-documented consequences of the L(M212)H mutation which causes replacement of H_A by a BChl (β_A). Features of these spectra include a loss of H_A absorptions at ~545 nm (Q_x) and ~760 nm (Q_y) and accompanying increased absorptions at ~600 nm and ~780 nm (Q_x and Q_y absorptions of BChl, respectively). The Q_y band of β_A at 780 nm appears as a more pronounced shoulder on the short-wavelength side of the absorption maximum at 800 nm due to B_A (and B_B if present), as is well documented.³⁶ The H(M180)L mutation in *R. capsulatus* is expected to result in replacement of

B_B with a BPh (Φ_B) as found previously for the analogous *R. sphaeroides* H(M182)L mutation²¹⁻²⁴ (including one RC also having the $H_A \rightarrow \beta_A$ pigment swap).²⁵ Hence, spectral changes that are the opposite of those due to the β_A mutation should ensue, i.e., loss of BChl absorption features and gain of BPh absorption features. These are qualitatively apparent in the spectrum of Φ_B - $F\beta_{AV}$ (blue) compared to $F\beta_{AV}$ (light green) RCs (middle pair in Figure 2A) and similarly for the spectrum of $E\Phi_B$ - $F\beta_{AV}$ (red) compared to E - $F\beta_{AV}$ (dark green) RCs (top pair in Figure 2A).

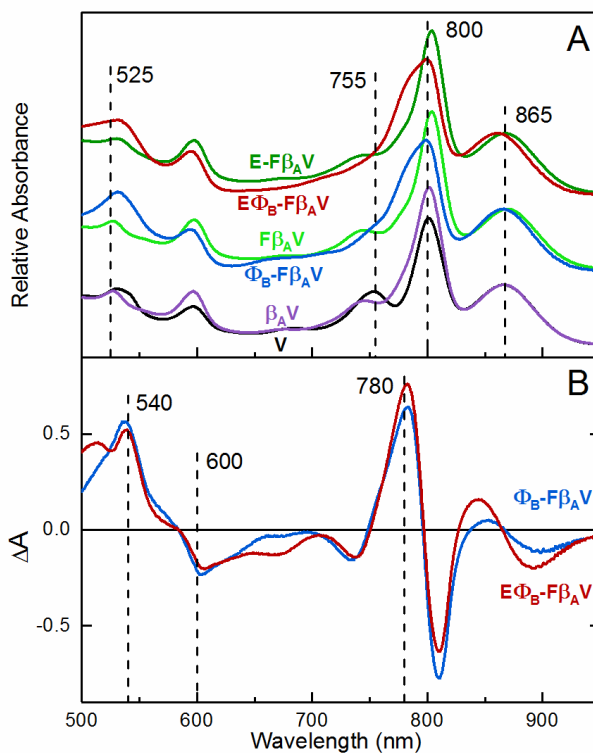


Figure. 2. (A) Room temperature ground-state absorption spectra, normalized at the P absorption maximum near 865 nm, for the Φ_B - $F\beta_{AV}$ (blue) and $E\Phi_B$ - $F\beta_{AV}$ (red) mutant RCs and comparison control mutant RCs: V (black), β_{AV} (purple), $F\beta_{AV}$ (light green) and E - $F\beta_{AV}$ (dark green). (B) Results of subtracting the $F\beta_{AV}$ absorption spectrum from that of Φ_B - $F\beta_{AV}$ (blue) and from that of $E\Phi_B$ - $F\beta_{AV}$ (red) mutant RCs. Dashed lines indicate wavelengths of particular interest.

The ground state spectra (and TA data below) confirm the presence of the β_A and Φ_B pigments expected to result from the L(M212)H and H(M180)L mutations, respectively, and thus

that the Φ_B -F β_A V and E Φ_B -F β_A V RCs have a pigment phenotype of two BChls on the A side (B_A and β_A) and two BPhs on the B side (Φ_B and H_B). The spectral differences owing to Φ_B are more apparent in Figure 2B where the spectrum of the F β_A V RC has been subtracted from that of Φ_B -F β_A V (blue) RC and that of E Φ_B -F β_A V (red) RC. (Essentially the same results are obtained if the β_A V spectrum is the one subtracted.) The subtracted spectrum for Φ_B -F β_A V in Figure 2B is almost identical to that presented by Katilius *et al.* for the equivalent difference absorption spectrum of the Φ_B mutant of *R. sphaeroides* compared to WT.²¹ Both spectra in Figure 2B have diminished BChl absorption (negative peaks) near 600 nm and 800 nm consistent with loss of BChl (the B_B pigment) and increased absorption near 540 nm and ~780 nm that is consistent with gain of BPh (the Φ_B pigment). Also, the red spectrum of E Φ_B -F β_A V in Figure 2B displays a small derivative feature near 527 nm and a slight red shift in the position of the Q_x absorption profile for the Glu(M131)-bearing mutant. This is consistent with formation of a hydrogen bond between an Glu (or Asp) at M131 and H_B as reported previously for several *R. capsulatus* mutant RCs,^{32,37,38} and similarly for Asp or Glu substituted at M133 in *R. sphaeroides*.^{24,33,39}

It is interesting to note that the ground state spectra in Figure 2 indicate that the H_A and B_B binding sites have consistent and different effects on the Q_y absorption bands of the BPh and BChl pigments. The absorption of BChl in the B_B binding site is red-shifted to ~800 nm (from 780 nm for BChl *in vitro*), whereas a BChl in the H_A binding site (β_A) absorbs near 780 nm. Similarly, in the B_B binding site, BPh (Φ_B) absorption is red-shifted to ~780 nm compared to BPh (H_A) absorption near 760 nm (~750 nm for BPh *in vitro*). Since these mutant RC samples share a common sequence background and were prepared using a consistent set of conditions, they can be compared directly, demonstrating that in the H_A site, BChl and BPh have absorption properties similar those found *in vitro* while they have red-shifted absorptions in the B_B site.

The results of the pigment extractions on Φ_B -F β_{AV} and E Φ_B -F β_{AV} RCs confirm the replacement of B_B by Φ_B , but leave open the possibility that a small fraction of the RCs retain B_B .

The BChl/BPh ratio for Φ_B -F β_{AV} (2.43 ± 0.05) and E Φ_B -F β_{AV} (2.4 ± 0.04) are ~15% greater than the expected value of 2. However, pellets that are pink/purple are observed upon centrifugation of the extracts, indicating incomplete extractions, perhaps of BPh such as Φ_B . This is illustrated by the reduction of the BChl/BPh ratio determined for Φ_B -F β_{AV} and E Φ_B -F β_{AV} from ~2.7 before washing the pellets to ~2.4 after washing, which (pellets) still retained some pink/purple color. We note that in earlier studies of two different mutants, the pellets from pigment extracts were blue and incomplete extraction of a BChl was suggested.^{17,40} The results for controls β_{AV} (4.8 ± 0.2), F β_{AV} (5.2 ± 0.2) and E-F β_{AV} (4.8 ± 0.4) are in line with the expected BChl/BPh ratio of 5. The values for controls V (1.93 ± 0.04) and WT (2.0 ± 0.2) have the expected ratio of 2. Note these results for the controls are closest to the expected values if the absorbance readings on the extracts are taken at 1 nm to shorter wavelength than used in the original publication.³⁵ This minor difference could arise from a variety of sources such as small differences in spectral bandwidths and wavelength calibration. Collectively the pigment extractions indicate that Φ_B replaces B_B in at least 80% of the Φ_B -F β_{AV} and E Φ_B -F β_{AV} RCs.

Millisecond $P^+Q_B^-$ Assay. The magnitude of bleaching of P at 865 nm obtained 1 ms after excitation was measured for mutant and control RCs and compared to that obtained for WT RCs which form $P^+Q_B^-$ in 100% yield. $P^+Q_A^- \rightarrow P^+Q_B^-$ in ~100 μ s is the final ET step in WT RCs but all mutants studied here employ the V substitution at M250 that prevents Q_A binding (Table 1). In RCs without Q_A , long-lived bleaching of P (\geq ms time scale) per force reflects formation of $P^+Q_B^-$ due to ET from P^* via the B-side cofactors.

For the two new Φ_B mutants (Figure 3, red and blue bars), the assay indicates an ~1% yield of $P^+Q_B^-$ formation in the Φ_B -F β_A V mutant and ~4% in the E Φ_B -F β_A V mutant. The screening of the new Φ_B -F β_A V and E Φ_B -F β_A V mutants (and comparison/control mutants) used both 7-ns and 15-ps excitation flashes at 532 nm.

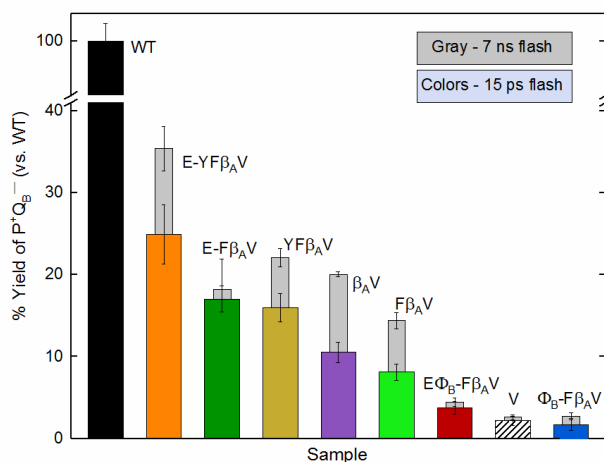


Figure 3. Relative $P^+Q_B^-$ yields of the two Φ_B -containing mutants (blue and red bars) and controls as determined from the millisecond screening assay. The narrow light gray bars give the yield of $P^+Q_B^-$ produced by a 7-ns flash and the wider bars in color give the yield of $P^+Q_B^-$ elicited by a 15-ps flash. The gray bar for WT is identical to and hidden under the black bar for WT and that for the V mutant is only barely visible at the top of the striped bar.

The 15-ps flashes were used here for the first time for this assay because the 7-ns excitation flashes normally used are *long* relative to some *fast* charge recombination processes (Figure 1B) that return RCs to the ground state. Such RCs have the potential to be re-excited within the duration of the excitation pulse, compounding the yield of $P^+Q_B^-$ that is measured. With complex partitioning of the decay of P^* and both A-side and B-side charge-separated states in mutants designed for improved B-side ET, the resultant summation of recycling effects is not predictable. Nonetheless, we expected that 15-ps flashes should diminish recycling and that is apparent in Figure 3. Note that the relative ordering of the mutants for their yields of B-side ET ($P^+Q_B^-$) in this small sampling is very well preserved regardless of the duration of the excitation

flash. An additional strong control for the assay is that it returns only a 2-3% signal for both 7-ns and 15-ps excitation of the V mutant where H_A (but no Q_A) is in place. Thus, the following two conclusions are reliable: (1) the $P^+Q_B^-$ yield is several percent in the $E\Phi_B-F\beta_{AV}$ mutant and (2) the $P^+Q_B^-$ yield is larger in the $E\Phi_B-F\beta_{AV}$ RCs than in the $\Phi_B-F\beta_{AV}$ RCs.

P* Lifetime. Figure 4 shows TA spectra for the $\Phi_B-F\beta_{AV}$ mutant in the NIR region encompassing bleaching of the 865-nm absorption band of P and P* stimulated emission at longer wavelengths. By 5-7 ns, only ~5-10% of the original bleaching of the P absorption band remains (Figures 4A and 4B), indicating low yield(s) of any long-lived (≥ 1 ns) species. This is consistent with the results of the ms screening assay where only a few percent yield of $P^+Q_B^-$ is found on the ms timescale (Figure 3). $P^+\beta_A^-$ formed by A-side charge separation would contribute <1% at 5-7 ns owing to both its low yield of formation (<10%) and its inherent charge recombination lifetime of ~800 ps. Very similar data are obtained for $E\Phi_B-F\beta_{AV}$ RCs.

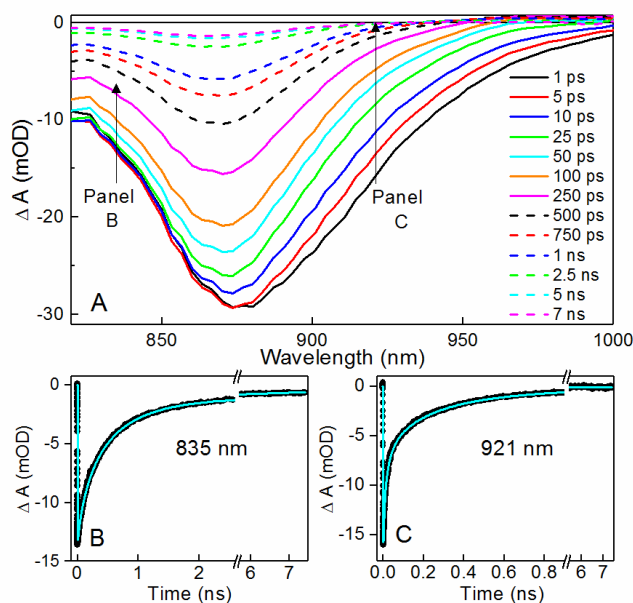


Figure 4. (A) NIR region TA spectra acquired at the time indicated for $\Phi_B-F\beta_{AV}$ RCs. Multi-exponential fits of (B) P-bleaching decay at 835 nm and (C) stimulated emission at ~920 nm. (920 nm is a near isosbestic point in the difference spectrum of P^+ compared to P, indicated by the right arrow in Panel A.)

It is well known that P^* decay in essentially all RCs, including WT, cannot be described by a single exponential.⁴¹⁻⁴⁵ A systematic way to distill this complexity is to examine the P^* decay kinetics at a $\Delta A = 0$ (isosbestic) point in the difference spectrum for P^+/P (and for charge-separated states such as $P^+H_B^-/PH_B$, $P^+\Phi_B^-/P\Phi_B$ and $P^+\beta_A^-/P\beta_A$). This point is usually near 920 nm for *R. capsulatus* RCs in Deriphat/Tris buffer), as indicated for the Φ_B - $F\beta_{AV}$ mutant by the arrow in the raw data shown in Figures 4A. This $\Delta A \sim 0$ point is also shown in the DADS, EADS and SADS for the products of P^* decay (the 680 ps $P^+\Phi_B^-$ and 4.7 ns $P^+H_B^-$ components) in Figure 5. At such a wavelength, the spectral/kinetic contribution associated with P bleaching is largely eliminated and, additionally, the (transient) absorption features of P^* and P^+ , $BChl^-$ and BPh^- produced upon charge separation are much smaller than P^* stimulated emission. This wavelength also corresponds roughly to the maximum of the stimulated-emission spectrum and similarly to the static fluorescence spectrum of P^* .^{46,47} The P^* decay kinetics at ~920 nm typically can be well fit by the sum of three exponentials and a constant (where the returned value is zero as expected because ~920 nm is an isosbestic point). At a minimum, this provides a consistent method to survey P^* decay and make comparisons between different mutant RCs. The three P^* lifetime components and their relative amplitudes returned from such analyses of Φ_B - $F\beta_{AV}$, $E\Phi_B$ - $F\beta_{AV}$, and some control mutant RCs are given in Table 2. Representative kinetic data and a fit of the decay of the stimulated emission kinetics for the Φ_B - $F\beta_{AV}$ RC are shown in Figure 4C. We note that the time constants listed in Table 2 are in good agreement with values obtained from global (and individual) fits across the entire near-infrared (P bleaching and stimulated emission) and visible (Q_x bleaching and anion absorption) regions, as described below.

Table 2. P* lifetime components and amplitudes from fits of P* stimulated emission near 920 nm.^a

Sample	λ (nm)	τ_1 (ps)	A ₁	τ_2 (ps)	A ₂	τ_3 (ps)	A ₃	$\tau_{1,2}^{avg}$ P* (ps) ^b	$\tau_{1,2,3}^{avg}$ P* (ps) ^c
Φ_B -F β_A V	922	9.6	0.47	42	0.22	204	0.31	20	77
E Φ_B -F β_A V	922	9.3	0.52	42	0.28	177	0.20	21	52
F β_A V	934	-	-	55	0.35	216	0.65	55	160
E-F β_A V	920	-	-	60	0.37	200	0.63	60	148
β_A V	915	5.5	0.49	36	0.28	182	0.23	17	55
V	915	4.1	0.75	18	0.23	184	0.02	7	11

^aThe reported values for the P* lifetimes have a typical error of $\pm 10\%$.

^bAmplitude-weighted average of the two shorter components, τ_1 and τ_2 .

^cAmplitude-weighted average of all three components, τ_1 , τ_2 and τ_3 .

The data in Table 2 reflect a general trend of increased P* kinetic heterogeneity in all mutants compared to the V mutant, which is essentially WT, having only a mutation-induced absence of Q_A. Some 98% of P* stimulated emission decay in the V mutant is accounted for by two components, ~4 ps (75%) and ~18 ps (23%). Similar time constants have been reported by many workers from two-exponential fits of P* decay in WT and other mutants.^{41,42} RCs of the F β_A V and E-F β_A V mutants have essentially no fast component (≤ 10 ps); instead, ~40% of P* decays with a time constant of ~60 ps and ~60% in ~200 ps. The addition of the H(M180)L mutation to give Φ_B -F β_A V and E Φ_B -F β_A V shifts the distribution back to a dominant fast phase (~9 ps, ~50%) and comparable amounts (~25%) of ~40 ps and ~200 ps components. We note that P* decay in many *R. capsulatus* mutants has a ~200 ps component.⁴⁸ This is known to be the time constant for P* internal conversion to the ground state for *R. capsulatus* RCs in Deriphath (~100 ps for *R. capsulatus* RCs in LDAO).^{49,50} This means that the rate constants for ET to the A and B sides are in competition with a (~ 200 ps)⁻¹ rate constant for deactivation (internal conversion) of P*. Thus, for example, a measured 50-ps P* lifetime component corresponds to 25% of P* decaying to the ground state and 75% to ET products. A measured 200-ps P* decay component reflects a P* population that is effectively photochemically inactive.^{17,38,48-51} Charge

recombination of $P^+B_A^-$ that involves some repopulation of P^* could also contribute to a ~ 200 -ps P^* decay component.

The natural presence of some P^* kinetic heterogeneity in WT RCs most likely arises from the small free-energy span (<0.5 eV, Figure 1B) between the five states at highest free energy (P^* , $P^+B_A^-$, $P^+H_A^-$, $P^+B_B^-$, and $P^+H_B^-$). Natural structural fluctuations of the pigment-protein complex – and associated effects on the free energies of these states – will give a distribution of P^* populations that differ in the rate constants and yields of the P^* decay pathways. In many mutants, such as the ones studied here, the free energy span is further narrowed and the observed kinetics become increasingly heterogeneous. This can include populations in which one or more charge-separated state (e.g., $P^+B_B^-$ and/or $P^+B_A^-$) is inaccessible from P^* . Clearly the V mutant (the most similar to WT) displays the least heterogeneity with very little ($\sim 2\%$) of the ~ 200 ps component. The data in Table 2 show that the other three control mutants and the Φ_B -F β_A V and E Φ_B -F β_A V mutants have increased contributions of the two longer components of P^* decay.

The idea that P^* populations differ in their decay pathways/products is manifest from global analysis of the NIR data set for the Φ_B -F β_A V (Figure 4), for which a contour surface and heat map are shown in Figures S3 and S4 of the Supporting Information. Figure 5 shows the results of the global analysis, including the DADS, EADS and SADS as described in Materials and Methods. The top three DADS in Figure 5 give the amplitude and sign as a function of wavelength of the pre-exponential factors of the three fit components (~ 9 , ~ 40 , ~ 200 ps) for P^* decay and formation of associated product states. It is seen that the ~ 9 -ps DADS contains primarily P^* stimulated emission (centered near 920 nm) with very little contribution of P ground-state state recovery (e.g., near 840 nm). The ~ 40 ps and ~ 200 ps components also show

stimulated emission along with progressively greater amounts of ground-state recovery accompanying P^* decay. These findings are consistent with the view that P^* charge separation (from any population) is competing with internal conversion to the ground state with a time constant on the order of 200 ps. Thus a ~ 9 ps component reflects mainly charge separation, the ~ 40 ps component somewhat less charge separation, and the ~ 200 ps component effectively little if any charge separation.

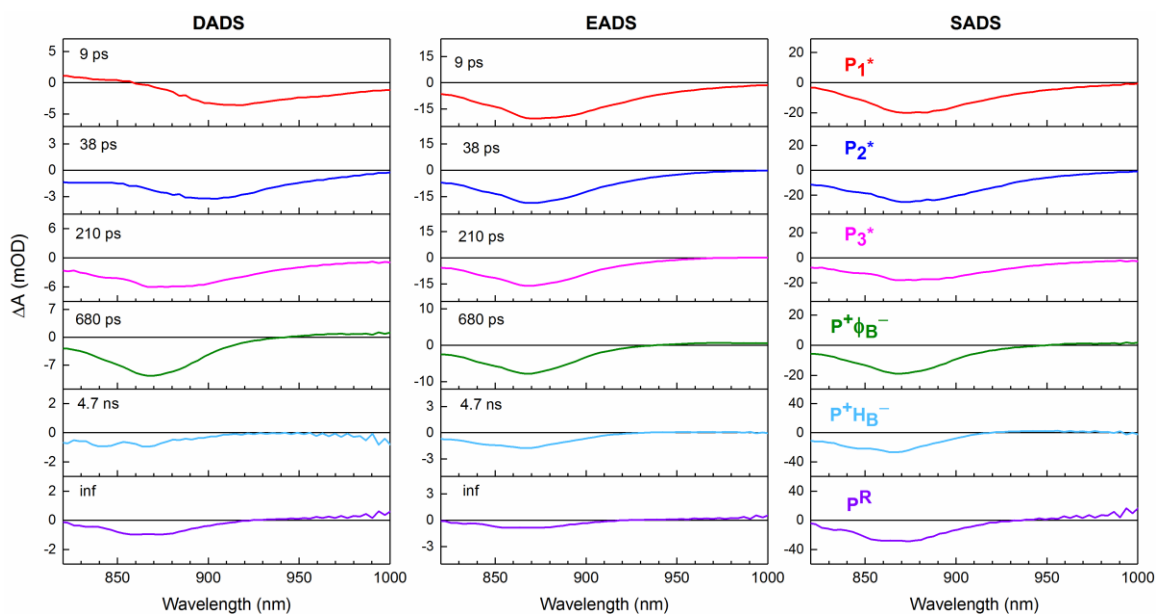


Figure 5. Spectra from global analysis (DADS, EADS, SADS) for the transient states/species from global analysis of the TA data in the NIR region for the Φ_B -F β_A V mutant.

Further information on the fate of the three P^* decay components can be seen in the top three DADS in Figure 6, which shows the global analysis results in the visible region. A contour surface and heat map are shown in Figures S5 and S6. The DADS for the three P^* decay components show some similarities but marked differences that again reflect the largely different fates of the three P^* populations. The ~ 200 -ps DADS shows no prominent features in the visible region that would reflect formation of ET products, consistent with our assignment that this

component primarily reflects P^* internal conversion to the ground state. The ~ 40 -ps DADS contains features associated mainly with formation of $P^+H_B^-$, and features of the ~ 9 -ps DADS relate mainly to formation of $P^+\Phi_B^-$. These assignments will be described below along with the presentation of the raw data in the visible region as well as the SADS, which reflect a simulation of the spectral dynamics assuming a kinetic model with input time constants and yields of the various competing processes. Similar findings are obtained for the $E\Phi_B-F\beta_{AV}$ mutant, for which the results of global analysis of the data sets in the visible and NIR region are given in Figures S9-S18.

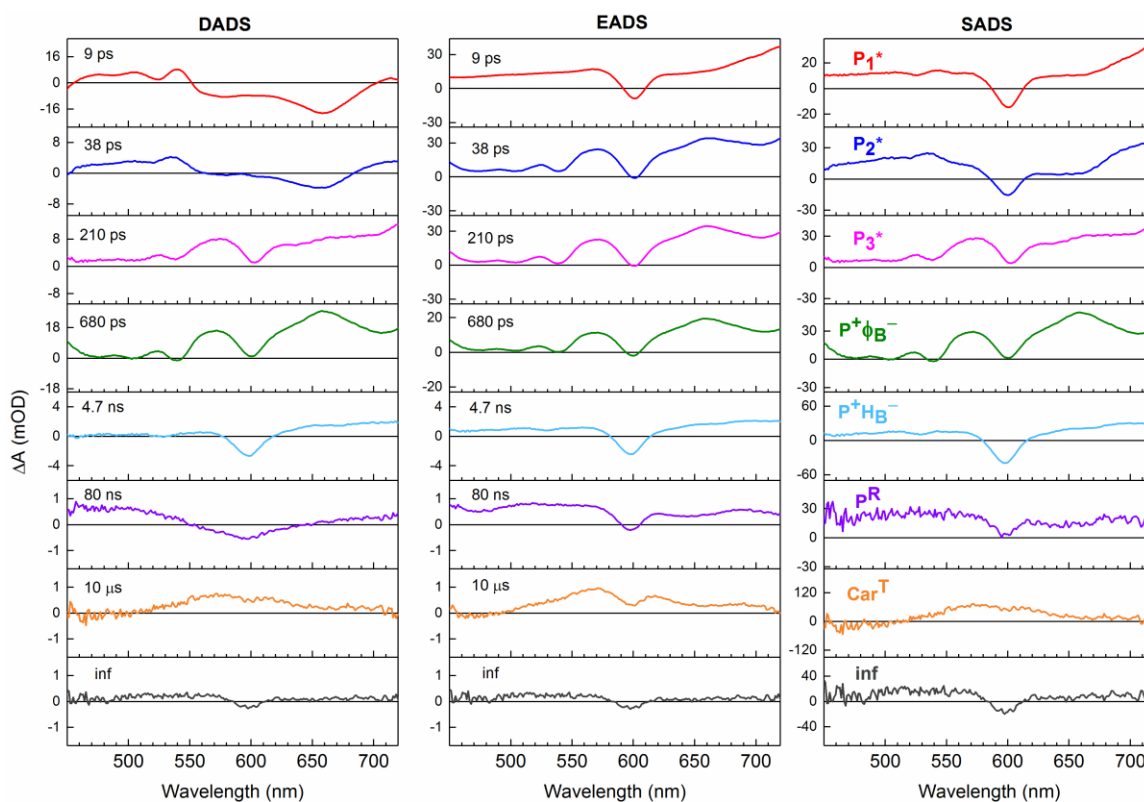


Figure 6. Spectra from global analysis (DADS, EADS, SADS) for the transient states/species from global analysis of the TA data in the visible region for the $\Phi_B-F\beta_{AV}$ mutant.

A-side and B-side Charge Separation. Figures 7A and 7B show visible region TA spectra for the Φ_B -F β_{AV} and E Φ_B -F β_{AV} mutants, respectively, over the time course of 0.5 ps to 1 ns. For the purposes of comparison (controls), analogous results are given for F β_{AV} (Figure 7C), E-F β_{AV} (Figure 7D), β_{AV} (Figure 7E) and V (Figure 7F) mutant RCs. Data spanning 1 ns to 40 μ s are given in paralleling panels A-F of Figure 8.

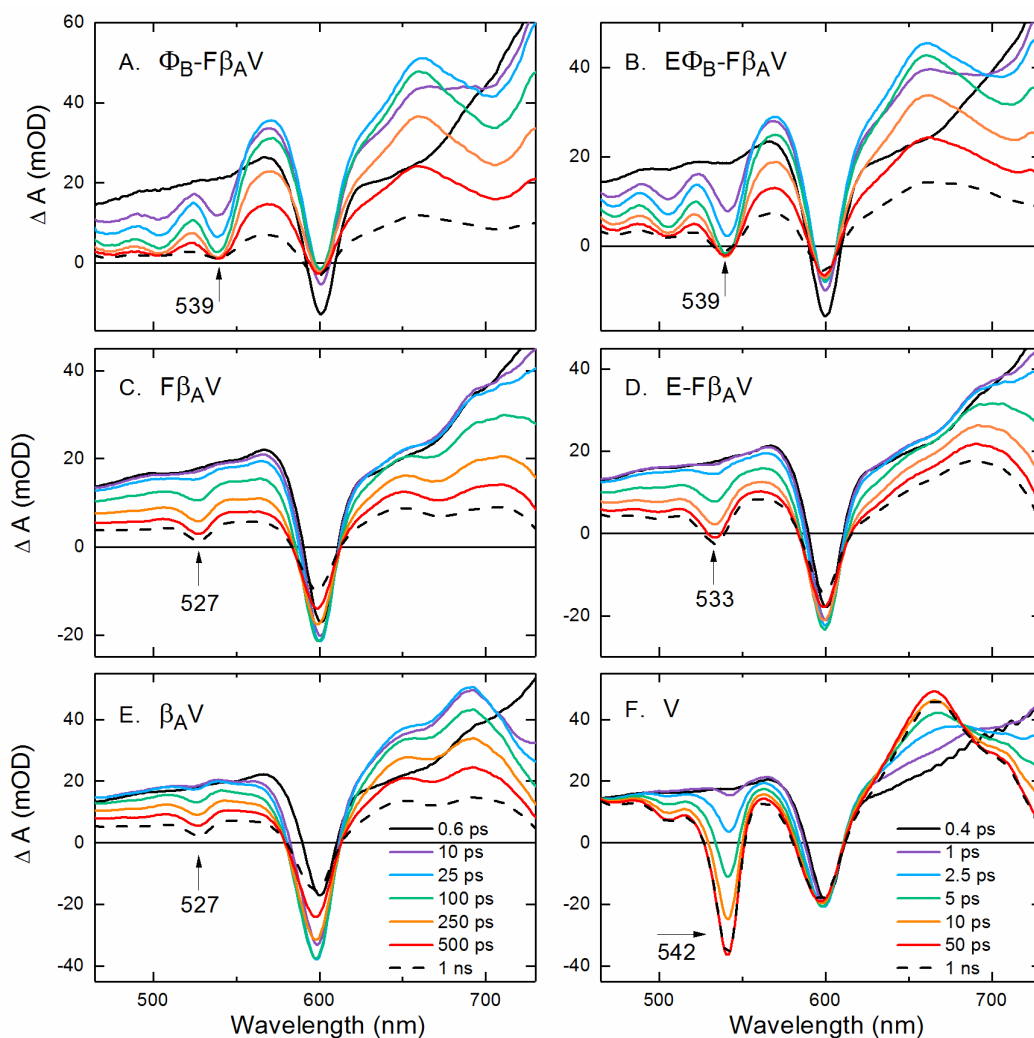


Figure 7. Visible-region TA spectra for the Φ_B mutant RCs (Panels A&B) and associated controls (Panels C-F) at times ranging from \sim 0.5 ps to 1 ns. Spectra were collected after a 100-fs excitation flash at 860 nm, at the times indicated in Panel E for samples in Panels A-E. Spectra for the V mutant RCs were collected at the times indicated in Panel F.

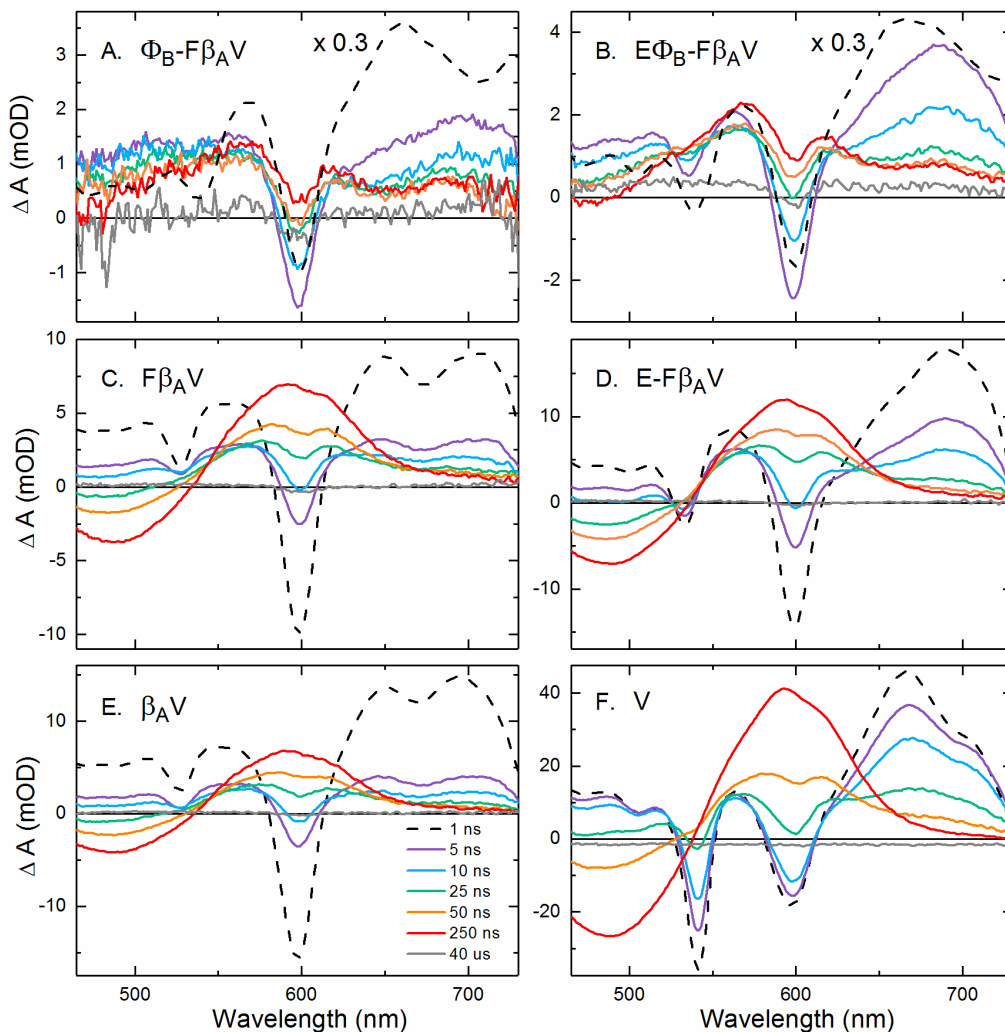


Figure 8. Visible-region TA spectra for the Φ_B mutant RCs (Panels A&B) and associated controls (Panels C-F) at times ranging from 1 ns to 40 μ s. Spectra for all samples were collected after an initial 100-fs excitation flash at 860 nm, at times indicated in Panel E. Note: these spectra have been scaled to an identical initial P^* concentration and the 1-ns spectra in A and B have been multiplied by 0.3.

In Figure 7, the ~ 0.5 ps spectra (black lines) in all cases largely reflect the TA spectrum of P^* . The position of bleaching of the BPh Q_x (0,0) absorption that develops as P^* decays, varying from 527 to 542 nm, is the distinguishing feature that identifies the B-side charge-separated product, or A-side $P^+H_A^-$ in the case of the V mutant. For both of the Φ_B -containing mutants, bleaching develops at 539 nm and we assign this to bleaching of the Q_x absorption band

of Φ_B due to formation of $P^+\Phi_B^-$. This is distinct from the 542-nm bleaching of H_A as seen in the TA spectrum of $P^+H_A^-$ in the V mutant (Figure 7F) and distinct from the equally well-established position of H_B bleaching at 527 nm (formation of $P^+H_B^-$) seen in the spectra of the $F\beta_{AV}$ and β_{AV} mutants (Figures 7C and 7E, respectively). The Glu substituted at M131 in the E- $F\beta_{AV}$ mutant forms a hydrogen bond to the ring V keto group of H_B and results in the red-shifted position (~ 533 nm) of bleaching of the Q_x band of H_B in Figure 7D.^{32,33} Note that since H_B is the *only* BPh in the $F\beta_{AV}$, E- $F\beta_{AV}$ and β_{AV} RCs, these spectral assignments are unambiguous. In all six RCs, the smaller Q_x (1,0) vibronic band is consistently $\sim 1,300$ cm^{-1} to the blue of the Q_x (0,0) bands noted above, most clearly seen for the V mutant and the two Φ_B mutants. This matches well with the spacing between the Q_x origin and vibronic satellite bands of BPh in solution. Interestingly, the Q_x (1,0) vibronic band of Φ_B appears to have gained intensity relative to the Q_x (0,0) band compared to the situation for H_A (in the V mutant) and H_B (in the other mutants). Note also the similar position of the BPh anion absorption near ~ 665 nm in the transient spectra of $P^+\Phi_B^-$ (e.g., 25 ps to 500 ps TA spectra of the Φ_B - $F\beta_{AV}$ and E Φ_B - $F\beta_{AV}$ mutants) and the TA spectrum of $P^+H_A^-$ (in the V mutant). The wavelengths of the key BPh features in the transient difference spectra of all six mutants are listed in Table S1.

The same spectral features are seen in the visible-region DADS (and SADS) of $P^+\Phi_B^-$ (~ 700 ps lifetime) obtained from global analysis of the TA data sets for the Φ_B - $F\beta_{AV}$ (Figure 6) and E Φ_B - $F\beta_{AV}$ (Figure S10) mutants. Note also how the BPh Q_x bleaching and BPh anion features in the DADS for $P^+\Phi_B^-$ are the main features in the DADS of the ~ 9 -ps P^* decay component but inverted because these features in the P^* DADS represent appearance of $P^+\Phi_B^-$ (with the P^* lifetime), rather than the decay of the charge-separated state.

The yield of $P^+\Phi_B^-$ in the Φ_B -F β_A V and E Φ_B -F β_A V mutants was determined as described previously.^{18,21,32} In brief, the integrated magnitude of BPh Q_x bleaching (origin band and vibronic component) in a mutant is compared to that of H_A in the V mutant (where $P^+H_A^-$ forms in ~100% yield) after normalizing to the initial P* concentration via the ~600 nm bleaching of P. This analysis indicates that the yield of $P^* \rightarrow P^+\Phi_B^-$ is in the range of 50-60% for both the Φ_B -F β_A V and E Φ_B -F β_A V mutants (larger in the latter) for the two mutant samples taken as a “whole.” These yields when input into the simplest kinetic model for the primary photochemistry in the two mutants also produce the expected SADS for the three P* components (~9, ~40, ~20 ps) and $P^+\Phi_B^-$ (~700 ps), including BPh Q_x bleaching at 539 nm for the latter state. The SADS for Φ_B -F β_A V are shown in Figures 5 and 6 and those for E Φ_B -F β_A V mutants in Figures S9 and S10 and are described below. If one factors out ~25% “inactive” P* (discussed in the previous section) in the two Φ_B -containing mutants, then the yield of $P^* \rightarrow P^+\Phi_B^-$ in the two “active” fractions (having an amplitude-weighted P* lifetime of ~20 ps; Table 2) is somewhat higher, ~75%. Our analysis of the Φ_B -F β_A V and E Φ_B -F β_A V mutants indicates further that the yield of P* decay via internal conversion is higher than the yield of $P^* \rightarrow P^+\beta_A^-$ ET, with A-side ET forming $P^+\beta_A^-$ in ≤10% yield (based on total P*). Similarly, a diminished yield of charge separation to β_A (15-25%) is obtained for the F β_A V and E-F β_A V mutants in which the residue at M208 is a Phe, whereas $P^+\beta_A^-$ is produced in 60-70% yield in the β_A V mutant where the native Tyr is in place at M208. These results are consistent with the known importance of Tyr(M208) in A-side ET and underscores our use of the template F β_A V mutations toward the goal of high B-side ET.

For the *R. sphaeroides* Φ_B mutant, Katilius *et al.* reported previously that P* has a lifetime of 2.6 ps and decays to $P^+H_A^-$ (~65%) and $P^+\Phi_B^-$ (~35%).²¹ Similar results were

obtained for the *R. sphaeroides* “D Φ_B ” mutant (“D” indicating substitution of an Asp at M133): P* lifetime of 2.7 ps and 67% and 33% yields of P⁺H_A⁻ and P⁺ Φ_B ⁻, respectively.²³ The higher yield of P⁺ Φ_B ⁻ observed here in the *R. capsulatus* Φ_B -F β_{AV} and E Φ_B -F β_{AV} mutant RCs is consistent with the effects of replacing Tyr(M208) with Phe and with β_A substituting for H_A, whereas the prior *R. sphaeroides* mutants had both the native Tyr(M210) and H_A. Both the β_A and Phe(M208) substitutions are known to slow ET to the A side,^{18,19,36,52} especially the latter. Their combined effect is reflected in the amplitude-weighted average of the two shorter components of the P* lifetime: ~60 ps for the F β_{AV} mutant versus ~7 ps for the V mutant (Table 2, column 9). Thus, other things being equal, the higher yield of P⁺ Φ_B ⁻ in the *R. capsulatus* Φ_B -F β_{AV} and E Φ_B -F β_{AV} mutants studied here is consistent with the prior work on *R. sphaeroides* Φ_B and D Φ_B mutants. Similarly, the amplitude-weighted P* lifetime in the Φ_B -F β_{AV} and E Φ_B -F β_{AV} mutants (~20 ps using the first two P* components, Table 2, column 9) is shorter than found in control F β_{AV} and E-F β_{AV} control mutants (~60 ps), reflecting rapid, favored P* → P⁺ Φ_B ⁻ ET in the two mutants having Φ_B .

The 539-nm wavelength of bleaching of the Φ_B Q_x (0,0) band for the *R. capsulatus* Φ_B mutants compares very well with 538 nm found previously for the *R. sphaeroides* Φ_B mutants. Another common finding is that P⁺ Φ_B ⁻, and not P⁺H_B⁻, is the main B-side ET product of P* decay. We conclude that P⁺ Φ_B ⁻ lies below P* in free energy in the *R. capsulatus* Φ_B -F β_{AV} and E Φ_B -F β_{AV} mutants, as previously concluded for the *R. sphaeroides* Φ_B mutants.²¹⁻²⁴

Low Yields of P⁺H_B⁻, Triplet P and Triplet Carotenoid. The lifetime of P⁺ Φ_B ⁻ in both the Φ_B -F β_{AV} and E Φ_B -F β_{AV} mutants as determined from global analysis (DADS in Figures 6 and S10) is ~700 ps. This lifetime is similar to the ~800 ps lifetime of P⁺ β_A ⁻ (e.g., in the β_{AV}

mutant; Figure S19), which state is indicated by our analysis to form in both Φ_B mutants but only in low yield (<10 %). In the prior work of Katilius *et al.*,²¹ a ~200 ps lifetime of $P^+\Phi_B^-$ was found and is more distinct from the ~15 ns lifetime of $P^+H_A^-$, though $P^+\Phi_B^-$ is formed in lesser, ~35%, yield than found here in the *R. capsulatus* Φ_B mutants. Having β_A on the A side in our mutants removes spectral congestion in the BPh Q_x spectral region and a very small yield of $P^+H_B^-$ is resolved. This is seen in Figure 9A for Φ_B -F β_A V and Figure 9B for E Φ_B -F β_A V with the diagnostic observations being a small bleaching at ~531 nm in the 5-ns spectrum of Φ_B -F β_A V (Figure 9A) and a (slightly larger) red-shifted bleaching at ~535 nm in the 5-ns spectrum of E Φ_B -F β_A V (Figure 9B). We assign these spectral features to formation of $P^+H_B^-$ and the 4-nm red shift again is consistent with Glu(M131) making a hydrogen bond to H_B . Based on the integrated magnitudes of these bleachings, the yield of $P^+H_B^-$ relative to the initial amount of P^* is very small, ~2% in Φ_B -F β_A V and ~6% in E Φ_B -F β_A V.

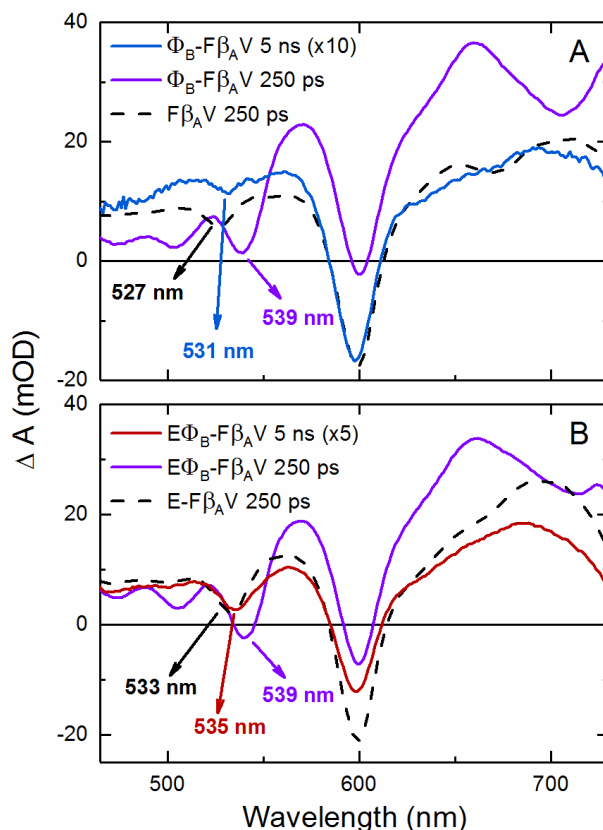


Figure 9. Visible-region TA spectra acquired at selected times that highlight key BPh Q_x bleaching features. (A) TA spectra featuring 539 nm bleaching for $P^+\Phi_B^-$ (purple) and 531 nm bleaching for $P^+H_B^-$ (blue) in the Φ -F β_A V mutant compared to 527 nm bleaching for $P^+H_B^-$ (dashed black) in the F β_A V control mutant. (B) TA spectra featuring 539-nm bleaching for $P^+\Phi_B^-$ (purple) and 535 nm bleaching for $P^+H_B^-$ (red) in the E Φ -F β_A V mutant compared to 533 nm bleaching for $P^+H_B^-$ (dashed black) in the E-F β_A V control mutant.

The DADS (and SADS) in Figures 5 and 6 for Φ_B -F β_A V and Figure S9 and S10 for E Φ_B -F β_A V show that a significant fraction of the $P^+H_B^-$ forms directly from P^* . Such a process could utilize Φ_B via a superexchange mechanism, just as formation of $P^+H_B^-$ from P^* utilizes B_B in the F β_A V and E-F β_A V mutants. Note that Φ_B could be a superexchange mediator between P and H_B even if $P^+\Phi_B^-$ lies below P^* (as we suggest it does) in the Φ_B -F β_A V and E Φ_B -F β_A V mutants. Similarly, even though $P^+B_A^-$ lies below P^* in WT and many mutants (Figure 1B), B_A has been

invoked as superexchange mediator between P and H_A on the A side to explain the longer component of P* decay that is generally observed (the shorter component being due to the two-step process P* → P⁺B_A⁻ → P⁺H_A⁻).^{53,54} Along the same lines, some of the P⁺H_B⁻ in the two Φ_B-containing mutants may also form from P⁺Φ_B⁻, with the hydrogen bond to H_B provided by Glu(M131) contributing at least in part to the increased (6%) yield of P⁺H_B⁻ in the EΦ_B-Fβ_AV mutant RC. Another potential source of P⁺H_B⁻ is raised by the results of the pigment extractions, which allow that up to 15% of the Φ_B-Fβ_AV and EΦ_B-Fβ_AV RCs could retain the native B_B (i.e., not have Φ_B); however, as noted above, the pigment extractions (e.g., of BPh Φ_B) are likely incomplete and the fraction of RCs that retain B_B less than 15%. If we take the pigment extractions at face value, and based on 15-25% yield P* → P⁺H_B⁻ in Fβ_AV and E-Fβ_AV RCs,³² one could account for much if not all of the P⁺H_B⁻ formed in Φ_B-Fβ_AV (2%) and in EΦ_B-Fβ_AV (6%) as arising from a ≤15% fraction of RCs that retains B_B, if that fraction is truly present.

The Glu(M131) substitution in the *R. capsulatus* mutant RCs may be more effective in facilitating the formation of P⁺H_B⁻ (from P⁺Φ_B⁻ or P*) in the Φ_B-containing in the RCs than the Asp substitution used previously at the analogous site (M133) in the *R. sphaeroides* RC. For example, there could be a difference in the strength of the hydrogen bond to H_B. We found previously that that Glu(M131) gives a higher yield of P⁺Q_B⁻ than Asp(M131) in a set of B_B-containing *R. capsulatus* mutants.³¹ In addition to differences in species and combined amino-acid substitutions, some differences in detail (e.g., lifetimes) may be expected because the RCs in the prior studies were solubilized in the detergent LDAO whereas the RCs studied here were in Deriphath.

Regardless of these mechanistic considerations, our assignment that P⁺H_B⁻ forms is also supported by the ~4-nm red shift of the position of H_B bleaching, from ~531 nm to ~535 nm, in

the Φ_B mutant carrying the V(M131)E substitution. This wavelength shift parallels the shift in the position of H_B Q_x bleaching observed in the $F\beta_{AV}$ mutant (527 nm, Figure 9A) compared to the E- $F\beta_{AV}$ mutant (533 nm, Figure 9B). We note that the absolute position of the Q_x band bleaching of (nominally) H_B in both of the Φ_B mutants is slightly red-shifted compared to that observed to date in other mutants where $P^+H_B^-$ is formed. For example in Figure 9, the H_B Q_x bleaching is at 531 nm in the Φ_B - $F\beta_{AV}$ mutant versus 527 nm in $F\beta_{AV}$ mutant (panel A), and similarly, in the E Φ_B - $F\beta_{AV}$ mutant the bleaching is at 535 nm compared to 533 nm in E- $F\beta_{AV}$ mutant (panel B). These results may reflect thermal/quantum-mechanical mixing of $P^+H_B^-$ and $P^+\Phi_B^-$ such as suggested by de Boer *et al.*²⁵ The $P^+H_B^-$ lifetime varies between 4 and 8 ns in the E Φ_B - $F\beta_{AV}$, Φ_B - $F\beta_{AV}$, E- $F\beta_{AV}$, $F\beta_{AV}$ and β_{AV} mutants. Also, the $P^+H_B^-$ decay kinetics are generally heterogeneous in these mutants, a detailed investigation of which is beyond the scope of this work.

Triplet P (P^R) and triplet carotenoid (Car^T) are found in all of the RCs studied here as seen in the evolution of the spectra between 5 ns and 40 μ s in Figure 8. The presence of these states is also seen in the DADS and SADS resulting from global analysis for the Φ_B - $F\beta_{AV}$ (Figure 6) and E Φ_B - $F\beta_{AV}$ (Figure S10) mutants. In the β_{AV} , $F\beta_{AV}$, and E- $F\beta_{AV}$ mutants, both $P^+\beta_A^-$ (~800 ps lifetime) and $P^+H_B^-$ (4-8 ns lifetime) form in differing yields and, in principle, both states can give rise to P^R and subsequent Car^T . These triplets can also arise from $P^+\Phi_B^-$ (~700 ps lifetime) in the two Φ_B mutants. In general, there is a correlation between the majority yield of P^R arising from the charge-separated state with the longest lifetime in each mutant, i.e., from $P^+H_B^-$. In other words, the magnitude of Car^T signal seen in Figures 6, 7 and S10 (broad, derivative shape; 250 ns spectrum) roughly tracks the $P^+H_B^-$ yield (or $P^+H_A^-$ in the V mutant).

As expected, the overall yield of Car^{T} amount the six mutants is smallest for $\Phi_{\text{B}}\text{-F}\beta_{\text{AV}}$ (Figure 8A) and only slightly larger for $\text{E}\Phi_{\text{B}}\text{-F}\beta_{\text{AV}}$ (Figure 8B).

The P^{R} lifetimes for the two mutants containing Φ_{B} (~80 ns) are at the upper end of the range for the four controls (60-80 ns), which may indicate slower triplet-triplet energy transfer to Car with Φ_{B} present. A reduced yield of Car^{T} relative to WT has been reported for the *R. sphaeroides* Φ_{B} mutant,⁵⁵ and is also found here for the two Φ_{B} mutants (Figures 7A and 7B, 250 ns). The Car^{T} spectrum and 5-10 μs Car^{T} lifetime seen for $\Phi_{\text{B}}\text{-F}\beta_{\text{AV}}$ and $\text{E}\Phi_{\text{B}}\text{-F}\beta_{\text{AV}}$ (and control RCs) are consistent with that expected for triplet spheroidenone, based on studies of various *R. sphaeroides* RCs.^{56,57}

Model for Φ_{B} mutants. A free energy diagram for the A- and B-side charge-separated states involving the BChl and BPh cofactors in the *R. capsulatus* $\Phi_{\text{B}}\text{-F}\beta_{\text{AV}}$ and $\text{E}\Phi_{\text{B}}\text{-F}\beta_{\text{AV}}$ mutants is proposed in Figure 10. In this model, $\text{P}^+\text{B}_{\text{A}}^-$ is placed above P^* in free energy owing to loss of the stabilizing influence of Tyr(M208). Calculations indicate that this Tyr may stabilize $\text{P}^+\text{B}_{\text{A}}^-$ by as much as ~200 meV compared to a Phe at the site,⁵⁸ which includes that Tyr may lower the P/P^+ potential (by as much as ~40 meV).^{10,41,59} Thus, using estimates that $\text{P}^+\text{B}_{\text{A}}^-$ is ~70 meV below P^* in WT RCs, a Phe at M208 could result in $\text{P}^+\text{B}_{\text{A}}^-$ being ~100 meV above P^* in free energy. Our global analysis shows that there is a greater heterogeneity in P^* decay kinetics in RCs when there is a Phe at M208. This may reflect increased sampling of populations/conformations of RCs in which charge separation to the A side is reduced or even suppressed due to the elevated free energy of $\text{P}^+\text{B}_{\text{A}}^-$. The free energy of $\text{P}^+\beta_{\text{A}}^-$ is likely ~200 meV higher than that of $\text{P}^+\text{H}_{\text{A}}^-$ in the WT RC, the latter of which lies ~250 meV below P^* when stabilized by relaxations.^{36,60-62} The free energies of the B-side states in Figure 10 for the $\Phi_{\text{B}}\text{-F}\beta_{\text{AV}}$ and $\text{E}\Phi_{\text{B}}\text{-F}\beta_{\text{AV}}$ mutants are the same as suggested by Katilius *et al.*, who placed $\text{P}^+\Phi_{\text{B}}^-$

~150 meV below P^* .²⁴ As depicted in Figure 10 by the shaded boxes, these values represent the centers of a distribution (static or dynamic) of free energies for each state. Thus, for example, even if the center of the distribution for $P^+H_B^-$ lies above that for $P^+\Phi_B^-$, the former state could lie below the latter in a fraction of the total population. In such case $P^+\Phi_B^- \rightarrow P^+H_B^-$ ET could readily proceed. State $P^+\Phi_B^-$ could also decay in part by thermally forming $P^+H_B^-$ in populations in which the latter state is the higher of the two in free energy. State $P^+\Phi_B^-$ could also decay in part by thermal repopulation of P^* , a possibility indicated in the extension of the negative feature (stimulated emission) in the NIR DADS past 920 nm for this state (~700 ps component) in Figures 5 and S9. Similarly, for A-side ET, populations may exist in which $P^+B_A^-/P^+\beta_A^-$ could decay in part by thermal repopulation of P^* .

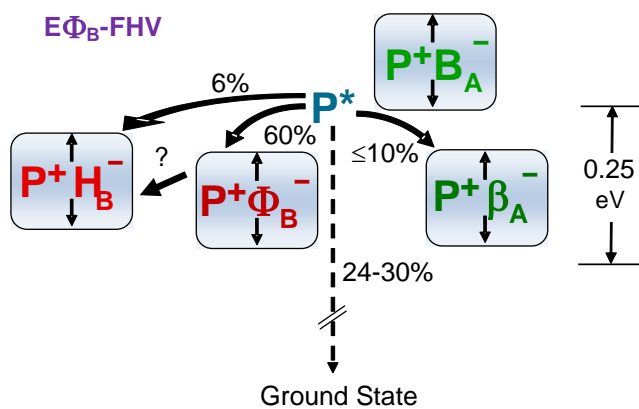


Figure 10. Model for the free energies of P^* and charge-separated states in the $E\Phi_B$ - $F\beta_A$ V mutant. In some populations, $P^+H_B^-$ lies below $P^+\Phi_B^-$ even though the center of the free-energy distribution of $P^+H_B^-$ lies above that for $P^+\Phi_B^-$. If some $P^+H_B^-$ forms from $P^+\Phi_B^-$, the 6% yield from P^* would be reduced proportionately. Note that the free energy gap between P^* and the ground state is 1.4 eV (not shown to scale); $P^+Q_B^-$ (not shown) is ~0.6 eV above the ground state.

This framework is qualitatively consistent with our finding of $\leq 10\%$ ET to the A side (e.g. to β_A) in the Φ_B -F β_A V and E Φ_B -F β_A V mutants. Consistency is also demonstrated by our finding that $P^+\beta_A^-$ forms in $\leq 10\%$ yield in the related control mutants F β_A V and E-F β_A V. In contrast, in the β_A V mutant where Tyr(M208) is in place, $P^+B_A^-$ and $P^+\beta_A^-$ are very close in free energy and the yield of $P^* \rightarrow P^+\beta_A^- / P^+B_A^-$ is 60-70% – where the designation “ $P^+\beta_A^- / P^+B_A^-$ ” reflects strong thermal and/or quantum mechanical mixing of these two states.^{36,63-65} One demonstration of this mixing is the ~ 800 ps charge recombination lifetime of $P^+\beta_A^- / P^+B_A^-$ compared to the 10-20 ns charge recombination lifetime of $P^+H_A^-$. The decay kinetics of $P^+H_A^-$ also have shorter components that have been attributed to subpopulations that involve degrees of mixing between $P^+H_A^-$ and $P^+B_A^-$ as well as protein relaxations that give rise to time-dependent free energy gaps.^{6,62,66,67} We have made similar arguments concerning the decay of $P^+H_B^-$ on the B side in a variety of mutants,^{32,52,68} although that state forms in very low yield in the Φ_B -containing RCs studied here. Our model for P^* decay is similar, with a potential contribution of both static and dynamic protein populations/conformations that may interconvert on varying time scales. In the mutants studied here we have clear evidence from our global analysis (DADS in Figure 5 and S9) that P^* decay is heterogeneous and with three populations giving rise primarily to three different products; $P^+\Phi_B^-$, $P^+H_B^-$ and the ground state. The fourth state $P^+\beta_A^-$ also forms, albeit in low yield ($\leq 10\%$), and based on results on F β_A V and E-F β_A V RCs it likely forms in the Φ_B -F β_A V and E Φ_B -F β_A V mutants from the 9-ps component along with $P^+\Phi_B^-$; however, it is spectrally difficult to discern a small contribution of $P^+\beta_A^-$ formation to any of the P^* DADS. We also note that although the three P^* decay components may each primarily reflect formation of a particular product state, each component has a branched decay (e.g., to $P^+\Phi_B^-$, $P^+H_B^-$, $P^+\beta_A^-$,

and the ground state) but the rate constant (and yield) of one process may dominate due to the relative free energies of the states, etc.).

The consistencies of the time constants and yields of the various states described above were examined further by applying the simplest possible (but still complex) kinetic model for the primary photochemistry in the two Φ_B -containing mutants to global simulations of the data sets in the visible and NIR regions to generate SADS for the transient states/species. The relative populations of the P^* decay components (~ 9 , ~ 20 , and ~ 200 ps), were taken to be the values determined from the stimulated emission decay (Table 1). Each P^* population was given a 200 ps time constant for internal conversion to the ground state. Time constants for competing formation of the charge-separated states were chosen to give the observed lifetimes such that the ~ 9 ps P^* population decays entirely to give $P^+\Phi_B^-$ and such that a small ($\sim 10\%$) fraction of the latter state also forms from the ~ 40 -ps P^* population, which in turn produces the majority of the $P^+H_B^-$. Simulations were performed assuming that decay of $P^+\Phi_B^-$ could also produce a fraction of $P^+H_B^-$ (arrow with ? in Figure 10) although firm conclusions regarding the importance of this step could not be drawn given the low yield of the latter state. The simulations were performed assuming that P^R is produced entirely from $P^+H_B^-$ with a yield in the range 30-60% and that Car^T is produced from P^R with a yield of 50-70%. The data in the visible regions for both mutants (Figures 6 and S10) also show a minor (infinity) component with a lifetime longer than the 40 μs extent of the measurements that has spectral characteristics expected for P^R . It was assumed that this population of P^R forms from $P^+H_B^-$ but is not capable of energy transfer to carotenoid. However, given the complexity already incorporated, the model included only one $P^+H_B^-$ population, did not account for any thermal-repopulation processes, and neglected

formation/decay of $P^+\beta_A^-$ that the data suggest is produced in $\leq 10\%$ yield from P^* in the two Φ_B -containing mutants.

Figures 6 (Φ_B -F β_{AV}) and S10 (E Φ_B -F β_{AV}) show the visible-region SADS for the three P^* components (~ 9 , ~ 40 , ~ 200 ps lifetimes), $P^+\Phi_B^-$ (~ 700 ps), $P^+H_B^-$ (~ 4.5 ns), P^R (80 ns) and Car^T (~ 10 μ s). The SADS are physically reasonable and show all the key features expected for the states. This consistency is excellent considering the complexity of even the first order model for the primary photochemistry, which includes three P^* populations that largely produce different product states, some of which in turn decay by competitive pathways. Figure 11 shows the associated time evolution of the concentrations of the transient states or the two Φ_B -containing mutants. The latter results are consistent with the yields of the states described above from detailed analysis of the raw data at key wavelengths that are known to give reliable measures of the formation of the charge-separated species.

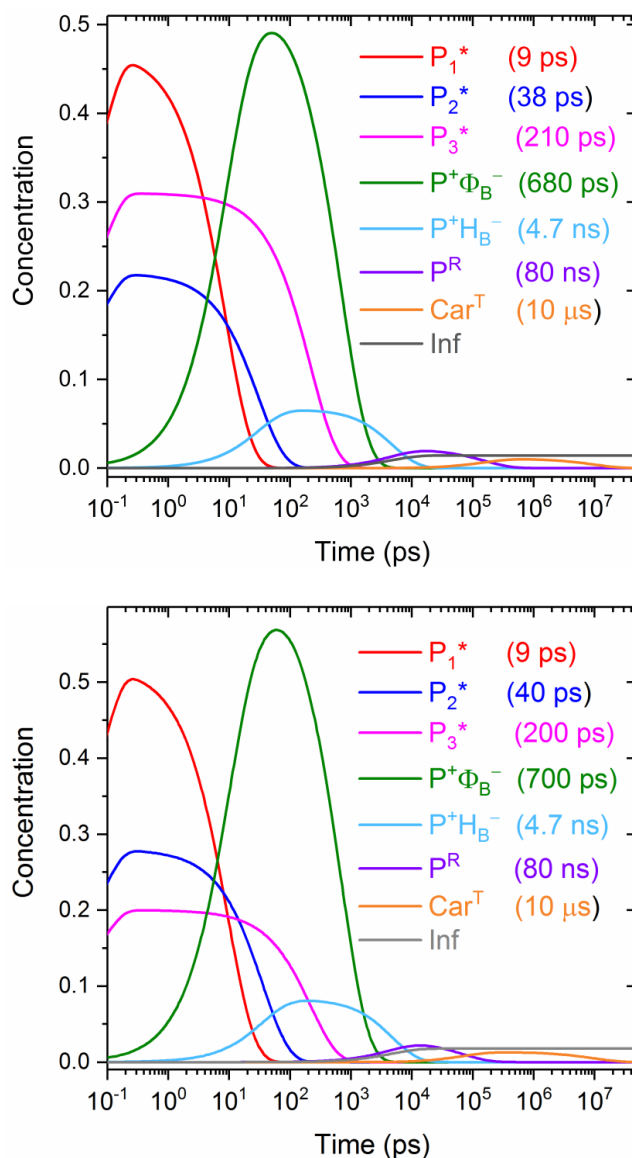


Figure 11. Concentrations of the species versus time for the SADS obtained from simulations of the TA data in the visible region for the Φ_B -F β_{AV} mutant (top) and $E\Phi_B$ -F β_{AV} mutant (bottom).

With ET to the A side suppressed in the *R. capsulatus* Φ_B -F β_{AV} and $E\Phi_B$ -F β_{AV} mutants, the outcome is that B-side ET to Φ_B is 50-60%, about 1.5-fold greater than the ~35% found for the *R. sphaeroides* Φ_B and $D\Phi_B$ mutants.^{21,22,24,25} In the *R. sphaeroides* mutants carrying the native A-side pigments and Tyr(M210), P^* has a very short lifetime (~3 ps) and supports majority ~65% yield of $P^+H_A^-$. A-side ET in our mutants is 10% at most. Thus, there is good

consistency of results between these mutants in terms of the effects of the mutations. One interesting difference is that the $P^+\Phi_B^-$ charge recombination lifetime is ~ 700 ps in the *R. capsulatus* Φ_B -F β_{AV} and E Φ_B -F β_{AV} RCs whereas it is ~ 200 ps in the *R. sphaeroides* Φ_B and D Φ_B mutants. Such a relatively small difference (factor of ~ 3) could have any number of molecular origins (including detergents used) that result, for example, in a different extent of mixing between $P^+\Phi_B^-$ and P^* in these RCs. Of course, there is more similarity than difference between these results when compared against the 10-20 ns lifetime of $P^+H_A^-$. In two *R. capsulatus* mutants devoid of BPh in the H_A binding site, $P^+B_A^-$ was trapped and has a 400-500 ps lifetime,¹⁶ a value that is nicely intermediate between the two lifetimes determined for the similar $P^+\Phi_B^-$ states in Φ_B -containing mutant RCs of *R. capsulatus* and *R. sphaeroides*.

Nature has optimized the RC energetics not only for fast stepwise charge separation on the A side but simultaneously for slow (in comparison) charge recombination processes, as in Figure 1B. Clearly the charge recombination reactions are sensitive to unavoidable thermal/quantum mechanical mixing involving neighboring pigments and charge-separated states that are close in free energy. In other words, the rates of these reactions are not governed simply by their free energies with respect to the ground state (i.e., the “energy-gap law” as in Marcus theory). If the latter tenet held simply, one would expect that $P^+\beta_A^-$ would have a longer lifetime than $P^+H_A^-$ whereas the reverse is true (~ 800 ps for $P^+\beta_A^-$ compared to ~ 15 ns for $P^+H_A^-$).^{36,64} Similar discussions have been presented for other mutant RCs in which the free energy gaps between states on the A side have been altered.^{66,69-71} The same theme applies to $P^+H_B^-$ on the B side where a 4-7 ns charge recombination lifetime is found for $P^+H_B^-$ in various mutants.³² Clearly the higher free energy of $P^+H_B^-$ versus $P^+H_A^-$ with consequent requirements for balancing charge separation and charge recombination dynamics presents quite an engineering

challenge for achieving a high yield of multi-step charge separation via the normally inactive B side of the RC.

Summary. Replacement of the H_A cofactor with a BChl (β_A) and substitution of Phe for Tyr at M208 in the *R. capsulatus* Φ_B -F β_A V and E Φ_B -F β_A V mutant RCs sufficiently slows ET to the A branch (yield $\leq 10\%$) to result in a larger yield (50-60%) of P⁺ Φ_B^- compared to previously studied *R. sphaeroides* Φ_B -containing mutants. The RCs studied herein also afford a very small yield of P⁺H_B⁻, $\sim 2\%$ in Φ_B -F β_A V and increased to $\sim 6\%$ in E Φ_B -F β_A V when H_B is hydrogen-bonded to Glu(M131). Global analysis of the TA data suggests that P⁺ Φ_B^- forms from the majority P* population that decays with a ~ 9 ps lifetime and that P⁺H_B⁻ forms from a P* population that has a ~ 40 -ps lifetime. It is possible that some P⁺H_B⁻ is also produced by ET from P⁺ Φ_B^- . The third P* population decays to the ground state with a lifetime of ~ 200 ps, which is the known time constant for P* internal conversion. Fast charge recombination involving P⁺B_A⁻/P⁺ β_A^- that involves repopulation of P* could also contribute to the ~ 200 ps component. A few percent yield P⁺Q_B⁻ is found for the E Φ_B -F β_A V mutant, which has not been observed previously for a Φ_B -containing RC. The P⁺Q_B⁻ is probably produced by ET from P⁺H_B⁻. Competing charge recombination of P⁺H_B⁻ likely gives rise to at least part of (if not most of) the observed excited triplet P (P^R) from which excited triplet carotenoid is produced via energy transfer.

The significantly higher yield of P⁺ Φ_B^- observed here for the *R. capsulatus* Φ_B -F β_A V and E Φ_B -F β_A V mutants compared to *R. sphaeroides* analogs studied previously derives from (1) more effective blocking of the A-side ET via replacement of Tyr(M208) with Phe and incorporation of β_A in place of H_A, (2) incorporation of Glu(M131) to lower the free energy of

$P^+H_B^-$, which may be more effective than Asp, (3) general differences of the two species and (4) detergents used. The first two points reflect the engineering considerations incorporated into the mutant design. The effects of the third and fourth points on the yields are not predictable. The net result is that $P^+\Phi_B^-$ forms with a yield as high as 60% in our *R. capsulatus* mutants. Unfortunately, our results indicate that in both mutants $P^+\Phi_B^-$ is likely lower in free energy than $P^+H_B^-$, at least in the majority of the RC population. As a result, the mutants do not afford a proportionately high yield of the subsequent ET steps needed to complete efficient B-side transmembrane charge separation. Regardless, the mutants studied here with their asymmetric distribution of two BChl and two BPh cofactors on the A and B branches, respectively, have provided new insights into how cofactor-cofactor and protein-cofactor interactions are managed to promote forward ET and hinder deactivation pathways simultaneously.

Acknowledgements

This work was supported by the U. S. Department of Energy, Office of Science, Office of Basic Energy Sciences under grant DE-SC0002036 (to CK and DH) and associated Field Work Proposal (to PDL). Argonne, a U.S. Department of Energy Office of Science laboratory, is operated under Contract No. DE-AC02-06CH11357. KMF was supported by National Science Foundation Graduate Research Fellowship grant DGE-1143954.

References

- (1) Deisenhofer, J.; Epp, O.; Miki, K.; Huber, R.; Michel, H. Structure of the Protein Subunits in the Photosynthetic Reaction Center from *Rhodospseudomonas viridis* at 3 Å Resolution. *Nature* **1985**, *318*, 618-624.
- (2) Allen, J. P.; Feher, G.; Yeates, T. O.; Komiya, H.; Rees, D. C. Structure of the Reaction Center from *Rhodobacter sphaeroides* R-26: The Cofactors. *Proc. Natl. Acad. Sci. U.S.A.* **1987**, *84*, 5730-5734.
- (3) Chang, C.-H.; El-Kabbani, O.; Tiede, D. M.; Norris, J. R.; Schiffer, M. The Structure of the Membrane-Bound Photosynthetic Reaction Center from *Rhodobacter sphaeroides* R-26. *Proc. Natl. Acad. Sci. U.S.A.* **1991**, *30*, 5352-5360.
- (4) Ermler, U.; Fritsch, G.; Buchanan, S. K.; Michel, H. Structure of the Photosynthetic Reaction Centre from *Rhodobacter sphaeroides* at 2.65 Å Resolution: Cofactors and Protein-Cofactor Interactions. *Structure* **1994**, *2*, 925-936.
- (5) Fyfe, P. K.; Jones, M. R. Re-emerging Structures: Continuing Crystallography of the Bacterial Reaction Centre. *Biochim. Biophys. Acta.* **2000**, *1459*, 413-421.
- (6) Peloquin, J. M.; Williams, J. C.; Lin, X.; Alden, R. G.; Taguchi, A. K. W.; Allen, J. P.; Woodbury, N. W. Time-Dependent Thermodynamics During Early Electron Transfer in Reaction Centers from *Rhodobacter sphaeroides*. *Biochemistry* **1994**, *33*, 8089-8100.
- (7) Gunner, M. The Reaction Center Protein from Purple Bacteria: Structure and Function. *Current Topics in Bioenergetics* **1991**, *16*, 319-367.
- (8) Goldstein, R. A.; Boxer, S. G. The Effect of Very High Magnetic Fields on the Reaction Dynamics in Bacterial Reaction Centers: Implication for the Reaction Mechanism. *Biochim. Biophys. Acta* **1989**, *977*, 78-86.
- (9) Hartwich, G.; Lossau, H.; Michel-Beyerle, M. E.; Ogrodnik, A. Nonexponential Fluorescence Decay in Reaction Centers of *Rhodobacter sphaeroides* Reflecting Dispersive Charge Separation up to 1 ns. *J. Phys. Chem. B* **1998**, *102*, 3815-3820.
- (10) Alden, R. G.; Parson, W. W.; Chu, Z. T.; Warshel, A. Orientation of the OH Dipole of Tyrosine (M)210 and Its Effect on Electrostatic Energies in Photosynthetic Bacterial Reaction Centers. *J. Phys. Chem.* **1996**, *100*, 16761-16770.
- (11) Bixon, M.; Jortner, J.; Michel-Beyerle, M. E. A Kinetic Analysis of the Primary Charge Separation in Bacterial Photosynthesis. Energy Gaps and Static Heterogeneity. *Chem. Phys.* **1995**, *197*, 389-404.
- (12) Schmidt, S.; Arlt, T.; Hamm, P.; Huber, H.; Nagele, T.; Wachtveitl, J.; Meyer, H.; Scheer, H.; Zinth, W. Energetics of the Primary Electron Transfer Reaction Revealed by Ultrafast Spectroscopy on Modified Bacterial Reaction Centers. *Chem. Phys. Lett.* **1994**, *223*, 116-120.
- (13) Kennis, J. T. M.; Shkuropatov, A. Y.; van Stokkum, I. H. M.; Gast, P.; Hoff, A. J.; Shuvalov, V. A.; Aartsma, T. J. Formation of a Long-Lived P⁺B_A⁻ State in Plant Pheophytin-Exchanged Reaction Centers of *Rhodobacter sphaeroides* R26 at Low Temperature. *Biochemistry* **1997**, *36*, 16231-16238.
- (14) Streltsov, A. M.; Vulto, S. I. E.; Shkuropatov, A. Y.; Hoff, A. J.; Aartsma, T. J.; Shuvalov, V. A. B_A and B_B Absorbance Perturbations Induced by Coherent Nuclear Motions in Reaction Centers from *Rhodobacter sphaeroides* upon 30-fs Excitation of the Primary Donor. *J. Phys. Chem. B* **1998**, *102*, 7293-7298.

- (15) Roberts, J. A.; Holten, D.; Kirmaier, C. Primary Events in Photosynthetic Reaction Centers with Multiple Mutations Near the Photoactive Electron Carriers. *J. Phys. Chem. B* **2001**, *105*, 5575-5584.
- (16) Carter, B.; Boxer, S. G.; Holten, D.; Kirmaier, C. Trapping the P⁺B_L⁻ Initial Intermediate State of Charge Separation in Photosynthetic Reaction Centers from *Rhodobacter capsulatus*. *Biochemistry* **2009**, *48*, 2571-2573.
- (17) Saggiu, M.; Carter, B.; Zhou, X.; Faries, K.; Cegelski, L.; Holten, D.; Boxer, S. G.; Kirmaier, C. Putative Hydrogen Bond to Tyrosine M208 in Photosynthetic Reaction Centers from *Rhodobacter capsulatus* Significantly Slows Primary Charge Separation. *J. Phys. Chem. B* **2014**, *118*, 6721-6732.
- (18) Kirmaier, C.; He, C.; Holten, D. Manipulating the Direction of Electron Transfer in the Bacterial Reaction Center by Swapping Phe for Tyr Near BChl_M (L181) and Tyr for Phe Near BChl_L (M208). *Biochemistry* **2001**, *40*, 12132-12139.
- (19) Heller, B. A.; Holten, D.; Kirmaier, C. Control of Electron Transfer to the L-side Versus the M-side of the Photosynthetic Reaction Center. *Science* **1995**, *269*, 940-945.
- (20) Kirmaier, C.; Weems, D.; Holten, D. M-side Electron Transfer in Reaction Center Mutants with a Lysine near the Nonphotoactive Bacteriochlorophyll. *Biochemistry* **1999**, *38*, 11516-11530.
- (21) Katilius, E.; Turanchik, T.; Lin, S.; Taguchi, A. K. W.; Woodbury, N. W. B-Side Electron Transfer in a *Rhodobacter sphaeroides* Reaction Center Mutant in Which the B-Side Monomer Bacteriochlorophyll is Replaced with Bacteriopheophytin. *J. Phys. Chem. B* **1999**, *103*, 7386-7389.
- (22) Katilius, E.; Katiliene, Z.; Lin, S.; Taguchi, A. K. W.; Woodbury, N. W. B Side Electron Transfer in a *Rhodobacter sphaeroides* Reaction Center Mutant in Which the B Side Monomer Bacteriochlorophyll is Replaced with Bacteriopheophytin: Low-Temperature Study and Energetics of Charge-Separated. *J. Phys. Chem. B* **2002**, *106*, 1471-1475.
- (23) Katilius, E.; Katiliene, Z.; Lin, S.; Taguchi, A. K. W.; Woodbury, N. W. B-Side Electron Transfer in the HE(M182) Reaction Center Mutant from *Rhodobacter sphaeroides*. *J. Phys. Chem. B* **2002**, *106*, 12344-12350.
- (24) Katilius, E.; Babendure, J. L.; Katiliene, Z.; Lin, S.; Taguchi, A. K.; Woodbury, N. W. Manipulations of the B-Side Charge-Separated States' Energetics in the *Rhodobacter sphaeroides* Reaction Center. *J. Phys. Chem. B* **2003**, *107*, 12029-12034.
- (25) de Boer, A. L.; Neerken, S.; de Wijn, R.; Permentier, H. P.; Gast, P.; Vijgenboom, E.; Hoff, A. J. High Yield of B-Branch Electron Transfer in a Quadruple Reaction Center Mutant of the Photosynthetic Bacterium *Rhodobacter sphaeroides*. *Biochemistry* **2002**, *41*, 3081-3088.
- (26) Fajer, J.; Borg, D. C.; Forman, A.; Dolphin, D.; Felton, R. H. Anion Radical of Bacteriochlorophyll. *J. Am. Chem. Soc.* **1973**, *95*, 2739-2741.
- (27) Fajer, J.; Brune, D. C.; Davis, M. S.; Forman, A.; Spaulding, L. D. Primary Charge Separation in Bacterial Photosynthesis: Oxidized Chlorophylls and Reduced Pheophytin. *Proc. Natl. Acad. Sci. U.S.A.* **1975**, *72*, 4956-4960.
- (28) Cotton, T. M.; Van Duyne, R. P. An Electrochemical Investigation of the Redox Properties of Bacteriochlorophyll and Bacteriopheophytin in Aprotic Solvents. *J. Am. Chem. Soc.* **1979**, *101*, 7605-7612.
- (29) Felton, R. H. Primary Redox Reactions of Metalloporphyrins. In *The Porphyrins*; Dolphin, D., Ed.; Academic Press: New York, 1978; Vol. V; pp 53-125.

- (30) Faries, K. M.; Kressel, L. L.; Wander, M. J.; Holten, D.; Laible, P. D.; Kirmaier, C.; Hanson, D. K. High Throughput Engineering to Revitalize a Vestigial Electron Transfer Pathway in Bacterial Photosynthetic Reaction Centers. *J. Biol. Chem.* **2012**, *287*, 8507-8514.
- (31) Kressel, L.; Faries, K. M.; Wander, M. J.; Zogzas, C. E.; Mejdrich, R. J.; Hanson, D. K.; Holten, D.; Laible, P. D.; Kirmaier, C. High Yield of Secondary B-side Electron Transfer in Mutant *Rhodobacter capsulatus* Reaction Centers. *Biochim. Biophys. Acta.* **2014**, *1837*, 1892-1903.
- (32) Faries, K. M.; Kressel, L. L.; Dylla, N. P.; Wander, W. J.; Hanson, D. K.; Holten, D.; Laible, P. D.; Kirmaier, C. Optimizing Multi-step B-side Charge Separation in Photosynthetic Reaction Centers from *Rhodobacter capsulatus*. *Biochim. Biophys. Acta.* **2016**, *1857*, 150-159.
- (33) Dylla, N. P.; Faries, K.; Wyllie, R. M.; Swenson, A. M.; Hanson, D. K.; Holten, D.; Kirmaier, C.; Laible, P. D. Species Differences in Unlocking B-side Electron Transfer in Bacterial Reaction Centers. *Febs Lett* **2016**, *590*, 2515-2526.
- (34) Kirmaier, C.; Laible, P. D.; Czarnecki, K.; Hata, A. N.; Hanson, D. K.; Bocian, D. F.; Holten, D. Comparison of M-side Electron Transfer in *Rb. sphaeroides* and *Rb. capsulatus* Reaction Centers. *J. Phys. Chem. B* **2002**, *106*, 1799-1808.
- (35) van der Rest, M.; Gingras, G. Pigment Complement of Photosynthetic Reaction Center Isolated from *Rhodospirillum rubrum*. *J. Biol. Chem.* **1974**, *249*, 6446-6453.
- (36) Kirmaier, C.; Gaul, D.; DeBey, R.; Holten, D.; Schenck, C. C. Charge Separation in a Reaction Center Incorporating Bacteriochlorophyll in Place of Photoactive Bacteriopheophytin. *Science* **1991**, *251*, 922-927.
- (37) Kirmaier, C.; Cua, A.; He, C.; Holten, D.; Bocian, D. F. Probing M-Branch Electron Transfer and Cofactor Environment in the Bacterial Photosynthetic Reaction Center by the Addition of a Hydrogen Bond to the M-side Bacteriopheophytin. *J. Phys. Chem. B* **2002**, *106*, 495-503.
- (38) Carter, B.; Boxer, S. G.; Holten, D.; Kirmaier, C. Photochemistry of a Bacterial Photosynthetic Reaction Center Missing the Initial Bacteriochlorophyll Electron Acceptor. *J. Phys. Chem. B* **2012**, *116*, 9971-9982.
- (39) Muh, F.; Williams, J. C.; Allen, J. P.; Lubitz, W. A Conformational Change of the Photoactive Bacteriopheophytin in Reaction Centers from *Rhodobacter sphaeroides*. *Biochemistry* **1998**, *37*, 13066-13074.
- (40) Fufina, T. Y.; Vasilieva, L. G.; Khatypov, R. A.; Shkuropatov, A. Y.; Shuvalov, V. A. Substitution of Isoleucine L177 by Histidine in *Rhodobacter sphaeroides* Reaction Center Results in the Covalent Binding of P-A Bacteriochlorophyll to the L Subunit. *Febs Lett* **2007**, *581*, 5769-5773.
- (41) Jia, Y.; DiMagno, T. J.; Chan, C.-K.; Wang, Z.; Du, M.; Hanson, D. K.; Schiffer, M.; Norris, J. R.; Fleming, G. R.; Popov, M. S. Primary Charge Separation in Mutant Reaction Centers of *Rhodobacter capsulatus*. *J. Phys. Chem.* **1993**, *97*, 13180-13191.
- (42) Laible, P. D.; Greenfield, S. R.; Wasielewski, M. R.; Hanson, D. K.; Pearlstein, R. M. Antenna Excited State Decay Kinetics Establish Primary Electron Transfer in Reaction Centers as Heterogeneous. *Biochemistry* **1997**, *36*, 8677-8685.
- (43) Kirmaier, C.; Holten, D. Evidence that a Distribution of Bacterial Reaction Centers Underlies the Temperature- and Detection-Wavelength-Dependence of the Rates of the Primary Electron Transfer Reactions. *Proc. Natl. Acad. Sci. U.S.A.* **1990**, *97*, 3522-3556.

- (44) Wang, H. Y.; Hao, Y. W.; Jiang, Y.; Lin, S.; Woodbury, N. W. Role of Protein Dynamics in Guiding Electron-Transfer Pathways in Reaction Centers from *Rhodobacter sphaeroides*. *J. Phys. Chem. B* **2012**, *116*, 711-717.
- (45) Guo, Z.; Woodbury, N. W.; Pan, J.; Lin, S. Protein Dielectric Environment Modulates the Electron-Transfer Pathway in Photosynthetic Reaction Centers. *Biophys J* **2012**, *103*, 1979-1988.
- (46) Zankel, K. L.; Reed, D. W.; Clayton, R. K. Fluorescence and Photochemical Quenching in Photosynthetic Reaction Centers. *Proc. Natl. Acad. Sci. U.S.A.* **1968**, *61*, 1243-&.
- (47) Lockhart, D. J.; Boxer, S. G. Electric-Field Modulation of the Fluorescence from *Rhodobacter-Sphaeroides* Reaction Centers. *Chem. Phys. Lett.* **1988**, *144*, 243-250.
- (48) Kirmaier, C.; Laible, P. D.; Hinden, E.; Hanson, D. K.; Holten, D. Detergent Effects on Primary Charge Separation in Wild-Type and Mutant *Rhodobacter capsulatus* Reaction Centers. *Chem. Phys.* **2003**, *294*, 305-318.
- (49) Chuang, J. I.; Boxer, S. G.; Holten, D.; Kirmaier, C. High Yield of M-side Electron Transfer in Mutants of *Rhodobacter capsulatus* Reaction Centers Lacking the L-side Bacteriopheophytin. *Biochemistry* **2006**, *45*, 3845-3851.
- (50) Chuang, J. I.; Boxer, S. G.; Holten, D.; Kirmaier, C. Temperature Dependence of Electron Transfer to the M-side Bacteriopheophytin in *Rhodobacter capsulatus* Reaction Centers. *J. Phys. Chem. B* **2008**, *112*, 5487-5499.
- (51) Kirmaier, C.; Holten, D. Low-Temperature Studies of Electron Transfer to the M Side of YFH Reaction Centers from *Rhodobacter capsulatus*. *J. Phys. Chem. B* **2009**, *113*, 1132-1142.
- (52) Kirmaier, C.; Laible, P. D.; Hanson, D. K.; Holten, D. B-side Charge Separation in Bacterial Photosynthetic Reaction Centers: Nanosecond-Timescale Electron Transfer from H_B⁻ to Q_B. *Biochemistry* **2003**, *42*, 2016-2024.
- (53) Nagarajan, V.; Parson, W. W.; Davis, D.; Schenck, C. C. Kinetics and Free Energy Gaps of Electron Transfer Reactions in *Rhodobacter sphaeroides* Reaction Centers. *Biochemistry* **1993**, *32*, 12324-12336.
- (54) Bixon, M.; Jortner, J.; Michel-Beyerle, M. E. On the Mechanism of Primary Charge Separation in Bacterial Photosynthesis. *Biochim. Biophys. Acta* **1991**, *1056*, 301-315.
- (55) de Winter, A.; Boxer, S. G. The Mechanism of Triplet Energy Transfer from the Special Pair to the Carotenoid in Bacterial Photosynthetic Reaction Centers. *J. Phys. Chem. B* **1999**, *103*, 8786-8789.
- (56) Bialek, R.; Burdzinski, G.; Jones, M. R.; Gibasiewicz, K. Bacteriopheophytin Triplet State in *Rhodobacter sphaeroides* Reaction Centers. *Photosynth. Res.* **2016**, *129*, 205-216.
- (57) Arellano, J. B.; Melo, T. B.; Fyfe, P. K.; Cogdell, R. J.; Naqvi, K. R. Multichannel Flash Spectroscopy of the Reaction Centers of Wild-Type and Mutant *Rhodobacter sphaeroides*: Bacteriochlorophyll(B)-Mediated Interaction Between the Carotenoid Triplet and the Special Pair. *Photochem. Photobiol.* **2004**, *79*, 68-75.
- (58) Alden, R. G.; Parson, W. W.; Chu, Z. T.; Warshel, A. Calculations of Electrostatic Energies in Photosynthetic Reaction Centers. *J. Am. Chem. Soc.* **1995**, *117*, 12284-12298.
- (59) Gunner, M. R.; Nicholls, A.; Honig, B. Electrostatic Potentials in *Rhodospseudomonas viridis* Reaction Centers: Implications for the Driving Force and Directionality of Electron Transfer. *J. Phys. Chem.* **1996**, *100*, 4277-4291.

- (60) Woodbury, N. W.; Parson, W. W. Nanosecond Fluorescence from Isolated Photosynthetic Reaction Centers of *Rhodospseudomonas sphaeroides*. *Biochim. Biophys. Acta* **1984**, *767*, 345-361.
- (61) Ogrodnik, A.; Keupp, W.; Volk, M.; Aumeier, G.; Michel-Beyerle, M. E. Inhomogeneity of Radical Pair Energies in Photosynthetic Reaction Centers Revealed by Differences in Recombination Dynamics of P^+H^- when Detected in Delayed Emission and in Absorption. *J. Phys. Chem.* **1994**, *98*, 3432-3439.
- (62) Dubas, K.; Baranowski, M.; Podhorodecki, A.; Jones, M. R.; Gibasiewicz, K. Unified Model of Nanosecond Charge Recombination in Closed Reaction Centers from *Rhodobacter sphaeroides*: Role of Protein Polarization Dynamics. *J. Phys. Chem. B* **2016**, *120*, 4890-4896.
- (63) Kirmaier, C.; Laporte, L.; Schenck, C. C.; Holten, D. The Nature and Dynamics of the Charge-Separated Intermediate in Reaction Centers in Which Bacteriochlorophyll Replaces the Photoactive Bacteriopheophytin .1. Spectral Characterization of the Transient State. *J. Phys. Chem.* **1995**, *99*, 8903-8909.
- (64) Kirmaier, C.; Laporte, L.; Schenck, C. C.; Holten, D. The Nature and Dynamics of the Charge-Separated Intermediate in Reaction Centers in Which Bacteriochlorophyll Replaces the Photoactive Bacteriopheophytin .2. The Rates and Yields of Charge Separation and Recombination. *J. Phys. Chem.* **1995**, *99*, 8910-8917.
- (65) Heller, B. A.; Holten, D.; Kirmaier, C. Effects of Asp Residues Near the L-side Pigments in Bacterial Reaction Centers. *Biochemistry* **1996**, *35*, 15418-15427.
- (66) Pan, J.; Saer, R. G.; Lin, S.; Guo, Z.; Beatty, J. T.; Woodbury, N. W. The Protein Environment of the Bacteriopheophytin Anion Modulates Charge Separation and Charge Recombination in Bacterial Reaction Centers. *J. Phys. Chem. B* **2013**, *117*, 7179-7189.
- (67) Gibasiewicz, K.; Bialek, R.; Pajzderska, M.; Karolczak, J.; Burdzinski, G.; Jones, M. R.; Brettel, K. Weak Temperature Dependence of $P^+H_A^-$ Recombination in Mutant *Rhodobacter sphaeroides* Reaction Centers. *Photosynth. Res.* **2016**, *128*, 243-258.
- (68) Kee, H. L.; Laible, P. D.; Bautista, J. A.; Hanson, D. K.; Holten, D.; Kirmaier, C. Determination of the Rate and Yield of B-side Quinone Reduction in *Rhodobacter capsulatus* Reaction Centers. *Biochemistry* **2006**, *45*, 7314-7322.
- (69) Laporte, L.; McDowell, L. M.; Kirmaier, C.; Schenck, C. C.; Holten, D. Insights into the Factors Controlling the Rates of the Deactivation Processes That Compete with Charge Separation in Photosynthetic Reaction Centers. *Chem. Phys.* **1993**, *176*, 615-629.
- (70) Saer, R. G.; Hardjasa, A.; Rosell, F. I.; Mauk, A. G.; Murphy, M. E. P.; Beatty, J. T. Role of *Rhodobacter sphaeroides* Photosynthetic Reaction Center Residue M214 in the Composition, Absorbance Properties, and Conformations of H-A and B-A Cofactors. *Biochemistry* **2013**, *52*, 2206-2217.
- (71) Gibasiewicz, K.; Pajzderska, M.; Potter, J. A.; Fyfe, P. K.; Dobek, A.; Brettel, K.; Jones, M. R. Mechanism of Recombination of the $P^+H_A^-$ Radical Pair in Mutant *Rhodobacter sphaeroides* Reaction Centers with Modified Free Energy Gaps Between $P^+B_A^-$ and $P^+H_A^-$. *J. Phys. Chem. B* **2011**, *115*, 13037-13050.

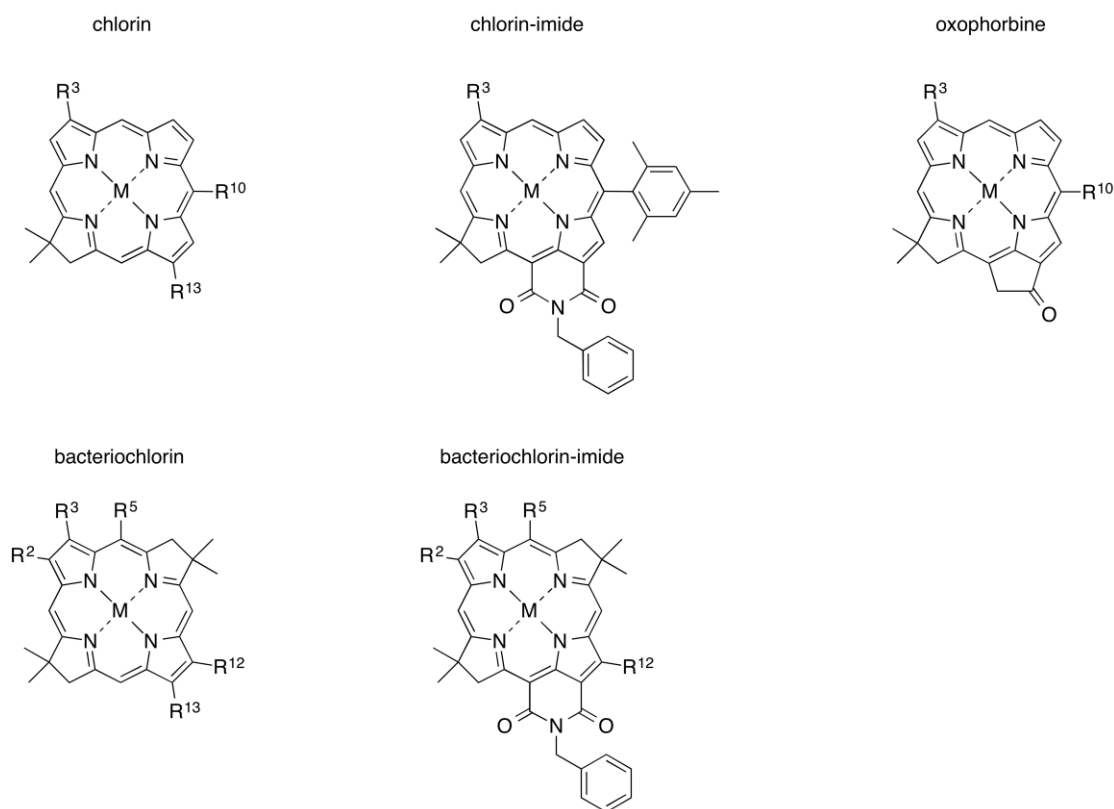
Conclusions/Outlook

The purpose of this thesis is to advance our understanding of the critical photosynthetic processes of light-harvesting and electron transfer, and to build upon those processes in semi-synthetic and artificial systems. In particular, I investigated chlorophyll-like chromophores containing unnatural functional groups to determine how the new structure altered their photophysical properties (such as red-shifted absorption). I also studied purple bacteria where the non-photosynthetic pigment-protein complex yellow fluorescent protein (YFP) from a jellyfish was added to the bacteria's natural reaction center, resulting in enhanced light-harvesting capacity. Finally, I examined purple bacterial reaction centers with modified native protein architectures and pigment contents with increased 'wrong-way' electron transfer. Much of this work was part of pilot projects and/or falls under the category of 'basic research', which are projects/research that are expanding our understanding of a system/process, but are not at this time being directly applied to human designed systems. However, much of this work lays the groundwork for future studies and applied systems, such as dye-sensitized solar cells utilizing chlorophyll-like pigments, bacteria used for biofuels with augmented light-harvesting (containing non-native chromophores produced *in vivo*), or even protein-based semi-synthetic electron transfer systems. It is my profound hope and desire to see this work used as a springboard for future projects, and more importantly, to be used in applied systems used to enrich the lives of people and preserve our environment.

Appendices

Appendix 1. Supporting Information for Chapter 2.

Chart S1. Structures of generic synthetic hydroporphyrins and hydroporphyrin-imides.



General descriptors for the following tables:

Macrocycles:

BC = bacteriochlorin, C = chlorin.

Metalation state:

Fb = free base (i.e., H, H); Zn = zinc.

Substituents:

A = acetyl, E = ethynyl (with H, trimethylsilyl, or triisopropylsilyl at the terminus), Es = ester [invariably methoxycarbonyl (for a chlorin) or ethoxycarbonyl (for a bacteriochlorin)], Et = ethyl, F = formyl, Hep = *n*-heptyl, Im = imide (spanning 13,15-positions; all imide substituents here are the *N*-benzyl unit), M = mesityl, MeO = methoxy (5-position of a bacteriochlorin), OP = oxophorbine (i.e., exocyclic ring spanning 13,15-positions), T = *p*-tolyl, V = vinyl.

Table S1. Photophysical properties of prior chlorins.^a

Code ^b	Compound	B _{max} abs (nm)	Q _y (0,0) abs (nm)	Q _y (0,0) emis (nm)	I _{Q_y} / I _B	ΣQ _y / Σ _B	Φ _f	τ _s (ns)	k _f ⁻¹ (ns)	k _{nr} ⁻¹ (ns)
<i>Prior zinc chlorins</i>										
a	ZnC⁰	398	602	604	0.29	0.24	0.057	1.5	26	1.6
b	ZnC-V³M¹⁰	412	620	624	0.29	0.28	0.075	1.8	24	1.9
c	ZnC-E³M¹⁰	416	627	630	0.37	0.27	0.12	2.3	19	2.6
d	ZnOP⁰	419	637	639	0.63	0.42	0.21	5.5	26	7.0
e	ZnC-M¹⁰F¹³	418	633	637	0.50	0.34	0.25	5.3	21	7.1
f	ZnC-M¹⁰A¹³	418	632	635	0.45	0.32	0.24	5.1	21	6.7
g	ZnC-M¹⁰E¹³	412	625	628	0.45	0.33	0.18	3.0	17	3.7
h	ZnC-M¹⁰F^{3,13}	439	667	672	0.71	0.45	0.31	6.3	20	9.1
i	ZnC-M¹⁰A^{3,13}	436	662	668	0.67	0.45	0.32	6.0	19	8.8
j	ZnC-M¹⁰E^{3,13}	423	646	649	0.63	0.40	0.23	4.1	18	5.3
k	ZnC-M¹⁰E¹⁵	420	618	621	0.22	0.22	0.070	2.0	29	2.2
<i>Prior free base chlorins</i>										
l	FbC⁰	389	633	635	0.42	0.19	0.20	9.4	47	11.8
m	FbOP⁰	408	654	656	0.67	0.24	0.27	12.5	46	17.1
n	FbOP-A³M¹⁰	427 ^c	683	686	0.77	0.29	0.26	11.5	44	15.5
o	FbC-M¹⁰E¹³	418	654	656	0.63	0.20	0.30	9.8	33	14.0
p	FbC-M¹⁰A^{3,13}	432	687	691	0.71	0.26	0.24	7.8	33	10.3
q	FbC-M¹⁰E^{3,13}	427	672	674	0.83	0.26	0.34	9.2	27	13.9
r	FbC-M¹⁰E¹⁵	413	655	657	0.26	0.13	0.23	12.7	55	16.5

^aAll data were obtained at room temperature in toluene from references 80-82. All synthetic compounds contain a 10-mesityl group except those that contain a superscript “0” after the macrocycle name (**ZnC⁰**, **ZnOP⁰**, **FbC⁰** and **FbOP⁰**). See Chart S1 for generic structures of the synthetic chlorins, chlorin-imides, oxophorbins, bacteriochlorins, and bacteriochlorin-imides. Columns 6 and 7 give the peak (I_{Q_y}/I_B) and integrated (ΣQ_y/Σ_B when plotted vs cm⁻¹) intensity ratios of the Q_y and Soret (B) absorption manifolds.

^bIdentifier for data shown in Figures 4, 5 and 7. ^cFeatures are observed at 427 and 446 nm.

Table S2. Molecular orbital energies of prior chlorins.^a

Code ^b	Compound	H-1	H	L	L+1	L – H	L+1 – H-1	ΔE_{avg}	ΔE_{dif}
<i>Prior zinc chlorins</i>									
a	ZnC⁰	-5.16	-4.79	-2.12	-1.55	2.67	3.61	3.14	0.94
b	ZnC-V³M¹⁰	-5.13	-4.79	-2.22	-1.61	2.57	3.52	3.05	0.95
c	ZnC-E³M¹⁰	-5.19	-4.85	-2.28	-1.67	2.57	3.52	3.05	0.95
d	ZnOP⁰	-5.34	-5.12	-2.57	-1.83	2.55	3.51	3.03	0.96
e	ZnC-M¹⁰F¹³	-5.30	-5.02	-2.49	-1.75	2.53	3.55	3.04	1.02
f	ZnC-M¹⁰A¹³	-5.23	-4.95	-2.42	-1.69	2.53	3.54	3.04	1.01
g	ZnC-M¹⁰E¹³	-5.19	-4.85	-2.27	-1.64	2.58	3.55	3.07	0.97
h	ZnC-M¹⁰F^{3,13}	-5.48	-5.23	-2.85	-2.04	2.38	3.44	2.91	1.06
i	ZnC-M¹⁰A^{3,13}	-5.33	-5.09	-2.69	-1.90	2.40	3.43	2.92	1.03
j	ZnC-M¹⁰E^{3,13}	-5.26	-4.91	-2.42	-1.75	2.49	3.51	3.00	1.02
k	ZnC-M¹⁰E¹⁵	-5.12	-4.88	-2.26	-1.67	2.62	3.45	3.04	0.83
<i>Prior free base chlorins</i>									
l	FbC⁰	-5.07	-4.89	-2.20	-1.67	2.69	3.40	3.05	0.71
m	FbOP⁰	-5.26	-5.20	-2.62	-1.93	2.58	3.33	2.96	0.75
n	FbOP-A³M¹⁰	-5.30	-5.29	-2.84	-2.13	2.45	3.17	2.81	0.72
o	FbC-M¹⁰E¹³	-5.10	-4.93	-2.33	-1.75	2.60	3.35	2.98	0.75
p	FbC-M¹⁰A^{3,13}	-5.24	-5.17	-2.76	-2.00	2.41	3.24	2.83	0.83
q	FbC-M¹⁰E^{3,13}	-5.16	-4.99	-2.47	-1.86	2.52	3.30	2.91	0.78
r	FbC-M¹⁰E¹⁵	-5.04	-4.96	-2.35	-1.78	2.61	3.26	2.94	0.65

^aObtained from DFT calculations described in references 80-82. All values are in eV. All synthetic compounds contain a 10-mesityl group except those that contain a superscript “0” after the macrocycle name (**ZnC⁰**, **ZnOP⁰**, **FbC⁰** and **FbOP⁰**). See Chart S1 for generic structures of the synthetic chlorins, chlorin-imides, oxophorbins, bacteriochlorins, and bacteriochlorin-imides. ^bIdentifier for data shown in Figures 4, 5 and 7.

Table S3. Photophysical properties of prior bacteriochlorins and bacteriochlorin-imides.^a

Code ^b	Compound	B _{max} abs (nm)	Q _y (0,0) abs (nm)	Q _y (0,0) emis (nm)	I _{Q_y} / I _B	ΣQ _y / Σ _B	Φ _f	τ _s (ns)	k _f ⁻¹ (ns)	k _{nr} ⁻¹ (ns)
<i>Prior zinc bacteriochlorins</i>										
α	ZnBC	375	723	725	1.7	0.28	0.1	3.4	34	3.8
β	MeO-ZnBC-Hep^{2,12}EEs^{3,13}	352	750	757	1.3	0.17	0.2	4.3	22	5.4
χ	ZnBC-T^{2,12}	344	749	756	1.3	0.37	0.11	2.9	26	3.3
δ	ZnBC Hep^{2,12}EEs^{3,12}	347	775	780	1.2	0.21	0.14	3.5	25	4.1
ε	MeO-ZnBC-M^{2,12}EEs^{3,12}	353	773	780	1.6	0.43	0.12	2.9	24	3.3
φ	ZnBC-Et^{2,12}EEs^{3,13}	347	773	778	1.6	0.23	0.08	2.6	33	2.8
γ	MeO-ZnBC-EEs^{2,3,12,13}	354	774	782	2.0	0.45	0.13	4.4	34	5.1
η	ZnBCIm-Et^{2,12}Es^{3,13}	356	830	835	1.7	0.24	0.033	2.2	67	2.3
<i>Prior free base bacteriochlorins</i>										
ι	MeO-FbBC	346	709	711	0.87	0.11	0.25	5.0	20	6.7
φ	FbBC	340	713	716	0.85	0.11	0.13	4.0	31	4.6
κ	FbBC-M^{3,13}	345	725	727	0.99	0.13	0.15	4.2	28	4.9
λ	MeO-FbBC-Es^{3,13}	355	734	740	1.01	0.14	0.19	4.8	25	5.9
μ	MeO-FbBC-A^{3,13}	363	740	748	0.96	0.15	0.14	3.8	27	4.4
ν	FbBC-V^{3,13}	352	750	754	0.94	0.17	0.17	3.3	19	4.0
ο	FbBC-Es^{3,13}	352	754	763	1.06	0.17	0.14	3.9	28	4.5
π	FbBC-A^{3,13}	360	768	771	1.19	0.19	0.11	3.3	30	3.7
θ	FbBC-F^{3,13}	363	771	775	0.80	0.20	0.11	2.9	26	3.3
ρ	MeO-FbBCIm-Et^{2,12}EEs^{3,13}	371	792	798	1.02	0.14	0.05	2.2	44	2.3
σ	FbBCIm-Et^{2,12}EEs^{3,13}	358	818	823	1.28	0.19	0.04	1.9	48	2.0

^aAll data were obtained at room temperature in toluene from references 73 and 74. See Chart S1 for generic structures of the synthetic chlorins, chlorin-imides, oxophorbines, bacteriochlorins, and bacteriochlorin-imides. Columns 6 and 7 give the peak (I_B/I_{Q_y}) and integrated (Σ_B/Σ_{Q_y}, when plotted vs cm⁻¹) intensity ratios of the Q_y and Soret (B) absorption manifolds. ^bIdentifier for data shown in Figures 4, 5 and 7. The typical errors (percent of value) are as follows: τ_s (±7%), Φ_f (±5%), Φ_{isc} (±15%), Φ_{ic} (±20), k_f (±10%), k_{isc} (±20%), k_{ic} (±25%). The error bars for τ_s, Φ_f, and Φ_{isc} were determined from select repeat measurements over a broad range of values and those for the Φ_{ic}, k_f, k_{isc} and k_{ic} were obtained from propagation of errors.

Table S4. Molecular orbital energies of prior bacteriochlorins and bacteriochlorin-imides.^a

Code ^b	Compound	H-1	H	L	L+1	L – H	L+1 – H-1	ΔE_{avg}	ΔE_{dif}
<i>Prior zinc bacteriochlorins</i>									
α	ZnBC	-5.08	-4.30	-2.16	-0.71	2.14	4.37	3.26	2.23
β	MeO-ZnBC-Hep^{2,12}EEs^{3,13}	-5.15	-4.48	-2.46	-0.93	2.02	4.22	3.12	2.20
χ	ZnBC-T^{2,12}	-5.06	-4.26	-2.20	-0.76	2.06	4.30	3.18	2.24
δ	ZnBC-Hep^{2,12}EEs^{3,12}	-5.20	-4.47	-2.52	-0.91	1.95	4.29	3.12	2.34
ε	MeO-ZnBC-M^{2,12}EEs^{3,12}	-5.18	-4.55	-2.51	-0.96	2.04	4.22	3.13	2.18
ϕ	ZnBC-Et^{2,12}EEs^{3,13}	-5.22	-4.48	-2.53	-0.92	1.95	4.30	3.13	2.35
γ	MeO-ZnBC-EEs^{2,3,12,13}	-5.42	-4.87	-2.92	-1.20	1.95	4.22	3.09	2.27
η	ZnBCIm-Et^{2,12}Es^{3,13}	-5.60	-4.78	-2.94	-1.39	1.84	4.21	3.03	2.37
<i>Prior free base bacteriochlorins</i>									
ι	MeO-FbBC	-4.91	-4.48	-2.20	-0.93	2.28	3.98	3.13	1.70
φ	FbBC	-4.99	-4.46	-2.20	-0.93	2.26	4.06	3.16	1.80
κ	FbBC-M^{3,13}	-4.98	-4.43	-2.19	-0.95	2.24	4.03	3.14	1.79
λ	MeO-FbBC-Es^{3,13}	-5.09	-4.75	-2.60	-1.21	2.15	3.88	3.02	1.73
μ	MeO-FbBC-A^{3,13}	-5.21	-4.84	-2.70	-1.33	2.14	3.88	3.01	1.74
ν	FbBC-V^{3,13}	-5.03	-4.48	-2.37	-1.04	2.11	3.99	3.05	1.88
\omicron	FbBC-Es^{3,13}	-5.20	-4.77	-2.67	-1.21	2.10	3.99	3.05	1.89
π	FbBC-A^{3,13}	-5.26	-4.83	-2.78	-1.31	2.05	3.95	3.00	1.90
θ	FbBC-F^{3,13}	-5.41	-4.97	-2.94	-1.49	2.03	3.92	2.98	1.89
ρ	MeO-FbBCIm-Et^{2,12}EEs^{3,13}	-5.43	-4.91	-2.89	-1.51	2.02	3.92	2.97	1.90
σ	FbBCIm-Et^{2,12}EEs^{3,13}	-5.51	-4.91	-2.99	-1.50	1.92	4.01	2.97	2.09

^aObtained from DFT calculations from references 73 and 74. All values are in eV. The synthetic bacteriochlorins do not contain a 10-mesityl group. See Chart S1 for generic structures of the synthetic chlorins, chlorin-imides, oxophorbins, bacteriochlorins, and bacteriochlorin-imides. ^bIdentifier for data shown in Figures 4, 5 and 7.

Complete reference:

(79) Except for molecular mechanics and semi-empirical models, the calculation methods used in Spartan '08 or '10 have been documented in: Shao, Y.; Molnar, L. F.; Jung, Y.; Kussmann, J. R.; Ochsenfeld, C.; Brown, S. T.; Gilbert, A. T. B.; Slipchenko, L. V.; Levchenko, S. V.; O'Neill, D. P.; DiStasio, R. A., Jr.; Lochan, R. C.; Wang, T.; Beran, G. J. O.; Besley, N. A.; Herbert, J. M.; Yeh Lin, C.; Van Voorhis, T.; Hung Chien, S.; Sodt, A.; Steele, R. P.; Rassolov, V. A.; Maslen, P. E.; Korambath, P. P.; Adamson, R. D.; Austin, B.; Baker, J.; Byrd, E. F. C.; Dachsel, H.; Doerksen, R. J.; Dreuw, A.; Dunietz, B. D.; Dutoi, A. D.; Furlani, T. R.; Gwaltney, S. R.; Heyden, A.; Hirata, S.; Hsu, C.-P.; Kedziora, G.; Khalliulin, R. Z.; Klunzinger, P.; Lee, A. M.; Lee, M. S.; Liang, W.; Lotan, I.; Nair, N.; Peters, B.; Proynov, E. I.; Pieniazek, P. A.; Min Rhee, Y.; Ritchie, J.; Rosta, E.; David Sherrill, C.; Simmonett, A. C.; Subotnik, J. E.; Lee Woodcock, H., III; Zhang, W.; Bell, A. T.; Chakraborty, A. K.; Chipman, D. M.; Keil, F. J.; Warshel, A.; Hehre, W. J.; Schaefer, H. F., III; Kong, J.; Krylov, A. I.; Gill, P. M. W.; Head-Gordon, M. Advances in Methods and Algorithms in a Modern Quantum Chemistry Program Package. *Phys. Chem. Chem. Phys.* **2006**, 8, 3172–3191.

Appendix 2. Supporting Information for Chapter 3.

Construction of the $\Delta crtB$ deletion strain

To create a baseline strain for the expression of YFP a *crtB* knockout strain was created in order to remove all carotenoids whose absorbance wavelengths overlap with that of YFP.

To delete the *crtB* ORF a construct containing the upstream and downstream flanking regions of the gene was created. Using the primers “crtBKOUF: CCGGAATTCCACATCACCATCACCACGGCG” and “crtBKOUR: GCGCTCTAGAGATCTAGGTTCTCATGAAGGTATACCG” a fragment of 361 bp (*EcoRI* and *XbaI* ended) upstream of the *crtB* ORF was amplified, which also included 7 bp of the *crtB* gene. A second fragment of 363 bp (*XbaI* and *SphI* ended) was amplified using the primers “crtBKODF: GCGCTCTAGAGGCAATCATTCCGCGGCAAGC” and “crtBKODR: CCCC GCATGCGGCTGTGGCCGAGCCCTA”. This produced the downstream flanking fragment which included 9 bp of the *crtB* gene. Following digestion, the fragments were ligated into the suicide vector pK18mobsacB.

The resulting plasmid was transformed into *E. coli* S17 cells and transferred *Rba. sphaeroides* WT via conjugation. The mutant was produced using the method detailed in Materials and methods. The recombination events involved are illustrated in Fig. S1.

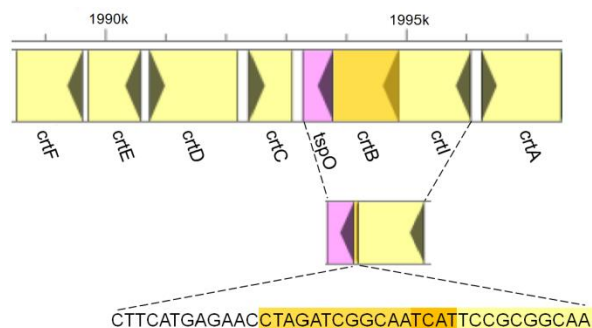


Figure S1. Deletion of *crtB* using pK18mobsacB

Schematic demonstrating the new DNA sequence of the *crtB* deletion strain.

Construction of the RC/YFP fusion strain

The gene encoding the yellow fluorescent protein (YFP) variant, SYFP2 (Kremers *et al.*, 2006), was fused to the 3' end of *puhA*, which encodes the reaction centre H subunit (H). To create the C-terminal YFP fusion, an upstream fragment was created using the primers “puhAYFPUF CCGGAATTCTCGGCCGGCAAGAACCCGATCGG” (*EcoRI*) and “puhAYFPUR GCTCCTCGCCCTTGCTCACCATGGCGTATTCGGCCAGCATCGCCG ” (an overlap extension primer). This fragment contained the last 354 bp of the *puhA* ORF excluding the stop codon. A third fragment containing the *syfp2* ORF was amplified using the primers “puhAYFPFor CGGCGATGCTGGCCGAATACGCCATGGTGAGCAAGGGCGAGGAGCTGTTCAC ” (an overlap extension primer) and “puhAYFPRev GCGCTCTAGATCATTACTTGTACAGCTCGTCCATGCCGAGAGTGAT” (*XbaI*). The upstream and YFP fragments were ligated together using overlap extension PCR. A downstream fragment was created using the primers “puhAYFPDF GCGCTCTAGATCCCCGCATGGCGCGGCC” and “puhAYFPDR CCCCAAGCTTTAGGGCACCGCATAGGCCACCGC” (*XbaI* and *HindIII* ended). This fragment contained 354 bp of the DNA immediately downstream of the *puhA* stop codon. Following digestion, the downstream fragment was ligated into the suicide vector pK18mobsacB first as after ligation the upstream *XbaI* site is dam methylated and can no longer be cut by *XbaI*. Both fragments (1428 bp in total) were ligated into pK18mobsacB.

RC/YFP in wild type *Rhodobacter sphaeroides*

The RC/YFP fusion was created in wild type *Rba. sphaeroides*. Absorbance spectra of WT RCH-YFP membranes were recorded at room temperature show no isolated YFP peak due to overlap with the 514 nm spheroidenone carotenoid peak (Fig. S2). High light photosynthetic growth curves of WT RCH-YFP showed no increase in growth rate when compared to WT (Fig. S3).

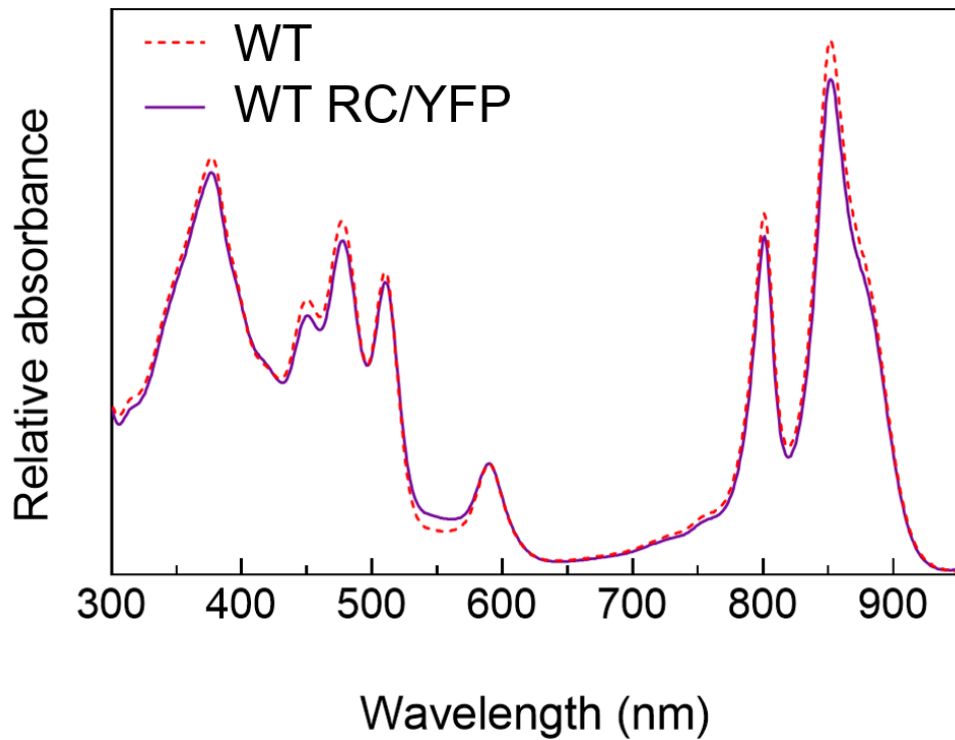


Figure S2. Room temperature absorption spectra of membranes from WT (red) and WT RC/YFP (purple) normalised to 590 nm. The peak for YFP is not visible in absorption spectrum of ICM from WT due to its overlap with the (0-0) vibronic band of the $S_0 \rightarrow S_2$ absorption of carotenoid spheroidene at 514 nm.

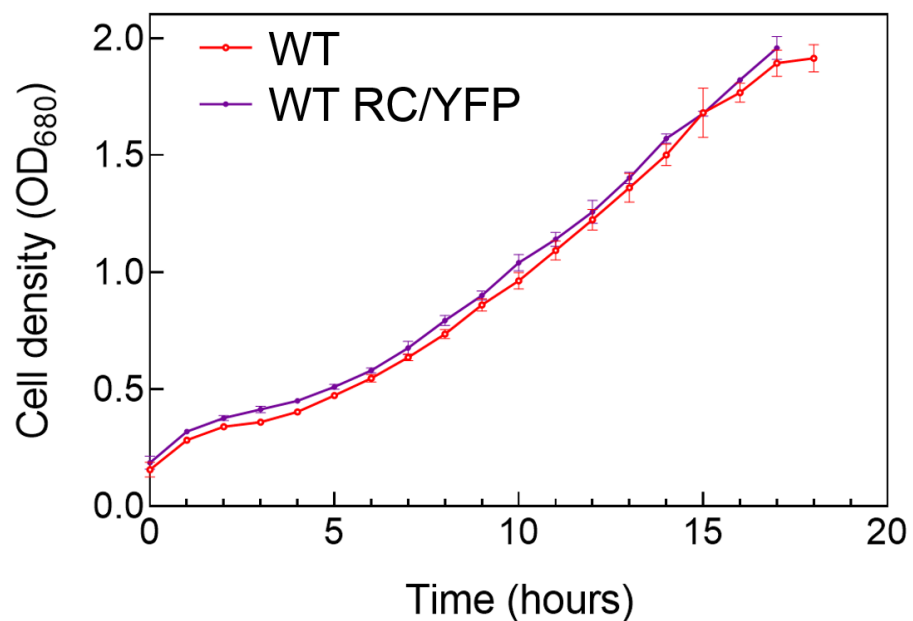


Figure S3. Photosynthetic growth curves of WT (red) and WT RC/YFP (purple). Each data point is an average from three replicate tubes. Light was provided using Osram Halogen Eco Po bulbs at an intensity of 100 $\mu\text{mol photons s}^{-1} \text{m}^{-2}$.

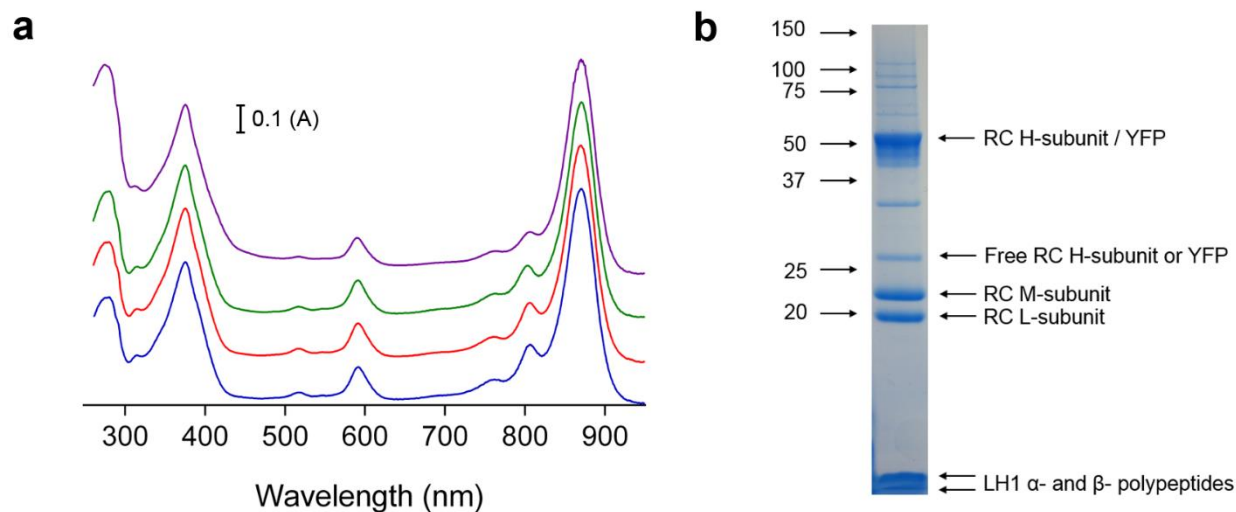


Figure S4. Purification of RC/YFP-LH1 complexes from *Rba. sphaeroides* $\Delta crtB$ RC/YFP-LH1

(a) Absorption spectra of stages in purification; A875:A280 nm ratios are indicated in brackets alongside each sample as indicators of sample purity.

Purple	ICM	(1)
Green	Core complexes harvested from multistep sucrose gradients	(1.63)
Red	Sample after DEAE Sepharose purification	(1.73)
Blue	Sample after gel filtration	(1.92)

(b) SDS-PAGE analysis of purified sample after gel filtration. Molecular masses of standards are shown on the left in kDa.

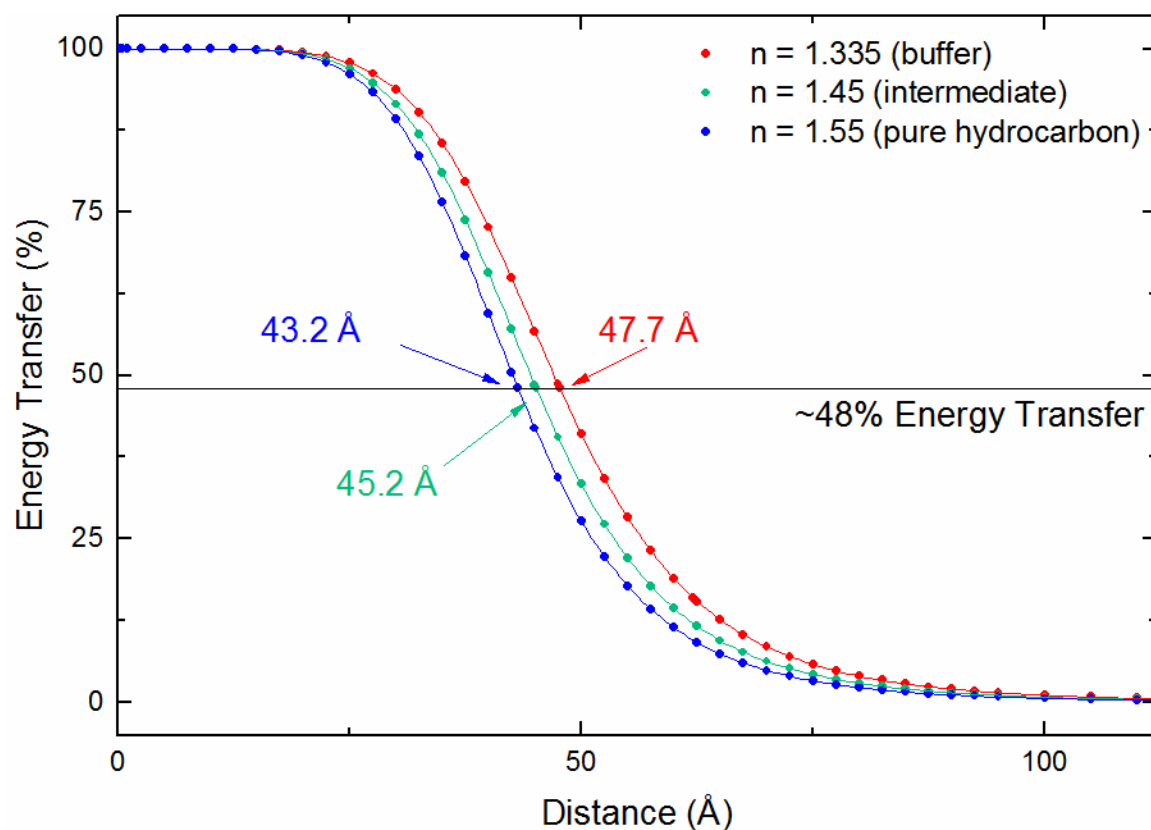


Figure S5. Estimations of the effective distance between the YFP chromophore and the RC/LH1 cofactors using Förster theory. The calculations employed PhotochemCad (Du et al., 1998) using photophysical parameters for the energy donor (YFP) and acceptor (RC). Three values of the refractive index (1.335, 1.45, and 1.55) were used to take into account the polarity of the cofactor/protein environments. The calculations, based on an average energy transfer of 48%, return a YFP to LH1 distance of 43 to 48 Å.

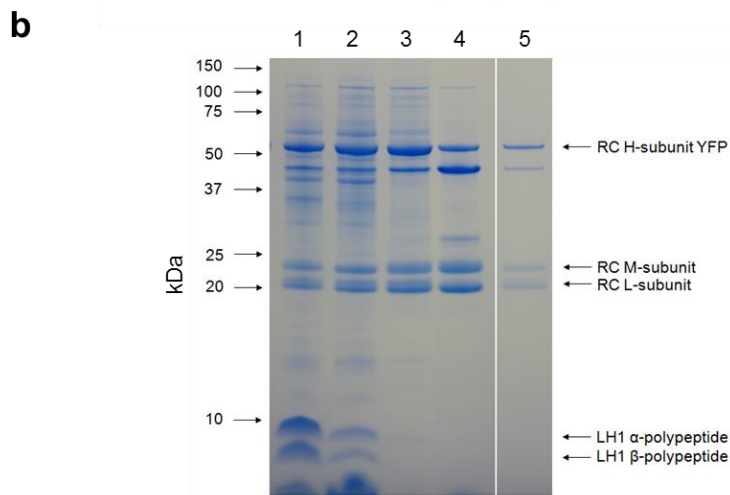
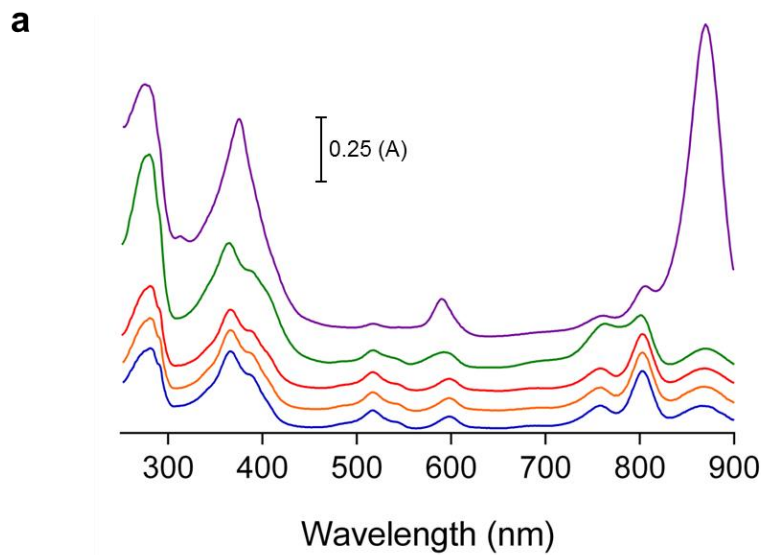


Figure S6. Purification of RC/YFP complexes from *Rba. sphaeroides* $\Delta crtB$ RC/YFP-LH1

(a) Absorption spectra of stages in purification

Purple ICM

Green LDAO solubilised membranes

Red Sample after DEAE Sepharose purification

Orange Sample after Q Sepharose purification

Blue Purified RC/YFP after gel filtration.

(b) SDS-PAGE analysis of stages in purification

Lane 1 Sample after DEAE Sepharose purification

Lane 2 Sample after Q Sepharose purification

Lane 3 Sample after Gel Filtration purification

Lane 4 Final sample

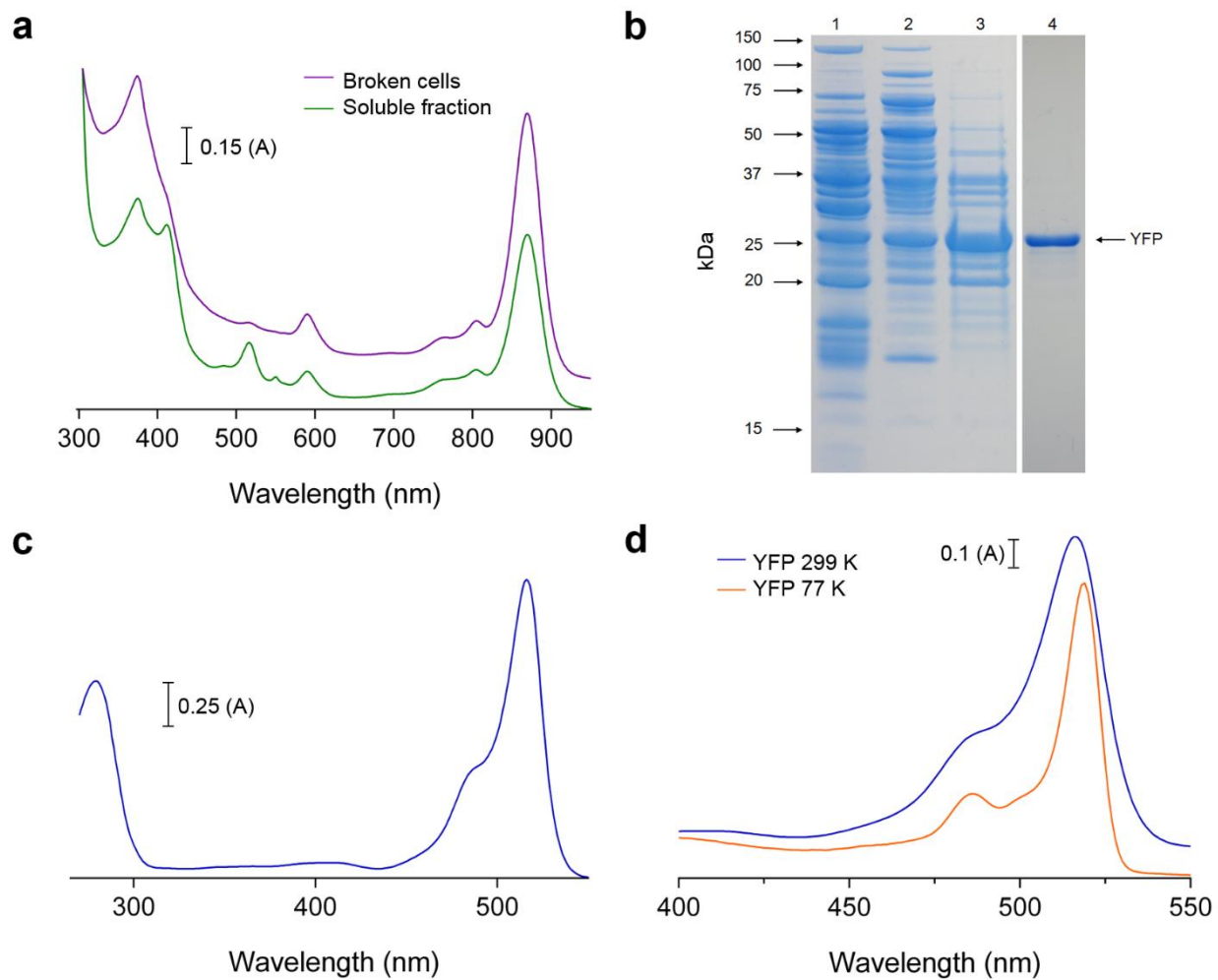


Figure S7. Purification of YFP from *Rba. sphaeroides* $\Delta crtB$ pBBRBB-YFP

(a) Absorption spectra of stages in purification

Purple Broken cells

Green Soluble fraction

(b) SDS-PAGE analysis of stages in purification

Lane 1 Sample after DEAE Sepharose purification

Lane 2 Sample after Q Sepharose purification

Lane 3 Sample after Gel Filtration purification

Lane 4 Final sample

(c) Room temperature absorption spectrum of purified YFP

(d) Room temperature (approximately 299 K) and 77 K absorption spectra of purified YFP

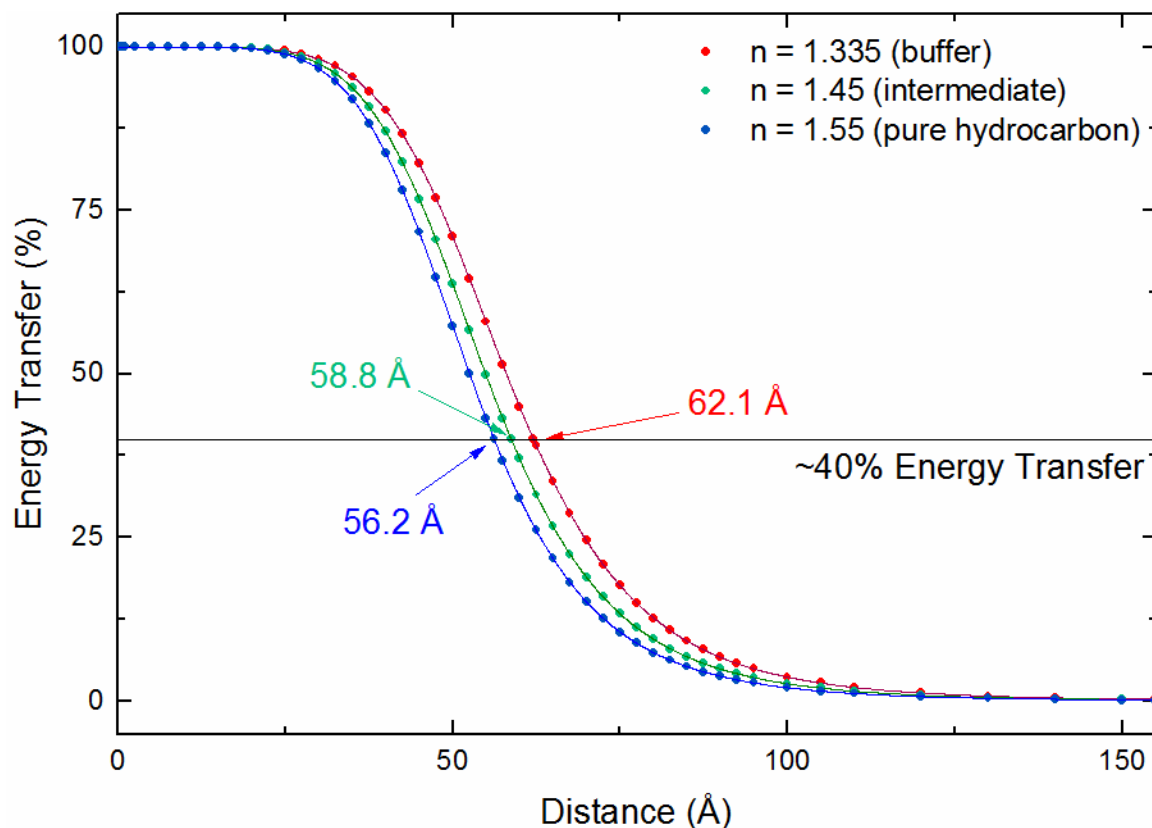


Figure S8. Estimations of the effective distance between the YFP chromophore and the RC cofactors using Förster theory. The calculations employed PhotochemCad (Du et al., 1998) using photophysical parameters for the energy donor (YFP) and acceptor (RC). Three values of the refractive index (1.335, 1.45, and 1.55) were used to take into account the polarity of the cofactor/protein environments. The calculations return a spectral-overlap integral of $J = 2.96 \times 10^{-13} \text{ cm}^6$, a Förster radius of $R_0 = 53\text{--}58 \text{ Å}$, and a YFP to RC distance of 56 to 62 Å.

References

Du, H., R.-C. A. Fuh, J. Li, L. A. Corkan and J. S. Lindsey (1998) PhotochemCAD. A computer-aided design and research tool in photochemistry and photobiology. *Photochem. Photobiol.* 68, 141–142

Kremers, G. J., Goedhart, J., van Munster, E. B. and Gadella, T. W. J. (2006). Cyan and yellow super fluorescent proteins with improved brightness, protein folding, and FRET Förster radius. *Biochemistry*, 45, 6570-6580.

Appendix 3. Supporting Information for Chapter 5.

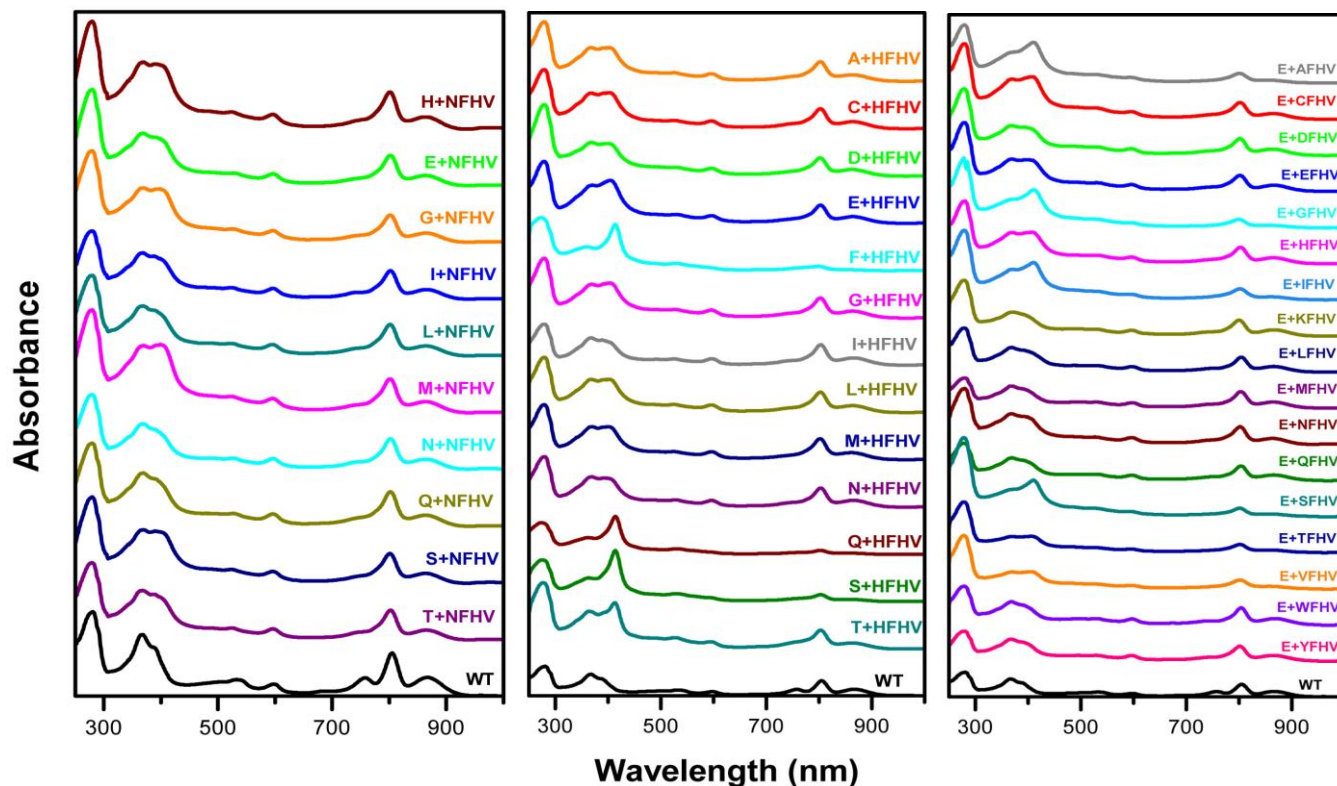


Figure S1A. Ground state absorption spectra of the V(M131)X+NFHV, V(M131)X+HFHV, and E+F(L181)X+FHV mutant sets. Mutant nomenclature is as given in Table 1. Protein concentration was adjusted such that the long-wavelength absorption of P at its maximum was similar in most samples. Exceptions include those RCs whose spectra were dominated by an impurity with 410-nm absorption; these spectra are shown at 2/5th strength to allow for stacking of the plots.

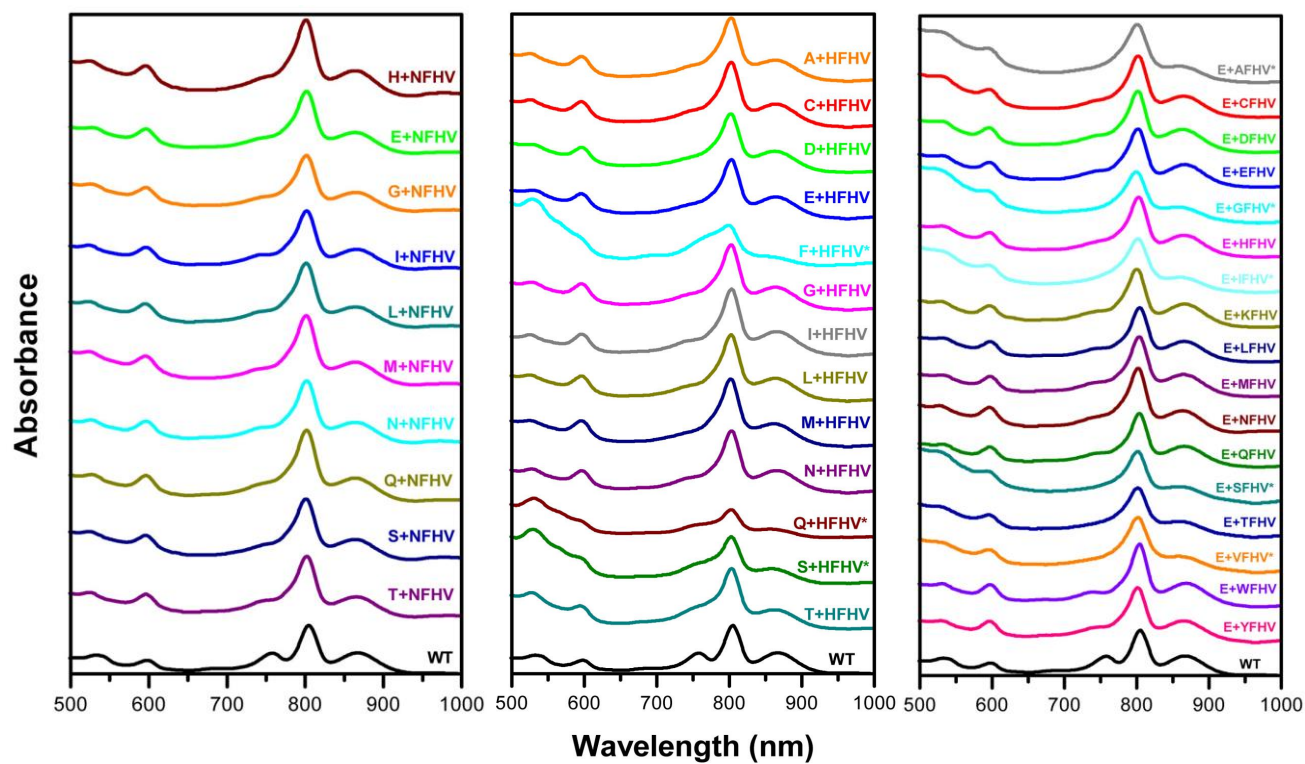


Figure S1B. Ground state absorption spectra of the V(M131)X+NFHV, V(M131)X+HFHV, and E+F(L181)X+FHV sets of mutant RCs. Mutant nomenclature is as given in Table 1. Spectra are normalized such that the maximum long-wavelength absorptions of P are identical, except for cases (denoted with *) of poor expression where normalization factors were reduced to prevent overlap of spectral lines at higher energy. Expanded versions of the three panels are on the three following pages.

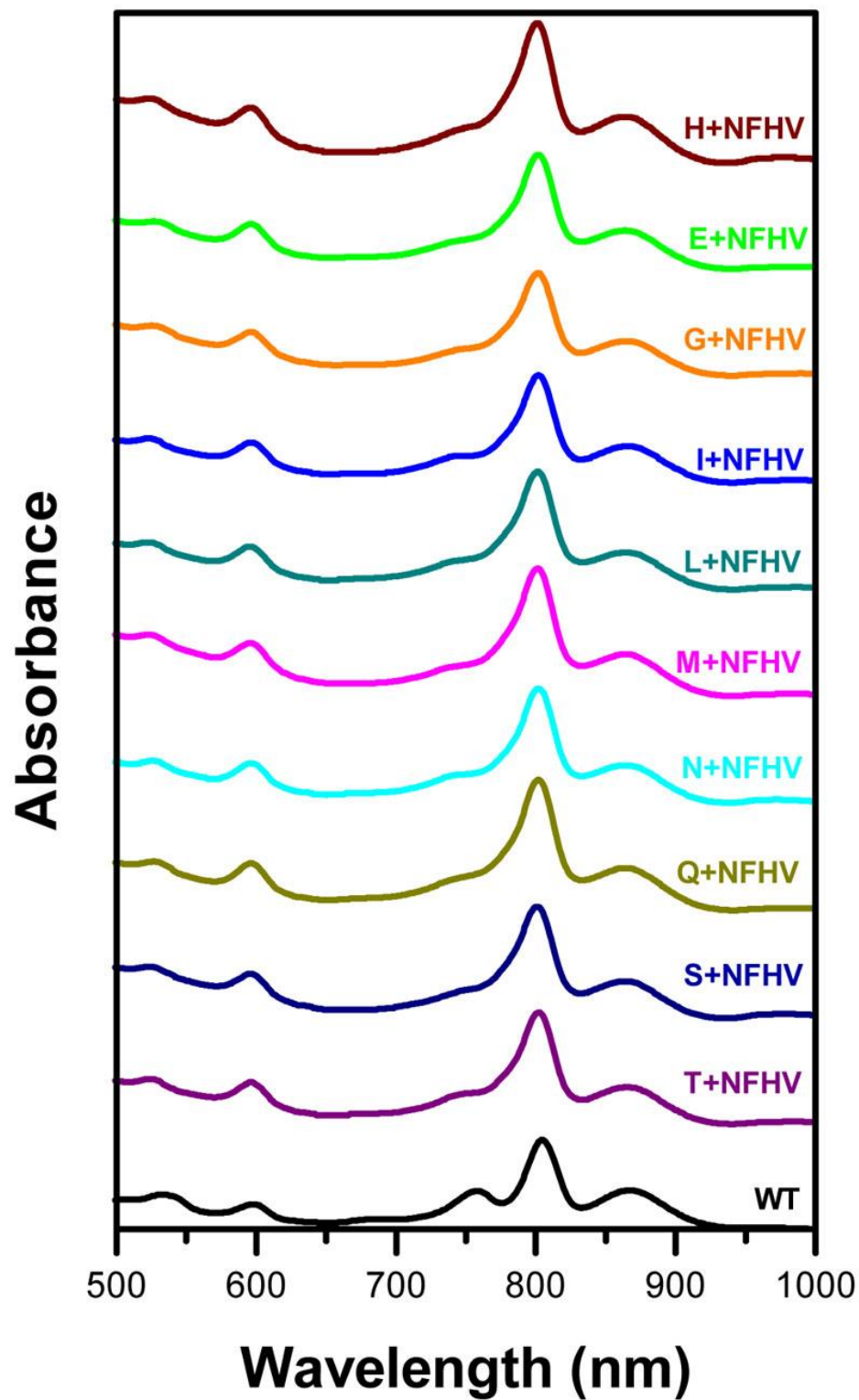


Figure S1C. Expanded view of the ground state absorption spectra of the V(M131)X+NFHV mutant set.

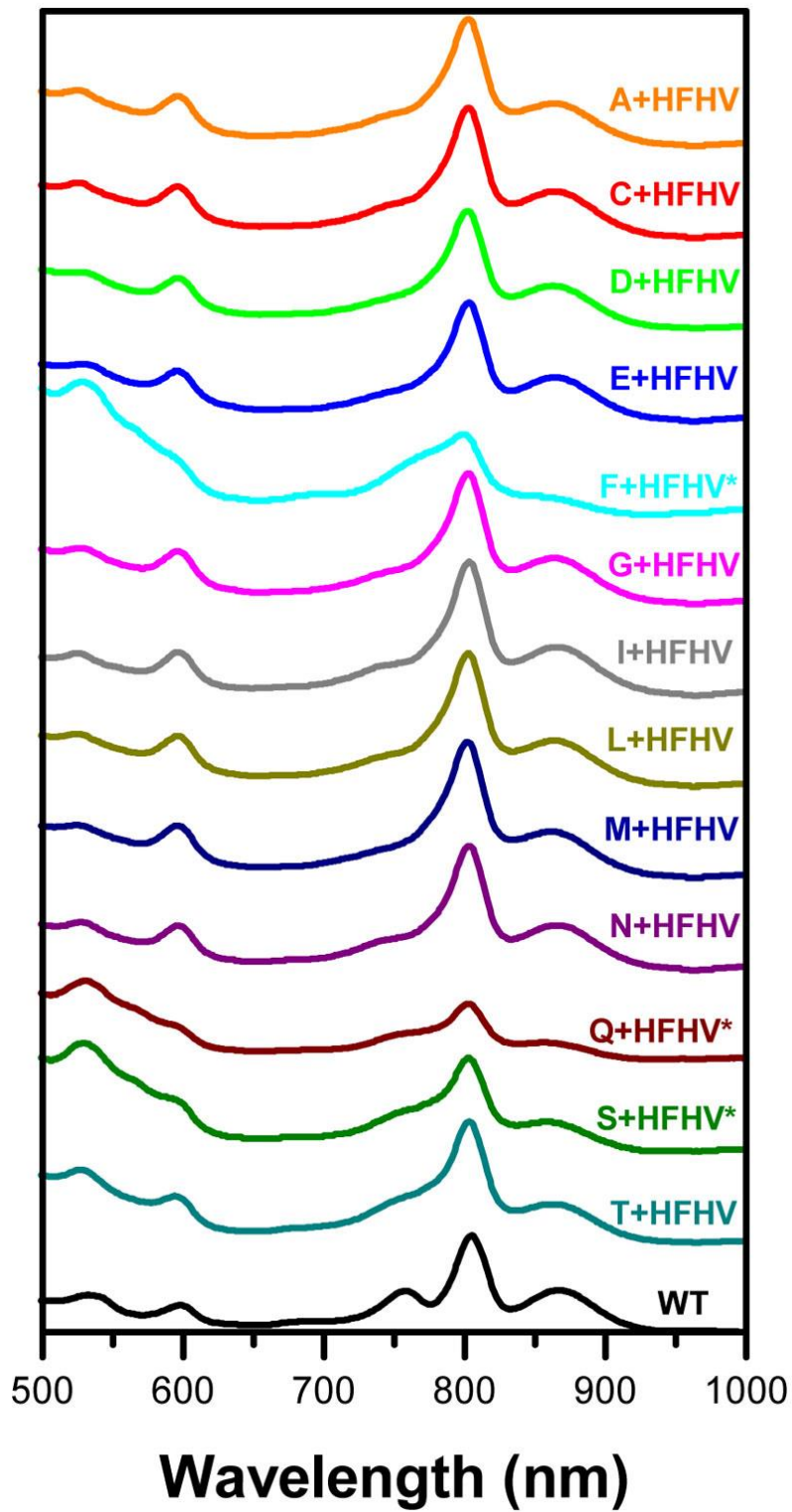


Figure S1D. Expanded view of the ground state absorption spectra of the V(M131)X+HFHV mutant set.

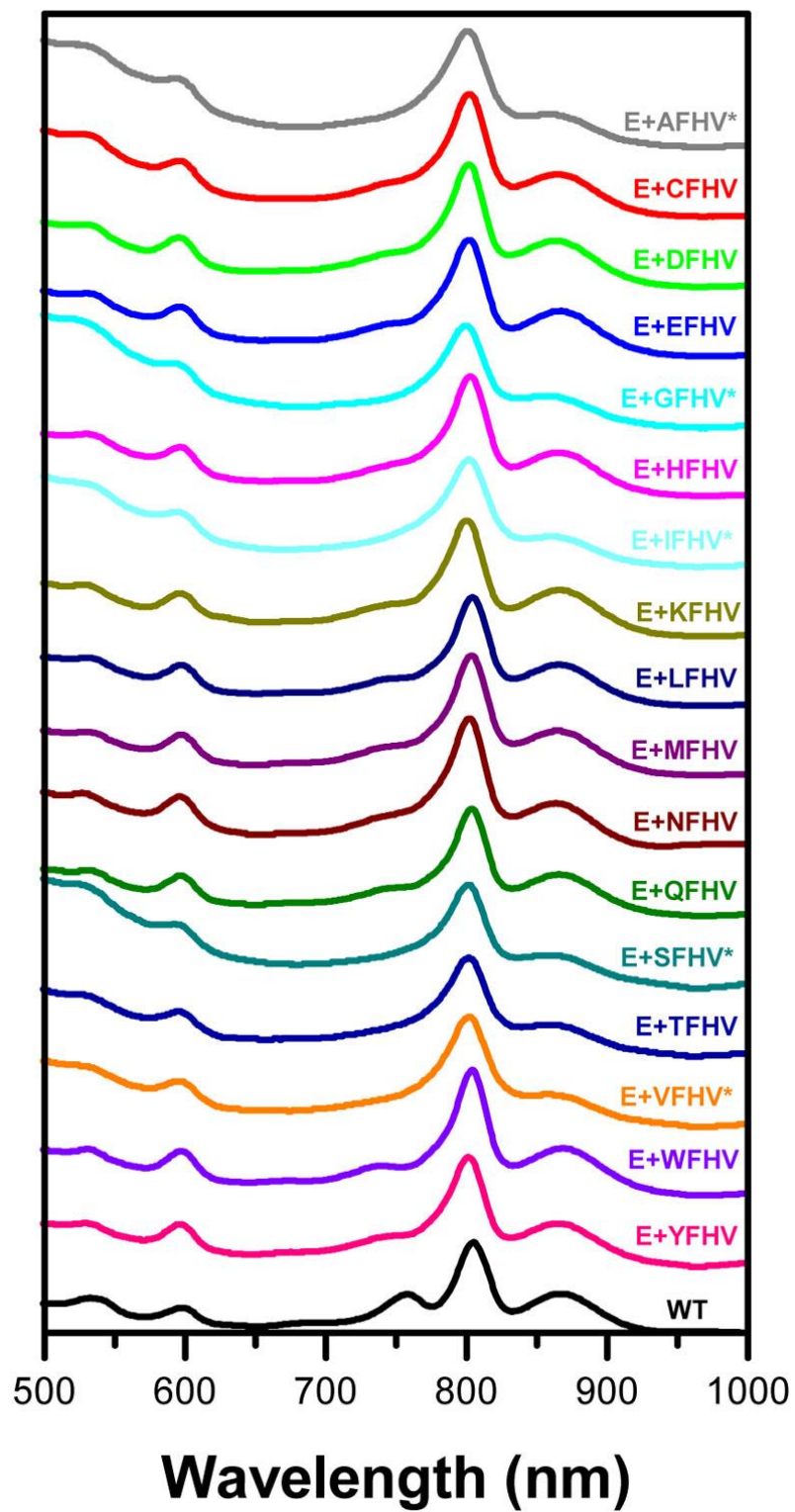


Figure S1E. Expanded view of the ground state absorption spectra of the M131E+F(L181)X+FHV mutant set.

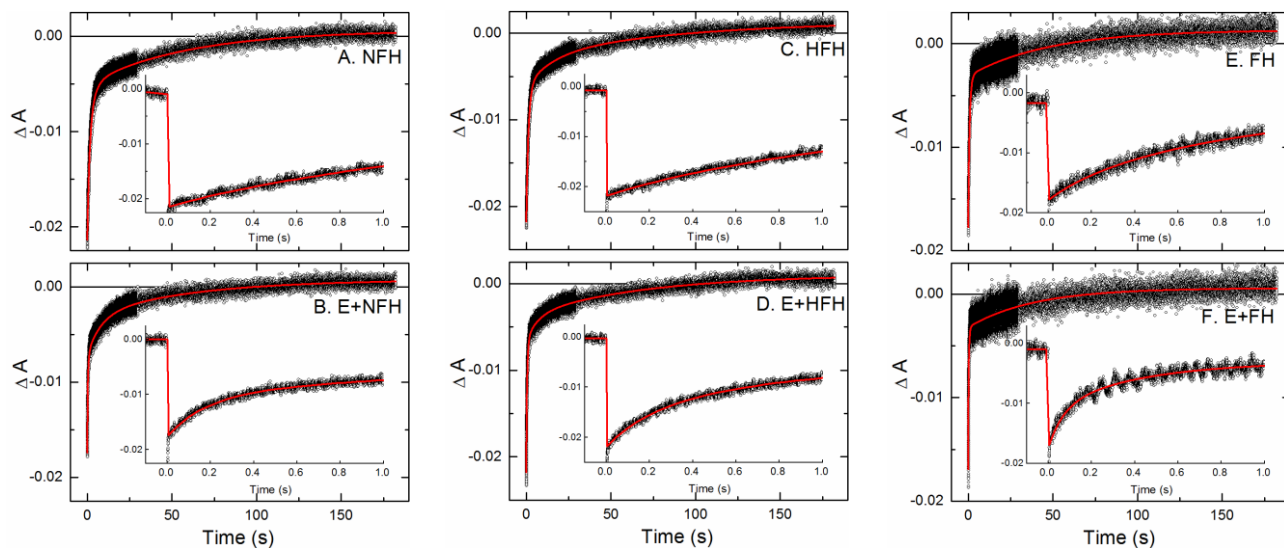


Figure S2. Kinetics of $P^+Q_A^-$ charge recombination in mutant RCs. A fast, ~ 100 -ms component attributed to $P^+Q_A^- \rightarrow$ ground state in RCs that lack Q_B , is observed for the mutants that have Glu at M131 (insets of each of the three bottom panels). The amplitude of this component relative to the total amplitude of the signal is the measure of the Q_B absent from the RC. Such component is not observed in the corresponding top panel insets for the mutants without M131Glu and which have full Q_B occupancy. Note that this assay for Q_B content is performed on a set of mutants in which Q_A is present (i.e., mutants that do not bear the M250V mutation).

Table S1. Amplitudes and Lifetimes of P-Bleaching Decay at 850 nm in Mutants Containing Q_A.

Sample	amp ₁ ^a	τ ₁ (s) ^a	amp ₂ ^b	τ ₂ (s) ^b	amp ₃ ^b	τ ₃ (s) ^b	amp ₄ ^b	τ ₄ (s) ^b
WT	0.02	0.15	0.66	2.1	0.13	14	0.19	68
YFH	0.03	0.15	0.72	1.3	0.07	6	0.18	59
E+YFH	0.22	0.15	0.54	0.8	0.24	18	n.a.	n.a.
NFH	0.01	0.15	0.54	1.4	0.19	3.7	0.26	59
E+NFH	0.31	0.15	0.27	0.6	0.21	8	0.21	60
HFH	0.01	0.15	0.66	1.3	0.15	15	0.18	90
E+HFH	0.20	0.15	0.48	0.6	0.12	7	0.20	68
FH	0.09	0.15	0.68	0.8	0.23	48	n.a.	n.a.
E+FH	0.36	0.15	0.43	0.4	0.21	39	n.a.	n.a.

^aFixed 150 ms component (τ₁) for P⁺Q_A⁻ decay. The fit amplitude of this component (amp₁) is the measure of RCs in which Q_B is *not* present and determines the Q_B occupancies reported in Table 2 in the text.

^bFit components for P⁺Q_B⁻ decay.

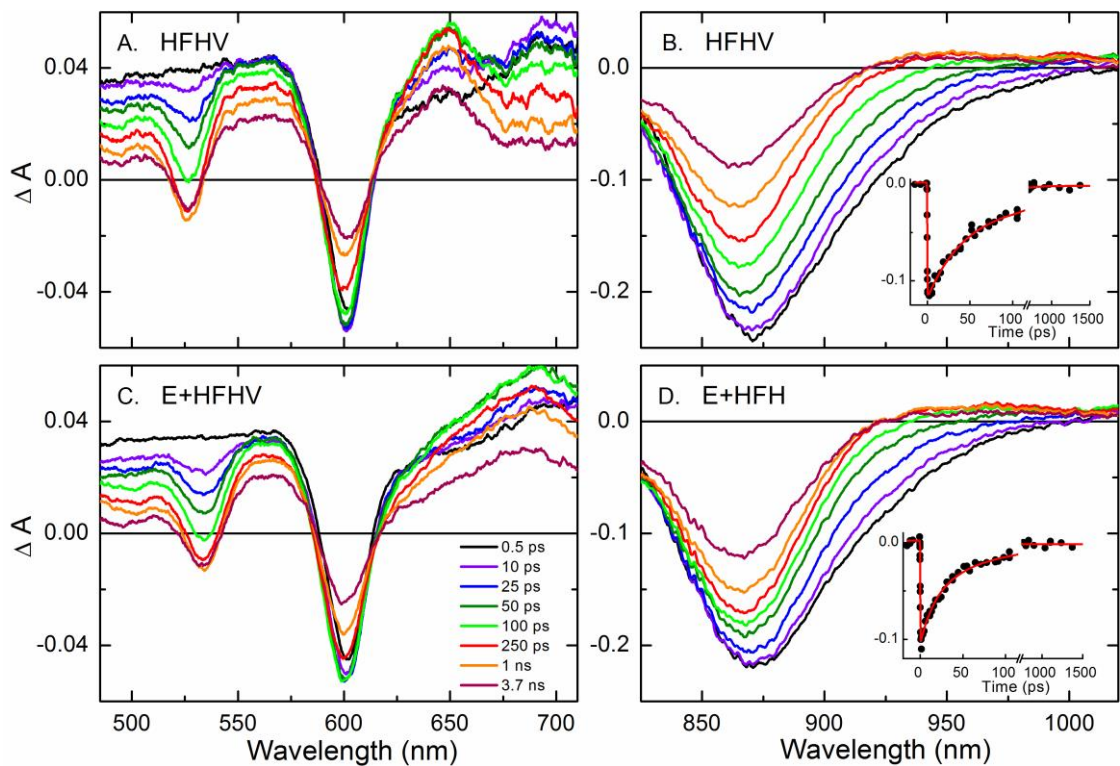


Figure S3. TA spectra and kinetics for HFHV (A and B) and E+HFHV (C and D) RCs, except that for panel D the variant without the V mutation was used due to sample limitation. The spectra were obtained at the times indicated (panel C) following an ~ 130 -fs excitation flash at either 860 nm (A and C) or 590 nm (B and D). The insets of (B) and (D) show the data (filled circles) averaged in a 10-nm interval centered on the stimulated emission isosbestic point at ~ 920 nm. The solid red lines are the fits of the data to the convolution of the instrument response function with two exponentials plus a constant.

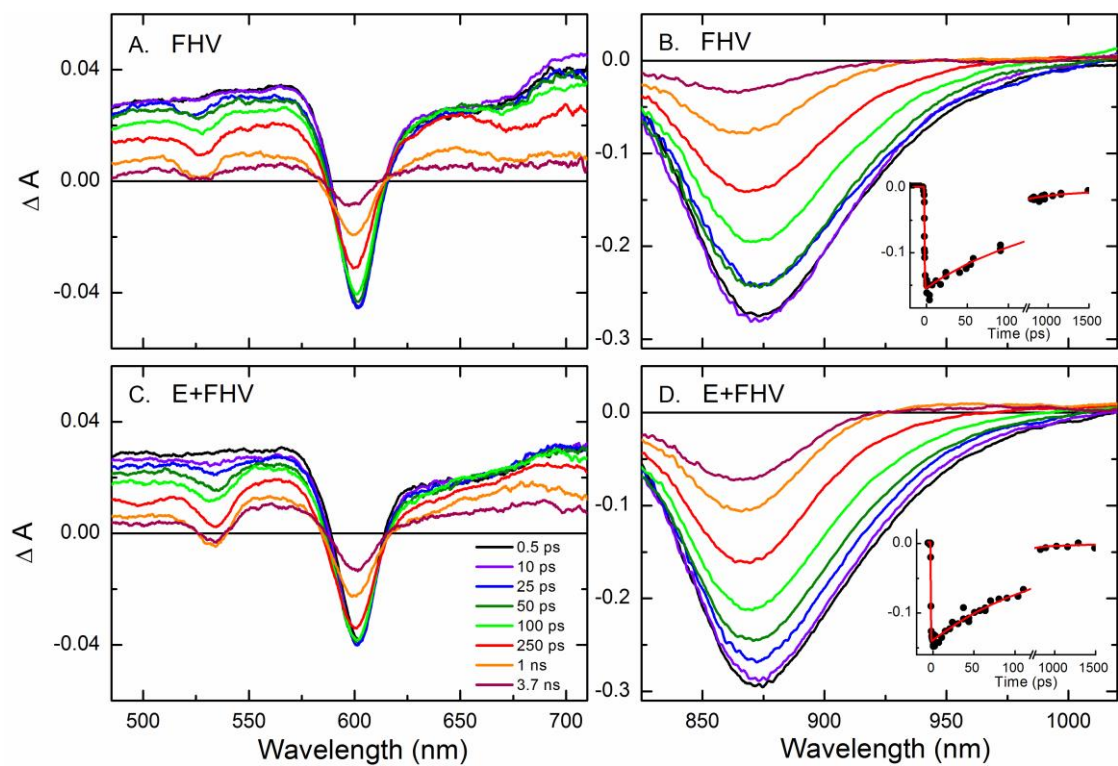


Figure S4. TA spectra and kinetics for the FHV (A and B) and the E+FHV (C and D) mutant RCs. The spectra were obtained at the times indicated (panel C) following an ~130-fs excitation flash at either 860 nm (panels A and C) or 590 nm (panels B and D). The insets of (B) and (D) show the data (filled circles) averaged in a 10-nm interval centered on the stimulated emission isosbestic point at ~920 nm. The solid lines are the fits of the data to the convolution of the instrument response with two exponentials plus a constant.

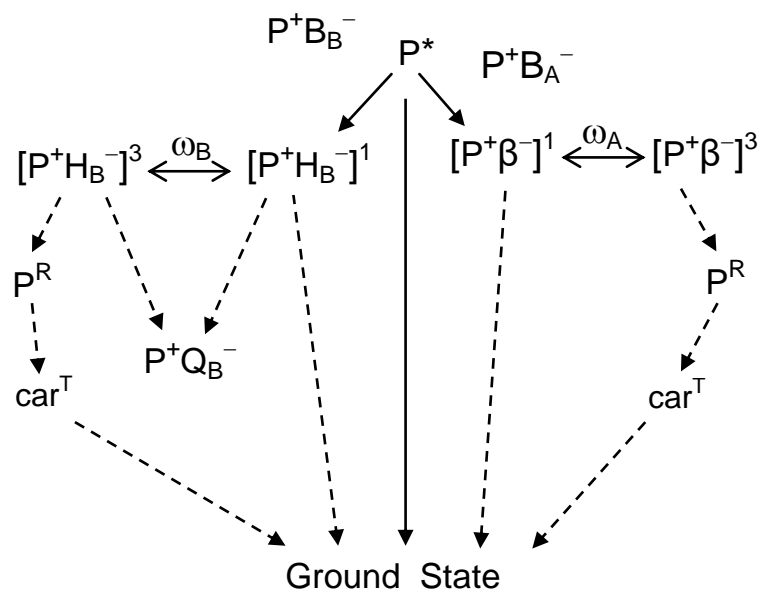


Figure S5. Photochemical scheme for bacterial RCs identifying potential reaction pathways, decay processes and charge-separated states in the bacterial reaction center.

Table S2. Triplet Lifetimes of P and Carotenoid.^a

Mutant	P ^R (ns)	Car ^T (μs)
YFHV	91	4.0
E+YFHV	70	1.6
NFHV	95	3.8
E+NFHV	126	4.1
HFHV	85	2.0
E+HFHV	128	4.0
FHV	69	3.0
E+FHV	76	3.2

^a P^R and car^T lifetimes measured in the presence of terbutryn. The lifetimes have an error of ±20% of the values given.

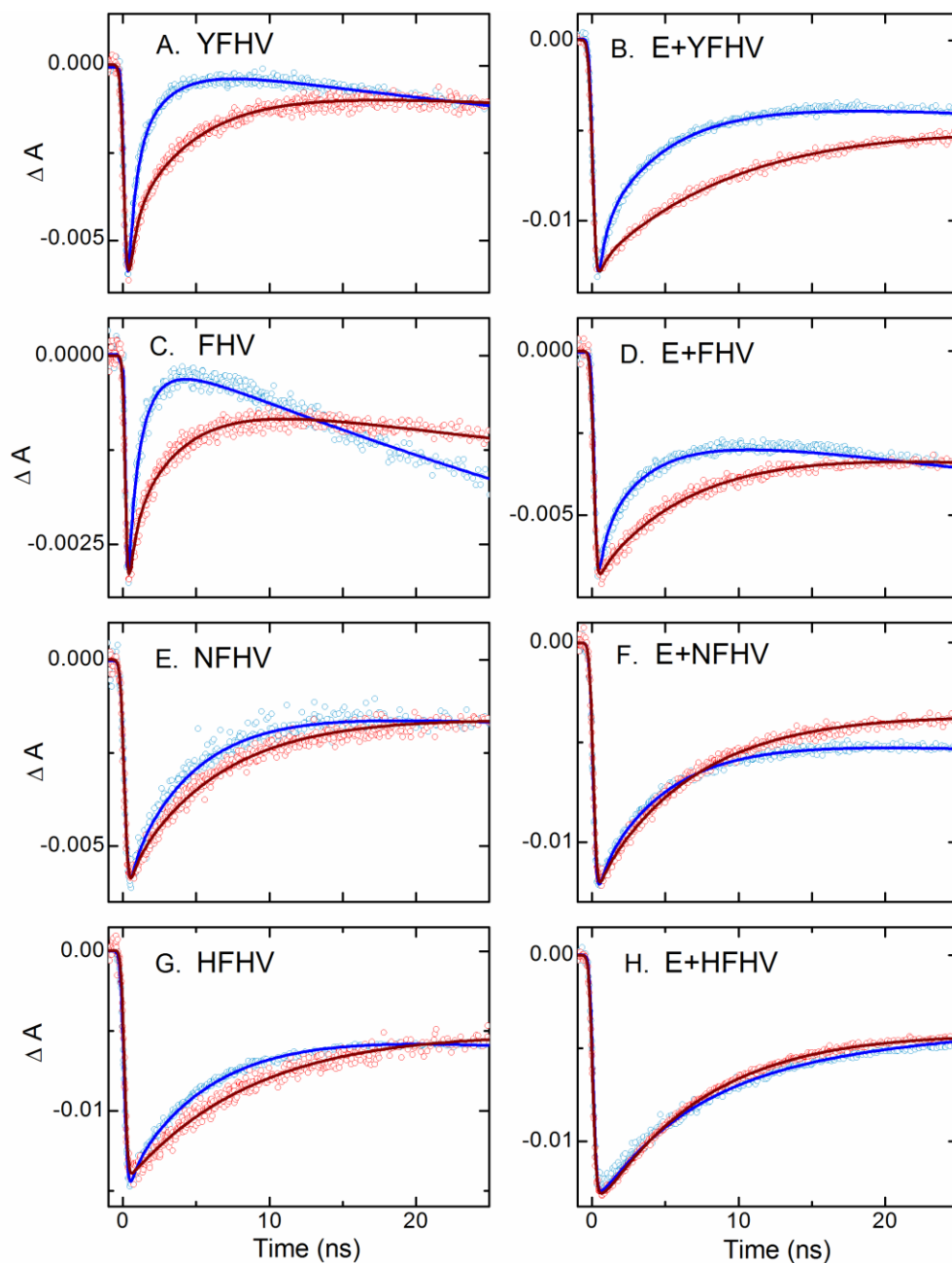


Figure S6. First 25 ns of the time course of the absorption changes averaged over a 10-nm interval centered at the maximum bleaching of the Q_X band of H_B in each respective mutant. The data sets and fits extend to 50 μ s. The red open circles are data for the RC samples with tb added and the dark red lines are fits of the data to the convolution of the instrument response with four exponentials plus a constant. The blue open circles are data for the RCs samples with no added tb and the dark blue lines are fits of the data to the convolution of the instrument response with five exponentials plus a constant.

Appendix 4. Supporting Information for Chapter 6.

EXPERIMENTAL PROCEDURES

Construction of *R. sphaeroides* expression host \square *rshI*. The Type II restriction enzyme RshI (locus tag RSP_3759; recognition sequence CGATCG) was deleted from strain $\Delta\Delta 11$ [58] to yield an expression host strain that is transformable by either chemical or electrical procedures. To construct the deletion strain, PCR products of sequences that flank *rshI* on both sides in the genome (*R. sphaeroides* strain 2.4.1, ATCC 17023) and a gene encoding gentamicin resistance (Gm^R , from pBBR1MCS-5; [67]) were joined in a multi-step procedure. First, the ~600 bp sequences comprising the 5' and 3' neighboring regions of *rshI* were amplified. Also, the Gm^R gene was amplified using primers that encode flanking *loxP* sequences to facilitate its excision by Cre recombinase in a marker recycling strategy [68]. The latter 858 bp fragment was cloned into *Sma*I-digested pBS⁻ (Stratagene). Second, additional primers were used to amplify *loxP*- Gm^R -*loxP* from the pBS⁻ intermediate and introduce sequences that overlapped with the two ~600 bp flanking segments. Third, overlap extension PCR was used to join the three fragments and the product was cloned via introduced *Xho*I and *Spe*I sites into a derivative of pSUP202 (Tc^R ; [69]) containing a modified polylinker, generating plasmid pSUP202rshIKO. All PCR primers used in this study are listed in Table S4.

Derivatives of pSUP202 are mobilizable plasmids that cannot be replicated in *R. sphaeroides*. Following transfer of pSUP202rshIKO to the *R. sphaeroides* recipient strain $\Delta\Delta 11$ via conjugal mating with *E. coli* donor strain S17-1 [69], $Gm^R Tc^S$ exconjugants that had lost the *rshI* gene as a result of a double-crossover event were selected. In brief, matings were performed with small nitrocellulose filter discs placed atop 2xTY agar plates at 37°C for 3 hours using an

equal ratio of donor cells to recipient cells. Selection of the desired deletion mutants proceeded on ^GYCC agar containing the appropriate antibiotics. Replacement of the *rshI* gene with the Gm^R cassette was confirmed by PCR with diagnostic primers that produced amplicons that bridged the regions between the flanking sequences and the antibiotic resistance cassette.

As the final step in the process, the gene encoding the Cre recombinase was amplified from plasmid pIC-Cre (Addgene) and was cloned into pRK442 [70] as an *EcoRI/PstI* fragment downstream of the *lac* promoter. Plasmid pRK442-Cre was transferred from S17-1 to the *rshI* knockout strain via conjugal mating; transconjugants were selected on ^GYCC agar containing Tc. Synthesis of the recombinase was induced by growth of the transconjugant in ^GYCC medium containing 1 mM IPTG, enabling excision of the Gm^R gene by Cre recombinase via the engineered *loxP* sites. The presence of the *rshI* knockout in the absence of the Gm^R cassette in Gm^S colonies was confirmed using PCR with the same diagnostic primers. Plasmid pRK442-Cre was cured from the deletion strain by repeated subculturing in the absence of Tc.

Platform for high-throughput mutagenesis of the R. sphaeroides RC. The plasmid used for expression of many of the *R. sphaeroides* RCs in this study was designed to enable a mutagenesis strategy that is analogous to that used for high-throughput mutagenesis of the *R. capsulatus* RC [10]. Regions of the *R. sphaeroides* *pufL* and *pufM* genes surrounding the cofactors were identified and targeted for mutagenesis (Table S2). The system was designed such that unique restriction sites flank the 5' and 3' ends of each region, thus facilitating the synthesis and cloning of oligonucleotide cassettes that encode mutations at one or more sites within a particular region. The expression plasmid was assembled in a series of steps.

i. Vector construction. The vector backbone – a derivative of broad-host-range cloning vector pBBR1MCS-2 [67] – was modified extensively to eliminate duplications of restriction

sites that were designed for cloning of the mutagenic oligonucleotide cassettes. In addition to seven restriction sites removed previously from pBBR1MCS-2 to generate the portion of pBBRKW2HTsLsM [10] that was employed herein, another site (*AgeI*) was removed by mung bean nuclease treatment (Table S3). Since the *R. sphaeroides* expression host is kanamycin resistant (Km^R ; [58]), a region of pBBR1MCS-5 encoding resistance to Gm [67] was PCR-amplified and used to replace the segment encoding Km^R via ligation-independent cloning into pBBRKW2(*AgeI*) that had been digested with *XcmI* and *RsrII* and blunted with mung bean nuclease; both sites were destroyed in the process. A duplicate *BglIII* site within the Gm^R gene was eliminated via silent site-directed mutagenesis (QuikChange, Stratagene), resulting in plasmid pBBRRW.

ii. *Operon construction.* The wild-type version of the *R. sphaeroides puf* operon (*pufQBALMX*) is encoded within a 4340 bp *EcoRI-PstI* segment of plasmid pRKHTMHBgl [67]. As an initial step in construction of the operon for expression of multiply-mutated RCs, synthesis of the LHI antenna complex was disabled by replacing the *NspI-FseI* region encompassing *pufB* and *pufA* by a synthetic cassette, resulting in the derivative pRKHTMHBgl: $\Delta\beta\alpha$. Since the *puc* operon encoding the LHII antenna complex is interrupted in the *R. sphaeroides* expression host $\Delta rshI$ [58,71], genes expressed in the host from this plasmid result in the antennaeless, “RC-only” photosynthetic membrane needed for quantitative extraction of RCs by mild detergents [72].

The segment of pRKHTMHBgl: $\Delta\beta\alpha$ carrying the *pufQ(BA)LM* genes was excised with *EcoRI* and *BamHI* [58]. The region encoding *pufX* was PCR-amplified with primers that carried flanking *BamHI* and *SacI* restriction sites, eliminating a duplicate *PstI* site in the process. These two segments were joined to *EcoRI/SacI*-digested pBBRRW in a three-way ligation. Two

duplicate restriction sites – *HindIII* in *pufL* and *RsrII* in *pufM* – were removed by silent mutagenesis by designing two overlapping cassettes that spanned this region and destroyed these sites on either end; the resulting plasmid was designated pBBRRWRs: $\Delta\beta\alpha$.

Portions of both the *pufL* and *pufM* genes were then synthesized (Eurofins) to encode silent changes that introduced unique restriction sites flanking each of the segments chosen for mutagenesis (Figure 2; Table S2) in addition to the F(L181)Y-T(M133)E-Y(M210)F-L(M214)H-W(M252)V mutations. The synthetic portion of *pufL* was then cloned into pBBRRWRs: $\Delta\beta\alpha$ as a *ClaI-SalI* fragment, and the synthetic *pufM* segment was cloned using *BglII* and *BamHI*, thus creating pBBRRWsLsMYEFHV: $\Delta\beta\alpha$. A C-terminal heptahistidine tag is encoded in *pufM*. A summary of substitutions carried by mutant RCs and the nomenclature used to refer to them is contained in Table 1.

One set of mutants described in this study utilized a background in which the WT threonine residue at M133 was present. This plasmid was constructed from pBBRRWsLsMYEFHV: $\Delta\beta\alpha$ by replacement of the segment carrying region F (flanked by *NheI* and *AvrII* sites; Table S2) with a synthetic oligonucleotide cassette encoding WT residues, resulting in plasmid pBBRRWsLsMYFHV: $\Delta\beta\alpha$.

Table S1: Plasmids and strains used in this study

Plasmid or Strain	Description	Source
Plasmids		
pBBRKW2HTsLsM	Broad-host-range expression plasmid for <i>R. capsulatus</i> mutant RC genes; Km ^R	[10]
pBBR1MCS-2	Broad-host-range plasmid; Km ^R	[67]
pBBR1MCS-5	Broad-host-range plasmid; Gm ^R	[67]
pRKHTMHBgl	Broad-host-range plasmid carrying WT <i>pufL</i> and polyhistidine-tagged <i>pufM</i> genes of <i>R. sphaeroides</i> , pRK404 derivative; Tc ^R	[58]
pBBRRWsLsM	Broad-host-range plasmid for expression of <i>R. sphaeroides</i> mutant RC genes; Gm ^R	this study
Strains		
<i>E. coli</i>		
DH5 α	F' Φ 80 <i>lacZ</i> Δ M15 Δ (<i>lacZYA-argF</i>) U169 <i>recA1 endA1 hsdR17</i> (rK ⁻ , mK ⁺) <i>phoA supE44 λ-thi-1 gyrA96 relA1</i>	Invitrogen
<i>E. coli</i> 10G	F' <i>mcrA</i> Δ (<i>mrr-hsdRMS-mcrBC</i>) <i>endA1 recA1</i> Φ 80 <i>lacZ</i> Δ M15 Δ <i>lacX74 araD139 Δ(ara, leu)7697 galU galK rpsL</i> (Str ^R) <i>nupG λ-tonA</i>	Lucigen
S17-1	<i>recA pro hsdR</i> RP4-2-Tc::Mu-Km::Tn7	[69]
<i>R. capsulatus</i>		
U43	<i>puc puf::ΩSt^R/Sp^R</i> ; recipient for above broad-host-range expression plasmids	[5]
<i>R. sphaeroides</i>		
$\Delta\Delta$ 11	<i>pucBA</i> (Km ^R) <i>pufQBALMX</i> (Sp ^R), derivative of wild-type 2.4.1	[58]
Δ rshI	<i>rshI pucBA</i> (Km ^R) <i>pufQBALMX</i> (Sp ^R), derivative of $\Delta\Delta$ 11	this study

Table S2. Regions targeted for mutagenesis in *R. sphaeroides*.

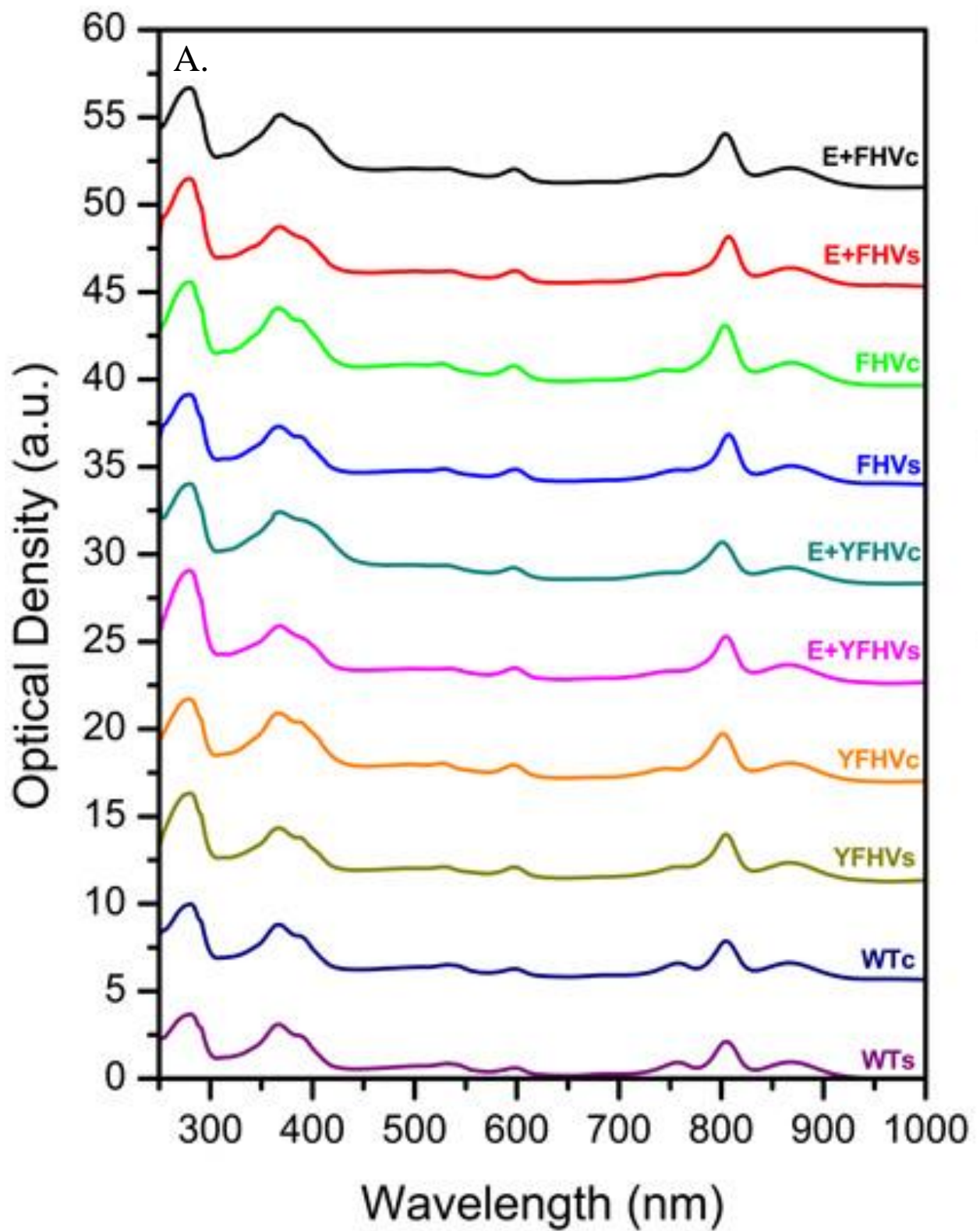
Region	Cofactor Proximity	Amino Acid Segment (Region)	5'-Flanking Enzyme	3'-Flanking Enzyme
A	B _B	M152-153	<i>AvrII</i>	<i>StuI</i>
B	B _B	M166-189	<i>StuI</i>	<i>SpeI</i>
C	B _B	L166-177	<i>NdeI</i>	<i>HindIII</i>
D	B _B /H _B	L180-190	<i>HindIII</i>	<i>BbvCI</i>
E	H _B	L215-220	<i>BsiWI</i>	<i>AflII</i>
F	H _B	M121-138	<i>NheI</i>	<i>AvrII</i>
G	H _B	M143-153	<i>AvrII</i>	<i>StuI</i>
H	H _B	M269-277	<i>AgeI</i>	<i>HpaI</i>
I	Q _B	L186-194	<i>HindIII</i>	<i>BbvCI</i>
J	Q _B	L210-216	<i>BsiWI</i>	<i>AflII</i>
K	Q _B	L220-234	<i>BsiWI</i>	<i>AflII</i>
L	B _A	L127-142	<i>NruI</i>	<i>MluI</i>
M	B _A	L146-162	<i>MluI</i>	<i>NdeI</i>
N	B _A	M194-210	<i>SpeI</i>	<i>ApaLI</i>
O	Q _A	M243-264	<i>RsrII</i>	<i>AgeI</i>
P	H _A	M214-238	<i>ApaLI</i>	<i>RsrII</i>

Table S3. Restriction sites removed from expression plasmid to enable cassette-based mutagenesis strategy in *R. sphaeroides*.

Site	Context	Method	Position (bp)
<i>Age</i> I	vector	mung bean nuclease	464
<i>Bal</i> I	mob	mutagenesis (C→G)	1419
<i>Bgl</i> III	Gm ^R	mutagenesis (G→A)	4188
<i>Nco</i> I	vector	mung bean nuclease	4729
<i>Eco</i> RV	vector	mung bean nuclease	5122
<i>Hind</i> III	vector	mung bean nuclease	5122
<i>Cla</i> I	vector	mung bean nuclease	5122
<i>Xho</i> I	vector	mung bean nuclease	5122
<i>Kpn</i> I	vector	mung bean nuclease	5122
<i>Hind</i> III	<i>pufL</i>	cassette mutagenesis (T→G)	7231
<i>Rsr</i> II	<i>pufM</i>	cassette mutagenesis (C→G)	7304
<i>Pst</i> I	intergenic	primer design	9099

Table S4. PCR primers used in this study.

Primer	Sequence (5'-3')	Purpose
<i>Primers used for construction and verification of ArshI</i>		
RshIFgmtIFwd	CTGTCTCGAGTGACTCCCTTCGCCGTGTACTGTC	<i>XhoI</i> at 5' end
RshIFgmtIRvs	GTATAATGTATGCTATACGAAGTTATCAAGATTGTCGTCGCCCAAGCGC	Overlaps 5' end of <i>loxP</i> ; Confirmation of genomic exchange of <i>rshI</i> with <i>Gm^R</i>
loxGentFwd	ATAACTTCGTATAGCATAACATTATACGAAGTTATGACGCACACCGTGGAAACG	Introduces <i>loxP</i> to 5' end of <i>Gm^R</i>
loxGentRvs	ATAACTTCGTATAATGTATGCTATACGAAGTTATTTAGGTGGCGGTACTTGGGTC	Adds <i>loxP</i> to 3' end of <i>Gm^R</i>
RshIFrgmt2Fwd	TTGGGGCGACGACAATCTTGGGTCGACTCTAGAGGATCCCC	Overlaps 3' end of RSP_3757
RshIFrgmt2Rvs	CGTGTGGTAAATGGCTGATCGGAATTCGAGCTCGGTACCC	Overlaps 5' end of RSP_3758
RshIFgmt3Fwd	GTATAGCATAACATTATACGAAGTTATGATCAGCCATTTACCACACGTAATTGG	Overlaps 3' end of <i>loxP</i> ; Confirmation of genomic exchange of <i>rshI</i> with <i>Gm^R</i>
RshIFgmt3Rvs	TGTAAC TAGTCTGAACAACGATGCCTGGCATTACG	<i>SpeI</i> at 3' end
RshIConfirmIFwd	CTAGGTGGATCGCTTCGAGGAGGG	Confirmation of genomic exchange of <i>rshI</i> with <i>Gm^R</i>
RshIConfirm3Rvs	GCCATGAAACCGCCACTGCGCCG	Confirmation of genomic exchange of <i>rshI</i> with <i>Gm^R</i>
RshIConfirm4Fwd	CTCTATACAAAGTTGGGCCATACGGG	Confirmation of genomic exchange of <i>rshI</i> with <i>Gm^R</i>
RshIConfirm6Rvs	CGCCCCAGACGAATGCAGCCG	Confirmation of genomic exchange of <i>rshI</i> with <i>Gm^R</i>
EcoCreFwd	CTGTGAATTCGGAGAAGCTGAATGTCCAATTTACTGACCGTACACC	Amplification/cloning of Cre recombinase
PstCreRvs	TGTACTGCAGCTAATCGCCATCTTCCAGCAGG	Amplification/cloning of Cre recombinase
<i>Primers used for construction of pBBRRWsLsM</i>		
GenBglIIMut.for	CCGCGTAGTAAAATCTATATCTATGATCTCGC	Silent site-directed mutagenesis of <i>BglII</i> site in <i>Gm^R</i>
GenBglIIMut.rev	GCGAGATCATAGATATAGATTTCACTACGCGG	Silent site-directed mutagenesis of <i>BglII</i> site in <i>Gm^R</i>
GenLIC.for	GCCGCCAAGGATGACGCACACCGTGGAAACGG	LIC insertion of <i>Gm^R</i> into pBBRKW2(AgeI).
GenLIC.rev	AGCGTTTAGGTGGCGGTACTTGGGTCG	LIC insertion of <i>Gm^R</i> into pBBRKW2(AgeI)
BamHISacI.for	ATATGGATCCATCACAATGGCTGACAAGACC	Amplification/cloning of <i>pufX</i> and 3' flanking sequences
BamHISacI.rev	ATATGAGCTCCGCCACGTCATGGGCGATCTGG	Amplification/cloning of <i>pufX</i> and 3' flanking sequences



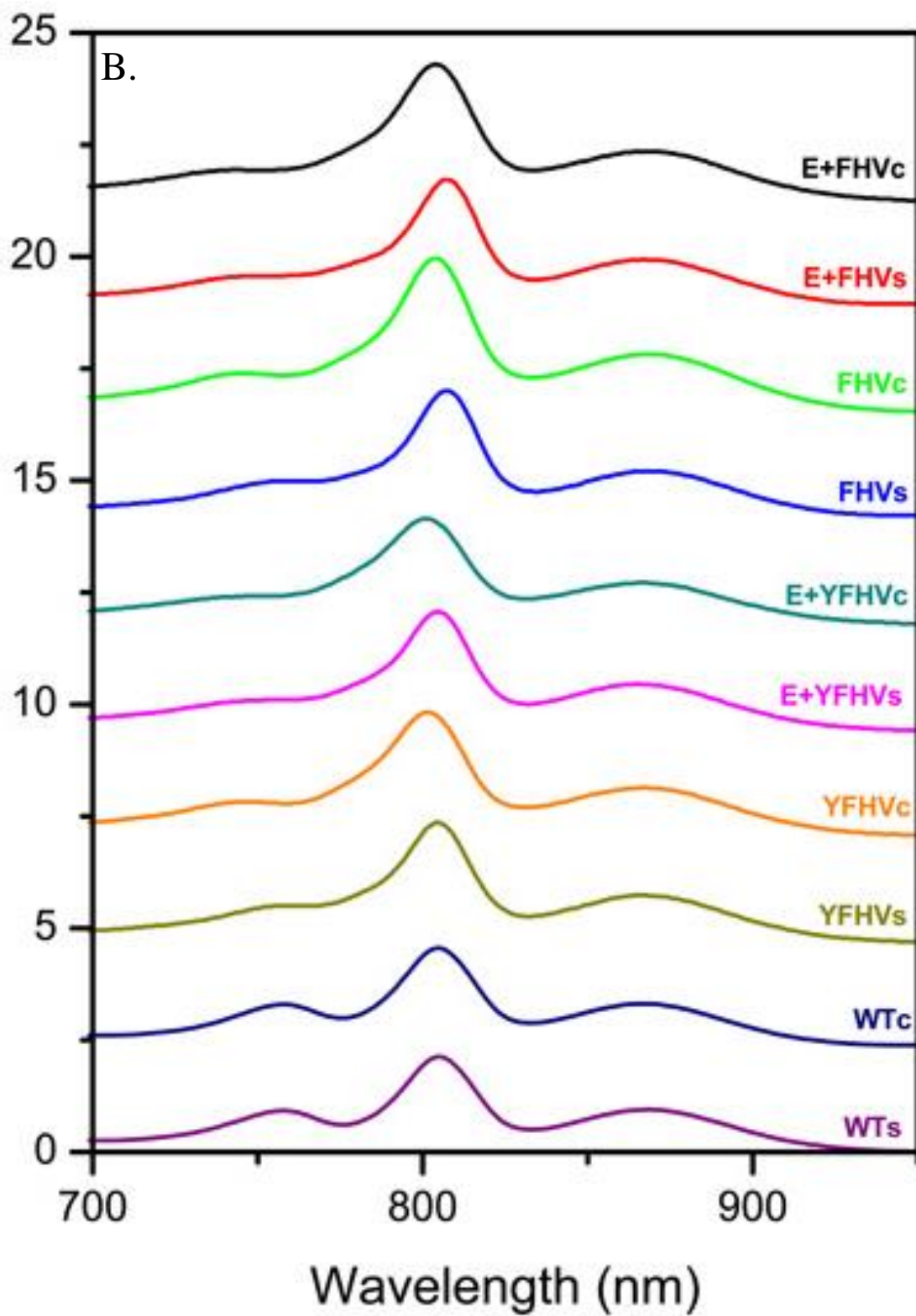
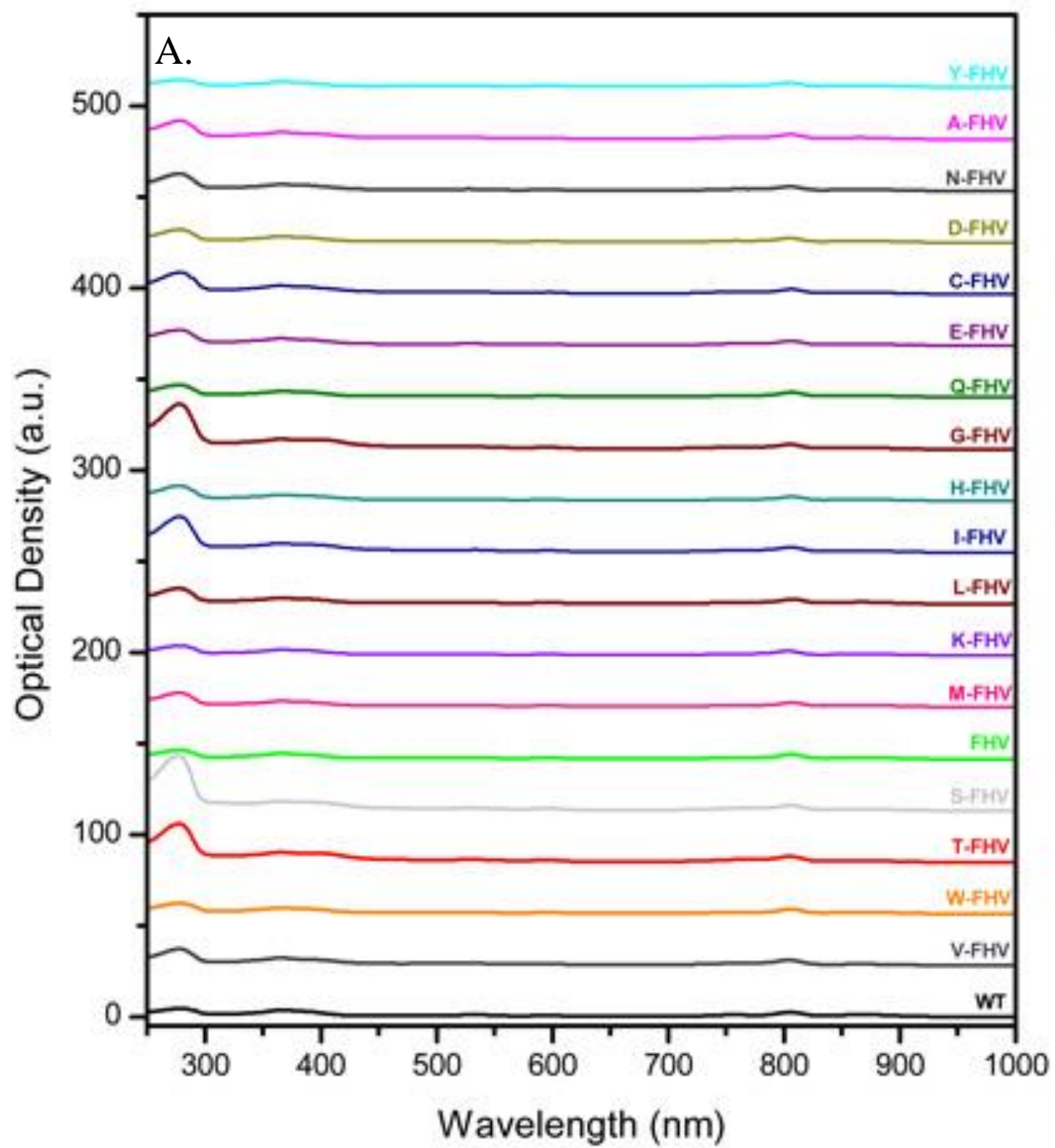


Figure S1. Ground-state absorption spectra of selected mutant and WT *R. sphaeroides* (s) and *R. capsulatus* (c) RCs that were subjected to further characterization. A: full spectrum from 250-1000 nm; B: expansion of the Q_y region from 700-950 nm.



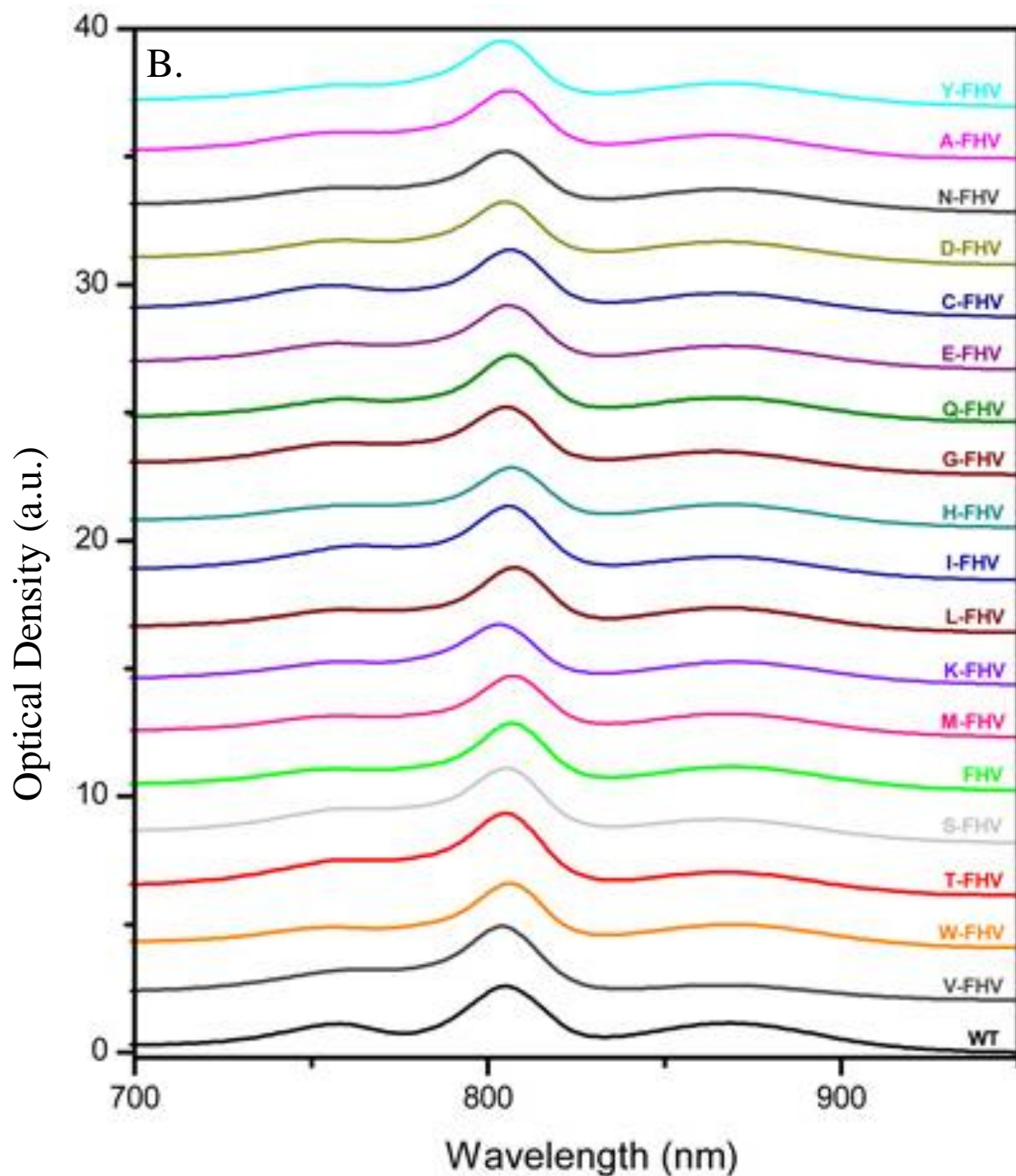
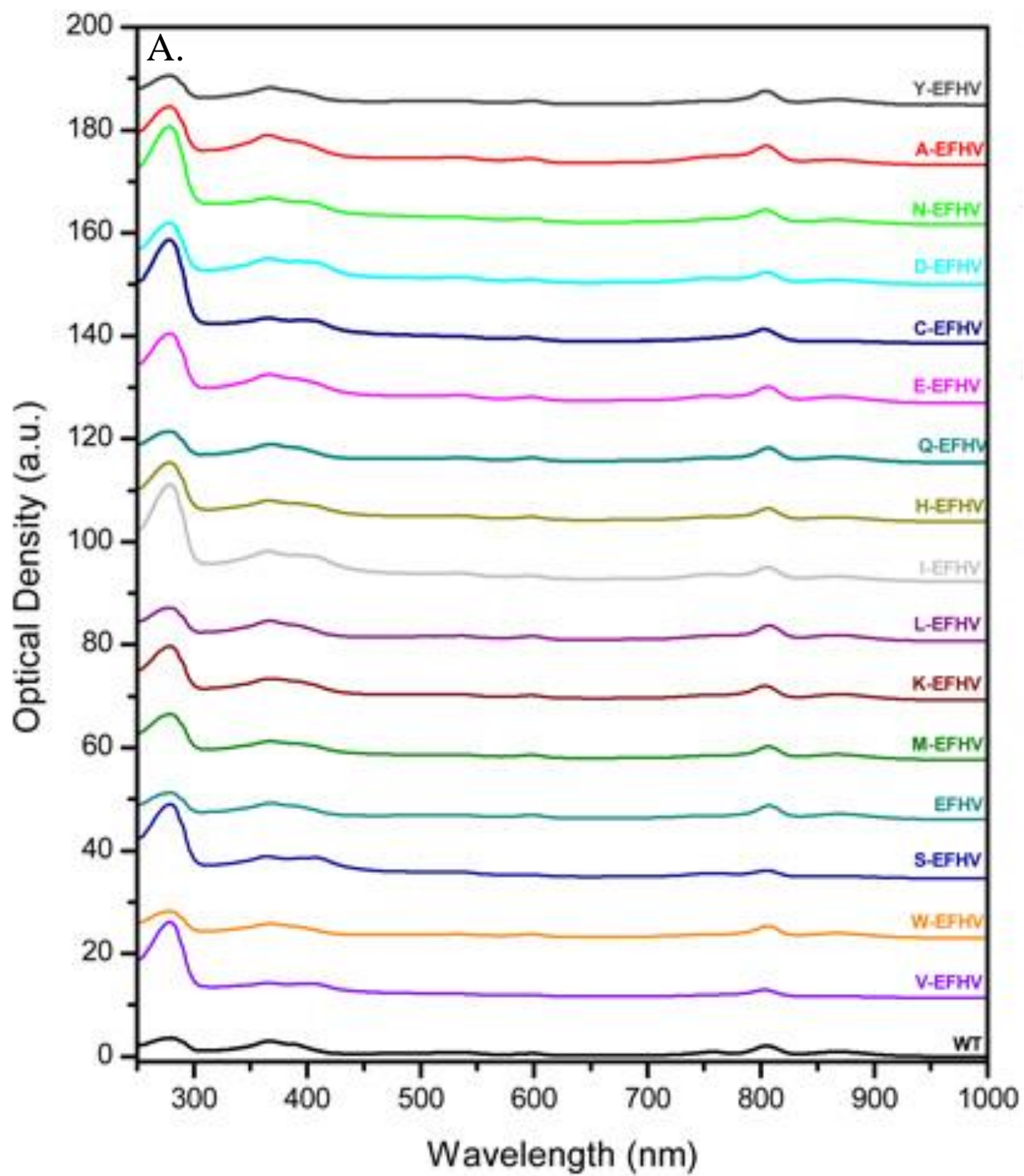


Figure S2. Ground-state absorption spectra of the *F(L181)X+ FHV* mutant and WT *R. sphaeroides* RCs. A: full spectrum from 250-1000 nm; B: expansion of the Q_y region from 700-950 nm.



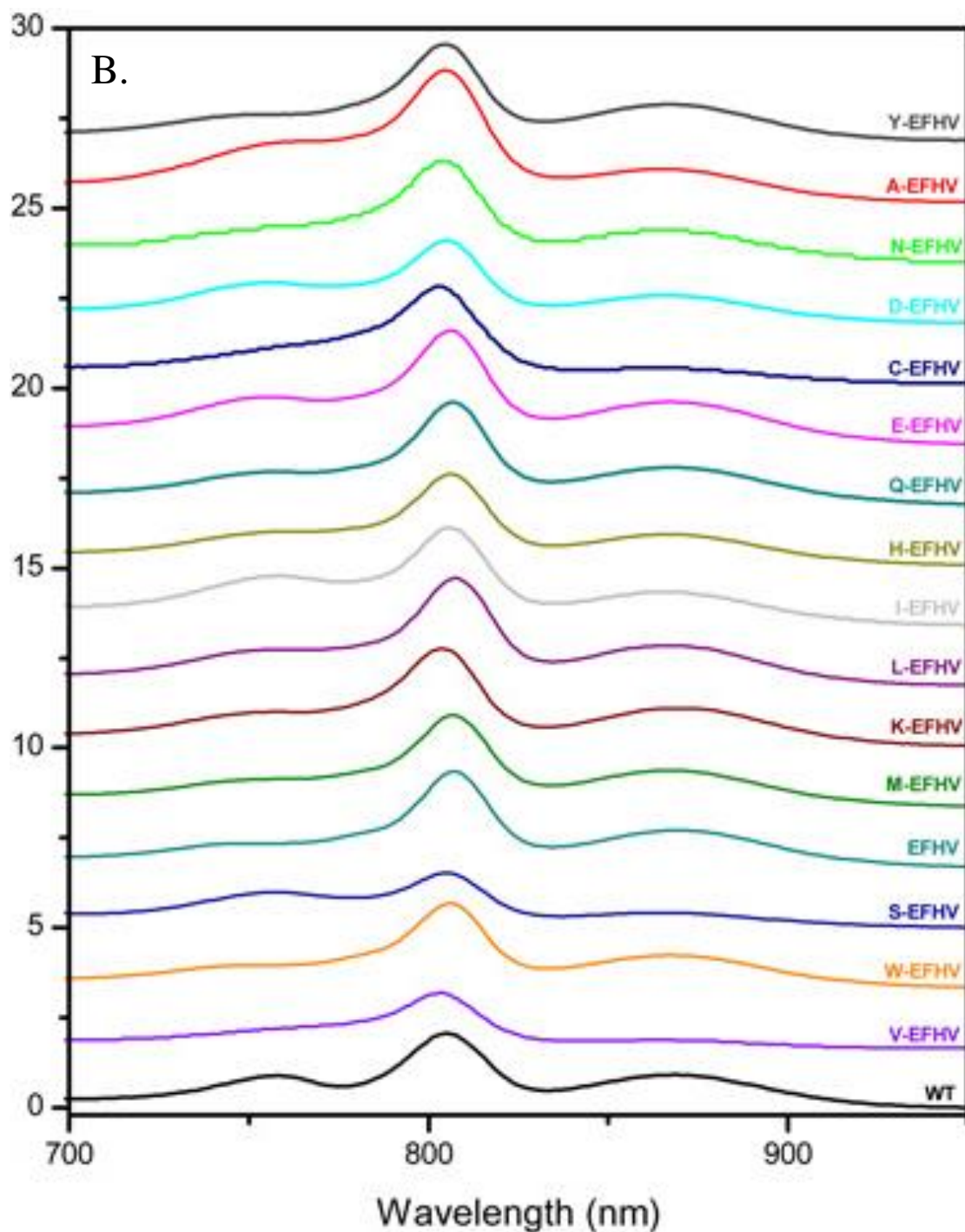


Figure S3. Ground-state absorption spectra of the T(M133)E + F(L181)X+ FHV mutant and WT *R. sphaeroides* RCs. A: full spectrum from 250-1000 nm; B: expansion of the Q_y region from 700-950 nm.

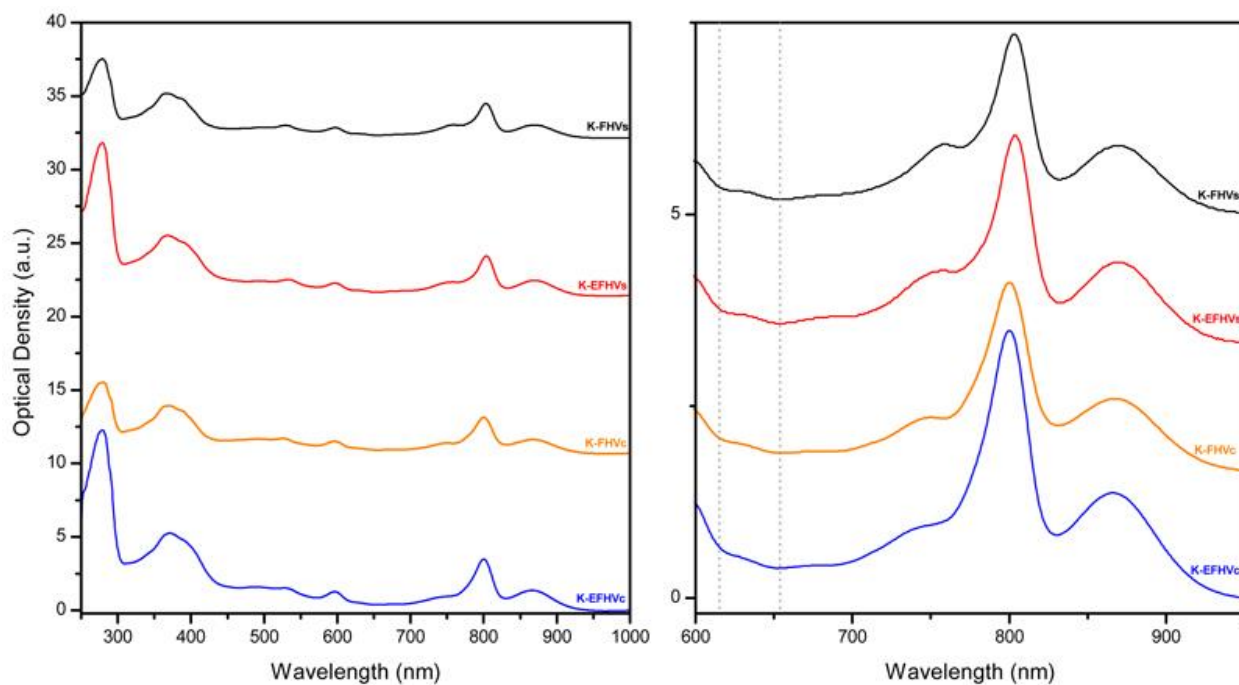


Figure S4. Ground-state absorption spectra of *R. sphaeroides* (s) and *R. capsulatus* (c) RCs containing *F(L181)K*. Left: full spectrum from 250-1000 nm; Right: expansion of the Q_y region from 600-950 nm, with dashed lines bracketing the absorption in the Q_x region that is indicative of hexacoordinated B_B .

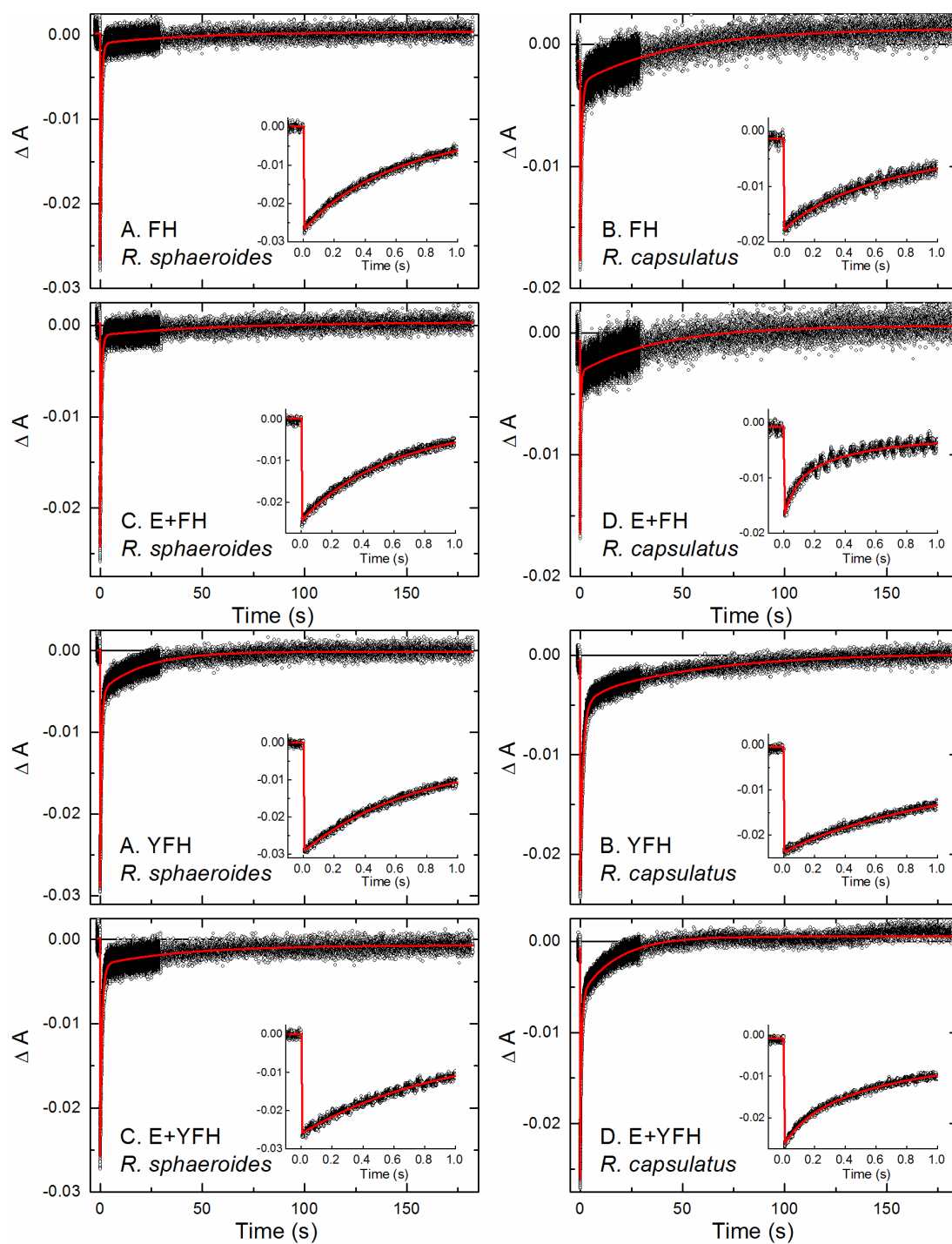


Figure S5. Kinetic profiles for $P^+Q_B^-$ charge recombination in a subset of mutant RCs containing Q_A . A fast, ~ 100 ms component that appears in *R. capsulatus* mutants (not seen in *R. sphaeroides* mutant RCs) with the V(M131)E substitution is attributed $P^+Q_A^-$ charge recombination in that fraction of RCs in which the Q_B site is not occupied (see insets).

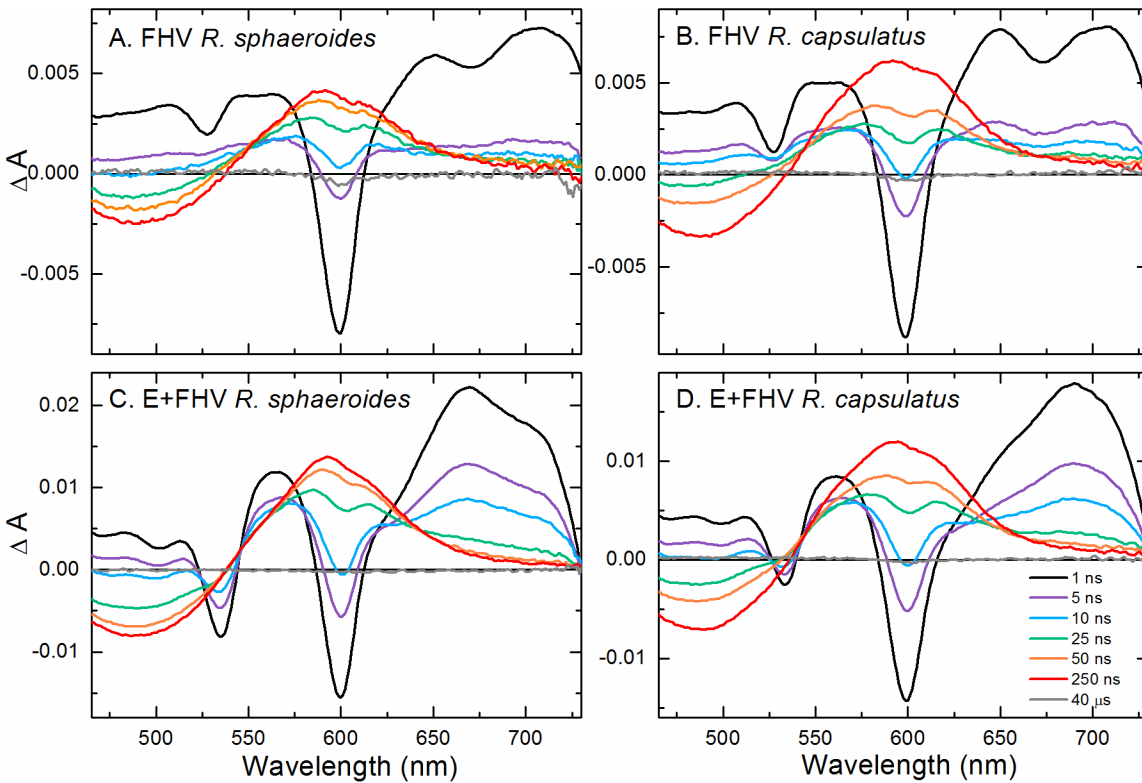


Figure S6. TA spectra obtained 1 ns to 40 μ s after a \sim 100-fs excitation flash at 865 nm for *R. sphaeroides* (panels A and C) and *R. capsulatus* (panels B and D) mutant RC samples in the FHV background without (panels A and B) and with (panels C and D) the V/T(M131/M133)E mutation.

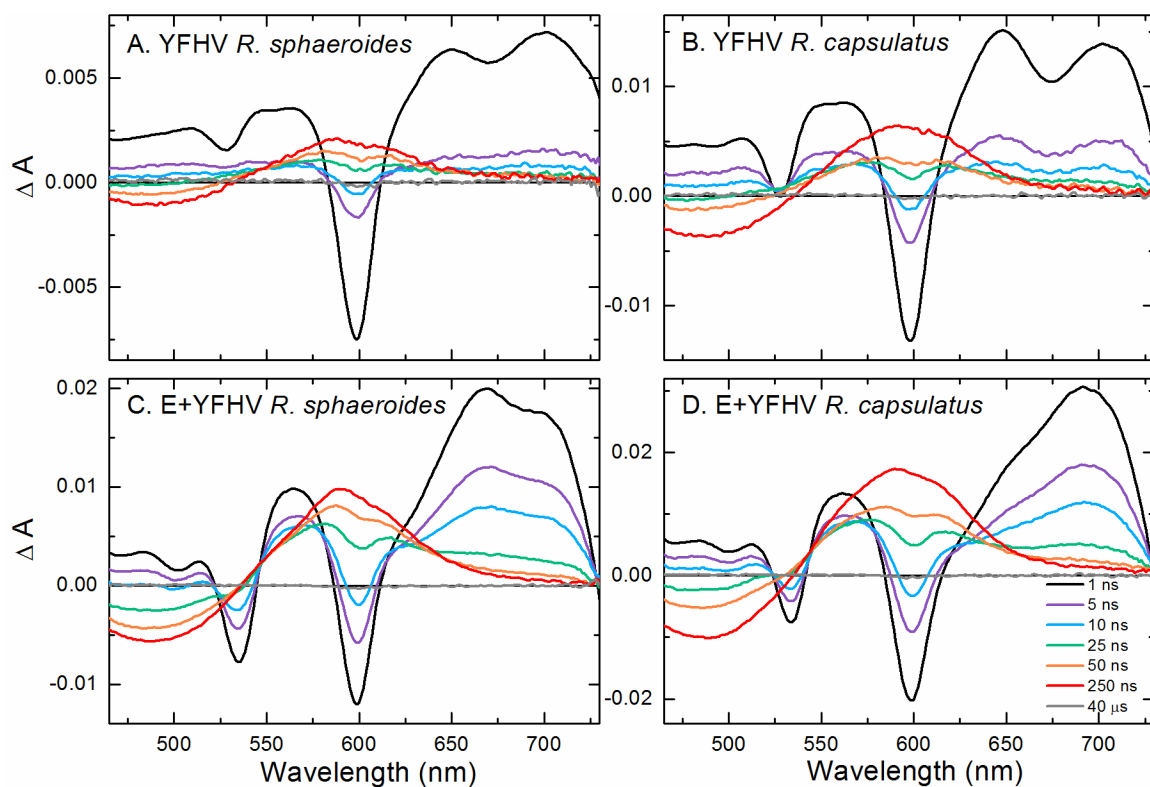


Figure S7. TA spectra obtained 1 ns to 40 μ s after a \sim 100-fs excitation flash at 865 nm for *R. sphaeroides* (panels A and C) and *R. capsulatus* (panels B and D) mutant RC samples in the YFHV background without (panels A and B) and with (panels C and D) the V/T(M131/M133)E mutation.

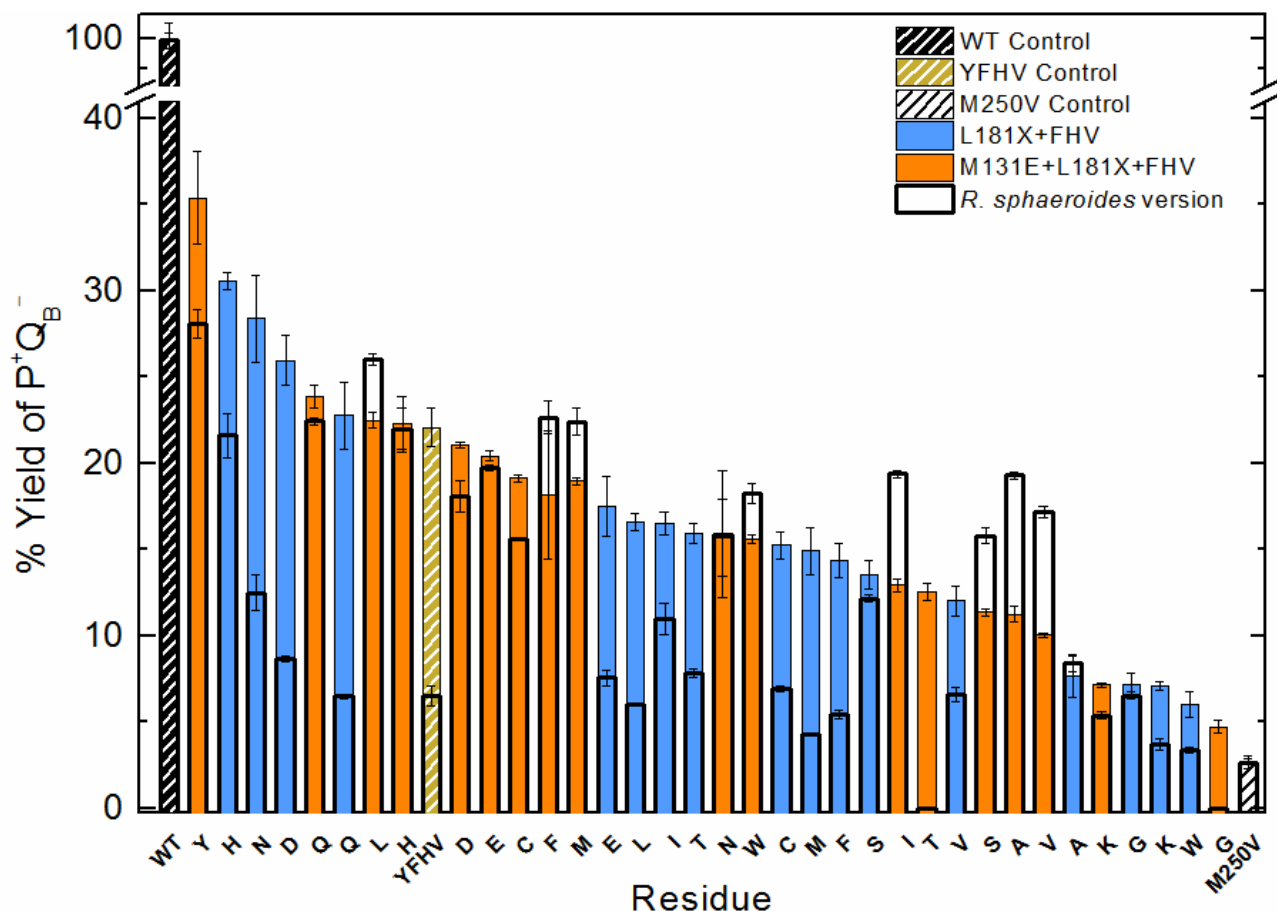


Figure S8. $P^+Q_B^-$ yields of *R. capsulatus* (filled bars) and *R. sphaeroides* (open bars) mutant RCs (as compared to WT, black dashed bar) obtained after a 7-ns, 532 nm excitation flash utilized by the millisecond screening assay. Filled, blue bars represent mutants with the F(L181)X+FHV background. Filled orange bars represent mutants with the V/T(M131/M133)E substitution in addition to the F(L181)X+FHV background. The open, black bars represent the *R. sphaeroides* versions of the mutant RCs.

Appendix 5. Supporting Information for Chapter 7.

Table S1. Wavelengths of BPh spectral features in ultrafast transient difference spectra.

Mutant	State	$Q_x(0,0)$	$Q_x(1,0)$	Q_x
RC		bleach λ (nm)	bleach λ (nm)	vibrational energy ^a (cm^{-1})
Φ_B -F β_A V	$P^+\Phi_B^-$	539	504	1288
E Φ_B -F β_A V	$P^+\Phi_B^-$	539	506	1210
F β_A V	$P^+H_B^-$	527	492	1350
E-F β_A V	$P^+H_B^-$	533	500	1358
β_A V	$P^+H_B^-$	527	492	1350
V	$P^+H_A^-$	542	505	1352

^a From prior two columns.

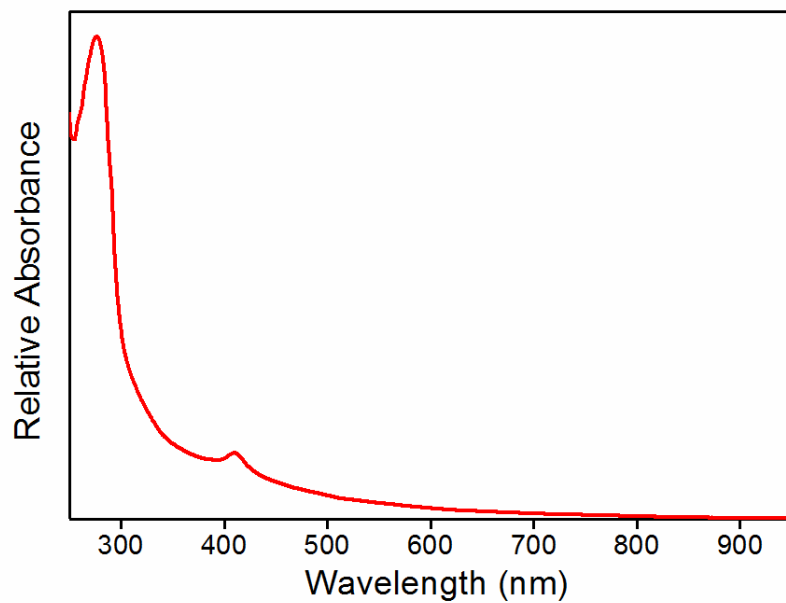


Figure S1. Spectrum of a component that co-purifies with the $E\Phi_B$ - $F\beta_{AV}$ and Φ_B - $F\beta_{AV}$ RCs. The ground state spectra of the two Φ_B mutants shown in Fig. 2 (main paper) had this spectrum subtracted from them in order to better resolve the 525-550 nm Q_x bands of the BPh pigments (Φ_B and H_B).

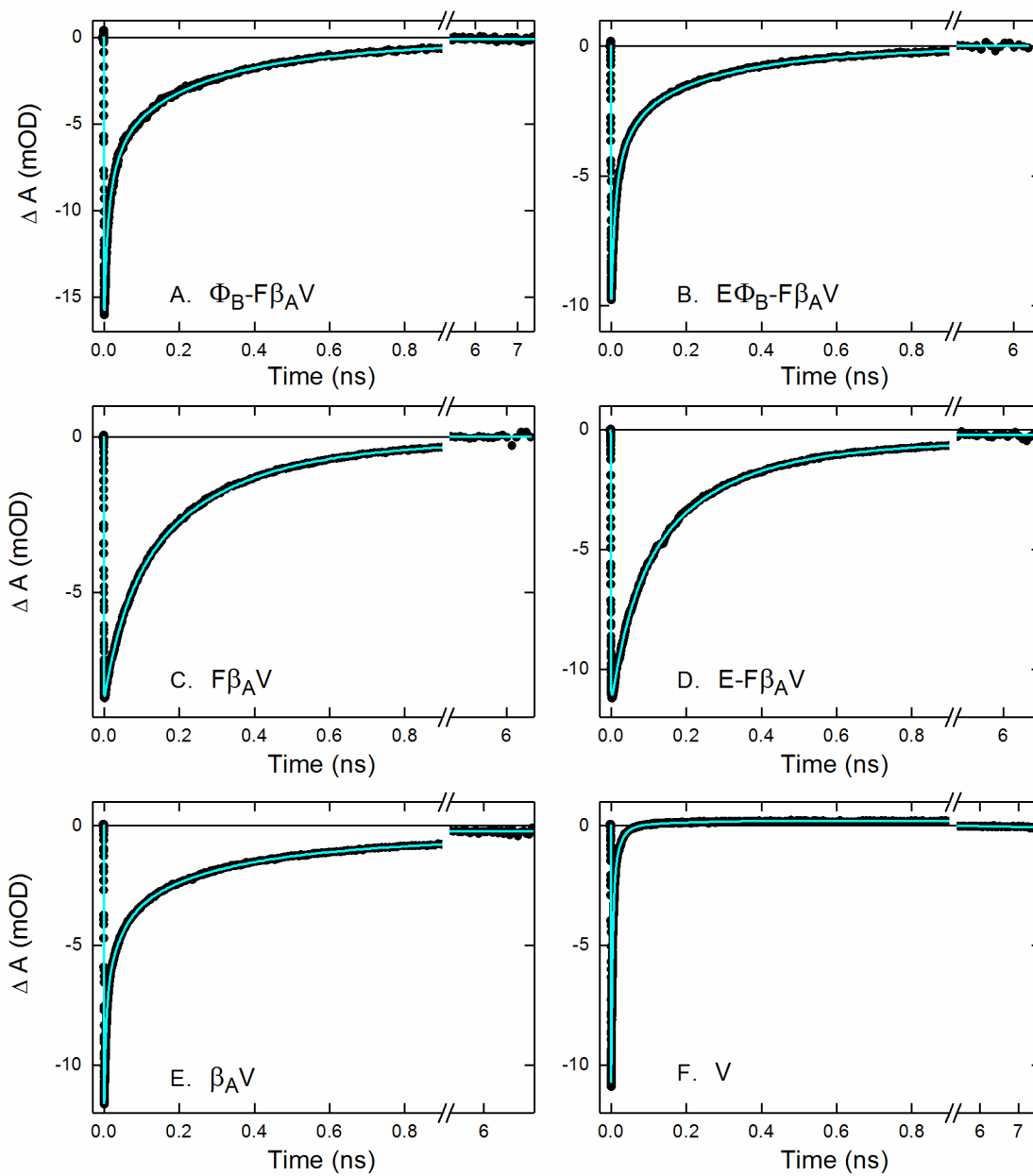


Figure S2. Multi-exponential fits of stimulated emission (~ 920 nm) for the Φ_B mutant RCs and associated controls. Lifetimes and amplitudes are given in Table 2.

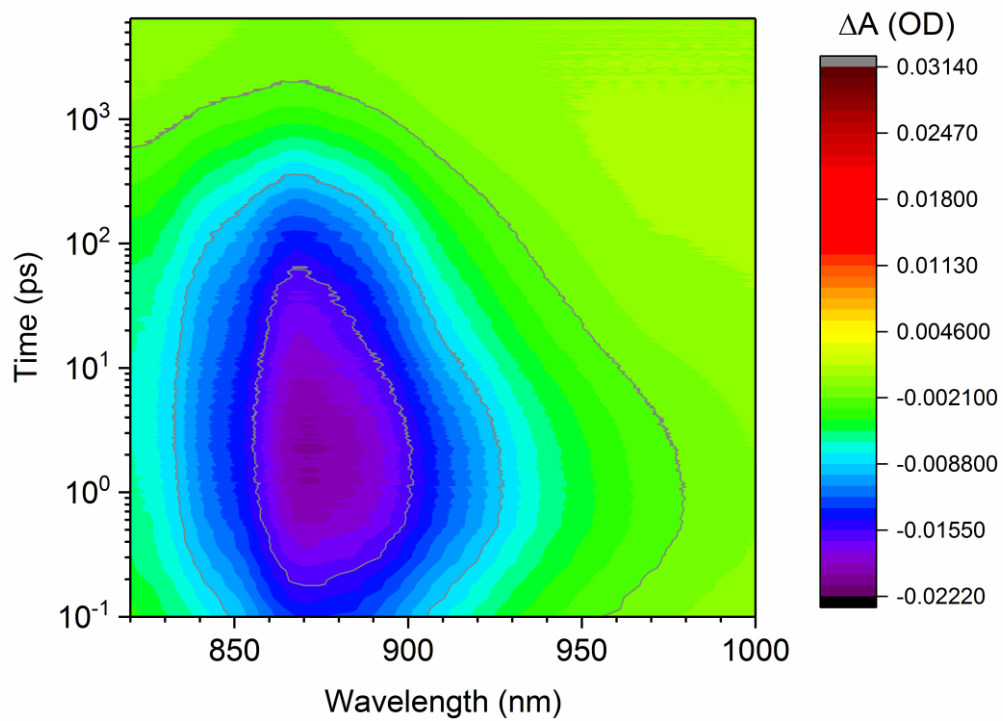


Figure S3. Contour surface for the TA data in the NIR region for the Φ_B -F β_{AV} mutant.

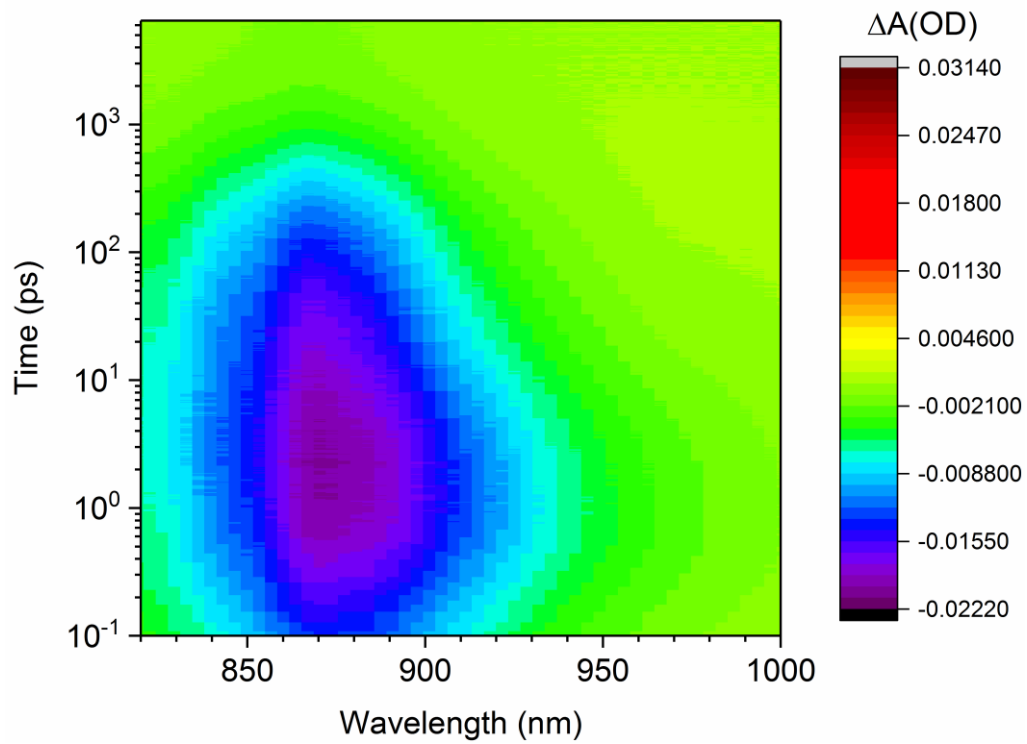


Figure S4. Heat map for the TA data in the NIR region for the Φ_B -F β_A V mutant.

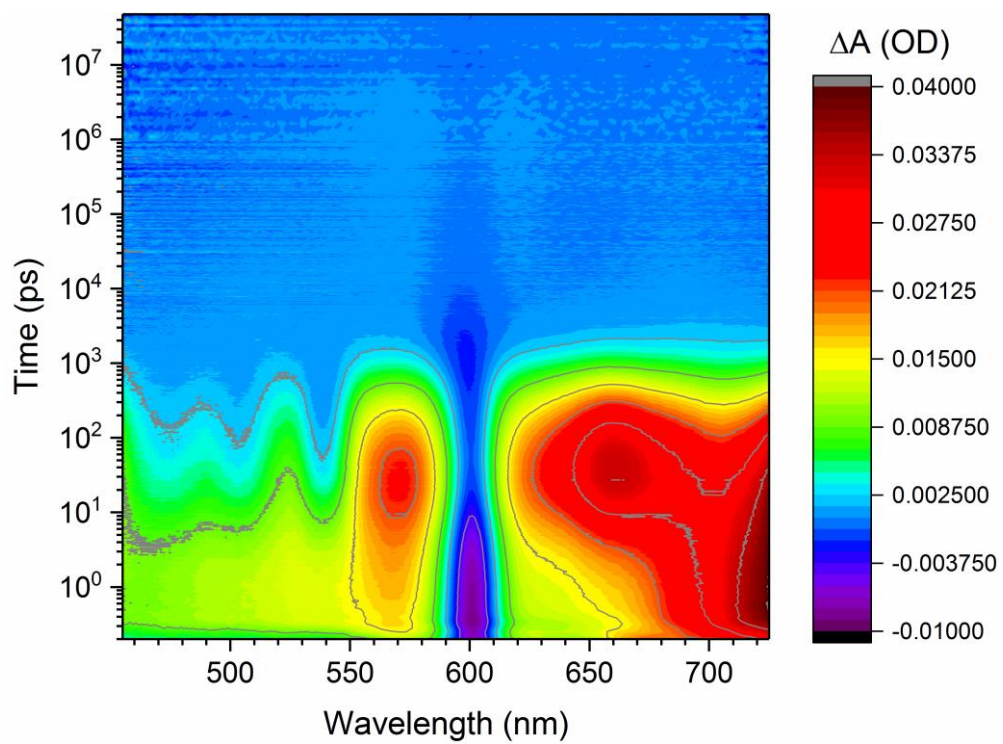


Figure S5. Contour surface for the TA data in the visible region for the Φ_B -F β_A V mutant.

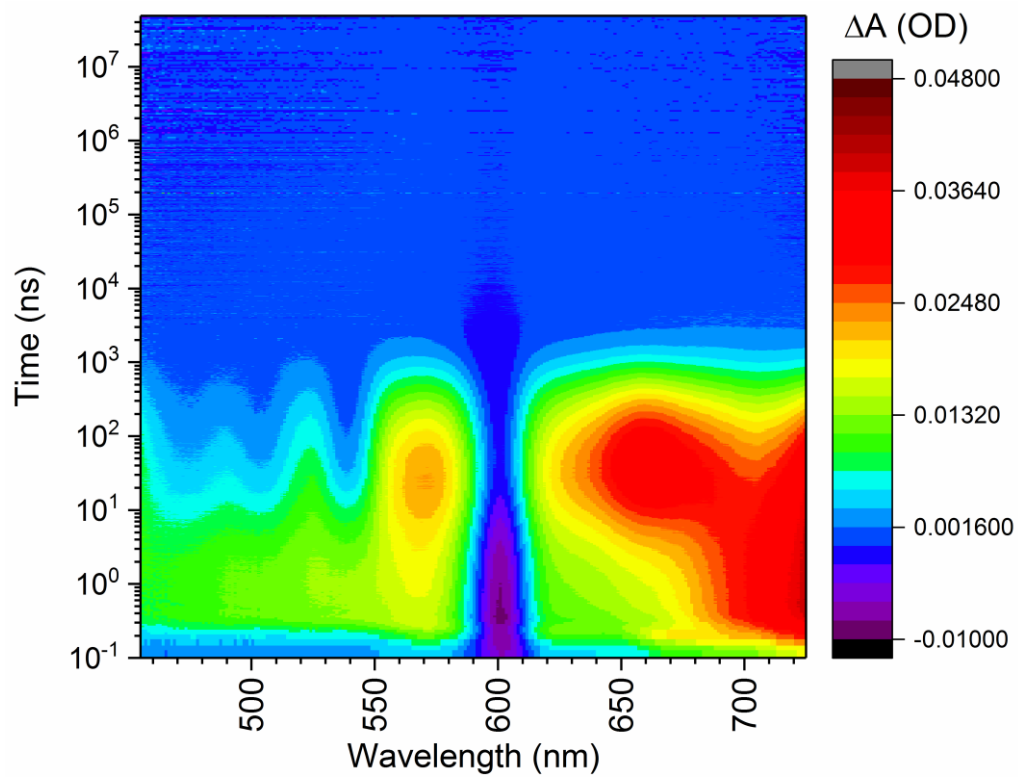


Figure S6. Heat map for the TA data in the visible region for the Φ_B -F β_{AV} mutant.

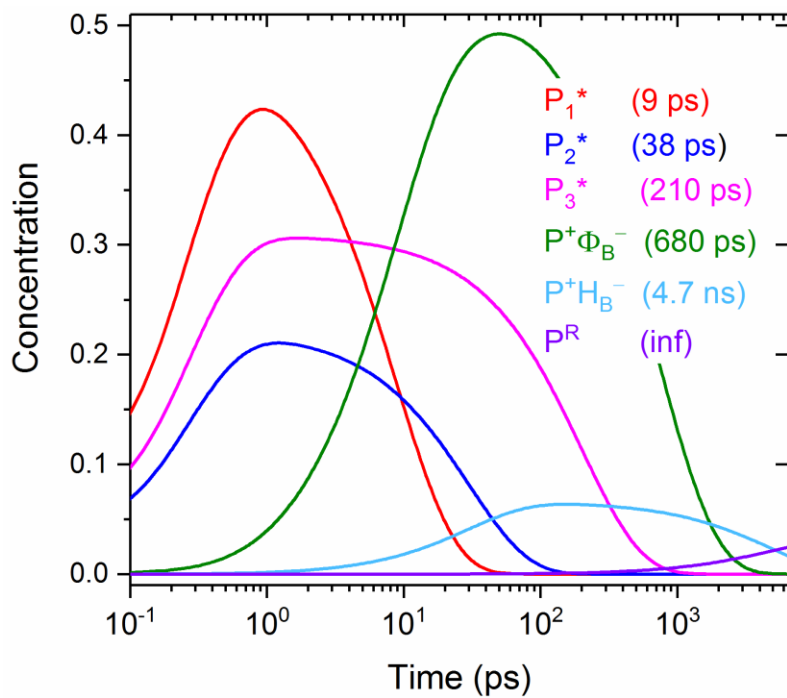


Figure S7. Concentrations of the species versus time for the SADS obtained from simulations of the near TA data in the NIR region for the Φ_B -F β_{AV} mutant.

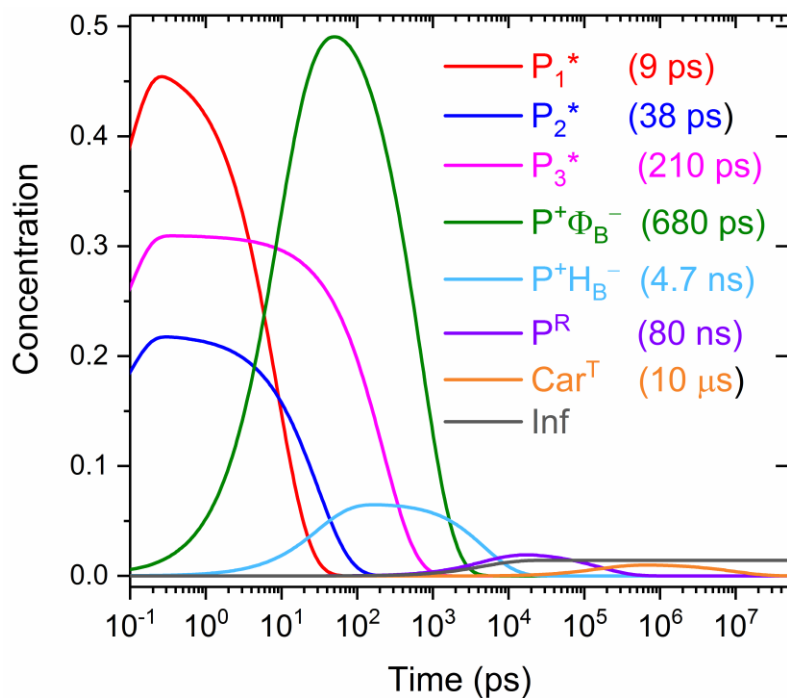


Figure S8. Concentrations of the species versus time for the SADS obtained from simulations of the TA data in the visible region for the Φ_B -F β_{AV} mutant. This figure reproduces the top panel of Figure 11 of the main paper.

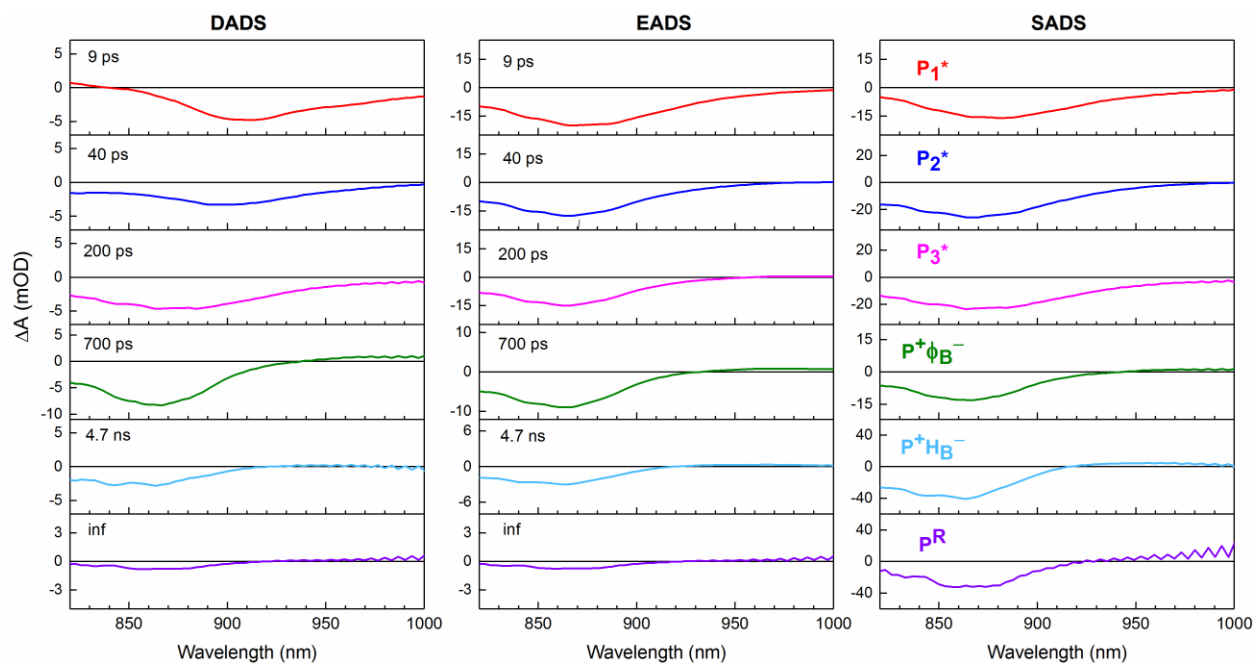


Figure S9. Spectra from global analysis (DADS, EADS, SADS) for the transient states/species of the NIR region TA data for the $E\Phi_B$ - $F\beta_{AV}$ mutant.

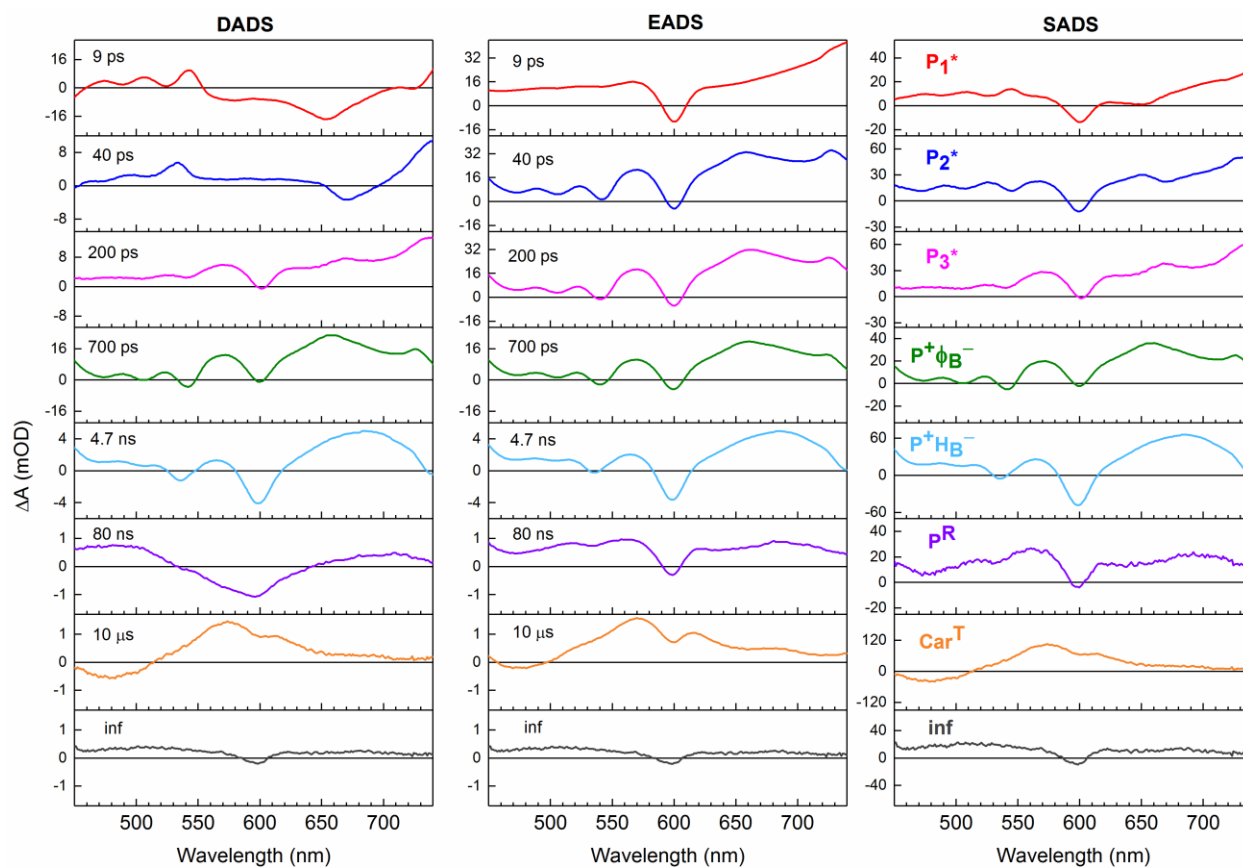


Figure S10. Spectra from global analysis (DADS, EADS, SADS) for the transient states/species of the TA data in the visible region for the $E\Phi_B$ - $F\beta_{AV}$ mutant.

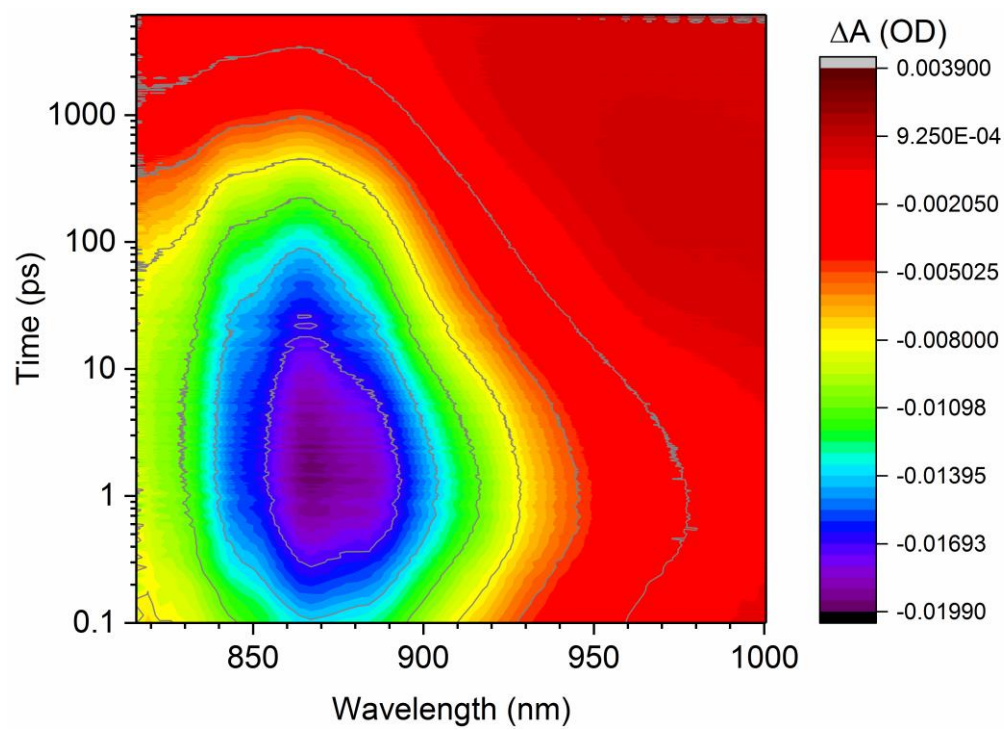


Figure S11. Contour surface for the TA data in the NIR region for the E Φ_B -F β_{AV} mutant.

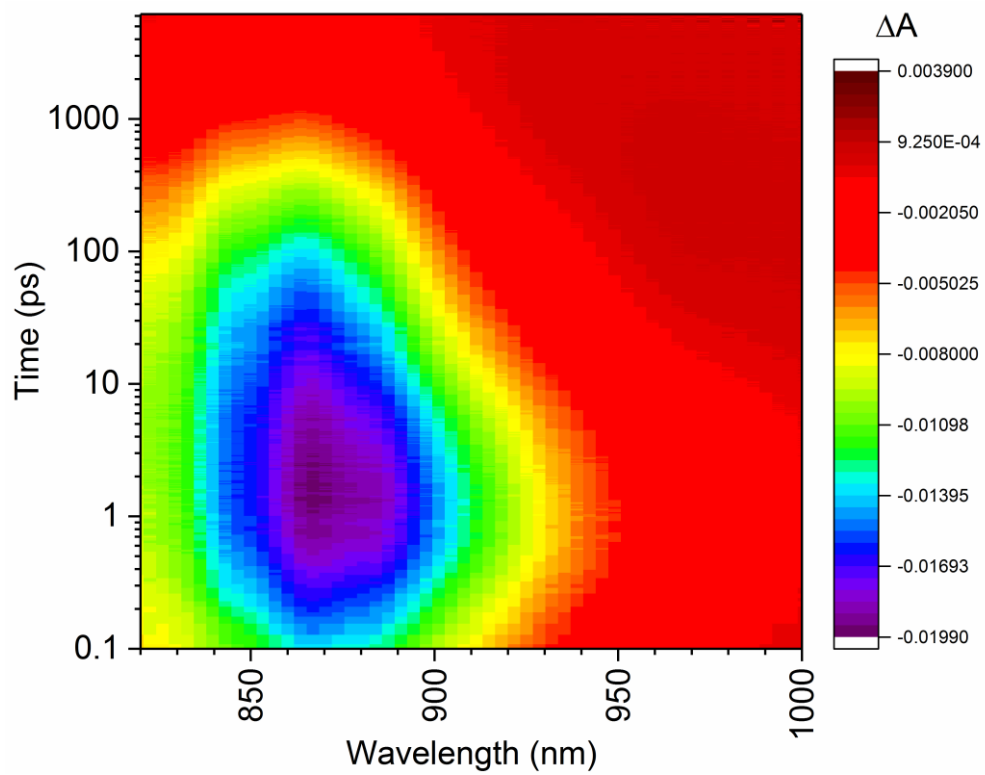


Figure S12. Heat map for the TA data in the NIR region for the E Φ_B -F β_{AV} mutant.

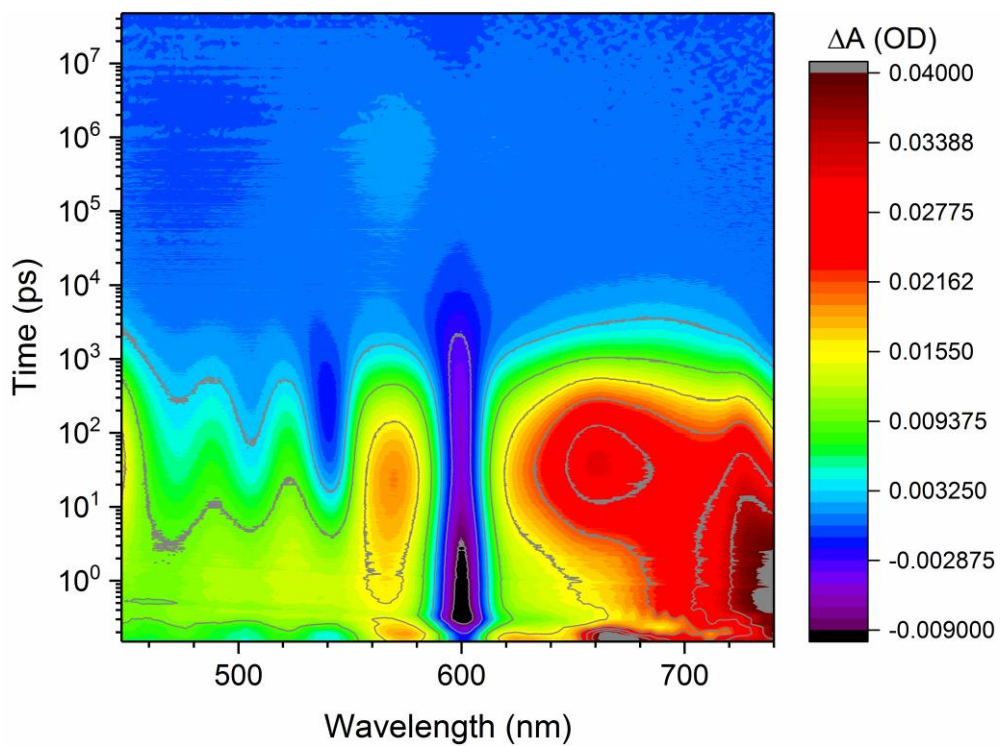


Figure S13. Contour surface for the TA data in the visible region for the $E\Phi_B$ - $F\beta_{AV}$ mutant.

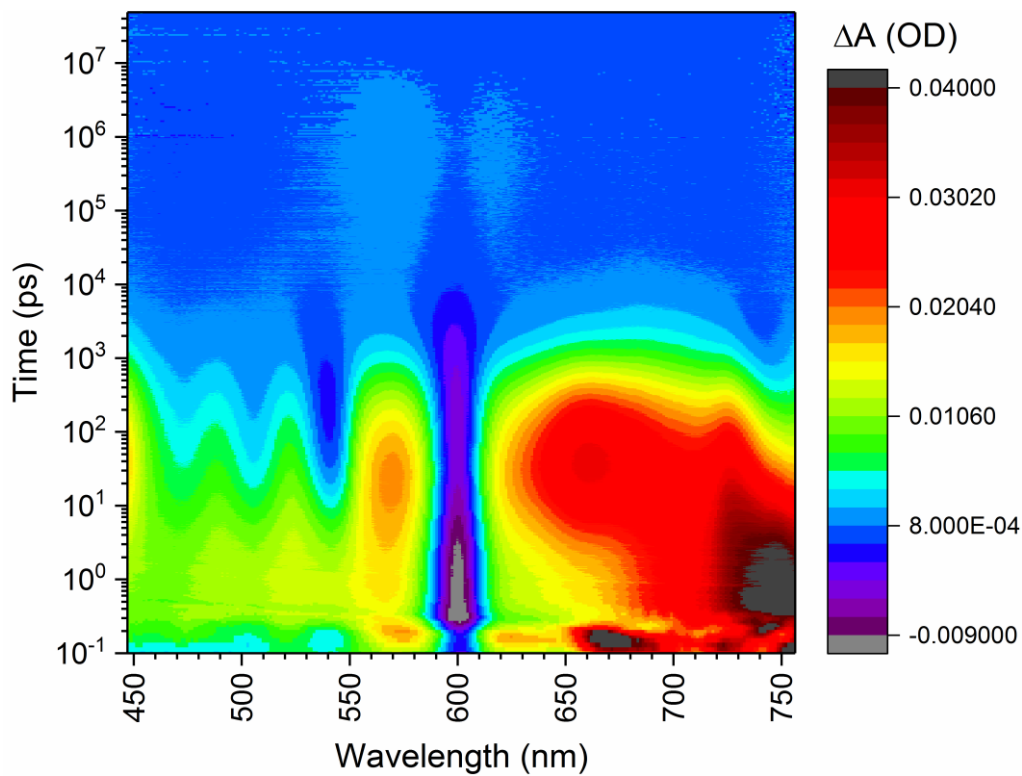


Figure S14. Heat map for the TA data in the visible region for the $E\Phi_B$ - $F\beta_{AV}$ mutant.

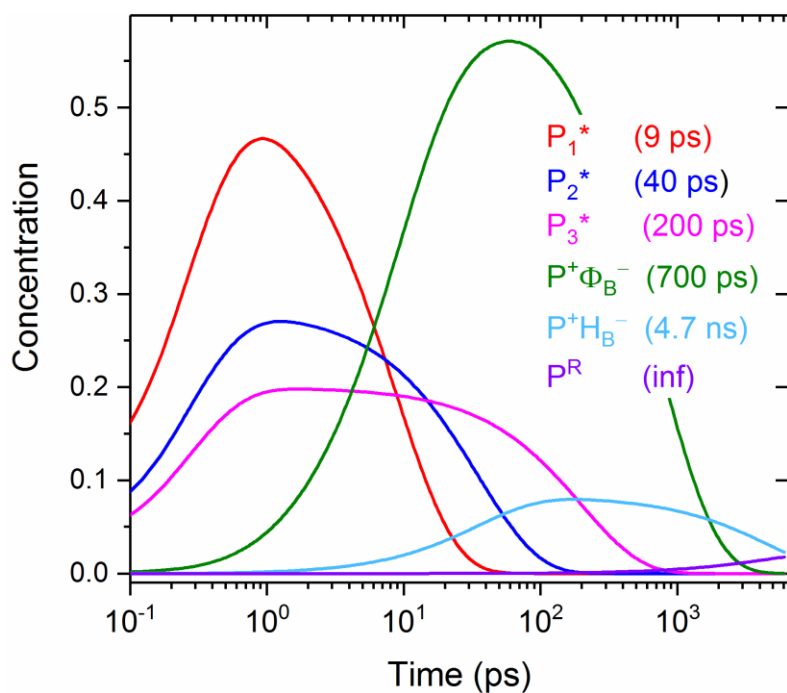


Figure S15. Concentrations of the species versus time for the SADS obtained from simulations of the data in the NIR region for the $E\Phi_B$ - $F\beta_{AV}$ mutant.

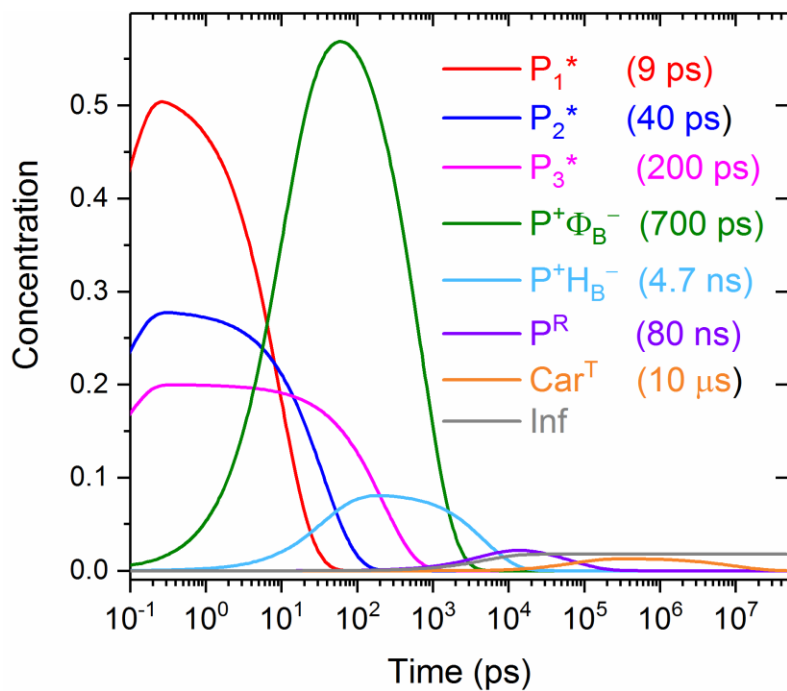


Figure S16. Concentrations of the species versus time for the SADS obtained from simulations of the TA data in the visible region for the $E\Phi_B$ - $F\beta_{AV}$ mutant. This figure reproduces the bottom panel of Figure 11 of the main paper.

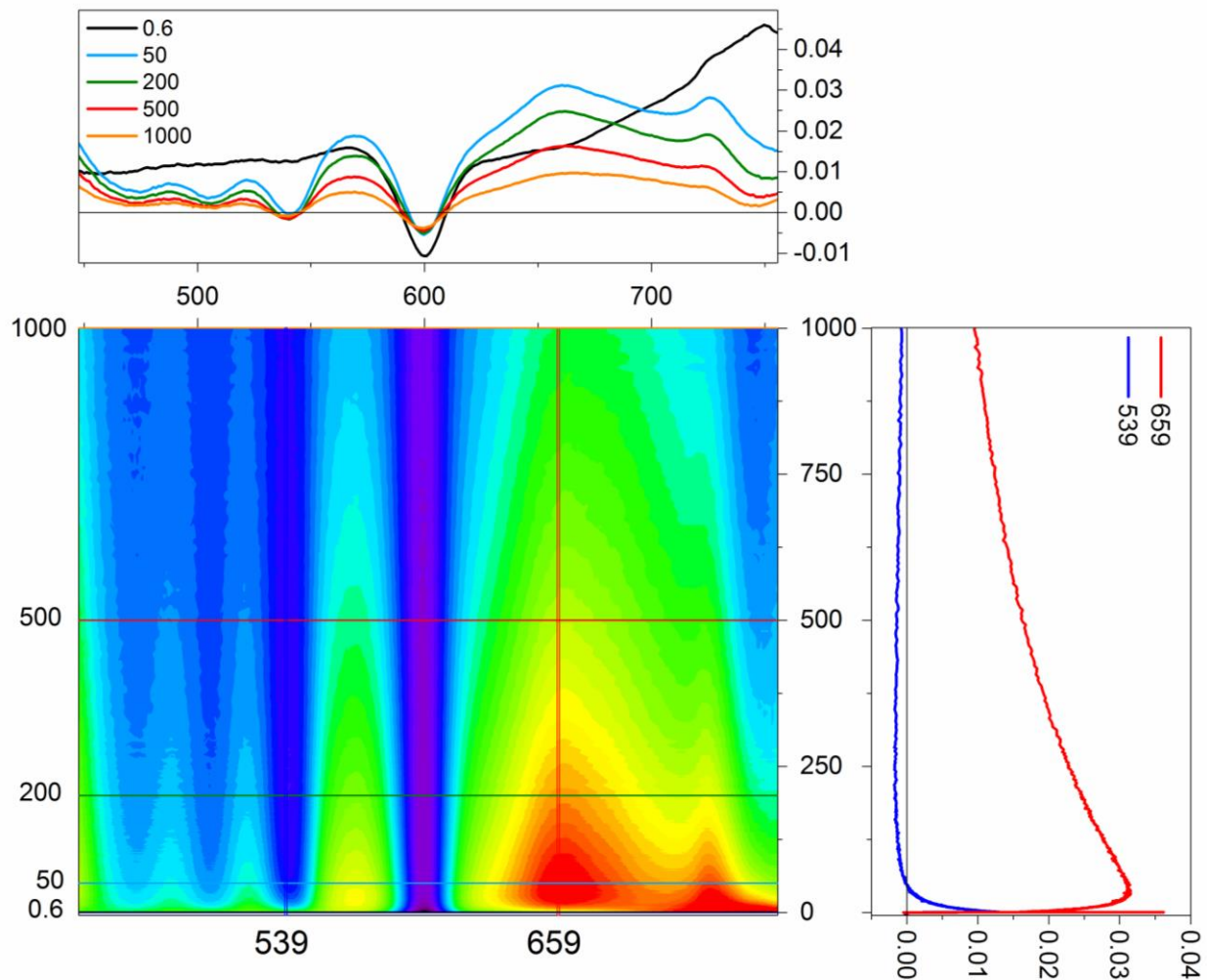


Figure S17. Contour plot of TA data in the visible region for the $E\Phi_B$ - $F\beta_{AV}$ mutant. While data were recorded to $\sim 40 \mu\text{s}$, only times from 0 – 1000 ps are included in the contour so that key features at early times are clearly shown.

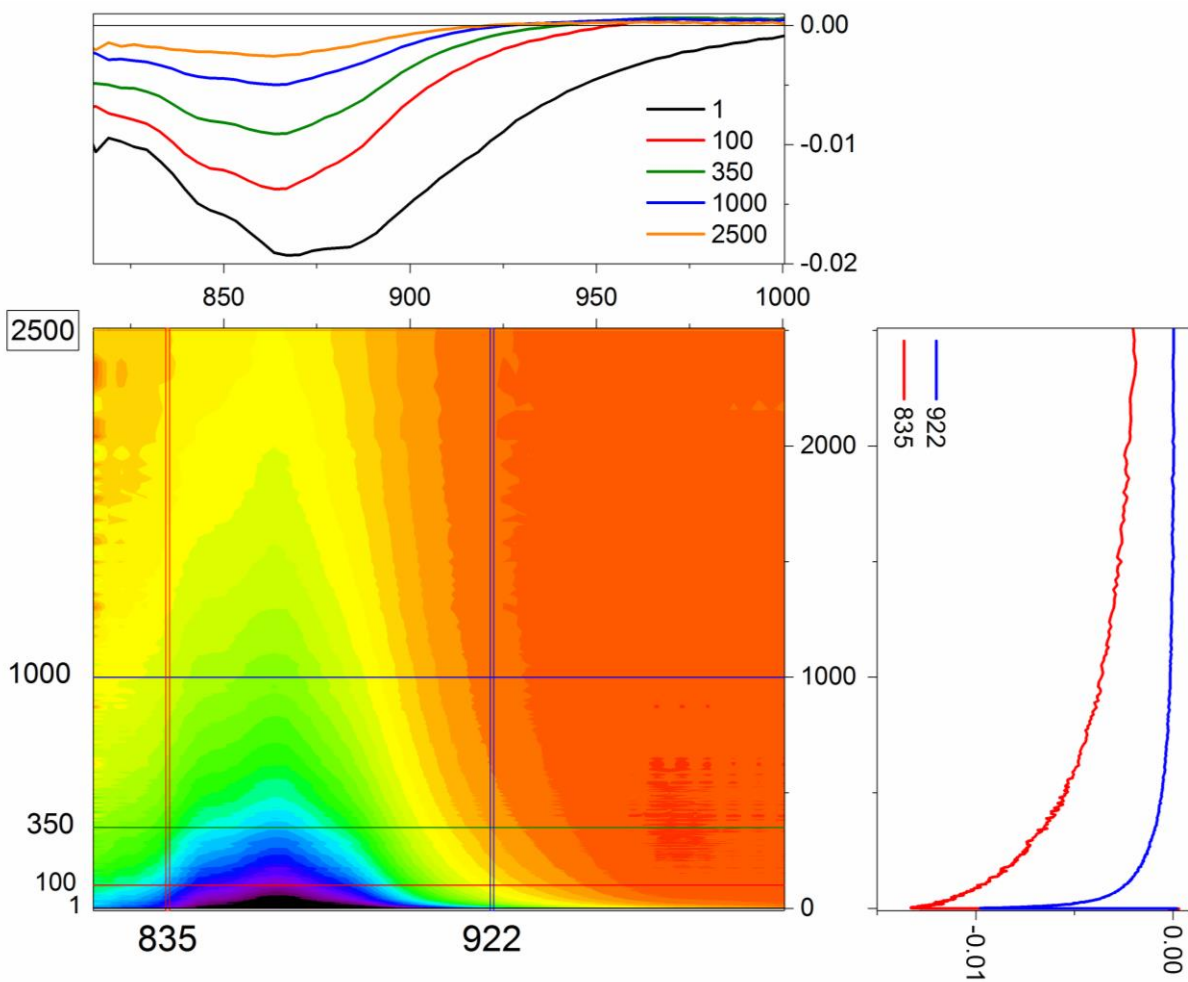


Figure S18. Contour plot of TA data in the NIR region for the $E\Phi_B$ - $F\beta_{AV}$ mutant. While data were recorded to ~ 7 ns, only times from 0 – 2500 ps are included in the contour so that key features at early times are clearly shown.

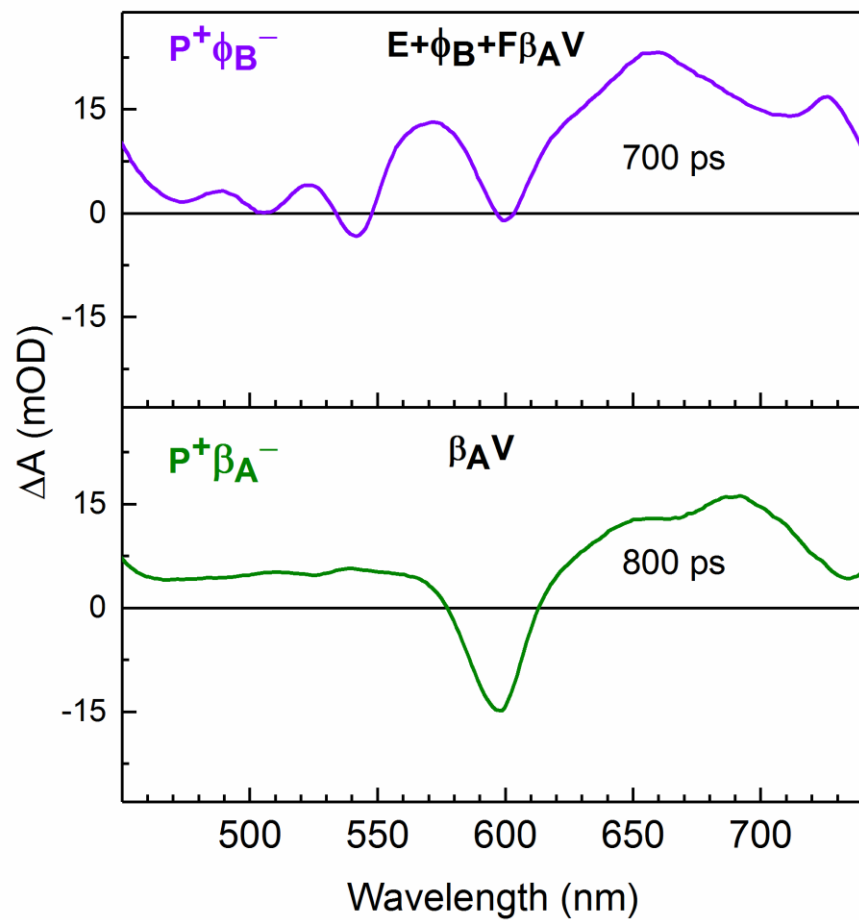


Figure S19. Comparison of DADS of charge-separated states in select mutant RCs. (A) $P^+\Phi_B^-$ in the $E\Phi_B-F\beta_{AV}$ mutant ($\Phi-F\beta_{AV}$ is similar). (B) $P^+\beta_A^-$ in the β_{AV} mutant.